New Pressure Swing Adsorption Cycles for Hydrogen Purification from Steam Reforming Off-Gases

A Dissertation presented to the
UNIVERSITY OF PORTO
for the degree of Doctor in
Chemical and Biological Engineering
by

Filipe V. S. Lopes

Supervisor: Prof. Alírio E. Rodrigues
Co-supervisor: Dr. Carlos A. Grande

Associated Laboratory LSRE-LCM
Department of Chemical Engineering
Faculty of Engineering
University of Porto
December, 2010

Acknowledgements

First I would like to express my sincere gratitude to my supervisor Prof. Alírio E. Rodrigues, for the opportunity given to me of performing research at the Associated Laboratory LSRE-LCM. I would also like to thank my co-supervisor Dr. Carlos A. Grande, for his constant presence in the laboratory and during the "homework" period, with the revision of several reports and drafts of manuscripts, encouraging me constantly; thank you so much for your availability and for your friendship. To my supervisors, thank you, too, for having accepted me to work with you.

Within the European Project HY2SEPS, besides Prof. Alírio E. Rodrigues and Dr. Carlos A. Grande, I also had the opportunity to work with Dr. Ana M. Ribeiro and Prof. José Miguel Loureiro. To the four, I'm deeply grateful for being always so understanding and for having always showed a constant cooperation, support and willingness so that nothing could remain incomplete or even less complete in the project, during the three years we worked together. I would like to acknowledge Prof. José Miguel Loureiro for providing the experimental set-up for the water vapour measurements. Moreover, I also would like to acknowledge the other project partners for their collaboration, particularly Dr. Vladimiros Nikolakis (FORTH/ICE-HT) and Dr. Michael Walter (Hygear B.V.).

To all LSRE colleagues, who were with me during these years, in particular Rui Ribeiro, Eduardo Oliveira, Daniel Araújo, Eduardo Borges da Silva, Simone Cavenati, Marta Abrantes, Manuela Vilarinho, Nabil Lamia, Filipe Cunha, Pedro Sá Gomes, Carla Pereira, Sofia Rodrigues, Viviana Silva, Miguel Granato, Pedro Madeira, João Pedro Lopes, Israel Pedruzzi, Isabel Martins, Miguel Teixeira, Nuno Garrido, Fátima Mota, Paulo Gomes, Raquel Cristóvão, Ganesh Kumar, Kishore Dasari, Michal Zabka, Miriam Zabkova, Ertugrul Erkoc, Paula Pinto, Vitor Vilar, Miguel Jorge, Óscar Rodriguez, Ricardo Santos, Susana Cruz, Nuno Lourenço, Paula Gomes, Vera Mata, Marta Plaza, Liu Zhen, Shen Chunzhi, Nuno Graça, Alexandre Ferreira, João Santos, Ana Paula Tavares, Sara Silvério, Mariana Moreira, Sílvia Santos, and everyone else, thanks too, for your fellowship and friendship.

Finally, I am grateful for the financial support from European Project HY2SEPS (Hybrid Hydrogen - Carbon Dioxide Separation Systems), Contract No. 019887; I also thankfully acknowledge to Foundation for Science and Technology (FCT, Portugal) the Ph. D. research fellowship SFRH/BD/44563/2008.

Porto, September 2010

Filipe V.S. Lopes

To Joana, my Parents, Family & Friends

You, Joana, my *love*, you deserve almost all my gratitude! Your tolerant support greatly encouraged me to finish this thesis! When we both share an objective, an ideal of life, in the present and for the future, everything becomes much easier! Thank you so much for having always believed in my skills and capacities!

As you, my parents, Isabel & Fernando, and my sister, Margarida, you all know that I have always and immensely appreciated your support. You have always been positive about my life decisions, although living so far away from you. Thanks for the love you give me! ... Bora too!

My close family, aunts Titi Dú & Rosa, cousins Lili, Nuno, Mia, Paulo & Belinha, Afonso & Rita, uncle Mário, Menina Amélia & Sr. Joaquim, Lurdes & Tó, João Pedro, and my friends, big-bro Edu, bro n'sis Puto & Sara, Vitinho, Joker, Josie, Zé Gate, Trace, Lopes, Punk, Cunha, Gonçalo, Filipe, Marcos, João Rui, Brito, Oliveira, Gaby, Nuno & Silvia, Zapata's Crew, FEUPsal & IndoorSoccer Teams, and so many others, thank you so much for the fun, for the parties, for the happy times we had together. Those moments were immensely important to relax and to recover energies! Love you guys!

Porto, September 2010

Filipe

Abstract

The environmental impact of hydrocarbons is so clear that applications of hydrogen as alternative energy carrier have gained the total acceptance. The development of processes to recover hydrogen provides a strong economic motivation, where for most of the applications a high purity hydrogen (> 99.99%) product is required. The most economic way to produce hydrogen is by steam methane reforming (SMR), which releases a gas mixture containing 70-72% of hydrogen contaminated with carbon dioxide, methane, carbon monoxide, nitrogen and saturated with water. To remove all these contaminants, pressure swing adsorption (PSA) processes are commonly applied.

The purpose of this work is to provide PSA studies for multicomponent mixtures of SMR off-gases, applying different cyclic sequences, operating conditions and using different adsorbent materials, in order to improve the operation of the process. Prior to the PSA studies, adsorption equilibrium data and the transport parameters of pure gases on different adsorbents and in a wide range of operation conditions were measured. These experiments were also extended to multicomponent mixtures of H_2, CO_2, CH_4, CO and N_2. For that, the upgrade of an experimental PSA facility was accomplished within this thesis, coupling a new analysis system able to determine the composition of several multicomponent SMR off-gas mixtures.

Supplementary studies were performed in two new laboratory-made adsorbents with enhanced capacity toward contaminants. These adsorbents were produced within this thesis. After the adsorption experiments of pure gases, it was disclosed an experimental protocol able to produce 400 g/batch of modified activated carbon with enhanced capacity mainly of CO_2, and another protocol able to produce 80 g/batch of ion exchanged zeolite with enhanced capacity toward N_2. The applicability of these materials in a layered bed PSA process was revealed.

A single column PSA experiment was performed in the “compact” PSA lab-scale unit for systems of SMR off-gases (H_2, CO_2, CH_4, CO and N_2) employing the modified activated carbon AC5-KS. A complete mathematical model was used to predict the full set of multicomponent experimental data previously determined and also the PSA experiment. After the validation of the model, it was used to simulate PSA behaviour according to different operating conditions and using two cycle sequences in order to suggest different and improved PSA cycles for H_2 purification systems.

Finally, the study of the fundamentals of RPSA was accomplished by analyzing the process performance of a binary H_2-CO_2 mixture. For this purpose, binary breakthrough curves at high superficial velocity were carried out as well as a RPSA experiment with a cycle time lasting less than one minute (52 s). It was observed that the PSA process can be improved by fast cycling schemes. However, other cycles or adsorbents should be employed to improve hydrogen recovery.

Resumo

O impacto ambiental de hidrocarbonetos é tão claro que a utilização de hidrogénio como vector energético tem vindo a ganhar total aceitação. O desenvolvimento de processos de recuperação de hidrogénio leva a uma forte motivação económica, sendo necessário hidrogénio de alta pureza (> 99,99%) para a maior parte das aplicações. O *reforming* de metano (SMR) é a maneira mais económica de produzir hidrogénio, sendo que este liberta uma mistura gasosa contendo 70-72% de hidrogénio contaminado com dióxido de carbono, metano, monóxido de carbono, azoto, saturada em água. A remoção de todos os contaminantes é normalmente efectuada através de processos de adsorção com modulação de pressão (PSA).

O objectivo deste trabalho é apresentar estudos de PSA para misturas multi-componente de gases de exaustão do SMR, aplicando diferentes sequências cíclicas, condições operacionais e utilizando diferentes materiais adsorventes, de forma a melhorar o processo. Antes dos estudos realizados em PSA, foram medidos dados de adsorção de equilíbrio e parâmetros de transporte de gases puros em diferentes adsorventes e numa ampla gama de condições de operação. Estas experiências também foram estendidas para misturas multi-componente de H_2, CO_2, CH_4, CO e N_2. Para isso e no âmbito desta tese, foi necessário melhorar uma instalação experimental de PSA, ligando-a a um novo sistema de análise capaz de determinar a composição de várias misturas multi-componente de gases de exaustão do SMR.

Foram realizados estudos complementares em dois adsorventes feitos em laboratório, os quais possuem maior capacidade para contaminantes. Estes adsorventes foram produzidos no âmbito desta tese. Após terem sido realizadas as experiências de adsorção de gases puros, foi divulgado um protocolo experimental capaz de produzir 400 g/lote de carvão activado modificado com maior capacidade para, principalmente, CO_2, e um outro protocolo capaz de produzir, através de permuta iónica, 80 g/lote de zeólito com maior capacidade para N_2. A aplicabilidade destes materiais foi reportada para um processo de PSA com uma coluna composto por diferentes camadas de adsorvente.

Foi realizada uma experiência de PSA numa única coluna para sistemas de gases de exaustão do SMR (H_2, CO_2, CH_4, CO e N_2) na unidade laboratorial "compacta" de PSA, utilizando o carvão activado modificado AC5-KS. Um modelo matemático completo foi utilizado para prever o conjunto de dados experimentais multi-componente previamente determinados bem como a experiência de PSA. Após validação do modelo, este foi utilizado para simular o comportamento do PSA de acordo com diferentes condições de operação e utilizando dois ciclos, de forma a poderem ser sugeridos para sistemas de purificação de H_2 ciclos de PSA diferentes e melhorados.

Por fim, foram efectuados estudos em fundamentos de RPSA através da análise do desempenho do processo utilizando uma mistura binária de H_2-CO_2. Para este efeito, foram realizadas curvas de ruptura binárias com velocidade superficial elevada, assim como foi efectuada uma experiência de RPSA com um tempo de ciclo de duração inferior a um minuto (52 s). Foi observado que o processo de PSA pode ser melhorado com a utilização de ciclos rápidos. No entanto, devem ser empregues outros ciclos ou adsorventes, de forma a melhorar a recuperação de hidrogénio.

Zusammenfassung

Die negativen Umwelteinflüsse der Kohlenwasserstoffe sind eindeutig nachgewiesen, deshalb hat man sich auf Wasserstoff als alternativen Energieträger einstimmig geeinigt. Die Entwicklung von Wasserstoffreinigungsprozessen, mit einer Wasserstoffreinheit von > 99.99%, sind hochmotivierend wenn man sich das wirtschaftliche Potenzial genauer betrachtet. Die preiswerteste Alternative für die Herstellung von Wasserstoff ist nach wie vor die katalytische Dampfreformierung von Methan (SMR). Die Produktgase setzen sich zusammen aus Wasserstoff (70-72%), welches verunreinigt ist mit Kohlendioxid, Methan, Kohlenmonoxid, Stickstoff und Wasser. Die Druck-Wechsel-Adsorption (PSA) ist die hierfür am häufigsten angewendete Methode, um Wasserstoff hochrein zu erhalten.

Das Ziel dieser Dissertation ist die systematische Studie von multikomponenten Mischungen der Methan-Dampfreformierten Austrittsgase. Zyklische Sequenzen, operatorische Bedingungen und Adsorbtionsmaterialien werden hierfür verwendet, so dass die Verbessung der PSA sichergestellt werden kann. Bevor die PSA Untersuchungen durchgeführ wurden, sind Gleichgewichtsdaten der Adsorption, und Transportparameter der reinen Gase an verschiedenen Adsorbentien, in einer breiten Länge von operatorischen Bedingungen, untersucht worden. Die Experimente wurden auch fuer Multikomponentensysteme, bestehend aus H_2, CO_2, CH_4, CO und N_2, erweitert und untersucht. Dafür wurde die PSA Einheit verbessert, d.h. neue Analysemethoden haben es erlaubt die Zusammensetzung der verschiedenen Multikomponenten der SMR-Austrittsgase zu bestimmen.

Zusätzliche Studien wurden im Rahmen dieser Dissertation an zwei neu hausentwickelten Adsorbentien durchgeführt. Diese zeigten eine beschleunigte Adsorptionskapazität bezüglich der Verunreinigungen. Es wurde Anhand der experimentellen Protokolle sichergestellt, dass 400 g pro Batch des erste Adsorbtionsmaterials, welches mit Aktivkohle verändert wurde, hergestellt werden konnten. Das synthetisierte Material zeigte bevorzugte Kapazität für die CO_2 adsorption auf. Im darauffolgenden Versuchsprotokoll wurden 80 g pro Batch des zweiten Adsorbtionsmaterials, mittels Ionenaustausch an einem Zeolith, hergestellt. Das synthetisierte Material zeigte bevorzugte Kapazität für die N_2 adsorption auf. Anschliessend wurde die Anwendbarkeit dieser Materialien an einer mehrschichtigen PSA Einheit bestätigt.

Eine einfache PSA Untersuchung wurde an einer “kompakten” PSA Laborskala-Einheit fuer SMR Austrittsgase (H_2, CO_2, CH_4, CO und N_2) verwendet, wobei die modifizierte AC5-KS Aktivkohle eingesetzt wurde. Um die experimentelle Zusammensätzung der Multikomponenten-systeme vorrauszusagen, wurde hierfür ein vollständiges mathematisches Model verwendet. Das Model wurde evaluiert, und falls gültig, für weitere Simulierungen, unter verschiedenen operatorischen Bedingungen an der PSA Einheit, verwendet. Die Benutzung von zwei zyklischer Sequenzen wurden gleichfalls vorgeschlagen, um die PSA Zyklen für die Wasserstoff-anreicherungssysteme zu verbessern.

Als Abschluss dieser Dissertation, wurden elementare Studien bezüglich der RPSA mit Analysen für die Leistungsfähigkeit an binäre H_2-CO_2 Mischungen verglichen. Dafür wurden binäre Durchbruchskurven für hohe Oberflächengeschwindigkeiten verwendet, wie auch eine RPSA Untersuchung mit einem Verweilzyklus kleiner als eine Minute (52 s). Die Beobachtungen zeigen, dass der PSA-Prozess durch schnelle Zyklen-Schemata verbessert werden kann. Trotz allem, andere Zyklen oder Adsorbtionsmaterial sollten hierfür in betracht gezogen werden, so dass die Wasserstoffanreicherung sichergestellt werden kann.

Table of contents

Acknowledgements **i**

Abstract **v**

Resumo **vii**

Zusammenfassung **ix**

List of Figures **xvii**

List of Tables **xxix**

Chapter 1

Introduction **1**

1.1 Relevance & Motivation 1

1.2 Pressure swing adsorption technologies 3

1.2.1 Layered beds 7

1.2.2 Modified adsorbents 9

1.2.3 PSA cycle steps 12

1.2.4 Integrated processes 14

1.3 Objectives & Outline 17

1.4 References 20

Chapter 2

Adsorption equilibrium of pure gases on commercial adsorbents **27**

2.1 Introduction 27

2.2 Adsorbent screening 28

2.3 Experimental 29

2.4 Theoretical 33

2.5 Adsorbent characterization 36

2.5.1 Activated carbon R2030 37

2.5.2 Activated carbon ACM-3mm 37
2.5.3 Activated carbon HY2SEPS-AC 38
2.5.4 Zeolite HY2SEPS-ZEO 40
2.6 Adsorption equilibrium results 41
2.6.1 Activated carbon R2030 41
2.6.2 Activated carbon ACM-3mm 46
2.6.3 Activated carbon HY2SEPS-AC 47
2.6.4 Zeolite HY2SEPS-ZEO 52
2.7 Conclusions 55
2.8 Notation 58
2.9 References 60

Chapter 3

Adsorption kinetics of pure gases on commercial adsorbents 65

3.1 Introduction 65
3.2 Experimental 66
3.2.1 Zero length column (ZLC) 66
3.2.2 Perturbation chromatography methods (pulses and breakthrough curves) 69
3.3 Theoretical 73
3.3.1 Zero length column (ZLC) 73
3.3.2 Perturbation chromatography methods (pulses and breakthrough curves) 76
3.4 Adsorption kinetic results 82
3.4.1 Activated carbon R2030 83
3.4.2 Activated carbon ACM-3mm 92
3.4.3 Activated carbon HY2SEPS-AC 94
3.4.4 Zeolite HY2SEPS-ZEO 99
3.5 Conclusions 104
3.6 Notation 106
3.7 References 109

Chapter 4

Large scale preparation of adsorbents for CO_2 and N_2 separations 111

4.1 Introduction 111
4.2 Modification of activated carbons for enhanced CO_2 capacity 112
4.2.1 Routes for enhanced CO_2 adsorption 112
4.2.2 Adsorbents preparation and characterization 113
4.2.2.1 Preparation protocol for physical activation 113
4.2.2.2 Sample characterization and reproducibility 115
4.2.2.3 Results 117
4.2.3 Adsorption equilibrium and kinetics of pure gases 121
4.2.3.1 Experimental 121
4.2.3.2 Theoretical 122
4.2.3.3 Results 125
4.3 Ion exchange of zeolites for enhanced N_2 capacity 130
4.3.1 Routes for enhanced N_2 adsorption 130
4.3.2 Adsorbents preparation and characterization 131
4.3.2.1 Preparation protocol for ion exchange 131
4.3.2.2 Sample characterization and reproducibility 131
4.3.2.3 Results 132
4.3.3 Nitrogen adsorption on ion exchanged zeolites 134
4.3.3.1 Experimental 134
4.3.3.2 Results 135
4.3.4 Adsorption kinetics of CO_2, CH_4, CO and H_2 139
4.3.4.1 Experimental 139
4.3.4.2 Results 139
4.3.5 Adsorption equilibrium of N_2, CO_2, CH_4, CO and H_2 143
4.3.5.1 Experimental and theoretical 143
4.3.5.2 Results 144
4.4 Conclusions 147
4.5 Notation 149
4.6 References 152

Chapter 5

Multicomponent breakthrough curves and PSA performance 157

5.1 Introduction 157

5.2 Experimental 158
5.2.1 Multicomponent breakthrough experiments 159
5.2.1.1 Fixed-bed unit for ternary mixtures 159
5.2.1.2 Two-column “compact” PSA unit for multicomponent mixtures 163
5.2.2 PSA experiment 166
5.3 Theoretical 167
5.4 Results and discussion 180
5.4.1 Multicomponent breakthrough experiments 181
5.4.1.1 Breakthrough curves in fixed-bed unit for ternary mixtures 181
5.4.1.2 Breakthrough curves in the “compact” PSA unit 187
5.4.2 PSA experiment 191
5.4.3 PSA simulations 194
5.5 Conclusions 200
5.6 Notation 202
5.7 References 205

Chapter 6

Fast cycling PSA 209

6.1 Introduction 209
6.2 Literature & Patent review 210
6.3 RPSA experimental unit 217
6.4 Cycle modelling and RPSA simulations 223
6.5 Experimental 224
6.5.1 Multicomponent breakthrough experiments 225
6.5.2 RPSA experiment 226
6.6 Results and discussion 226
6.6.1 Multicomponent breakthrough experiments 227
6.6.2 RPSA experiment 236
6.6.3 RPSA simulations 241
6.7 Conclusions 246
6.8 Notation 248
6.9 References 249

Chapter 7

Conclusions and suggestions for future work **253**

7.1 Conclusions 253

7.2 Suggestions for future work 257

7.3 References 260

List of Figures

Chapter 1

Figure 1.1: Carbon dioxide emissions: a) percent of global CO_2 emissions in 2008; b) annual CO_2 emissions between 2000 and 2008 [1]. 2

Figure 1.2: The PSA process: a) change in equilibrium loading with pressure; b) idealized diagram showing movement of the adsorbed phase concentration profile for the more strongly adsorbed compounds in a PSA process (adsorption vs desorption). 4

Figure 1.3: The Skarstrom cycle: (1) co-current pressurization step with feed; (2) feed step; (3) counter-current blowdown step; (4) counter-current purge step with the "light product" [27]. 5

Figure 1.4: The modified Skarstrom cycle [9, 18, 35]: (1) co-current pressurization step with feed; (2) feed step; (3) co-current pressure-equalization depressurization step; (4) counter-current blowdown step; (5) counter-current purge step with the "light product"; (6) counter-current pressure-equalization pressurization step. 6

Figure 1.5: Single adsorbent bed (a) and different configurations for multilayered beds filled with activated carbons, zeolites and alumina: beds with 2 (b), 3 (c) and 4 layers (d). 7

Figure 1.6: Ion exchange of the non-framework cation (Na^+) of the zeolite X with calcium cations. 10

Figure 1.7: Backfill cycle of 2-bed PSA process: (1) feed; (2) pressure-equalization depressurization; (3) blowdown; (4) purge; (5) pressure-equalization pressurization; (6) backfill; (7) pressurization [16]. 13

Figure 1.8: Five-bed 11-step PSA process for hydrogen purification: (1) feed; (2) pressure-equalization depressurization 1; (3) pressure-equalization depressurization 2; (4) provide purge; (5) pressure-equalization depressurization 3; (6) blowdown; (7) purge; (8) pressure-equalization pressurization 3; (9) pressure-equalization pressurization 2; (10) pressure-equalization pressurization 1; (7) pressurization [60]. 14

Figure 1.9: Schematic two stage PSA process: first stage of 6 beds and second stage of 3 beds [79]. 15

Figure 1.10: Schematic PSA process diagram using four beds and a tank (intermediate gases reservoir) [67]. 16

Chapter 2

Figure 2.1: Adsorption isotherms of H_2 (open symbols) and CO_2 (closed symbols) on zeolite 13X (a) and activated carbons (b); references: Siriwardane *et al.*, 2001 [12]; Siriwardane *et al.*, 2005 [15]; Siriwardane *et al.*, 2001 [16]; Choi *et al.*, 2003 [17]; Ritter *et al.*, 1987 [19]. 29

Figure 2.2: a) Magnetic suspension microbalance (Rubotherm, Bochum, Germany); b) Acquisition system of the magnetic suspension microbalance connected to the computer. 30

Figure 2.3: Schematic diagram of the experimental set-up for adsorption measurements. Labelling: ADS, adsorbate; V1, V2, on-off valves; VT1, 3 port valve; VP, vacuum pump; PT, pressure transducer; TT, thermocouple. 30

Figure 2.4: Magnetic suspension microbalance (Rubotherm, Bochum, Germany) with a system operating in open mode with a continuous flow passing through the sample. 32

Figure 2.5: Schematic diagram of the experimental set-up for water vapour adsorption measurements. Labelling: MFC, mass flow controller; V1 to V4, on-off valves; PT, pressure transducer; TT, thermocouple. 33

Figure 2.6: a) Pore size distribution by mercury intrusion of activated carbon R2030; b) Adsorption isotherm of nitrogen on R2030 at 77 K. 37

Figure 2.7: a) Pore size distribution by mercury intrusion of activated carbon ACM-3mm; b) Adsorption isotherm of nitrogen on ACM-3mm at 77 K. 38

Figure 2.8: a) Pore size frequency distribution functions of the HY2SEPS-AC; b) adsorption isotherm of nitrogen on HY2SEPS-AC at 77 K with the pore size distribution of the HY2SEPS-AC calculated using the HK method. 39

Figure 2.9: a) Pore (──) and throat (- - -) size frequency distribution functions of the HY2SEPS-ZEO; b) adsorption isotherm of nitrogen on HY2SEPS-ZEO at 77 K with the pore size distribution of the HY2SEPS-ZEO calculated using the HK method. 40

Figure 2.10: Helium measurements on R2030 at 303 K (■); —— the fitting of equation (2.4). 41

Figure 2.11: a) Excess (□) and absolute (■) amount of CO_2 (a) and H_2 (b) adsorbed on activated carbon R2030 at 303 K. 42

Figure 2.12: Amount of CO_2 (a) and H_2 (b) adsorbed on activated carbon R2030: experimental points at 303 (■), 323 (◆) and 343 K (▲) and —— Virial isotherm fitting. 42

Figure 2.13: Amount of CH_4 (a), CO (b) and N_2 (c) adsorbed on activated carbon R2030: experimental points at 303 (■), 323 (◆) and 343 K (▲) and —— Virial isotherm fitting. 43

Figure 2.14: Amount of H_2O adsorbed on activated carbon R2030 at 303 K reported by Ribeiro *et al.* (2008) [27]: (■) experimental points and —— Virial isotherm fitting. 44

Figure 2.15: Amount of CO_2 (a) and H_2 (b) adsorbed on activated carbon ACM-3mm: experimental points at 303 (■), 323 (◆) and 343 K (▲) and —— multisite Langmuir isotherm fitting. 46

Figure 2.16: Amount of CO_2 (a) and H_2 (b) adsorbed on activated carbon HY2SEPS-AC: experimental points at 303 (■), 323 (◆) and 343 K (▲) and —— multisite Langmuir isotherm fitting. 48

Figure 2.17: Amount of CH_4 (a), CO (b) and N_2 (c) adsorbed on activated carbon HY2SEPS-AC: experimental points at 303 (■), 323 (◆) and 343 K (▲) and —— multisite Langmuir isotherm fitting. 49

Figure 2.18: Virial domain plot of CO_2 and N_2 (a) and of CH_4 and CO (b) adsorption equilibrium on activated carbon HY2SEPS-AC: experimental points at 303 (■,□), 323 (◆,◇) and 343 K (▲,△) and —— multisite Langmuir isotherm fitting. 50

Figure 2.19: Single-component isosteric heats of adsorption on HY2SEPS-AC for CO_2 (■), CH_4 (▲), CO (◆), N_2 (●) and H_2 (×) as a function of equilibrium pressure in the temperature range of 303-343 K; Lines are the values obtained through the multisite Langmuir model. 51

Figure 2.20: Amount of H_2O adsorbed on activated carbon HY2SEPS-AC at 303 K (■); open symbol (□) obtained from the analysis of the breakthrough experiment. 51

Figure 2.21: Amount of CO_2 (a) and H_2 (b) adsorbed on activated carbon HY2SEPS-ZEO: experimental points at 303 (■), 323 (◆) and 343 K (▲) and —— multisite Langmuir isotherm fitting. 52

Figure 2.22: Amount of CH_4 (a), CO (b) and N_2 (c) adsorbed on activated carbon HY2SEPS-ZEO: experimental points at 303 (■), 323 (◆) and 343 K (▲) and —— multisite Langmuir isotherm fitting. 53

Figure 2.23: Single-component isosteric heats of adsorption on HY2SEPS-ZEO for CO_2 (■), CH_4 (▲), CO (◆), N_2 (●) and H_2 (×) as a function of equilibrium pressure in the temperature range of 303-343 K; Lines are the values obtained through the multisite Langmuir model. 55

Chapter 3

Figure 3.1: a) Varian gas chromatograph (Varian, Netherlands); b) Multiport valve and injector connected to the gas chromatograph. 67

Figure 3.2: Zero length column (ZLC) experimental set-up with ZCL cell geometry description. 67

Figure 3.3: a) Gas mixture bottle set-up; b) Sampling tank to prepare gas mixtures. 68

Figure 3.4: Pulse experimental set-up and the gas sample collection in a gas-tight syringe. 69

Figure 3.5: a) Column in the gas chromatograph (left); b) Mixture bottle connected to the multiport valve (right). 70

Figure 3.6: Diluted breakthrough experimental set-up with the column geometry description. 71

Figure 3.7: Breakthrough experimental set-up with generation of adsorbate vapours by flowing helium through glass bubblers filled with water. 71

Figure 3.8: Schematic diagram of the experimental set-up for water vapour breakthrough measurements. Labelling: V1, V2, on-off valves; VT1, 3 port valve; VP, vacuum pump; PT, pressure transducer; TT, thermocouple. 72

Figure 3.9: ZLC curves for CO_2 (a), CH_4 (b) and CO (c) on R2030 at three different temperatures: 303 (■), 323 (◆) and 343 K (▲); flow rate $Q_T(1)$ of 2.42×10^{-7} m^3 s^{-1} (measured at 298 K and 1 bar); flow rate $Q_T(2)$ of 6.25×10^{-7} m^3 s^{-1} (measured at 298 K and 1 bar); experimental conditions are detailed in Table 3.2. 84

Figure 3.10: ZLC curves for CO_2 (a), CH_4 (b) and CO (c) on R2030 at three different temperatures: 303 (■), 323 (◆) and 343 K (▲); straight lines (——) are the complete ZLC model results using the parameters from LTR; experimental conditions are detailed in Table 3.2. 86

Figure 3.11: Pulse experiments of H_2 (a), CH_4 (b) and CO (c) on R2030 at three different temperatures: 303 (■), 323 (◆) and 343 K (▲); —— simulation with the kinetic parameters obtained; experimental conditions are detailed in Table 3.4. 87

Figure 3.12: Dilute breakthrough curves of carbon dioxide on R2030 at three different temperatures: 303 (■), 323 (◆) and 343 K (▲); —— simulation with the kinetic parameters obtained; experimental conditions are detailed in Table 3.6. 90

Figure 3.13: ZLC curves for CO_2 on ACM-3mm at three different temperatures: 303 (■), 323 (◆) and 343 K (▲); a) flow rate $Q_T(1)$ of 2.42×10^{-7} m^3 s^{-1} (measured at 298 K and 1 bar); b) flow rate $Q_T(2)$ of 6.25×10^{-7} m^3 s^{-1} (measured at 298 K and 1 bar); experimental conditions are detailed in Table 3.9. 93

Figure 3.14: Diluted breakthrough curves of CO_2 (a), CH_4 (b), CO (c) and N_2 (d) on HY2SEPS-AC at 303 (■), 323 (◆) and 343 K (▲); 1 bar of total pressure; —— simulation with the kinetic parameters obtained; experimental conditions are detailed in Table 3.10. 95

Figure 3.15: Breakthrough curves of pure H_2 on HY2SEPS-AC at 303 (■), 323 (◆) and 343 K (▲); 1 bar of total pressure; —— simulation with the kinetic parameters obtained; experimental conditions are detailed in Table 3.10. 96

Figure 3.16: Water vapour breakthrough curve on activated carbon at 303 K (■) obtained with activated carbon for 89% of humidity; experimental conditions are detailed in Table 3.10. 99

Figure 3.17: Diluted breakthrough curves of CO_2 (a), CH_4 (b), CO (c) and N_2 (d) on HY2SEPS-ZEO at 303 (■), 323 (◆) and 343 K (▲); 1 bar of total pressure; —— simulation with the kinetic parameters obtained; experimental conditions are detailed in Table 3.13. 100

Figure 3.18: Breakthrough curves of pure H_2 on HY2SEPS-ZEO at 303 (■), 323 (◆) and 343 K (▲); 1 bar of total pressure; —— simulation with the kinetic parameters obtained; experimental conditions are detailed in Table 3.13. 101

Chapter 4

Figure 4.1: Experimental set-up for the activated carbon modification by physical activation. 114

Figure 4.2: Schematic diagram of the experimental set-up for the activated carbon modification by physical activation. 114

Figure 4.3: Schematic diagram of the different columns employed in the activation process to enhance adsorption properties of activated carbon extrudates. 116

Figure 4.4: The 4-column PSA prototype for H_2 purification developed within the European Project HY2SEPS [23] by Hygear B.V.; Courtesy of Hygear B.V. 117

Figure 4.5: Nitrogen adsorption isotherms for the original activated carbon R2030 (-∗-; Grande et al., 2008) and for the modified activated carbon samples AC1 (-■-), AC2 (-◆-), AC3 (-▲-), AC5 (-□-), AC5-I (-◇-) and AC5-KS (-△-). 118

Figure 4.6: Nitrogen adsorption isotherms for the modified activated carbon samples AC5-KS (-△-), AC5-KS-2 (-∗-), AC5-KS-3 (-×-) and AC5-KS-4 (-┼-). 120

Figure 4.7: Preparation of approximately four kilograms of AC5-KS-Mix through physical activation of the activated carbon R2030. 120

Figure 4.8: Pore size distribution of the original activated carbon R2030 (-■-; Grande et al., 2008) and of the modified activated carbon AC5-KS (-□-) obtained from mercury porosimetry intrusion. 121

Figure 4.9. Amount adsorbed of CO_2 on the original AC (closed symbols; Grande et al., 2008), on the modified AC5-I and AC5-KS (open symbols): experimental points at 303 (■,×,□), 323 (◆,◇) and 343 K (▲). Fitting with the Virial isotherm model of the original AC (—) and of the AC5-KS (- - -). 125

Figure 4.10: Amount adsorbed of H_2 (a), CH_4 (b), CO (c) and N_2 (d) on the original AC (closed symbols; Grande et al., 2008) and on the modified AC5-KS (open symbols): experimental points at 303 (■,□), 323 (◆,◇) and 343 K (▲). Fitting with the Virial isotherm model of the original AC (—) and of the AC5-KS (- - -). 126

Figure 4.11: Diluted breakthrough curves of CO_2 (0.5% of CO_2 balanced with He) on the modified activated carbon AC5-KS at 303 (□) and 323 K (◇); Total pressure of 1 bar; Flow rate of 6.25×10^{-7} $m^3 s^{-1}$ (measured at 298 K and 1 bar); —— Simulation with the kinetic parameters obtained. 128

Figure 4.12: Breakthrough curves of pure H_2 (a) and diluted breakthrough curves of CH_4 (b), CO (c) and N_2 (d) (0.5% of adsorbate balanced with He) on the modified activated carbon AC5-KS at 303 (□) and 323 K (◇); Total pressure of 1 bar; Flow rates (measured at 298 K and 1 bar) of 8.67×10^{-7} (a), 9.00×10^{-7} (b, c) and 6.67×10^{-7} $m^3 s^{-1}$ (d); —— Simulation with the kinetic parameters obtained. 129

Figure 4.13: Scanning electron microscopy (SEM) image of zeolite 13X (a) and ion exchanged zeolites 13X-Li (b), 13X-Ba (c) and 13X-Ca (d). 132

Figure 4.14: Energy dispersive X-ray (EDX) pattern of zeolite 13X (a) and ion exchanged zeolites 13X-Li (b), 13X-Ba (c) and 13X-Ca (d). 133

Figure 4.15: Concentration history of the Na^+ cations exchange in zeolite 13X using 400 mL of 1N Ca^{2+} solutions and 80 g of zeolite: Exchange no 1 (-∗-), 2 (-■-), 3 (-◆-) and 4 (-▲-). 134

Figure 4.16: Breakthrough curves of 0.01 bar of N_2 balanced in He [a) 303 K and b) 323 K] and 0.25 bar of N_2 balanced in He [c) 303 K and d) 323 K] on the zeolite 13X (■), 13X-Li (□), 13X-Ba ( ) and 13X-Ca (◆); experimental conditions and results reported in Table 4.11 and Table 4.12. 136

Figure 4.17: Diluted breakthrough curves (0.005 bar of adsorbate balanced in He) of CO_2 (a), CH_4 (b) and CO (c) and breakthrough of pure H_2 (d) on zeolite 13X-Ca at 303 (■) and 323 K (◇); experimental conditions and results reported in Table 4.14 and Table 4.15. 140

Figure 4.18: Amount adsorbed of N_2 on zeolite 13X-Ca: experimental points at 303 (■) and 323 K (◆) and —— Virial isotherm fitting; comparison to published results of N_2 amount adsorbed on the studied sample of zeolite 13X (▲,◆) and other samples of zeolite 13X (□,◇,+,×). 144

Figure 4.19: Amount adsorbed of CO_2 (a), CH_4 (b), CO (c) and H_2 (d) on zeolite 13X-Ca: experimental points at 303 (■) and 323 K (◆) and —— Virial isotherm fitting. 145

Figure 4.20: Isosteric heats of adsorption of CO_2 (■), CH_4 (▲), CO (◆), N_2 (×) and H_2 (○) on zeolite 13X-Ca as a function of equilibrium pressure in the temperature range of 303-323 K; lines are the values obtained through the Virial model. 146

Chapter 5

Figure 5.1: Schematic representation of the 1-column PSA-VSA experimental set-up used for multicomponent fixed-bed breakthroughs developed by Da Silva (1999) [23]: unit connected to a flue gas analyser to measure the bed outlet concentration. 159

Figure 5.2: Flue gas analyser (Madur, Austria) used for the measurements of the bed outlet concentration. 160

Figure 5.3: Schematic representation of the 1-column PSA-VSA experimental set-up used for multicomponent fixed-bed breakthroughs developed by Da Silva (1999) [23]: unit connected to a GC analysis system to measure the bed outlet concentration. 162

Figure 5.4: The 2-column PSA experimental set-up connected to a GC analysis system. 163

Figure 5.5: Schematic representation of the 2-column “compact” PSA experimental set-up used for multicomponent fixed-bed breakthroughs and PSA experiments connected to a GC analysis system to measure the bed outlet concentration. 164

Figure 5.6: a) Column used in the “compact” PSA; b) Schematic representation with the heater. 165

Figure 5.7: Schematic diagram of the cycle sequence used in the PSA experiment for H_2 purification: Cycle sequence: (1) co-current feed step; (2) first, (3) second and (4) third pressure equalization-depressurization steps; (5) counter-current blowdown step; (6) counter-current purge step with hydrogen; (7) third, (8) second and (9) first pressure equalization-pressurization steps; (10) counter-current pressurization step with hydrogen. 166

Figure 5.8: Schematic representation of the adsorption bed: column wall, gas phase and solid phase composed by bidisperse adsorbent (macro and micropores) [30]. 169

Figure 5.9: Schematic diagram of the cycle sequences used in the PSA simulations for H_2 purification: Cycle A: (1) co-current feed step; (2) pressure equalization-depressurization step; (3) counter-current blowdown step; (4) counter-current purge step with hydrogen; (5) pressure equalization-pressurization step; (6) counter-current pressurization step with hydrogen; Cycle B: (1) co-current feed step; (2) first, (3) second and (4) third pressure equalization-depressurization steps; (5) counter-current blowdown step; (6) counter-current purge step with hydrogen; (7) third, (8) second and (9) first pressure equalization-pressurization steps; (10) counter-current pressurization step with hydrogen. 177

Figure 5.10: H_2 (----) and CO_2 (□,——) molar flow rate histories at the column outlet (a) and temperature histories (b) obtained for binary H_2-CO_2 breakthrough curves at 323 (1) and 343 K (2) and 2.5 bar on activated carbon R2030; Mixture: 17.6% of CO_2 balanced with H_2; Temperatures measured at 0.170 m (Bottom (■,——)), 0.430 m (Middle (◆,——)) and 0.680 m (Top (▲,——)) from feed inlet and the wall temperature T_w at 0.680 m (- - -); Flow rate of 1.596×10^{-5} m^3 s^{-1} (measured at 298 K and 1 bar); Experimental data (symbols); Simulation (lines). 182

Figure 5.11: H_2 (----), CO_2 (□,——) and CH_4 (+,·····) molar flow rate histories at the column outlet (a) and temperature histories (b) obtained for the ternary H_2-CO_2-CH_4 breakthrough curve at 305 K and 2.5 bar on activated carbon R2030; Mixture: 15.5% of CO_2 and 4.5% of CH_4 balanced with H_2; Temperatures measured at 0.170 m (Bottom (■,——)), 0.430 m (Middle (◆,——)) and 0.680 m (Top (▲,——)) from feed inlet and the wall temperature T_w at 0.680 m (- - -); Flow rate of 1.584×10^{-5} m^3 s^{-1} (measured at 298 K and 1 bar); Experimental data (symbols); Simulation (lines). 183

Figure 5.12: Total flow rate (○) at the column outlet obtained for the ternary H_2-CO_2-CH_4 breakthrough curve at 305 K and 2.5 bar on R2030; Mixture: 15.5% of CO_2 and 4.5% of CH_4 balanced with H_2. 183

Figure 5.13: CO_2 (□,——) molar flow rate history at the column outlet (a) and temperature histories (b) obtained for the CO_2 breakthrough curve at 303 K and 1.2 bar on activated carbon AC5-KS; Mixtures: 14.8% of CO_2 balanced with He (1) and 63.1% of CO_2 balanced with He (2); Temperatures measured at 0.175 m (Bottom (■,——)), 0.424 m (Middle (◆,——)) and 0.677 m (Top (▲,——)) from feed inlet; Flow rates (measured at 298 K and 1 bar) of 1.543×10^{-5} (1) and 1.575×10^{-5} m^3 s^{-1} (2); Experimental data (symbols); Simulation (lines). 185

Figure 5.14: H_2 (----), CO_2 (□,——) and CH_4 (+,·····) molar flow rate histories at the column outlet (a) and temperature histories (b) obtained for the ternary H_2-CO_2-CH_4 breakthrough curve at 303 K and 1.2 bar on activated carbon AC5-KS; Mixtures: 69.0% of CO_2 and 17.3% of CH_4 (1) and 58.0% of CO_2 and 28.2% of CH_4 (2) both balanced with H_2; Temperatures measured at 0.175 m (Bottom (■,——)), 0.424 m (Middle (◆,——)) and 0.677 m (Top (▲,——)) from feed inlet; Flow rates (measured at 298 K and 1 bar) of 1.848×10^{-5} (1) and 1.871×10^{-5} m^3 s^{-1} (2); Experimental data (symbols); Simulation (lines). 186

Figure 5.15: H_2 (△,----) and CO_2 (□,——) molar flow rate histories (a) at the column outlet and temperature histories (b) obtained for binary H_2-CO_2 breakthrough curves at 323 K and 5 bar on activated carbon AC5-KS; Mixtures: CO_2 content (balanced with H_2) of 30% (1), 10% (2) and 80% (3); Temperatures measured at 0.059 m (Bottom (■,——)), 0.151 m (Middle (◆,——)) and 0.239 m (Top (▲,——)) from feed inlet; Flow rate of 5.00×10^{-5} m^3 s^{-1} (measured at 298 K and 1 bar); Experimental data (symbols); Simulation (lines). 188

Figure 5.16: H_2 (△,----), CO_2 (□,——) and CO (×,— —) molar flow rate histories (a) at the column outlet and temperature histories (b) obtained for ternary H_2-CO_2-CO breakthrough curve at 323 K and 5 bar on activated carbon AC5-KS; Mixture: 26% of CO_2 and 4% of CO balanced with H_2; Temperatures measured at 0.059 m (Bottom (■,——)), 0.151 m (Middle (◆,——)) and 0.239 m (Top (▲,——)) from feed inlet; Flow rate of 5.00×10^{-5} m^3 s^{-1} (measured at 298 K and 1 bar); Experimental data (symbols); Simulation (lines). 189

Figure 5.17: H_2 (△,----), CO_2 (□,——), CH_4 (+,·····), CO (×,— —) and N_2 (◇,—·—·) molar flow rate histories (a) at the column outlet and temperature histories (b) obtained for multicomponent H_2-CO_2-CH_4-CO-N_2 breakthrough curve at 323 K and 5 bar on activated carbon AC5-KS; Mixture: 23% of CO_2, 2.1% of CH_4, 1.2% of CO and 0.7% of N_2 balanced with H_2; Temperatures measured at 0.059 m (Bottom (■,——)), 0.151 m (Middle (◆,——)) and 0.239 m (Top (▲,——)) from feed inlet; Flow rate of 5.00×10^{-5} m^3 s^{-1} (measured at 298 K and 1 bar); Experimental data (symbols); Simulation (lines). 190

Figure 5.18: Pressure (a; ○,——) and temperature (b) histories; Cycle sequence: (1) co-current feed step; (2) first, (3) second and (4) third pressure equalization-depressurization steps; (5) counter-current blowdown step; (6) counter-current purge step with hydrogen; (7) third, (8) second and (9) first pressure equalization-pressurization steps; (10) counter-current pressurization step with hydrogen; Temperatures measured at 0.059 (Bottom (□,----)), 0.151 (Middle (◇,— —)) and 0.239 m (Top (△,——)) from feed inlet; Adsorbent: AC5-KS; Experimental data (symbols); Simulation (lines). 192

Figure 5.19: H_2 (△,----), CO_2 (□,——), CH_4 (+,·····), CO (×,— —) and N_2 (◇,—·—·) molar flow rate histories (a) obtained for cycle 1 (1) and 37 (2) at the outlet of a bed packed with AC5-KS; Temperature histories (b) measured for cycle 1 (1) and 37 (2) at 0.059 m (Bottom (■,----)), 0.151 m (Middle (◆,— —)) and 0.239 m (Top (▲,——)) from feed inlet; Flow rate of 5.00×10^{-5} m^3 s^{-1} (measured at 298 K and 1 bar); Experimental data (symbols); Simulation (lines). 193

Figure 5.20: Pressure (a) and molar flow rate (b, c) histories obtained for simulation 13 at the outlet of a bed packed with AC5-KS and at cyclic steady state: (1) co-current feed step; (2) first, (3) second and (4) third pressure equalization-depressurization steps; (5) counter-current blowdown step; (6) counter-current purge step with hydrogen; (7) third, (8) second and (9) first pressure equalization-pressurization steps; (10) counter-current pressurization step with hydrogen. 197

Figure 5.21: Solid phase concentration profiles of H_2 (a), CO_2 (b), CH_4 (c), CO (d) and N_2 (e) obtained for simulation 13 along the bed packed with AC5-KS at the end of each step at cyclic steady state. 198

Figure 5.22: Hydrogen purity and recovery evolution along the cycles of simulation 13 for an PSA adsorption process using a single adsorbent bed packed with AC5-KS. 199

Figure 5.23: Evolution of the gas temperature (a) and nitrogen gas phase concentration (b) profiles with the cycle number at the end of the feed step obtained for simulation 13; Bed packed with AC5-KS. 199

Chapter 6

Figure 6.1: a) Column used in the previous experiments of PSA processes (left) and column used in the RPSA experiments (right); b) Column installed in the "adapted" RPSA facility with the flexible heating rope for the degassing of the adsorbent. 218

Figure 6.2: Schematic representation of the 2-column RPSA experimental set-up connected to a GC analysis system to measure the bed outlet concentration. 218

Figure 6.3: Flow rate signal obtained by the mass flow controllers (MFC) installed in the RPSA unit at column inlet: 1) MFC 1 (--□--); 2) MFC 2 (--△--); flow rates of 1.67×10^{-5} m^3 s^{-1} (a) and 1.50×10^{-6} m^3 s^{-1} (b), both measured at 298 K and 1 bar. 219

Figure 6.4: Flow rate signal measured by the flow meter (FM, ·-◇-·) installed in the RPSA unit at column outlet; flow rates of 2.50×10^{-5} m^3 s^{-1} (a) and 3.00×10^{-5} m^3 s^{-1} (b), both measured at 298 K and 1 bar. 220

Figure 6.5: Pressure signal obtained by the back-pressure regulator (BPR) at column outlet: pressure of 1.5 bar (a) and 5 bar (b). 221

Figure 6.6: Schematic representation of the dead volumes (highlighted in red) of the different sections of the RPSA unit and GC analysis system. 222

Figure 6.7: Pressure signal obtained by the pressure transducer (PT) placed at the outlet of column 2 (initially pressurized at 1 bar) during different equalization steps: column 1 was pressurized at 5 bar (─□─,--□--), 4 bar (─△─,--△--) and 3 bar (─◇─,--◇--). 222

Figure 6.8: Schematic diagram of the cycle sequence used in the RPSA experiments and simulations for H_2 purification: (1) co-current feed step; (2) counter-current depressurization step; (3) counter-current blowdown step; (4) counter-current purge step with hydrogen; (5) co-current pressurization step with feed. 223

Figure 6.9: Temperature measured at 0.271 m (□,——) from feed inlet during a cooling experiment from 334 K until 298 K; Helium flow rate of 5.00×10^{-5} m^3 s^{-1} (measured at 298 K and 1 bar); Experimental data (symbols); Simulation (lines). 227

Figure 6.10: H_2 (△,----) and CO_2 (□,——) molar flow rate histories (a) at the column outlet and temperature histories (b) obtained for binary H_2-CO_2 breakthrough curve (run 1) at 298 K and 5 bar on activated carbon AC5-KS; Mixture: 30% of CO_2 balanced with H_2; Temperatures measured at 0.050 m (Bottom (■,——)), 0.159 m (Middle (◆,——)) and 0.271 m (Top (▲,——)) from feed inlet; Flow rate of 1.167×10^{-5} m^3 s^{-1} (measured at 298 K and 1 bar); Experimental data (symbols); Simulation (lines). 228

Figure 6.11: H_2 (△,----) and CO_2 (□,——) molar flow rate histories (a) at the column outlet and temperature histories (b) obtained for binary H_2-CO_2 breakthrough curve (run 2) at 298 K and 5 bar on activated carbon AC5-KS; Mixture: 30% of CO_2 balanced with H_2; Temperatures measured at 0.050 m (Bottom (■,——)), 0.159 m (Middle (◆,——)) and 0.271 m (Top (▲,——)) from feed inlet; Flow rate of 5.00×10^{-5} m^3 s^{-1} (measured at 298 K and 1 bar); Experimental data (symbols); Simulation (lines). 229

Figure 6.12: H_2 (△,----) and CO_2 (□,——) molar flow rate histories (a) at the column outlet and temperature histories (b) obtained for binary H_2-CO_2 breakthrough curve (run 3) at 298 K and 1.5 bar on activated carbon AC5-KS; Mixture: 20% of CO_2 balanced with H_2; Temperatures measured at 0.050 m (Bottom (■,——)), 0.159 m (Middle (◆,——)) and 0.271 m (Top (▲,——)) from feed inlet; Flow rate of 8.33×10^{-5} m^3 s^{-1} (measured at 298 K and 1 bar); Experimental data (symbols); Simulation (lines). 230

Figure 6.13: a) CO_2 gas phase concentration histories (——) and CO_2 concentration in the macropores (— · · —) at the bed outlet; b) Temperature histories at 0.050 m (Bottom (——)), 0.159 m (Middle (——)) and 0.271 m (Top (——)) from feed inlet; c) Adsorbed phase concentration profiles of CO_2 at breakthrough time (----) [$C_g(CO_2) > 1 \times 10^{-4}$ mol m^{-3}] and at equilibrium (— · —); Results for the binary breakthrough experimental run 1; Column packed with AC5-KS; Mixture: 30% of CO_2 balanced with H_2; Pressure of 5 bar, temperature of 298 K and flow rate of 1.167×10^{-5} m^3 s^{-1} (measured at 298 K and 1 bar). 233

Figure 6.14: a) CO_2 gas phase concentration histories (——) and CO_2 concentration in the macropores (— · · —) at the bed outlet; b) Temperature histories at 0.050 m (Bottom (——)), 0.159 m (Middle (——)) and 0.271 m (Top (——)) from feed inlet; c) Adsorbed phase concentration profiles of CO_2 at breakthrough time (----) [$C_g(CO_2) > 1 \times 10^{-4}$ mol m^{-3}] and at equilibrium (— · —); Results for the binary breakthrough experimental run 2; Column packed with AC5-KS; Mixture: 30% of CO_2 balanced with H_2; Pressure of 5 bar, temperature of 298 K and flow rate of 5.00×10^{-5} m^3 s^{-1} (measured at 298 K and 1 bar). 234

Figure 6.15: a) CO_2 gas phase concentration histories (——) and CO_2 concentration in the macropores (— · · —) at the bed outlet; b) Temperature histories at 0.050 m (Bottom (——)), 0.159 m (Middle (——)) and 0.271 m (Top (——)) from feed inlet; c) Adsorbed phase concentration profiles of CO_2 at breakthrough time (----) [$C_g(CO_2) > 1 \times 10^{-4}$ mol m^{-3}] and at equilibrium (— · —); Results for the binary breakthrough experimental run 3; Column packed with AC5-KS; Mixture: 20% of CO_2 balanced with H_2; Pressure of 1.5 bar, temperature of 298 K and flow rate of 8.33×10^{-5} m^3 s^{-1} (measured at 298 K and 1 bar). 235

Figure 6.16: Normalized gas phase concentration profiles of CO_2 at breakthrough time [$C_g(CO_2) > 1 \times 10^{-4}$ mol m^{-3}] for each breakthrough run: 1 (——), 2 (— —) and 3 (— · —). 236

Figure 6.17: Pressure (a; ○,——) and temperature (b) histories; Cycle sequence: (1) co-current feed step, (2) co-current depressurization step, (3) counter-current blowdown step, (4) counter-current purge step with hydrogen, (5) co-current pressurization step with feed; Temperatures measured at 0.050 (Bottom (□,----)), 0.159 (Middle (◇,— —)) and 0.271 m (Top (△,——)) from feed inlet; Adsorbent: AC5-KS; Experimental data (symbols); Simulation (lines). 238

Figure 6.18: H_2 (△,----) and CO_2 (□,——) molar flow rate histories (a) obtained for cycle 1 (1) and 2 (2) at the outlet of a bed packed with AC5-KS; Temperature histories (b) measured for cycle 1 (1) and 2 (2) at 0.050 m (Bottom (■,----)), 0.159 m (Middle (◆,— —)) and 0.271 m (Top (▲,——)) from feed inlet; Flow rate of 5.00×10^{-5} m^3 s^{-1} (measured at 298 K and 1 bar); Experimental data (symbols); Simulation (lines). 239

Figure 6.19: H_2 (△,----) and CO_2 (□,——) molar flow rate histories (a) obtained for cycle 60 (1) and 250 (2) at the outlet of a bed packed with AC5-KS; Temperature histories (b) measured for cycle 60 (1) and 250 (2) at 0.050 m (Bottom (■,----)), 0.159 m (Middle (◆,— —)) and 0.271 m (Top (▲,——)) from feed inlet; Flow rate of 5.00×10^{-5} m^3 s^{-1} (measured at 298 K and 1 bar); Experimental data (symbols); Simulation (lines). 240

Figure 6.20: Hydrogen purity, hydrogen recovery and process productivity for different feed flow rates using the same parameters described in simulation 9; Simulation of the RPSA adsorption process using a single adsorbent bed packed with AC5-KS; Red symbols (RPSA simulation 9). 244

Figure 6.21: Hydrogen purity, hydrogen recovery and process productivity for different purge/feed ratios using the same parameters described in simulation 9; Simulation of the RPSA adsorption process using a single adsorbent bed packed with AC5-KS; Red symbols (RPSA simulation 9). 244

Figure 6.22: Hydrogen purity, hydrogen recovery and process productivity for different purge pressures using the same parameters described in simulation 9; Simulation of the RPSA adsorption process using a single adsorbent bed packed with AC5-KS; Red symbols (RPSA simulation 9). 245

List of Tables

Chapter 2

Table 2.1: Physical properties of activated carbon R2030 pellets. 37

Table 2.2: Table 2.2: Physical properties of activated carbon ACM-3mm pellets. 38

Table 2.3: Specific surface area, total pore volume and average pore size of the HY2SEPS-AC sample estimated from the N_2 physisorption data and using mercury porosimetry. 39

Table 2.4: Specific surface area, total pore volume and average pore size of the HY2SEPS-ZEO sample estimated from the N_2 physisorption data and using mercury porosimetry. 40

Table 2.5: Virial adsorption isotherm fitting parameters of CO_2, H_2, CH_4, CO, N_2 and H_2O on activated carbon R2030. 45

Table 2.6: Fitting parameters of the multisite Langmuir model for CO_2 and H_2 adsorption equilibrium on activated carbon ACM-3mm at 303, 323 and 343 K. 46

Table 2.7: Fitting parameters of the multisite Langmuir model for CO_2, H_2, CH_4, CO and N_2 adsorption equilibrium on HY2SEPS-AC at 303, 323 and 343 K. 49

Table 2.8: Fitting parameters of the multisite Langmuir model for CO_2, H_2, CH_4, CO and N_2 adsorption equilibrium on HY2SEPS-ZEO at 303, 323 and 343 K. 54

Chapter 3

Table 3.1: Molecular weight and Lennard-Jones parameters of each compound [15]. 76

Table 3.2: Experimental conditions used on the ZLC measurements of CO_2, CH_4 and CO in activated carbon R2030 at 1 bar of total pressure. 83

Table 3.3: Micropore diffusivity (divided by r_c^2) obtained through ZLC experiments for CO_2, CH_4 and CO in R2030 within 303-343 K at infinite dilution. 85

Table 3.4: Experimental conditions used on the pulse experiments of H_2, CH_4 and CO in R2030 at 1 bar of pressure. 88

Table 3.5: Pulse experimental results obtained for H_2, CH_4 and CO in R2030 at 1 bar and 303-343 K. 88

Table 3.6: Experimental conditions used on the dilute breakthrough experiments of CO_2 in R2030 at 1 bar of pressure. 89

Table 3.7: Diluted breakthrough experimental results obtained for CO_2 in R2030 at 1 bar and 303-343 K. 91

Table 3.8: Micropore diffusivity (divided by r_c^2) obtained through ZLC experiments and pulse or breakthrough experiments for CH_4, CO and CO_2 in R2030 within 303-343 K at infinite dilution. 92

Table 3.9: Experimental conditions used on the ZLC measurements of CO_2 in ACM-3mm at 1 bar of pressure. 93

Table 3.10: Experimental conditions used on the measurement of the breakthrough curves of CO_2, CH_4, CO, N_2, H_2 and H_2O on HY2SEPS-AC at 1 bar of pressure. 94

Table 3.11: Contributions of the axial dispersion term, film mass transfer term, pore resistance term and micropore resistance term for CO_2, H_2, CH_4, CO and N_2 in HY2SEPS-AC at 303, 323 and 343 K. 97

Table 3.12: Micropore diffusivity (divided by r_c^2) and the parameters to describe temperature dependence of micropore diffusion of CO_2, H_2, CH_4, CO and N_2 in HY2SEPS-AC within 303-343 K at infinite dilution. 98

Table 3.13: Experimental conditions used on the measurement of the breakthrough curves of CO_2, CH_4, CO, N_2, H_2 and H_2O on HY2SEPS-ZEO at 1 bar of pressure. 101

Table 3.14: Contributions of the axial dispersion term, film mass transfer term, pore resistance term and crystal resistance term for CO_2, H_2, CH_4, CO and N_2 in HY2SEPS-ZEO at 303, 323 and 343 K. 102

Table 3.15: Crystal diffusivity (divided by r_c^2) and the parameters to describe temperature dependence of crystal diffusion of CO_2, H_2, CH_4, CO and N_2 in HY2SEPS-ZEO within 303-343 K at infinite dilution. 103

Chapter 4

Table 4.1: Conditions of the activation process. 114

Table 4.2: Characteristics of the column employed in the activation process; adsorbent physical properties. 115

Table 4.3: Conditions and results of the activation process. 116

Table 4.4: Characteristics of the different columns employed in the activation process. 117

Table 4.5: Experimental conditions used in the measurement of the breakthrough curves (single component) on the modified activated carbon sample AC5-KS. 122

Table 4.6: Virial adsorption isotherm model. 123

Table 4.7: Moment analysis based on the derivative of diluted breakthrough curves and correlations used to estimate the diffusivity constants. 123

Table 4.8: Mathematical model used for fixed-bed experiments of CO_2-H_2-CH_4 multicomponent mixtures. 124

Table 4.9: Virial adsorption isotherm fitting parameters of CO_2, H_2, CH_4, CO and N_2 for the modified activated carbon AC5-KS at 303-323 K. 127

Table 4.10: Micropore diffusivity (divided by r_c^2) and activation energy of CO_2, H_2, CH_4, CO and N_2 in the original and modified activated carbons. 128

Table 4.11: Experimental conditions used on the measurement of the breakthrough curves of N_2 (1.0% and 25.0% of N_2 balanced in He) in zeolites 13X, 13X-Li, 13X-Ba and 13X-Ca at 303 and 323 K and 1 bar of total pressure. 135

Table 4.12: Breakthrough experimental results obtained for nitrogen (mixtures of 1.0% or 25.0% of N_2 balanced in He) in zeolites 13X, 13X-Li, 13X-Ba and 13X-Ca at 303 and 323 K and 1 bar of total pressure. 137

Table 4.13: Contributions of the axial dispersion term, film mass transfer term, pore resistance term and crystal resistance term for N_2 in zeolites 13X, 13X-Li, 13X-Ba and 13X-Ca at 303 and 323 K and 1 bar of total pressure. 138

Table 4.14: Experimental conditions used on the measurement of the breakthrough curves of CO_2, CH_4, CO (0.5% of adsorbate balanced in He) and of pure H_2 in zeolite 13X-Ca at 303 and 323 K and 1 bar of total pressure. 139

Table 4.15: Breakthrough experimental results obtained for carbon dioxide, methane, carbon monoxide and hydrogen in ion exchanged zeolite 13X-Ca at 303 and 323 K and 1 bar of total pressure. 141

Table 4.16: Contributions of the axial dispersion term, film mass transfer term, pore resistance term and crystal resistance term for CO_2, H_2, CH_4, CO and N_2 in zeolite 13X-Ca at 303 and 323 K and 1 bar of total pressure. 141

Table 4.17: Breakthrough experimental results obtained for carbon dioxide, methane, carbon monoxide and hydrogen in ion exchanged zeolite 13X-Ca at 303 and 323 K and 1 bar of total pressure changing the tortuosity factor or axial dispersion correlation. 142

Table 4.18: Virial adsorption isotherm fitting parameters of N_2, CO_2, CH_4, CO and H_2 for the ion exchanged zeolite 13X-Ca at 303-323 K. 146

Chapter 5

Table 5.1. Properties of the column used and experimental conditions of the fixed-bed breakthrough curves on the activated carbon R2030. 162

Table 5.2: Properties of the column used and experimental conditions of the fixed-bed breakthrough curves on the modified activated carbon AC5-KS. 162

Table 5.3: Properties of the column used and experimental conditions of the fixed-bed breakthrough curves on AC5-KS performed in the “compact” PSA. 165

Table 5.4: Experimental conditions of the PSA experiment using the modified activated carbon AC5-KS. 167

Table 5.5: Virial isotherm fitting parameters of pure H_2, CO_2, CO, CH_4 and N_2 at 303-323 K on activated carbons R2030 and AC5-KS. 168

Table 5.6: Transport parameters used in the breakthrough simulations of activated carbons R2030 and AC5-KS performed in the fixed-bed unit for ternary mixtures. 174

Table 5.7: Transport parameters used in the breakthrough simulations of modified activated carbon AC5-KS performed in the “compact” PSA unit for multicomponent mixtures. 175

Table 5.8: H_2 PSA simulations using a single bed packed with AC5-KS. 176

Table 5.9: Transport parameters used in the PSA simulations of modified activated carbon AC5-KS performed in the "compact" PSA unit for multicomponent mixtures. 177

Table 5.10: Performance parameters for the H_2 PSA simulations using a bed packed with AC5-KS. 195

Chapter 6

Table 6.1: Properties of the column used and experimental conditions of the fixed-bed breakthrough curves on the modified activated carbon AC5-KS performed in the "adapted" RPSA facility. 225

Table 6.2: Experimental conditions of the RPSA experiment using the activated carbon AC5-KS; Virial isotherm fitting parameters of pure H_2 and CO_2 at 303-323 K on the same adsorbent. 226

Table 6.3: Transport parameters applied in the simulations of the fixed-bed experiments using a column packed with the activated carbon AC5-KS. 231

Table 6.4: Transport parameters applied in the simulation of the RPSA process using a single column packed with the activated carbon AC5-KS. 237

Table 6.5: Performance parameters for the H_2 RPSA simulations using a bed packed with AC5-KS. 242

1.

Introduction

1.1 Relevance & Motivation

Billion tonnes of greenhouse gases (GHG) are annually released into the atmosphere due to various activities that use fossil fuels. In 2008, the three CO_2 top emitters were China (21.5%) followed by U.S.A. (19.2%) and Europe (15.3%) (see Figure 1.1 a). Due to the continuous raise of CO_2 emissions (illustrated in Figure 1.1 b), the industrialized nations were trying to agree to limit GHG emissions [1]. To avoid unknown consequences in global weather, there is a general consensus that the emission of anthropogenic GHG to atmosphere should be reduced significantly. This environmental pressure is translated to economic penalties to countries included in the Annex B of the Kyoto protocol [2-3], forcing the reduction of GHG emissions. Therefore, alternative fuels and new routes for energy production have gained total acceptance to avoid economic and environmental problems.

The use of hydrogen as advanced energy carrier has received much attention in the last years, due to the environmental concerns mentioned before. Hydrogen can be an environmentally cleaner supply of energy without release of pollutants or GHG. Developments in the fuel cell industry were encouraging to replace the conventional fossil fuels by hydrogen, primarily in transportation and power generation, due to the extremely efficient energy conversion of fuel cell devices [4]. Thus, it is expected that the worldwide production of hydrogen may strongly increase. This increase boost the development of processes to recover hydrogen. This last aspect is particularly essential in petroleum refining and processing industries, where for most of the

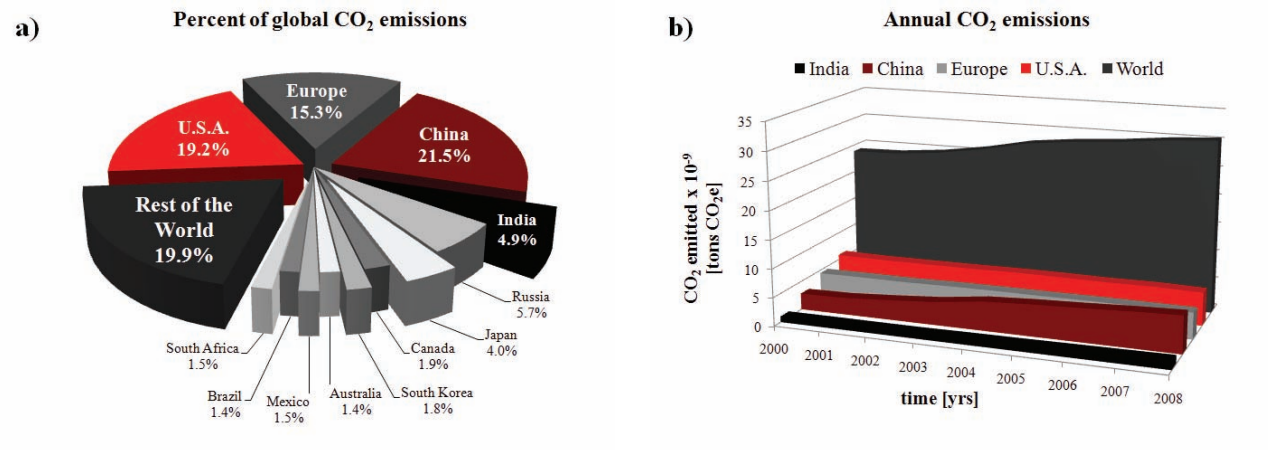


Figure 1.1: Carbon dioxide emissions: a) percent of global CO_2 emissions in 2008; b) annual CO_2 emissions between 2000 and 2008 [1].

applications a high purity hydrogen product is required [5]. Moreover, industrial applications such as hydrocracking, steel annealing, glass making, hydrogenation of fats and oils, methanol production and manufacture of silicon use hydrogen with high purity [6].

Since hydrogen is scarce in its natural and elemental form its production is essential. Hydrogen can be produced from many sources: fossil fuels, renewable resources and nuclear energy. The annual production of hydrogen is around 50 million tones, for industrial and commercial purposes [7]. At the moment, hydrogen is produced via steam methane reforming (SMR) of natural gas, steam reforming of naphtha and gasification of residue-coke-coal [8-9]. However, the major production of hydrogen is essentially from natural gas with approximately half of its global production by SMR process [10-12]. The SMR to produce hydrogen is generally privileged due to the lower capital cost of this process, especially if natural gas is obtainable at reasonable prices. Note that there are also gasification plants producing hydrogen from coal and oil refinery residues [8]. The hydrogen produced from renewable sources (wind turbines, solar collectors, and biomass) is nowadays considerably more expensive than H_2 produced from natural gas, residual oil and coal. For this reason, the production of hydrogen is more economically efficient using fossil fuels with the additional cost of capture and storage of carbon dioxide [7-8].

When steam reforming of hydrocarbons is used for the production of hydrogen, carbon oxides are generated. The SMR reactor releases a gas mixture containing 70-72% of hydrogen, 15-20% of carbon dioxide, < 4% of carbon monoxide, < 8% of unreacted methane and is saturated with water. If the methane employed as fuel contains nitrogen as contaminant, the SMR off-gases contain nitrogen (< 4%) [9, 13]. Therefore, to obtain high purity hydrogen (99.99+% for fuel cell

applications with less than 10 ppm of carbon monoxide contamination) [14-15], the contaminants should be removed. Since the number of gases to be separated is extensive (i.e., water vapour, hydrocarbons, carbon oxides, nitrogen), it is essential to consider the characteristics of the different separation processes. The removal of the majority of the contaminants is normally accomplished in a pressure swing adsorption (PSA) unit that follows the SMR reactor [10, 12-13, 16-23].

1.2 Pressure swing adsorption technologies

The first pressure swing adsorption (PSA) process was patented in 1932 by Finlayson and Sharp [24], comprising a single bed cycle with a pressurization step and a sequence of depressurization steps. Twenty years later, Kahle (1952) [25] disclosed a two beds PSA process for water and carbon dioxide removal from air [26]. The PSA technology was introduced as a commercial process for air separation in the 1960s by Skarstrom (1960) [27] and, in different and independent version, by Guerin de Montgareuil and Domine (1964) [28]. Today, the PSA technology is widely applied for hydrogen purification systems [9-10, 12-13, 18, 21, 26], 44 years after the commercialization of the first unit, installed with a steam reformer in Toronto, Canada [9, 26, 29].

A PSA separation process is a gas-solid system operated in cycles where one or more fixed bed columns are packed with an appropriate adsorbent (solid phase) that preferentially adsorbs one or more components from a gas mixture [18, 30-34]. The PSA process is based on the principle that adsorbents are capable of adsorbing more impurities at a higher partial pressure than at a lower partial pressure [29]. That is, contacting the gas with the solid, some of the compounds of the gas mixture are more selectively adsorbed on the microporous/mesoporous structure of the adsorbent [34]. This selectivity essentially depends on the difference in adsorption equilibrium, difference in adsorption rates (kinetic selectivity) and/or steric effects of the different adsorbate molecules of the mixture (size exclusion) [18, 31].

These adsorptive separation processes are characterized by an ordered sequence of adsorption-desorption steps, “swinging” between two different points of the same equilibrium isotherm (see Figure 1.2 a) [18]. The two main steps of a PSA process are: (1) the adsorption step, carried out at the higher pressure, where the preferentially adsorbed compounds are separated from the feed mixture; (2) the desorption or regeneration step, accomplished at lower pressure, where the most adsorbed species are partially removed from the adsorbent preparing the column for the next cycle (see Figure 1.2 b) [18, 33-34]. As Figure 1.2 (a) shows, the useful capacity is the difference

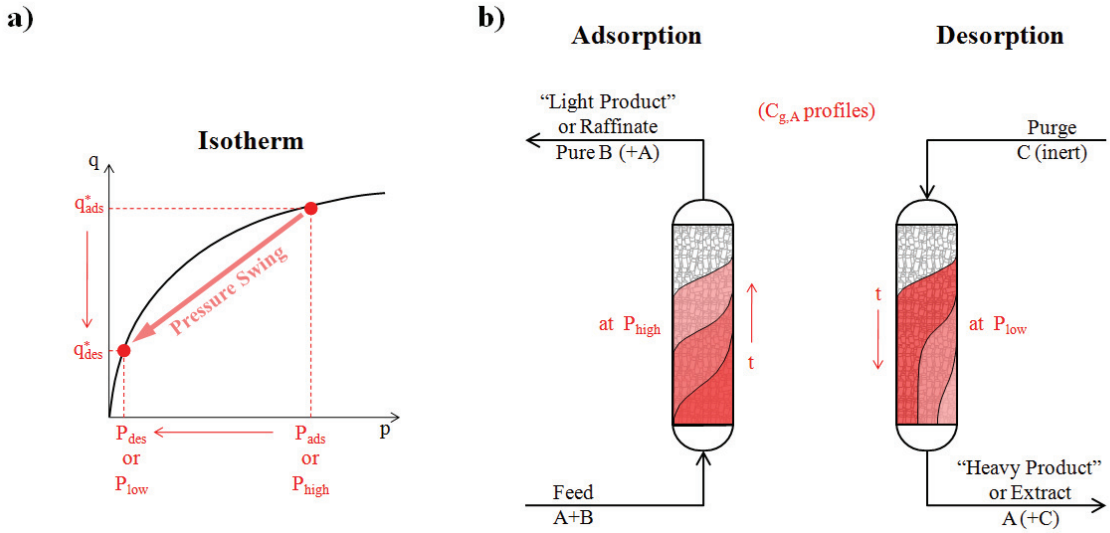


Figure 1.2: The PSA process: a) change in equilibrium loading with pressure; b) idealized diagram showing movement of the adsorbed phase concentration profile for the more strongly adsorbed compounds in a PSA process (adsorption vs desorption).

in loading between the adsorption and desorption step pressures, on the same isotherm.

Thus, at least two streams are produced in a PSA process. During the adsorption step, a "light product" or raffinate stream is produced (high amount of the gases with the less affinity to the adsorbent) and during the desorption or regeneration step, a "heavy product" or extract stream is recovered (mainly the gases with more affinity to the adsorbent) [31]. It is possible to obtain useful products from either the adsorption or desorption steps or from both steps [18, 30-31]. Note that the adsorption step is usually terminated before the more strongly adsorbed compound breaks through the bed. Therefore, a high purity "light product" stream is obtained. On the other hand, the desorption step is commonly terminated before the bed is completely desorbed, producing a "heavy product" stream with the preferentially adsorbed compounds [18].

As previously mentioned, the mostly employed PSA cycle to produce the less retained compound was proposed and introduced as commercial process in 1960 by Skarstrom [27]. Figure 1.3 illustrates the Skarstrom cycle composed by the following steps: (1) co-current pressurization with feed; (2) feed; (3) counter-current blowdown; (4) counter-current purge with the "light product". The pressurization step, can be performed in co-current way with the feed stream or in counter-current way with the "light product" produced. Then, the "light product" is obtained at high pressure during the feed step. Alternatively, the "heavy product" is obtained at lower pressure in the counter-current blowdown. Finally, a counter-current purge step with the less retained compound is performed.

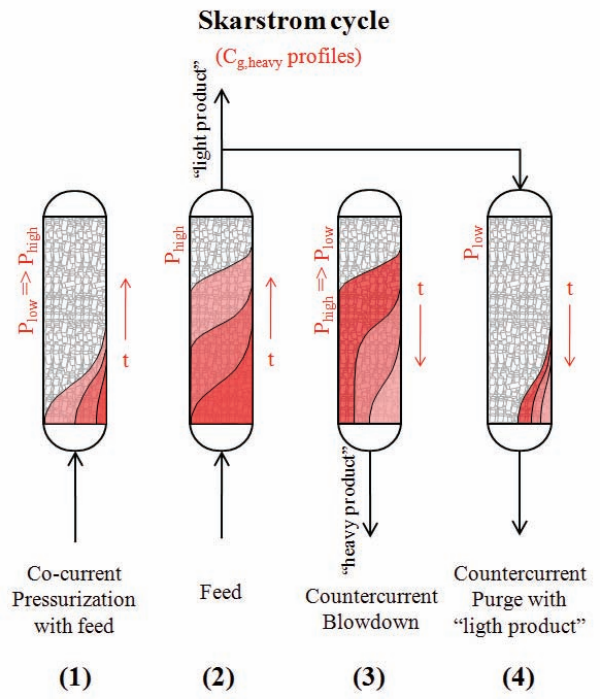


Figure 1.3: The Skarstrom cycle: (1) co-current pressurization step with feed; (2) feed step; (3) counter-current blowdown step; (4) counter-current purge step with the "light product" [27].

This cycle was the basic configuration adopted for PSA processes for different gas separation systems. It was modified and rearranged to improve process performance in different occasions. For example, Berlin (1966) [35] introduced in the Skarstrom cycle an equalization step (composed by a pressure-equalization pressurization step and a pressure-equalization depressurization step). The so-called modified Skarstrom cycle is illustrated in Figure 1.4 [9, 18, 35]. In this case, a PSA process with two columns is needed. After the initial co-current pressurization step with feed and the following feed step in column A, it is depressurized (with the previous flow direction) connecting it to column B where the pressure-equalization pressurization step starts in counter-current way until the pressure in both columns is equalized. After the equalization, the blowdown step starts in column A while the pressurization step begins in column B. Because the compressed gas from the high pressure column A is partially used to pressurize the low pressure column B through a pressure equalization step, the energy consumption of the process and the gas wasted during the cycle (blowdown step) are reduced [18, 31].

Based on the modified Skarstrom cycle proposed by Berlin (1966) [35], studies to develop PSA processes to recover hydrogen from different sources, such as steam methane reforming (SMR) off-gases, refinery fuel gases, coke oven gases and others, were performed [12, 18, 36]. The

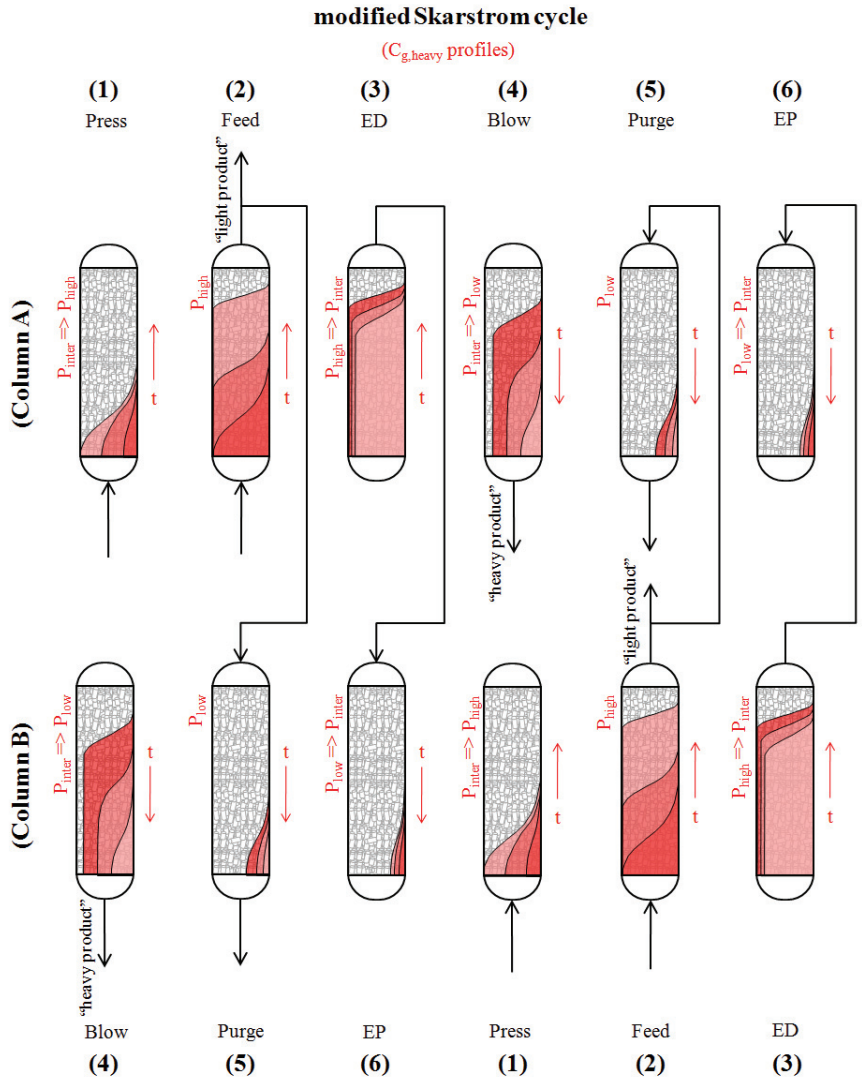


Figure 1.4: The modified Skarstrom cycle [9, 18, 35]: (1) co-current pressurization step with feed; (2) feed step; (3) co-current pressure-equalization depressurization step; (4) counter-current blowdown step; (5) counter-current purge step with the "light product"; (6) counter-current pressure-equalization pressurization step.

SMR off-gases contain 70-80% of hydrogen balanced with several impurities, namely water vapour, carbon dioxide, methane, carbon monoxide and nitrogen [13]. To attain an economically attractive process, high purity (99.99+%) hydrogen product is required with recovering as much hydrogen as possible. Complex column schemes were developed in order to achieve 80% of recovery from this multicomponent feed mixture [18, 31]. Since the number of gases to be removed from the feed stream is large, different aspects of the PSA process employed in hydrogen purification were considered to enhance the process performance and reduce unit size and energetic costs. Thus, the design and operation of the PSA systems present complex engineering challenges

because of the large number of parameters and variables involved. From the beginnings of the PSA studies for hydrogen purification [19] until more recently, the bed where they take place (in the same bed distributed as layers or in distinct beds) [6, 19, 37-46], the type of adsorbents [10, 12, 19, 47-58], the cycle steps [16, 29, 42, 59-67] and also integrated processes (with tanks, two stage processes or rapid PSA) [5, 22, 67-80] have been studied. Major achievements reported in literature are considered below.

1.2.1 Layered beds

As mentioned before, the number of gases to remove from the stream under scope is significant. Therefore, different layers of adsorbents are commonly used to remove one targeted contaminant or group of contaminants. Figure 1.5 shows a single adsorbent bed and different configurations for multi-layered beds packed with activated carbons, zeolites and alumina [6, 16, 20, 38-40, 68, 81].

In all PSA processes, it is crucial to avoid the breakthrough of the most adsorbed impurity (or impurities) from the whole bed to achieve a high purity product. However, in layered PSA configurations other restrictions may have to be satisfied. It can happen that one impurity must be kept in the first layer because it is very strongly adsorbed in the second layer. This means that it may also be important to avoid the breakthrough of the heaviest impurities from their specific adsorbents into the following layers, otherwise, the following layers will lose adsorption capacity

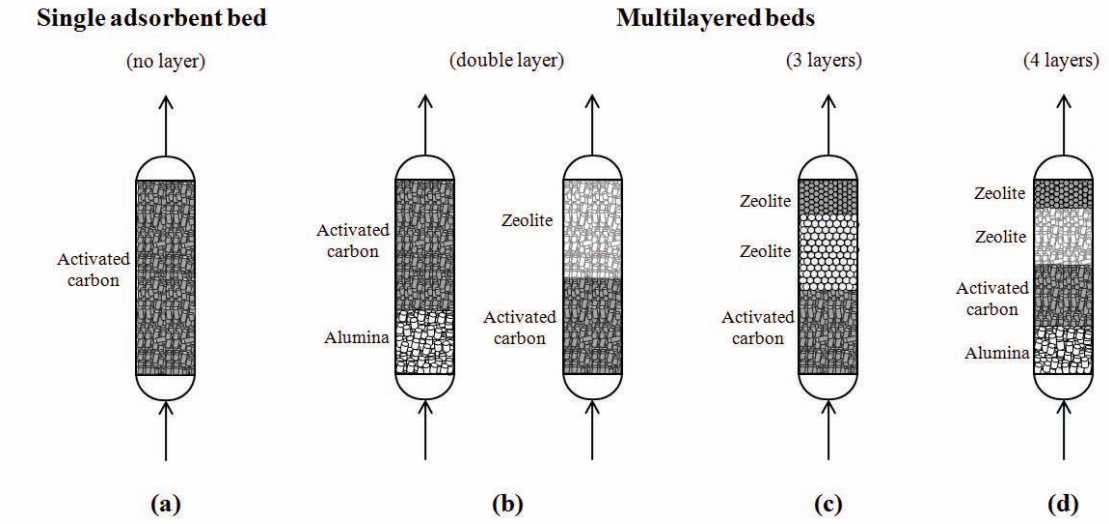


Figure 1.5: Single adsorbent bed (a) and different configurations for multi-layered beds packed with activated carbons, zeolites and alumina: beds with 2 (b), 3 (c) and 4 layers (d).

for the desired contaminants [41]. A common layered bed configuration is composed by a first layer (alumina or silica) to preferably retain the water vapour, followed by an activated carbon layer to selectively adsorb carbon dioxide and hydrocarbons (i.e., methane) and finally a zeolite layer with enhanced capacity for carbon monoxide and nitrogen [6, 68].

Several processes have been proposed where different types of adsorbents are either placed in the same bed as layers or put in distinct beds. In 1969, Wagner (1969) [19] filled the first patent for hydrogen purification from SMR off-gases (77.1% of H_2, 0.013% of CH_4, 0.35% of CO and 2.5% of CO_2) through PSA technology, where two types of adsorbents distributed as layers were considered. The author proposed an activated carbon for the first layer, to retain the heavy compounds (water vapour, carbon dioxide and methane); a zeolite 5A (zeolite CaA type) for the second layer, to selectively adsorb the lighter contaminants (carbon monoxide and nitrogen) and remaining methane. Wagner reported an example where hydrogen can be produced with 99.9999% of purity and 76.5% of recovery, using for that a 4 layered-beds (activated carbon and zeolite CaA) unit.

Fuderer and Rudelstorfer (1976) [42], from Union Carbide Corporation, disclosed the Polybed process in the U.S. Patent 3,986,849: an adiabatic multi-bed (at least 7 beds) PSA process for H_2 purification from a mixture of SMR off-gases (77.1% of H_2, 22.5% of CO_2, 0.35% of CO and 0.013% of CH_4). The authors reported an adiabatic 11 steps 10 layered-bed (activated carbon and zeolite A) process that produces hydrogen with a purity of 99.999% and recovery of 86.0%. For larger productions (above 0.4 M $Nm^3 day^{-1}$), Union's Carbide's Polybed process, based on Fuderer and Rudelstorfer patent, has proved to be more economical [26, 42].

In 1997, Warmuziński and Tańczyk [46] modelled large-scale layered multi-beds PSA installations for multicomponent processes using a H_2 purification plant as a test case. The authors reported that almost pure hydrogen with 74% of hydrogen recovery can be achieved applying the modelled process. Tańczyk and Warmuziński (1998) [45] also validated the model developed based on experimental data for the separation of H_2-CH_4 systems on activated carbon and the production of H_2 on 5A zeolite. It was stated that a satisfactory agreement is found between the theoretical model and the experiments for a wide range of operating parameters [45].

Malek and Farooq (1998) [44] studied the performance of a 6-bed (double layered) PSA process for hydrogen purification from refinery fuel gas through simulations. The authors verified that it is preferable to use double layered beds of silica gel followed by an activated carbon instead of beds only packed with activated carbon. It was concluded that the initial layer of silica gel prevents the gradual degradation of the activated carbon layer improving the process performance.

Park *et al.* (1998) [82] studied the adsorbed dynamics for multicomponent adsorption in layered beds (activated carbon followed by zeolite 5A) through experimental measurements and simulations. The authors concluded that exist an optimum relative length of activated carbon layer to total bed length which maximizes the bed utilization that can be achieved, and this value should be determined according to the feed composition and feed velocity. The authors reported that different optimum values could be attained if isothermal or adiabatic assumption is considered [82]. Park *et al.* (1998) [82] also concluded through simulation studies that, the optimum values increase with contact time.

Lee *et al.* (1999) [43] and Ahn *et al.* (2001) [37] studied the effects of carbon-to-zeolite ratio on layered (activated carbon and zeolite 5A) 2-bed 7-step H_2 PSA for the production of high purity hydrogen from a mixture of H_2, CH_4, CO, N_2 and CO_2 (coke oven gas). In this case, to develop the model of each layered bed, two independent beds with a single adsorbent were assumed [43].

In 2002, Baksh and Ackley [6] claimed that 80% (or greater) hydrogen recovery and higher than 99.9% of purity are obtained in a multi-layer adsorbent bed process when it is used a prior layer of zeolite with 2.0-2.5 SiO_2/Al_2O_3 ratio (CaX or LiX zeolite or VSA6 adsorbent) to remove substantially all the nitrogen in the feed stream. Two years later, Baksh *et al.* (2004) [38-39] proposed a layered-bed PSA system for H_2 purification where each bed is divided into four layers. The first layer (alumina, silica gel, silicalite or zeolite) comprises an adsorbent for the removal of water from the feed stream. The second layer (activated carbon, alumina-activated carbon mixture or zeolite) functions to reduce high level contaminants in the hydrogen containing feed to less than 10% (in particular CO_2). The third layer (activated carbon) comprises an adsorbent capable of reducing the concentrations of all impurities entering this layer to less than 1%. Finally, the fourth layer (CaX, LiX or LiCaX zeolite or VSA6 adsorbent) consist of adsorbents having high Henry' law constant for nitrogen (preferably >2.3 $mol\,kg^{-1}\,atm^{-1}$) and carbon monoxide (>2.94 $mol\,kg^{-1}\,atm^{-1}$) to remove the remaining impurities. The authors also reported a layered bed where the second layer is omitted and/or combined with the third layer. According to the layers configuration, the authors claim a hydrogen recovery of 76-84% for a hydrogen purity of 99.99%.

1.2.2 Modified adsorbents

For the design of a hydrogen purification PSA unit, the adsorbent materials applied for the separation have a strong relevance in the performance of the process. The thermodynamic

properties of the adsorbents directly affect the separation of the different compounds present in the mixture. For hydrogen purification processes, the most important aspects for the adsorbent selection are the adsorption equilibrium capacities/selectivities and the isosteric heats of adsorption of the multicomponent mixture. Also the equilibrium-controlled desorption of the contaminants during the different PSA process steps plays an important role on the selection of the adsorbent [12].

Due to the large number of gases to be separated in the H_2 purification PSA process, different types of adsorbents have been proposed to remove a single or group of contaminants. In 1984, Reiss (1984) [58] proposed an improvement of the process patented by Wagner (1969) [19]. Instead of zeolite 5A, the author proposed the use of a zeolite CaX (zeolite X in the calcium form), with at least 50% of the ions exchanged with calcium. With this new adsorbent, an enhancement of the carbon monoxide and nitrogen capacities were observed. As an example, the ion exchange of the non-framework cation (Na^+) of the zeolite X with calcium cations is illustrated in Figure 1.6.

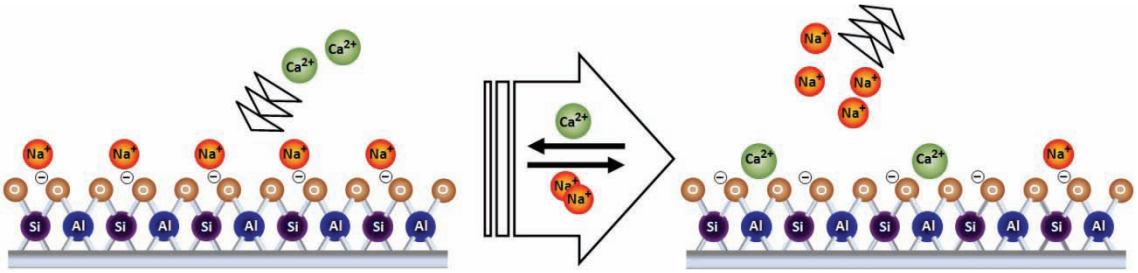


Figure 1.6: Ion exchange of the non-framework cation (Na^+) of the zeolite X with calcium cations.

Golden *et al.* (1990) [51] disclosed in their U.S. Patent 4,957,514 the use of a BaX zeolite (zeolite X exchanged with barium) for the separation of hydrogen from a stream containing methane, carbon monoxide and nitrogen. According to the authors, for a given stream flow rate and purity of hydrogen, the bed length is reduced when BaX zeolite is used. According to the examples showed in the patent, it can be observed that the authors used a nitrogen molar fraction lower than 0.2%. Therefore, only the enhanced ability of the new proposed adsorbent towards methane and carbon monoxide is emphasised.

Afterwards, Bomard *et al.* (1997) [48] reported in their Patent WO97/45363 the higher CO and N_2 adsorption capacities of LiX zeolite (lithium exchanged zeolite X). In this patent, a three layer bed is proposed: a first layer of silica gel for the removal of water vapour; a second layer of

activated carbon for the removal of carbon dioxide and hydrocarbons; a third layer of LiX zeolite, with at least 80% of the ions exchanged with lithium and with a Si/Al ratio of less than 1.5, for the final removal of carbon monoxide and nitrogen. These studies were followed by Plee (1998) [55-56] (European Patent 855,209 A1 and B1) and Plee and Masini (2001) [57] (European Patent 1,116,691 A1) and afterwards by Plee (2004) (U.S. Patent 6,464,756 B1), considering the use of a zeolite LiX and also a zeolite LiCaX (both with 1.0-1.5 Si/Al ratio). He found that a Li/(Li+Ca) greater than 0.7 was preferable. At that time, the authors found that it was preferable for nitrogen adsorption a binary lithium and calcium ion exchanged zeolite X for a Li/(Li+Ca) ratio higher than 0.7.

On the other hand, few years before, it was disclosed by Coe *et al.* (1992, 1993) [49-50] the use of zeolite X at least binary exchanged with lithium, calcium and/or strontium ions for nitrogen separation from less adsorbed components (oxygen, hydrogen or argon). The influence of the zeolite composition (according to the percentage of each exchanged ion) on the nitrogen capacity was studied by the authors and it was found that the best performance was obtained using zeolite X exchanged 85% with lithium and 15% with a second ion (calcium or strontium).

In 2001, Johnson *et al.* (2001) [54] reported in U.S. Patent 6,302,943 B1 an improved adsorption process provided for purifying hydrogen from a feed gas mixture including hydrogen and at least one impurity selected from the group consisting of CO and N_2. For this process, an adsorbent with a preferred range value of Henry' law constant was placed at the outlet end of the bed. The authors declared that, the optimum adsorbent for the CO-H_2 separation had a Henry' law constant at 70 ºF of 0.8-2.2 mol kg^{-1} atm^{-1}, while for N_2-H_2 separation, it had 0.55-0.83 or 0.85–1.40 mol kg^{-1} atm^{-1}.

Hirano and Harada (2001, 2003) [52-53] studied the purification of a mixture containing hydrogen, carbon monoxide, nitrogen and methane. The authors revealed a high purity low silica type X zeolite substantially free from binder to attain higher CO and N_2 adsorption capacities. The kaolin clay used as binder is converted to a low-silica type X zeolite. It is claimed that, the cation contained in the shaped adsorbent is at least one kind of cation selected from the group consisting of lithium, sodium, potassium, magnesium, calcium and zinc.

As Bomard *et al.* [48] patented in 1997, also Bec (2003, 2005) [10, 47] in U.S. Patent Application 2003/0172808 A1 and U.S. Patent 6,849,106 B2 proposed an adsorption bed packed with three adsorbent layers for H_2 purification. In this case, the adsorbents proposed were: an activated carbon (1^{st} layer) for the removal of heavy compounds (water vapour, carbon dioxide and hydrocarbons); followed by a CaA zeolite (type A zeolite exchanged at least 60% with calcium as

2nd layer) for selective adsorption of carbon monoxide; finally, a low silica CaX or LiX zeolite (type X zeolite exchanged at least 60% with calcium or, more preferable, lithium as 3rd layer) for the removal of remaing carbon monoxide and nitrogen.

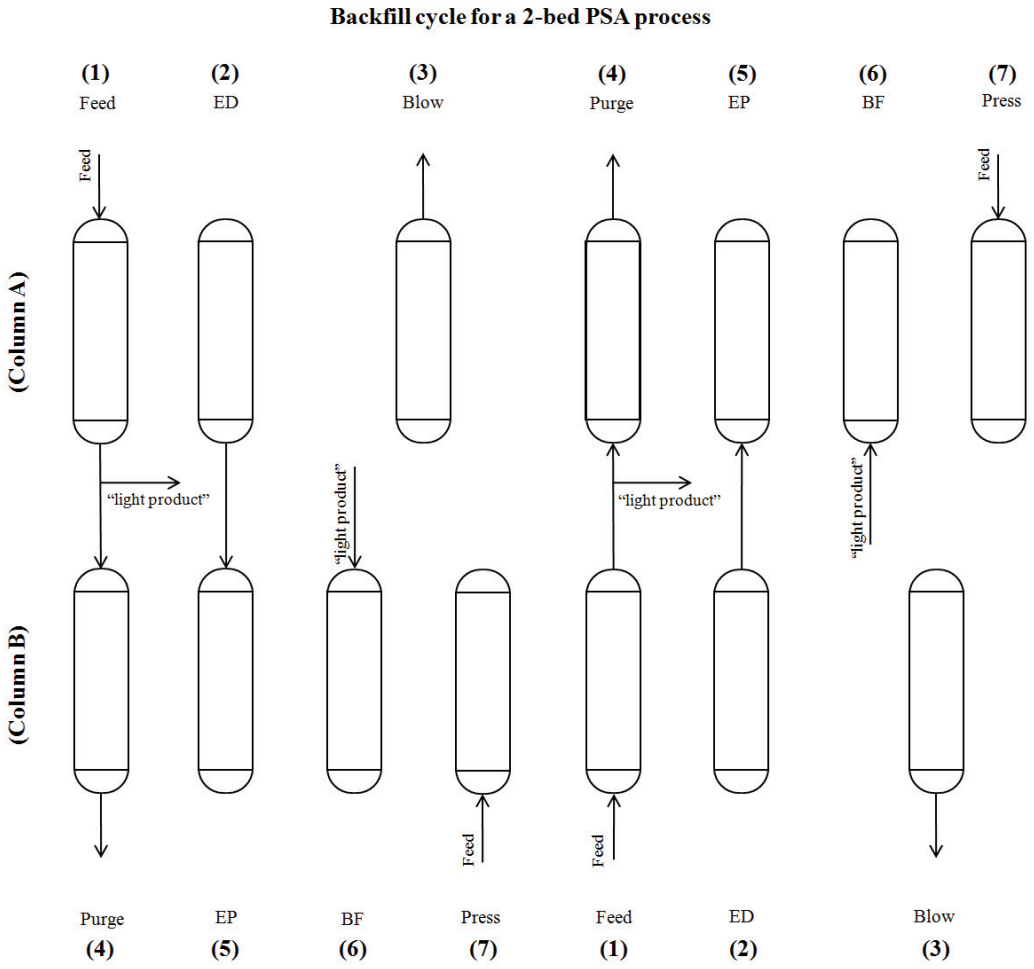
1.2.3 PSA cycle steps

The hydrogen economic demand promoted a strong motivation for the improvement of new PSA processes, specifically the development of multi-step multi-bed processes [42, 59, 67]. Since the end of the 20th Century, numerous modifications to the basic scheme of a hydrogen purification PSA process proposed by UOP (Feed; Cocurrent depressurization; Counter-current depressurization; Purge; Repressurization) have been suggested [29, 61]. As reported by Kohl and Nielsen, in most cases the changes consist of adding supplementary depressurization and pressurization steps to increase the hydrogen recovery [61]. On the other hand, new cycling sequences of operating steps for hydrogen purification were proposed [29].

Prior to Fuderer and Rudelstorfer (1976) [42] and their Polybed process, Batta (1971), also from Union Carbide Corporation, disclosed in the U.S. Patent 3,564,816 a three or four bed process configuration for lower capacities of hydrogen product (below 0.4 M $Nm^3 day^{-1}$). The author reported the importance of employing a sequence of pressure equalization steps between high and low pressure beds in order to attain higher product recoveries.

Ahn *et al.* (1999) [16] reported a different experimental and theoretical study to recover high purity hydrogen from coke oven gas by a backfill cycle of 2-bed PSA process that employed activated carbon beds, zeolite 5A beds or layered beds. Figure 1.7 illustrates the backfill cycle. The authors stated that, since the backfill step (counter-current pressurization of the column with product) leads to a rather steep concentration wave front at the feed pressurization step (due to the adsorption bed rich in H_2), an increase in product purity is obtained. However, the hydrogen recovery decreases using the backfill step [16].

In 2000, Waldron and Sircar [62] reported a parametric study of an adiabatic PSA process for the production of high H_2 purity from a binary mixture of hydrogen and methane. They evaluated the effects of several independent process variables (feed gas pressure and composition, purge gas pressure and flow rate, configuration of the steps) on the hydrogen recovery at high purity and on the hydrogen production capacity. The authors stated that identical product with different H_2 recovery and productivity can be achieved for different PSA process steps, operating conditions and/or feed conditions. It is reported that the H_2 product purity can be upgraded from



Column A	Feed	ED	Blow		Purge	EP	BF	Press
Column B	Purge	EP	BF	Press	Feed	ED	Blow	

Figure 1.7: Backfill cycle of 2-bed PSA process: (1) feed; (2) pressure-equalization depressurization; (3) blowdown; (4) purge; (5) pressure-equalization pressurization; (6) backfill; (7) pressurization [16].

99.0% to 99.999% from a feed gas mixture containing 60-90% H_2 with relatively small penalties in H_2 recovery (from 87.4% to 84.8%) and productivity (from 27.62 to 24.21 $Nm^3 ft^{-3}$) [62].

Whysall and Wagemans (2001) [63] disclosed in their U.S. Patent 6,210,466 B1 that capacities in excess of about 110 $Nm^3 h^{-1}$ can be achieved in a single integrated process of 16 adsorption beds by increasing the time of the purge step. The authors demonstrated that the time of the purge step does not have to be equal or lower than the time of the adsorption step. It is patented that, the capacity of the process can be increased with a minimum loss in recovery or performance when is combined: the duration of the purge step is increased relatively to the adsorption step; the supply of the purge gas for any adsorption bed from one or more other beds; during the provide

purge step, the other adsorption beds simultaneously provide the purge gas to essentially all beds undergoing the purge step.

Xu and Weist Jr. (2002) [66] patented a PSA process with six beds particularly suitable for hydrogen purification that comprised the equalization of the pressure of each bed in four steps, wherein at all times during the process, at least one of the six beds provided off-gas. One year later, Xu *et al.* (2003) [64-65] disclosed in their U.S. Patent Application 2003/70015091 A1 and U.S. Patent 6,565,628 B2 that the product recovery per unit of adsorbent used is increased when the required pressure equalization time is reduced. Using this PSA process, the amount of adsorbent required in the beds for an acceptable product purity can be reduced, decreasing the capital costs of the equipment required for the same production rate.

Jiang *et al.* (2004) [60] presented a simulation and optimal design study of multi-bed PSA systems. They illustrated their studies with a 5-bed 11-step separation process (see Figure 1.8) that removes hydrogen from a mixture of H_2, N_2, CO_2, CO and CH_4, optimizing the H_2 recovery for product purity and pressure specifications by manipulation of step times and also valve constants, flow rates and bed geometry.

Five-bed 11-step PSA process

	(1)			(2)	(3)	(4)	(5)	(6)	(7)	(8)	(9)		(10)	(11)	
Column A	Feed			ED1	ED2	PP	ED3	Blow	Purge	EP3	EP2	Idle	EP1	Press	
Column B	EP1	Press		Feed			ED1	ED2	PP	ED3	Blow	Purge	EP3	EP2	Idle
Column C	EP3	EP2	Idle	EP1	Press		Feed			ED1	ED2	PP	ED3	Blow	Purge
Column D	ED3	Blow	Purge	EP3	EP2	Idle	EP1	Press		Feed			ED1	ED2	PP
Column E	ED1	ED2	PP	ED3	Blow	Purge	EP3	EP2	Idle	EP1	Press		Feed		

Figure 1.8: Five-bed 11-step PSA process for hydrogen purification: (1) feed; (2) pressure-equalization depressurization 1; (3) pressure-equalization depressurization 2; (4) provide purge; (5) pressure-equalization depressurization 3; (6) blowdown; (7) purge; (8) pressure-equalization pressurization 3; (9) pressure-equalization pressurization 2; (10) pressure-equalization pressurization 1; (7) pressurization [60].

1.2.4 Integrated processes

In 1979, Sircar [79] disclosed in his U.S. Patent 4,171,206 a two stage PSA process for the separation of multicomponent gas mixtures. The first stage of the PSA process contains six beds for selective adsorption of CO_2 from the feed gas mixture, while the second stage contains three beds for selective adsorption of minor impurities, such as CH_4 and/or CO. With this two-stage PSA

process, the author claims that high purity and recovery of hydrogen can be achieved as well as a recovery at high purity of carbon dioxide. Nine years later, the same author disclosed in his U.S. Patent 4,790,858 an improvement of the two stage PSA process, integrating one more stage (of two beds) with the second one [80]. This "extra" stage was integrated with the second stage to remove contained minor impurities (CH_4 and/or CO) and further increase the recovery of pure hydrogen. The author claims that the 91.1% of hydrogen recovery (at 99.9% purity) from SMR off-gases described in U.S. Patent 4,171,20 [79] can be raised to about 95.0% hydrogen recovery at the same high purity in accordance to this three stage PSA unit [80]. A schematic two stage PSA process using a first stage of 6 beds and a second stage of 3 beds is illustrated in Figure 1.9.

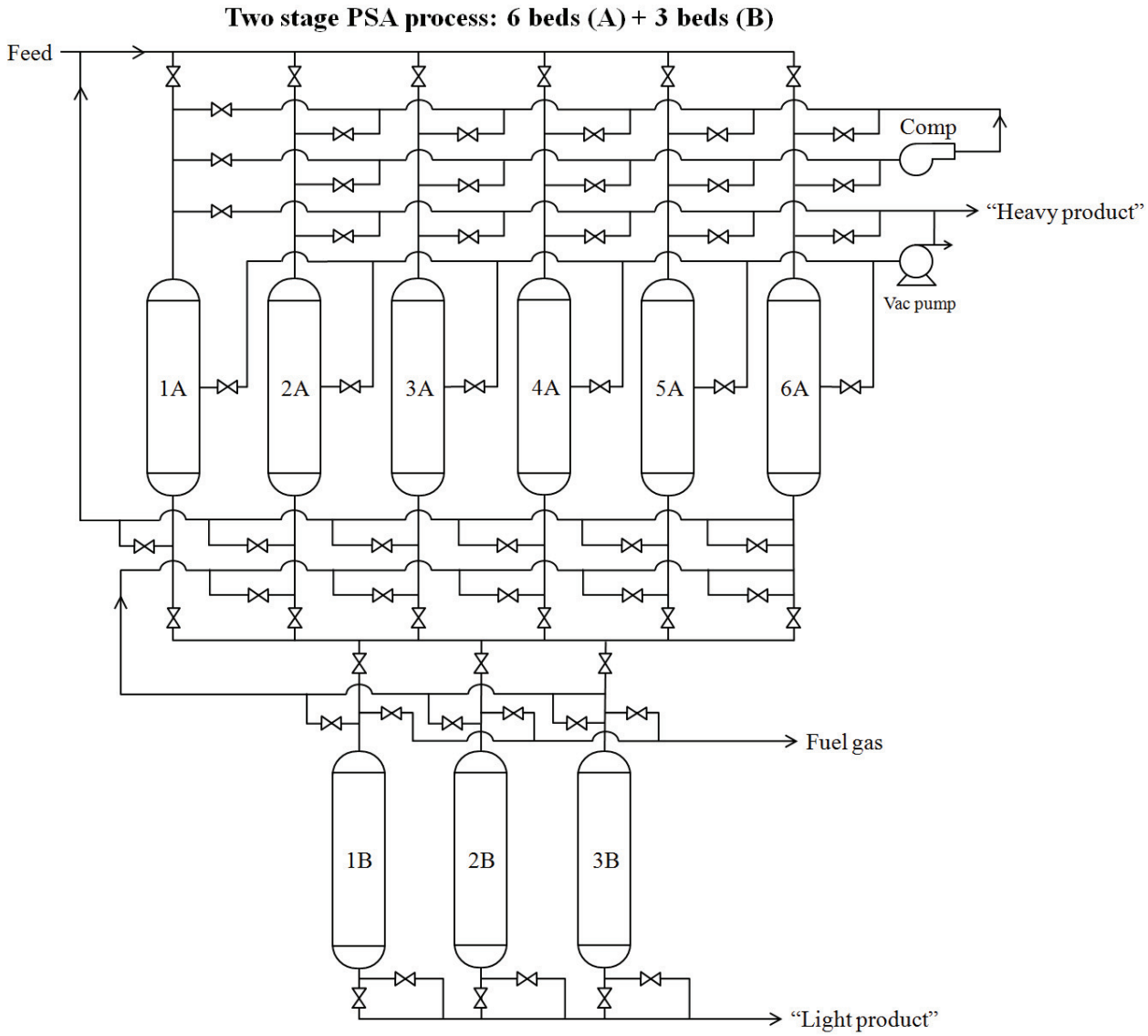


Figure 1.9: Schematic two stage PSA process: first stage of 6 beds and second stage of 3 beds [79].

Studies on multi-layered multi-bed PSA processes that use tanks as intermediate gas reservoirs to improve the efficiency of the separation have been taken into consideration. Yamaguchi and Kobayashi (1993) [67] disclosed in their U.S. Patent 5,250,088 a multi-layered bed (silica gel and activated carbon) 1-tank PSA process for the separation of hydrogen from refinery off-gases (78.8–79.2% of H_2, 14.9-15.3% of CH_4, 4.0-4.1% of C_2H_6, 1.3-1.6% of C_3H_8, 0.3% of n-C_4H_{10} and 0.1% of H_2O). The tank used in this process is used as holding column; this means the tank works as an intermediate gas reservoir to improve the efficiency of the separation. In the case of a 4-bed 1-tank PSA process, it can produce hydrogen with 99.96% of purity and 86.0-86.3% of recovery. When two more beds are included in the process, the hydrogen purity and recovery increase to 99.97% and 87.9-88.3%, respectively. A schematic PSA process diagram that uses four beds and a tank is illustrated in Figure 1.10.

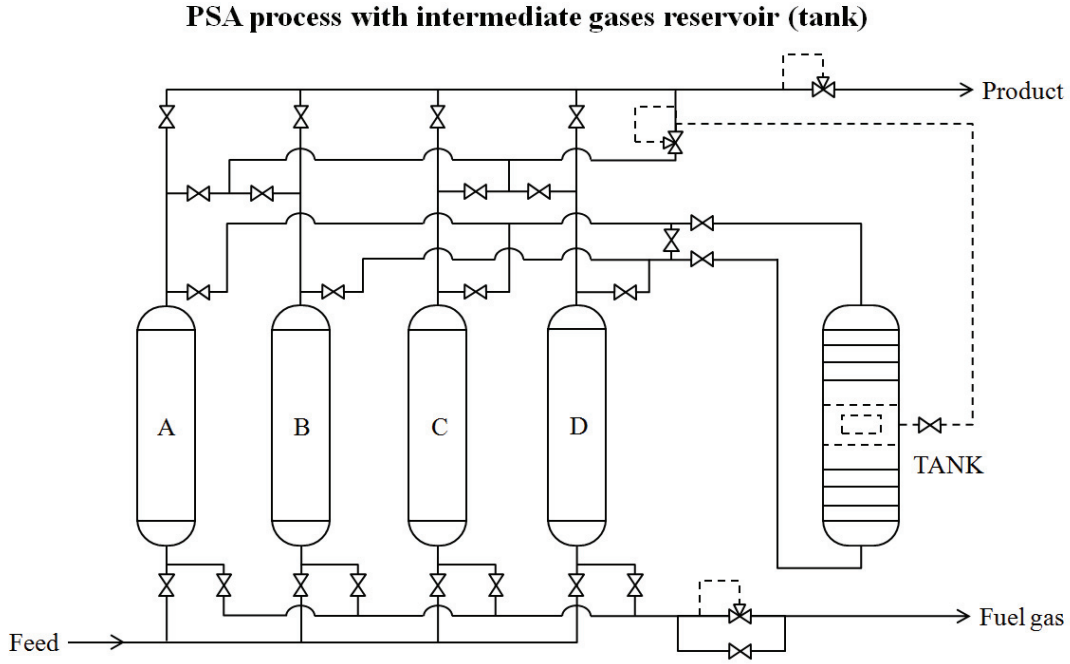


Figure 1.10: Schematic PSA process diagram using four beds and a tank (intermediate gases reservoir) [67].

In 2002, Zhou *et al.* [22] presented a novel PSA technology that featured in uncoupling of the columns in terms of pressure equalization by the use of storage tanks and a new cycling sequence of operation steps. In addition to the four columns, this unit was also composed by two buffer tanks at different levels of pressure between adsorption and regeneration used for pressure equalization with the columns. The authors reported that this new PSA process exhibits a very

good separation performance even at low operating pressure, avoiding the need of pre-compression of many low pressure industrial flue gases. Applying the cycling sequence proposed by Zhou *et al.* (2002) [22], hydrogen with a purity of 99.99% could be produced with relatively high recovery at pressure lower than 10 bar.

Baksh and Terbot (2003) [68] showed in their U.S. Patent 6,503,299 B2 a 2-bed PSA process that uses separate tanks to store and reuse gas at different steps. This invention was created to recover a primary gaseous component at a purity of over 99% from a feed gas comprising the primary component (H_2) and one or more impurities (CO, CO_2, CH_4, N_2 and/or H_2O). The authors claim that this process is capable to increase the primary component production of each bed.

In 1999, Chen *et al.* [69] claimed that high purity carbon monoxide can be separated from a mixture of CO, CO_2, CH_4, H_2 and, possibly, other impurities by a two stage PSA process carried out in a series of beds containing an adsorbent selective to carbon monoxide. In this particular case, the PSA process was designed to recover the more strongly adsorbed component of the gas mixture in very high purity using a cycle process that includes one evacuation step and one purge step. For that, a CuY zeolite (Cu^+ exchanged zeolite Y) was used to adsorb more readily carbon monoxide than the other compounds of the gas stream. Five months later, in their U.S. Patent 6,045,603, the same authors designed a PSA process cycle that includes two evacuation steps and two or more purge steps to enhance the purity of the strongly adsorbed product without sacrificing the product gas yield [70].

New trends in PSA technology for hydrogen purification point to the use of fast cycling or rapid Pressure Swing Adsorption (RPSA) [5, 71-78, 83-92]. Using this fast cycling approach higher unit productivities (10-1000 higher than classic PSA) may be achieved and thus significant reductions in equipment and adsorbent costs. Since this approach was considered in this thesis, a complete state of the art of RPSA processes for hydrogen purification systems was reported in chapter 6.

1.3 Objectives & Outline

The purpose of this work is to improve the process of hydrogen purification through PSA technology from multicomponent mixtures, essentially SMR off-gases. This work was developed within the European Project HY2SEPS (Hybrid Hydrogen – Carbon Dioxide Separation Systems) [93] where the PSA technology should be combined with a membrane process to produce high purity hydrogen (>99.99%) integrating a carbon capture technology.

The first accomplishments deal with adsorption equilibrium and kinetic data on different commercial adsorbent materials (activated carbons and zeolites) at different temperatures and in a wide range of pressure. Further, large amounts (kilogram scale) of two materials with enhanced capacity toward contaminants were produced and characterized to improve the performance of a PSA process: (1) modified activated carbon with enhanced capacity (mainly) of carbon dioxide; (2) ion exchanged zeolite with enhanced capacity toward the less adsorbed contaminant (nitrogen). Breakthrough experiments were performed considering different feed compositions, temperatures and pressures in order to determine some multicomponent adsorption data.

The upgrade of an experimental PSA facility already existing at LSRE was accomplished within this thesis. Due to the complexity of the mixture under consideration, the experimental studies implied the integration of a new analysis system coupled with the PSA facility.

Further, PSA behaviour was simulated with a mathematical model and validated against experimental results obtained from the lab-scale facility. The effect of operating conditions was tested for some adsorbents. After a clear understanding of the system dynamics, different, improved, PSA cycles were suggested during this work. The proposed cycles take into consideration the flexibility of using different types of adsorbents, layered beds and multi-beds PSA processes.

Within this thesis, the upgraded PSA unit was then adapted for fast cycling PSA processes (each cycle lasting around one minute) for purification of hydrogen. The study of the fundamentals of RPSA was accomplished by considering only binary H_2-CO_2 mixtures. Binary breakthrough curves at high superficial velocity and a single column RPSA experiment were carried out in the experimental unit to validate the mathematical model in this operating mode.

This thesis is outlined as follows:

In chapter 2, adsorption equilibrium of pure hydrogen, carbon dioxide, methane, carbon monoxide, nitrogen and water vapour on different commercial adsorbents (activated carbons and zeolite) were studied. The multisite Langmuir model and the Virial model were employed to fit the experimental data.

In chapter 3, the adsorption kinetic parameters of the pure gases were evaluated for the mentioned adsorbents through Zero Length Column (ZLC), pulse and/or breakthrough experiments.

In chapter 4, two commercial adsorbents were modified in order to enhance their adsorption capacity and kinetics toward carbon dioxide and nitrogen, respectively. From a commercial activated carbon (R2030, Norit, Holland), a new material with enhanced capacity toward

contaminants (CH_4, CO, N_2 and mainly CO_2) was prepared by physical activation with carbon dioxide. A zeolite 13X (sodium-form) was also modified by changing the cation with calcium. The synthesis scale-up, characterization and adsorption equilibrium and kinetic properties on these materials were evaluated.

In chapter 5, adsorption data of multicomponent mixtures of SMR off-gases were studied. Both adsorption equilibrium and kinetic behaviour of binary H_2-CO_2, ternary H_2-CO_2-CO and five-component H_2-CO_2-CH_4-CO-N_2 mixtures were measured. Modeling of the multicomponent adsorption data was performed using a mathematical model already developed at LSRE. Furthermore, a single column PSA experiment was performed for the complete validation of the model. Finally, a cycle sequence of 6 steps and other of 10 steps were considered for the simulation of two single column PSA processes in order to achieve high purity H_2 coupled with high product recovery.

In Chapter 6, an introductory research to understand the basics of how the PSA system can be improved by fast cycling was assessed. A PSA unit was adapted to perform fast cycling processes. Using the mathematical model employed in chapter 5, binary adsorption data at high superficial velocities were modeled. Also simulations of a 5 step single column RPSA process were performed in order to attain high adsorption productivities.

Finally, chapter 7 contains the main conclusions of this work and some suggestions for future work identidied within the course of this work.

1.4 References

[1] DOE/EIA, World carbon dioxide emissions, 2009, Available from: http://tonto.eia.doe.gov/cfapps/ipdbproject/iedindex3.cfm?tid=90&pid=44&aid=8&cid=regions,&syid=2000&eyid=2008&unit=MMTCD.

[2] U.N.F.C., Kyoto Protocol, in United Nations Framework Convention on Climate Change, 1997, Kyoto, Japan.

[3] U.N.F.C., United Nations Framework Convention on Climate Change, in Ad Hoc Working Group on Further Commitments for Annex I Parties under the Kyoto Protocol, 2009, Copenhagen, Denmark.

[4] J. Kärger, D.M. Ruthven, Diffusion in zeolites and other microporous solids, 1st Edition, John Wiley & Sons, New York, 1992.

[5] T.C. Golden, E.L. Weist, Activated carbon as sole absorbent in rapid cycle hydrogen PSA (2003) U.S. Patent 6,660,064 B2.

[6] M.S.A. Baksh, M.W. Ackley, Pressure swing adsorption process for the production of hydrogen (2002) U.S. Patent 6,340,382 B1.

[7] D. Gardner, Hydrogen production from renewables, Renewable Energy Focus. 9 (2009) 34-37.

[8] D.R. Simbeck, CO_2 capture and storage - The essential bridge to the hydrogen economy, Energy. 29 (2004) 1633-1641.

[9] R.T. Yang, Gas separation by adsorption processes, Butterworths, Boston, 1987.

[10] R.L. Bec, Method for purifying hydrogen-based gas mixtures using calcium X-zeolite (2005) U.S. Patent 6,849,106 B2.

[11] C.C. Elam, R.J. Evans, Overview of hydrogen production, Preprint Papers - American Chemical Society, Division of Fuel Chemistry. 49 (2004) 481-482.

[12] S. Sircar, T.C. Golden, Purification of hydrogen by pressure swing adsorption, Separation Science and Technology. 35 (2000) 667-687.

[13] S. Sircar, W.E. Waldron, M.B. Rao, M. Anand, Hydrogen production by hybrid SMR-PSA-SSF membrane system, Separation and Purification Technology. 17 (1999) 11-20.

[14] DOE, Fuel cell handbook, 5th Edition, DOE, EG&G Services, Parsons, Inc. Science Applications International Corporation. Contract No. DE-AM26-99FT40575, 2000.

[15] OECD/IEA, Hydrogen & Fuel cells: Review of National R&D Programs, Organisation for Economic Co-operation and Development & International Energy Agency. ISBN 92-64-

108-831, 2004.

[16] H. Ahn, C.-H. Lee, B. Seo, J. Yang, K. Baek, Backfill cycle of a layered bed H_2 PSA process, Adsorption. 5 (1999) 419-433.

[17] I.A.A.C. Esteves, J.P.B. Mota, Simulation of a new hybrid membrane/pressure swing adsorption process for gas separation, Desalination. 148 (2002) 275-280.

[18] D.M. Ruthven, S. Farooq, K.S. Knabel, Pressure swing adsorption, VCH Publishers, New York, 1994.

[19] J.L. Wagner, Selective adsorption process (1969) U.S. Patent 3,430,418.

[20] J. Yang, C.-H. Lee, Adsorption dynamics of a layered bed PSA for H_2 recovery from coke oven gas, AIChE Journal. 44 (1998) 1325-1334.

[21] R.T. Yang, Adsorbents: Fundamentals and applications, John Wiley & Sons, Hoboken, NJ, 2003.

[22] L. Zhou, C.-Z. Lü, S.-J. Bian, Y.-P. Zhou, Pure hydrogen from the dry gas of refineries via a novel pressure swing adsorption process, Industrial and Engineering Chemistry Research. 41 (2002) 5290-5297.

[23] A.E. Rodrigues, G.-H. Xiu, P. Li, C.A. Grande, E.L.G. Oliveira, Strategies for H_2 production by pressure swing adsorption reactor, in Sorption Enhanced Reaction Concepts for Hydrogen Production: Materials & Processes, S. Sircar and K.B. Lee, Editors, Research Signpost, Kerala, India, 2010.

[24] D. Finlayson, A.J. Sharp, Improvements in or relating to the treatment of gaseous mixtures for the purpose of separating them into their components or enriching them with respect to one ore more of their components (1932) G.B. Patent 365,092.

[25] H. Kahle, Verfahren und vorrichtung zur abführung bzw. verwertung der verdichtungswärme von gasen (1952) DE Patent 857,644.

[26] J.C. Santos, A.M. Ribeiro, A.E. Rodrigues, Hydrogen purification by adsorption processes, in CYTED - Programa Iberoamericano de Ciencia y Tecnologia para el Desarrollo. Curso 307RT0324 - "Hidrógeno: Producción y Purificación, Almacenamiento y Transporte", Oviedo, Spain, 2009.

[27] C.W. Skarstrom, Fractionating gas mixtures by adsorption (1960) U.S. Patent 2,944,627.

[28] P. Guerin de Montgareuil, D. Domine, Process for separating a binary gaseous mixture by adsorption (1964) U.S. Patent 3,155,468.

[29] J. Stöcker, M. Whysall, G.Q. Miller, 30 years of PSA technology for hydrogen purification, UOP LLC, Des Plaines, Illinois, 1998.

[30] S. Cavenati, Adsorptive processes for separation of $CH_4/CO_2/N_2$ mixtures, Ph.D. Dissertation, University of Porto, Porto, Portugal, 2005.

[31] F.A. Da Silva, Cyclic adsorption processes: Application to propane/propylene separation, Ph.D. Dissertation, University of Porto, Porto, Portugal, 1999.

[32] C.A. Grande, Propane/propylene separation by pressure swing adsorption, Ph.D. Dissertation, University of Porto, Porto, Portugal, 2005.

[33] D.M. Ruthven, Principles of adsorption and adsorption processes, John Wiley & Sons, New York, 1984.

[34] S. Sircar, Pressure swing adsorption, Industrial and Engineering Chemistry Research. 41 (2002) 1389-1392.

[35] N.H. Berlin, Method for providing an oxygen-enriched environment (1966) U.S. Patent 3,280,536.

[36] S. Sircar, Pressure swing adsorption technology for hydrogen purification - A status review, in Adsorption: Progress in Fundamental and Appication Research, L. Zhou, Editor, World Scientific Publishing Co. Pte. Ltd., Singapore, 2006.

[37] H. Ahn, J. Yang, C.-H. Lee, Effects of feed composition of coke oven gas on a layered bed H_2 PSA process, Adsorption. 7 (2001) 339-356.

[38] M.S.A. Baksh, M.W. Ackley, F. Notaro, Process and apparatus for hydrogen purification (2004) W.O. Patent 2004/058630 A3.

[39] M.S.A. Baksh, M.W. Ackley, F. Notaro, Process and apparatus for hydrogen purification (2004) W.O. Patent 2004/058630 A2.

[40] M.S.A. Baksh, M.W. Ackley, F. Notaro, Process and adsorbent for hydrogen purification (2009) U.S. Patent 7,537,742 B2.

[41] M. Chlendi, D. Tondeur, Dynamic behaviour of layered columns in pressure swing adsorption, Gas Separation & Purification. 9 (1995) 231-242.

[42] A. Fuderer, E. Rudelstorfer, Selective adsorption process (1976) U.S. Patent 3,986,849.

[43] C.-H. Lee, J. Yang, H. Ahn, Effects of carbon-to-zeolite ratio on layered bed H_2 PSA for coke oven gas, AIChE Journal. 45 (1999) 535-545.

[44] A. Malek, S. Farooq, Hydrogen purification from refinery fuel gas by pressure swing adsorption, AIChE Journal. 44 (1998) 1985-1992.

[45] M. Tańczyk, K. Warmuziński, Multicomponent pressure swing adsorption Part II. Experimental verification of the model, Chemical Engineering and Processing. 37 (1998) 301-315.

[46] K. Warmuziński, M. Tańczyk, Multicomponent pressure swing adsorption Part I. Modelling of large-scale PSA installations, Chemical Engineering and Processing. 36 (1997) 89-99.

[47] R.L. Bec, Method for purifying hydrogen-based gas mixtures using calcium X-zeolite (2003) U.S. Patent Application Publication 2003/0172808 A1.

[48] O. Bomard, J. Jutard, S. Moreau, X. Vigor, Method for purifying hydrogen based gas mixtures using a lithium-exchanged X zeolite (1997) W.O. Patent 97/45363.

[49] C.G. Coe, J.F. Kirner, R. Pierantozzi, T.R. White, Nitrogen adsorption with Ca and or Sr exchanged lithium X-zeolites (1992) U.S. Patent 5,152,813.

[50] C.G. Coe, J.F. Kirner, R. Pierantozzi, T.R. White, Nitrogen adsorption with Ca and or Sr exchanged lithium X-zeolites (1993) European Patent Application 0,548,755 A1.

[51] T.C. Golden, R. Kumar, W.C. Kratz, Hydrogen purification (1990) U.S. Patent 4,957,514.

[52] S. Hirano, A. Harada, Method for purifying hydrogen-based gas mixture (2001) U.S. Patent Application Publication 2001/0045160 A1.

[53] S. Hirano, A. Harada, Method for purifying hydrogen-based gas mixture (2003) U.S. Patent 6,514,317 B2.

[54] L.M. Johnson, T.S. Farris, T.C. Golden, E.L. Weist Jr, J.M. Occhialini, Optimum adsorbents for H_2 recovery by pressure and vacuum swing absorption (2001) U.S. Patent 6,302,943 B1.

[55] D. Plee, Procédé psa de purification de l'hydrogène (1998) European Patent Application 0,855,209 A1.

[56] D. Plee, Procédé psa de purification de l'hydrogène (1998) European Patent 0,855,209 B1.

[57] D. Plee, J.-J. Masini, Zéolites X éxchangés notamment au lithium, leur procédé de preparation et leur utilisation comme absorbants de l'azote dans séparation des gaz de l'air (2001) European Patent Application 1,116,691 A1.

[58] G. Reiss, Molecular sieve zeolite for producing hydrogen by pressure variation adsorption technique (1984) U.S. Patent 4,477,267.

[59] L.B. Batta, Selective adsorption process (1971) U.S. Patent 3,564,816.

[60] L. Jiang, V.G. Fox, L.T. Biegler, Simulation and optimal design of multiple-bed pressure swing adsorption systems, AIChE Journal. 50 (2004) 2904-2917.

[61] A.L. Kohl, R. Nielsen, Gas purification, 5th Edition, Gulf Professional Publishing, UK, 1997.

[62] W.E. Waldron, S. Sircar, Parametric study of a pressure swing adsorption process,

Adsorption. 6 (2000) 179-188.

[63] M. Whysall, L.J.M. Wagemans, Very large-scale pressure swing adsorption processes (2001) U.S. Patent 6,210,466 B1.

[64] J. Xu, D.L. Rarig, T.A. Cook, K.-K. Hsu, M. Schoonover, R. Agrawal, Pressure swing adsorption process with reduced pressure equalization time (2003) U.S. Patent Application Publication 2003/0015091 A1.

[65] J. Xu, D.L. Rarig, T.A. Cook, K.-K. Hsu, M. Schoonover, R. Agrawal, Pressure swing adsorption process with reduced pressure equalization time (2003) U.S. Patent 6,565,628 B2.

[66] J. Xu, E.L. Weist Jr., Six bed pressure swing adsorption process with four steps of pressure equalization (2002) U.S. Patent 6,454,838 B1.

[67] T. Yamaguchi, Y. Kobayashi, Gas separation process (1993) U.S. Patent 5,250,088.

[68] M.S.A. Baksh, C.E. Terbot, Pressure swing adsorption process for the production of hydrogen (2003) U.S. Patent 6,503,299 B2.

[69] Y. Chen, A. Kapoor, R. Ramachandran, Two stage pressure swing adsorption process (1999) U.S. Patent 5,993,517.

[70] Y. Chen, A. Kapoor, N. Ramprasad, Two phase pressure swing adsorption process (2000) U.S. Patent 6,045,603.

[71] D.J. Connor, D.G. Doman, L. Jeziorowski, B.G. Keefer, B. Larisch, C. Mclean, I. Shaw, Rotary pressure swing adsorption apparatus (2002) U.S. Patent 6,406,523 B1.

[72] C.M.A. Golden, T.C. Golden, P.J. Battavio, Multilayered adsorbent system for gas separations by pressure swing adsorption (2003) U.S. Patent Application Publication 2003/0205131 A1.

[73] T.C. Golden, C.M.A. Golden, D.P. Zwilling, Self-supported structured adsorbent for gas separation (2003) U.S. Patent 6,565,627 B1.

[74] T.C. Golden, E.L. Weist Jr, P.A. Novosat, Adsorbents for rapid cycle pressure swing adsorption processes (2006) U.S. Patent Application Publication 2006/0236862 A1.

[75] T.C. Golden, E.L. Weist Jr, P.A. Novosat, Adsorbents for rapid cycle pressure swing adsorption processes (2008) U.S. Patent 7,404,846 B2.

[76] B.G. Keefer, High frequency pressure swing adsorption (2001) U.S. Patent 6,176,897 B1.

[77] B.G. Keefer, A. Carel, B. Sellars, I. Shaw, B. Larisch, Adsorbent laminate structures (2004) U.S. Patent 6,692,626 B2.

[78] B.G. Keefer, D.G. Doman, Flow regulated pressure swing adsorption system (2000) U.S.

Patent 6,063,161.

[79] S. Sircar, Separation of multicomponent gas mixtures (1979) U.S. Patent 4,171,206.

[80] S. Sircar, Fractionation of multicomponent gas mixtures by pressure swing adsorption (1988) U.S. Patent 4,790,858.

[81] J.-H. Park, J.-N. Kim, S.-H. Cho, Performance analysis of a four-bed H_2 PSA process using layered beds, AIChE Journal. 46 (2000) 790-802.

[82] J.-H. Park, J.-N. Kim, S.-H. Cho, J.-D. Kim, R.T. Yang, Adsorber dynamics and optimal design of layered beds for multicomponent gas adsorption, Chemical Engineering Science. 53 (1998) 3951-3963.

[83] R.L. Jones, G.E. Keller II, R.C. Wells, Rapid adiabatic pressure swing adsorption process (1980) European Patent Application 0,008,619 A1.

[84] R.L. Jones, G.E. Keller II, R.C. Wells, Rapid pressure swing adsorption process with high enrichment factor (1980) U.S. Patent 4,194,892.

[85] R.L. Jones, G.E. Keller II, R.C. Wells, Rapid adiabatic pressure swing adsorption process (1984) European Patent 0,008,619 B1.

[86] G.E. Keller II, C.-H.A. Kua, Enhanced gas separation by selective adsorption (1982) U.S. Patent 4,354,859.

[87] R.S. Todd, P.A. Webley, Mass-transfer models for rapid pressure swing adsorption simulation, AIChE Journal. 52 (2006) 3126-3145.

[88] S. Sircar, Gas separation by rapid pressure swing adsorption (1991) U.S. Patent 5,071,449.

[89] B.G. Keefer, D.G. Doman, Flow regulated pressure swing adsorption system (2004) U.S. Reissued Patent RE38,493 E.

[90] S. Alizadeh-Khiavi, J.A. Sawada, A.C. Gibbs, J. Alvaji, Rapid cycle syngas pressure swing adsorption system (2007) U.S. Patent Application Publication 2007/0125228 A1.

[91] N. Sundaram, B.K. Kaul, E.W. Corcoran, C.Y. Sabottke, R.L. Eckes, Integration of rapid cycle pressure swing adsorption with refinery process units (hydroprocessing, hydrocracking, etc.) (2006) U.S. Patent Application Publication 2006/0174764 A1.

[92] N. Sundaram, B.K. Kaul, E.W. Corcoran, C.Y. Sabottke, R.L. Eckes, Integration of rapid cycle pressure swing adsorption with refinery process units (hydroprocessing, hydrocracking, etc.) (2009) U.S. Patent 7,591,879 B2.

[93] HY2SEPS, Hybrid Hydrogen Carbon Dioxide Separation Processes, E.U. Res. Project 2005, Available from: http://hy2seps.iceht.forth.gr/.

2.

Adsorption equilibrium of pure gases on commercial adsorbents*

2.1 Introduction

The adsorption equilibrium of pure compounds is the fundamental information to do the theoretical design of an adsorption process. Therefore, adsorption equilibrium of the gases exiting the SMR reactor for the design of a PSA unit for H_2 purification must be studied.

As stated in chapter 1, many different PSA process schemes have been designed according to different column arrangements and/or cycle scheduling and/or adsorbent layer dispositions [1-9]. Layered columns with a first layer of activated carbon to completely remove strongly adsorbed compounds (H_2O and CO_2 and some CH_4) and a second layer of a zeolite material to remove the light components (remaining CH_4, CO and N_2) are commonly used [10]. Consequently it is important to study adsorption equilibrium of the pure gases on both activated carbon and zeolite materials. In this chapter, experimental data of carbon dioxide, hydrogen, methane, carbon monoxide, nitrogen and water on several commercial materials are presented. The adsorbent

* The content of this chapter is part of the following articles:

C.A. Grande, F.V.S. Lopes, A.M. Ribeiro, J.M. Loureiro, A.E. Rodrigues, Adsorption of off-gases from steam methane reforming (H_2, CO_2, CH_4, CO and N_2) on activated carbon, Separation Science and Technology. 43 (2008) 1338-1364.

F.V.S. Lopes, C.A. Grande, A.M. Ribeiro, J.M. Loureiro, O. Evaggelos, V. Nikolakis, A.E. Rodrigues, Adsorption of H_2, CO_2, CH_4, CO, N_2 and H_2O in activated carbon and zeolite for hydrogen production, Separation Science and Technology. 44 (2009) 1045-1073.

materials studied were the activated carbons R2030 (Norit, Holland) and ACM-3mm (CECA, France). Within the framework of the European Project HY2SEPS [11], two commercial adsorbents provided by an industrial partner were also evaluated: one activated carbon (HY2SEPS-AC) and one zeolite sample (HY2SEPS-ZEO). For confidentiality reasons, in these adsorbents, specific data (more than those reported in this work) cannot be provided. Adsorption equilibrium is reported at three different temperatures (303, 323 and 343 K). The measurements cover a wide range of operating conditions of the PSA unit to obtain hydrogen with high purity (>99.99%).

2.2 Adsorbent screening

In order to select commercial available sorbents, the initial work performed was the revision of existing data in open literature. It was observed that in many works the adsorption equilibrium of carbon dioxide was reported, but data on both gases (CO_2 and H_2) in the same sample were scarce. Reports for both hydrogen and carbon dioxide were thus employed for the initial selection.

The published works can be divided in two general categories: inorganic materials (zeolite 4A [12], zeolite 5A [13-14], zeolite 13X [12, 15-16] and natural zeolites [16]) and activated carbons [12, 16-19]. From the bibliographic review, it was concluded that zeolite 13X and activated carbons were the materials with higher affinity to carbon dioxide. The adsorption equilibrium of pure hydrogen and carbon dioxide on these materials is presented in Figure 2.1. In the whole pressure range (0-21 bar) reported in these publications [12, 15-17, 19], the adsorption isotherms of hydrogen are significantly lower than adsorption isotherms of carbon dioxide. The amount adsorbed of H_2 at the temperatures studied (298 to 303 K) on activated carbons and zeolite 13X are lower than 2 and 1 mol kg^{-1}, respectively.

Another interesting difference of these materials is the shape of the adsorption isotherms. The isotherms of CO_2 on zeolite 13X are much steeper than in activated carbons: at pressures lower than 3 bar, the capacity for CO_2 on activated carbons is lower than on zeolite 13X, while at higher pressures (3-21 bar) activated carbons exhibited significantly higher carbon dioxide capacities than zeolite 13X. Considering a pressure interval of 3-21 bar, the CO_2 adsorption capacity on activated carbons are 8-9.5 mol kg^{-1} and 4.5-6 mol kg^{-1} in zeolite 13X. The H_2 adsorption capacity is low on both materials, showing CO_2/H_2 adsorption amount ratio (amount of CO_2/amount of H_2) higher than 4 in the pressure range studied. Due to the higher CO_2 adsorption capacity on activated carbons, this type of material was initially chosen. Therefore, activated

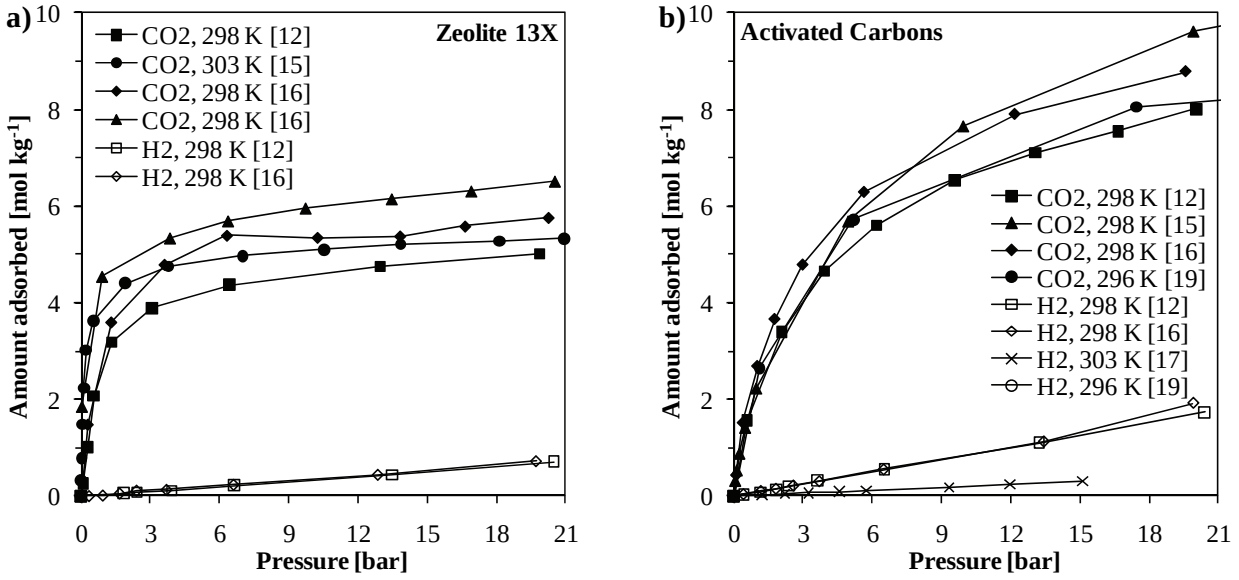


Figure 2.1: Adsorption isotherms of H_2 (open symbols) and CO_2 (closed symbols) on zeolite 13X (a) and activated carbons (b); references: Siriwardane *et al.*, 2001 [12]; Siriwardane *et al.*, 2005 [15]; Siriwardane *et al.*, 2001 [16]; Choi *et al.*, 2003 [17]; Ritter *et al.*, 1987 [19].

carbon was selected as the benchmark adsorbent of this study. Since the properties of activated carbon vary from sample to sample, different samples were tested. Also, data on a zeolite sample is presented to have the possibility to design a layered PSA unit for improved operation.

2.3 Experimental

Adsorption equilibrium of pure gases (H_2, CO_2, CH_4, CO and N_2) was measured in a magnetic suspension microbalance (Rubotherm, Bochum, Germany) shown in Figure 2.2, with a precision of 0.01 mg and operated in closed system. The schematic diagram of the experimental set-up used for adsorption measurements is given by Figure 2.3. A certain amount of adsorbent sample is weighed and placed in a basket linked to a permanent magnet placed in the adsorption chamber. This permanent magnet works together with an electromagnet (magnetic suspension coupling) located outside the chamber and connected to an analytical balance. Employing this magnetic coupling is possible to measure the weight variations inside the cell and through an acquisition system the data are recorded in a computer. Three Lucas Schaevitz pressure transducers were used to measure the pressure inside the adsorption chamber: one from 0-1 bar, other from 0-7 bar and one from 0-250 bar to acquire data with good accuracy at low, intermediate and high-pressures, respectively. Adsorption equilibrium was established after some time without visible

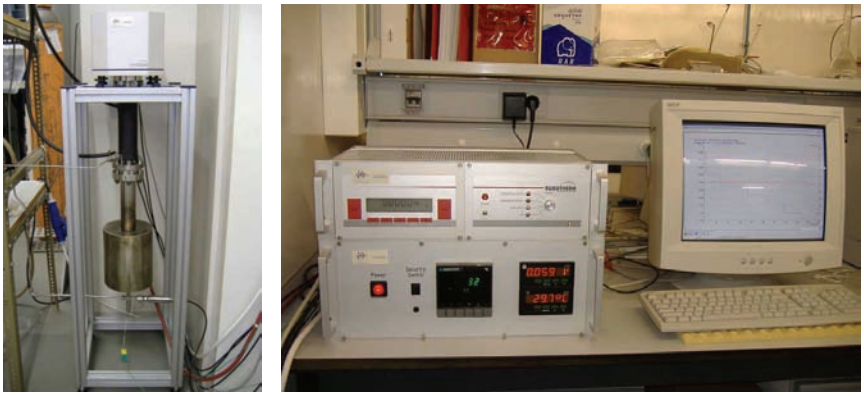


Figure 2.2: a) Magnetic suspension microbalance (Rubotherm, Bochum, Germany); b) Acquisition system of the magnetic suspension microbalance connected to the computer.

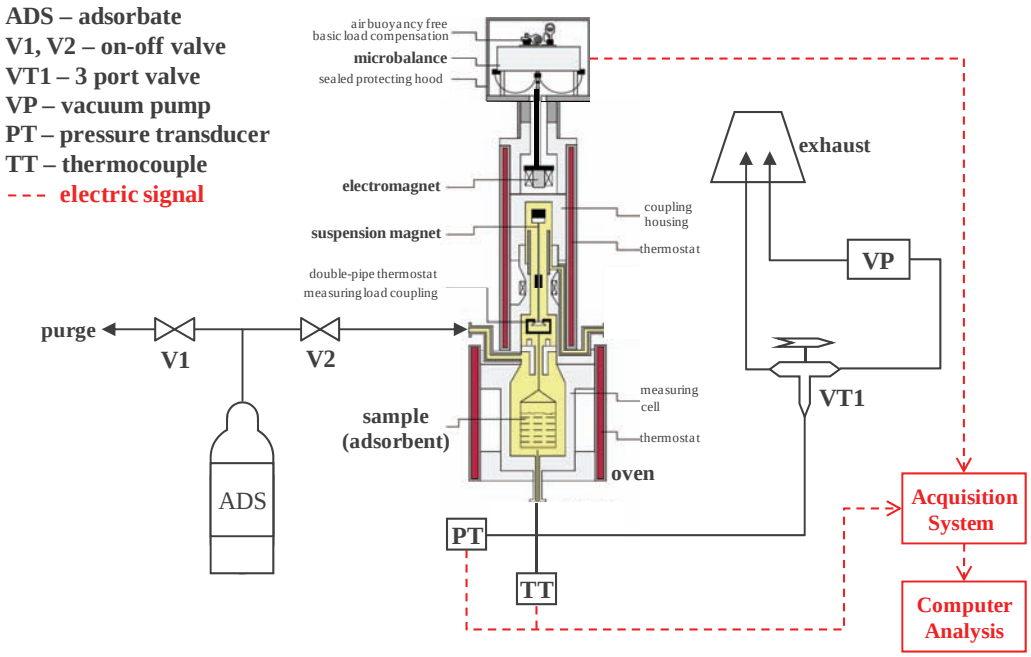


Figure 2.3: Schematic diagram of the experimental set-up for adsorption measurements. Labelling: ADS, adsorbate; V1, V2, on-off valves; VT1, 3 port valve; VP, vacuum pump; PT, pressure transducer; TT, thermocouple.

variation of the weight and pressure. According to the adsorbent material analysed, for the case of CO_2 this contact period with the adsorbent was about 45-60 min (activated carbons) and 80 min (zeolite) per equilibrium point, the same for methane, around 40-50 min for H_2 while for carbon monoxide about 50-80 minutes were established (for all materials).

Degassing of the zeolite sample was performed under vacuum ($< 10^{-7}$ bar) at 593 K overnight while maximum temperature for the different activated carbons samples was 423 K. The heating rate to reach these temperatures was 1 K min^{-1}. Isotherms were measured at 303, 323 and

343 K. The reversibility of each isotherm was confirmed with adsorption and desorption measurements. All gases were provided by Air Liquide: hydrogen N60, carbon dioxide N48, methane N35, carbon monoxide N35, nitrogen N45 and helium N50 (purities greater than 99.9999, 99.998, 99.95, 99.95, 99.995 and 99.999%, respectively).

As a first step in the description of the adsorption equilibrium, we must distinguish between absolute adsorption and excess adsorption. The relation between these quantities is shown in equation (2.1) [20]:

$$q = q_{exc} + \frac{\rho_g V_{ads}}{m_s M_W} \tag{2.1}$$

where q is absolute adsorbed phase concentration, q_{exc} is excess adsorbed phase concentration, ρ_g is the density of the gas phase, V_{ads} is the volume of the adsorbed phase, m_s is the mass of adsorbent placed in the basket of the microbalance and M_W is the molecular weight of the gas. The second term in the right hand side of equation (2.1) corresponds to the "buoyancy" correction term.

In all the experiments performed, the values obtained correspond to the excess adsorbed phase concentration [21]. The buoyancy effect becomes important when pressure increases, i.e. when the gas density becomes closer to the density of the adsorbed phase [22]. The buoyancy corrections can be neglected only at low partial pressures. As the density of the adsorbed phase cannot be measured directly, the absolute amount adsorbed cannot be obtained experimentally and many approximate methods to calculate it from the excess adsorption were published [18, 20, 22]. To perform the buoyancy corrections, we have assumed that the density of the adsorbed phase is equal to the density of the liquid at its boiling point at 1 atm [18]. Therefore, a constant value for liquid phase density was employed for all the temperatures studied: 1277.78, 422.53 and 808.60 kg m^{-3}, for carbon dioxide, methane and nitrogen, respectively [18]. For hydrogen the liquid phase density (ρ_ℓ) was 78 kg m^{-3} and for carbon monoxide 788.6 kg m^{-3} [3, 23]. For gas phase density calculations, we employed a polynomial equation fitting previously reported experimental values of carbon dioxide gas density, as well as for methane and nitrogen gas densities [24]; for hydrogen ideality was assumed and for carbon monoxide experimental compressibility factors were used [25]. In low-pressure measurements (0-1 bar) of carbon monoxide, the buoyancy correction was not performed. Employing the buoyancy correction, the final equation to calculate the absolute amount adsorbed from experimental data is [26]:

$$q = \frac{\Delta m + \rho_g \left(V_s + V_c\right)}{m_s M_W} \frac{\rho_\ell}{\rho_\ell - \rho_g} \tag{2.2}$$

where q is absolute adsorbed phase concentration, Δm is the difference of weight between one measurement and the previous one, ρ_g is the density of the gas phase, ρ_ℓ is the density of the adsorbed phase, V_s is the volume of the solid adsorbent and V_c is the volume of the cell where the adsorbent is located (plus ancillary connections), m_s is the mass of adsorbent placed in the basket of the microbalance and M_W is the molecular weight of the gas. In equation (2.2), it was assumed that the volume of the adsorbed phase is approximated by [18]:

$$V_{ads} \cong \frac{m_{ads}}{\rho_\ell} \tag{2.3}$$

In order to determine the volumes that contribute to the buoyancy effect ($V_s + V_c$), a calibration with helium was performed. Assuming that this gas is not adsorbed ($m_{ads} = V_{ads} = 0$), it is possible to obtain:

$$\Delta m = (\Delta ZP) - \frac{M_W}{R_g T}(V_s + V_c)P \tag{2.4}$$

and, from the slope of equation (2.4), the volume of the cell and the volume of the solid adsorbent ($V_s + V_c$) can be determined. (ΔZP) is the difference of weight between two measurements of zero point.

Water vapour adsorption equilibrium isotherms were measured in another magnetic suspension microbalance (Rubotherm, Bochum, Germany) operating in open mode with a continuous gas flow passing through the sample. A picture of the experimental set-up used is shown in Figure 2.4. The schematic diagram of the experimental set-up for water vapour adsorption measurements is shown in Figure 2.5. The precision of the measurements was 0.01 mg.

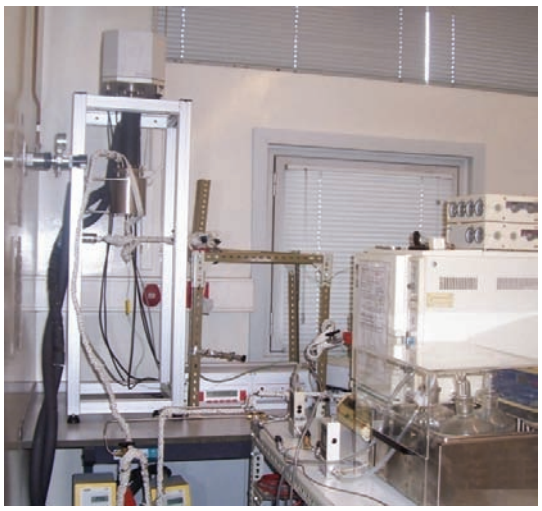


Figure 2.4: Magnetic suspension microbalance (Rubotherm, Bochum, Germany) with a system operating in open mode with a continuous flow passing through the sample.

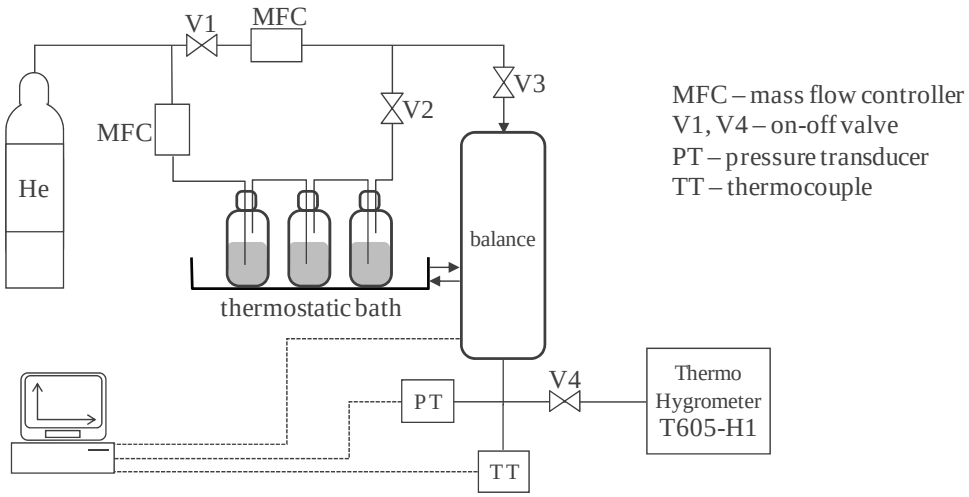


Figure 2.5: Schematic diagram of the experimental set-up for water vapour adsorption measurements. Labelling: MFC, mass flow controller; V1 to V4, on-off valves; PT, pressure transducer; TT, thermocouple.

The water vapour was generated by flowing helium through glass bubblers filled with water. The "saturated" stream was mixed with a second stream of pure helium before entering the balance.

The composition of the inlet gas was regulated by balancing the flow rates of these two streams. When the sample reached a constant mass, the concentration of the outlet stream was determined with a humidity sensor SHT71 (Sensirion, Switzerland). This experimental procedure was also used by Ribeiro *et al.* (2008) [27], for the measurements of adsorption equilibrium of water vapour on different adsorbents, including activated carbon R2030.

2.4 Theoretical

The adsorption isotherm represents the amount of adsorbate (q) retained by amount of adsorbent which is in equilibrium with the gas phase partial pressure (P) for a certain constant temperature (T). Single-component adsorption isotherms have been correlated widely in practice by means of empirical expressions such as the Freundlich equation, Dubinin's volume filling theory, etc [28].

A mathematical model that describes the adsorption equilibrium has to have flexibility to fit diverse and in some cases very different gases for a wide range of temperatures and pressures, it must be very flexible to fit isotherms with different degrees of steepness and also it has to satisfy thermodynamic constraints. The Virial isotherm, suggested by Kiselev (1971) [29] and Barrer

(1981) [30], satisfies these conditions. It is obtained by applying the bidimensional Virial equation of state to the Gibbs isotherm and is given by:

$$P = \frac{q}{K_H}\exp\left(\frac{2}{S}Aq + \frac{3}{2S^2}Bq^2 + ...\right) \tag{2.5}$$

In equation (2.5), S is the adsorbent specific surface area, A and B are Virial coefficients, and K_H is the Henry constant. The Henry constant is related to the temperature (T) through the Van't Hoff equation:

$$K_H = K_\infty \exp\left(\frac{-\Delta H}{R_g T}\right) \tag{2.6}$$

where K_∞ is the adsorption constant at infinite temperature, ($-\Delta H$) is the heat of adsorption at zero coverage and R_g is the universal gas constant. For most systems the Virial equation can be truncated after the second Virial coefficient which depends on the temperature through the following equation (2.7):

$$A = \sum_{m=0}^{\infty}\frac{A_m}{T^m} \quad , \quad B = \sum_{m=0}^{\infty}\frac{B_m}{T^m} \tag{2.7}$$

Another advantage of the Virial isotherm is that it allows the prediction of multicomponent adsorption directly from the single-component data through analytical expressions. The multicomponent adsorption equilibrium was then predicted using the extension of the Virial isotherm to multicomponent systems (equation (2.8)) proposed by Taqvi and LeVan (1997) [31]:

$$P_i = \frac{q_i}{K_{Hi}}\exp\left(\frac{2}{S}\sum_{j=1}^{N}A_{ij}q_i + \frac{3}{2S^2}\sum_{j=1}^{N}\sum_{k=1}^{N}B_{ijk}q_j q_k\right) \tag{2.8}$$

Taqvi and LeVan (1997) [31] studied and compared quantitatively two predictive approaches (method 1 and method 2), the correlative approach and the ideal adsorbed solution theory (IAST). Since the two predictive methods give similar results, the second method was chosen and thus the mixing Virial coefficients A_{ij} and B_{ijk} were calculated by [32]:

$$A_{ij} = \frac{\left(A_i + A_j\right)}{2} \quad , \quad B_{ijk} = \frac{\left(B_i + B_j + B_k\right)}{3} \tag{2.9}$$

Other model that has been capable to fit correctly adsorption data of a wide variety of gases in different adsorbents is the multisite Langmuir model [33]. The model proposed by Nitta *et al.* (1984) [33] was able to fit correctly adsorption data of hydrocarbons and carbon dioxide on activated carbon, molecular sieving carbon 5A and molecular sieve 5A [33] and also C_1 - C_{10} paraffins in zeolite 5A [26, 34-35]. The multisite Langmuir model [33] results in the description of

adsorption equilibrium as a localized monolayer model in which each molecule occupies more than one site on a homogeneous surface. This model saves computational time when compared to the previous Virial equation model. Neglecting the adsorbate – adsorbate interactions and considering a homogeneous adsorbent [26, 34], the multisite Langmuir model is represented by:

$$\left(\frac{q_i}{q_{i,\max}}\right) = a_i K_i P\left[1-\left(\frac{q_i}{q_{i,\max}}\right)\right]^{a_i} \tag{2.10}$$

where q_i is the amount of adsorbate i in the adsorbed phase, $q_{i,\max}$ is the specific saturation adsorption capacity of component i, a_i is the number of neighbouring sites occupied by adsorbate molecule i, K_i is the equilibrium constant of component i and P is the pressure. The previously mentioned Van't Hoff law (equation (2.6)) describes the exponential temperature dependence of the equilibrium constant [36].

The isosteric heat of adsorption $(-\Delta H_i)_q$ can also be estimated by the Clausius-Clapeyron equation:

$$\left(-\Delta H_i\right) = R_g T^2\left(\frac{\partial \ln P_i}{\partial T}\right)_q \tag{2.11}$$

where the derivative has to be evaluated at constant amount adsorbed q. Plotting ln P_i versus $1/T$, the isosteric heat of adsorption can be determined through the straight line equation with a slope equal to $-(-\Delta H_i)/R_g$. The parameters $q_{i,\max}$ and a_i of the multisite Langmuir model [33] are independent of the temperature. A site or space balance of the adsorbed phase gives:

$$a_i q_{i,\max} = \text{constant} \tag{2.12}$$

which is a requirement for thermodynamic consistency of the multisite Langmuir model for prediction of multicomponent adsorption equilibrium [37].

Both models described before can be employed for fitting experimental data. However, only the Virial model can be employed in the fitting of non Type I isotherms (for example water on activated carbon). The parameters obtained from the fitting of pure gases can be employed in the prediction of multicomponent adsorption equilibrium to design a PSA unit. Using MATLAB (The MathWorks, Inc.), the solution of the multi-parametric nonlinear fitting can be obtained with an accuracy of 10^{-9} for all the variables involved [38]. Since the minimization routine used finds the minimum of the objective funcion using the Nelder – Mean Simplex Method of direct search [38-39]; an error function must be defined [38]. This means, for the non-linear set of equations that have to be solved simultaneously, for each equilibrium point the mathematical function for the parameter optimization one error function that can be applied is defined by:

$$ERR(\%) = 100\left[\frac{w}{N}\sum_{T=1}^{m\geq 3}\sum_{P=0}^{P_{max}}\left(q_{cal,T,P} - q_{exp,T,P}\right)^2 + \frac{(1-w)}{N}\sum_{T=1}^{m\geq 3}\sum_{P=0}^{P_{max}}\left(\frac{q_{cal,T,P} - q_{exp,T,P}}{q_{cal,T,P}}\right)^2\right] \quad (2.13)$$

where T is each experimental temperature, P is the pressure, P_{max} is the maximum pressure of each isotherm, N is the number of points of each isotherm, $q_{exp,T,P}$ is the experimental adsorbed phase concentration and $q_{cal,T,P}$ is the calculated adsorbed phase concentration, both for each temperature (T) and pressure (P). The term w is the weight *SOR-ARE* parameter ($0 \leq w \leq 1$). This error function is composed by two terms defined as square of residuals and average of residuals [28, 40].

2.5 Adsorbent characterization

In order to understand and model the adsorption equilibrium and transport properties, some properties of the adsorbents must be known.

In this work, for the activated carbon samples R2030 and ACM-3mm, the surface area and the macro and micro porous structure were determined by nitrogen adsorption at 77 K with a Micromeritics Accusorb 2100E (Instituto Pedro Nunes, Coimbra, Portugal). The macropore size distributions of these materials were measured by mercury intrusion (Instituto Pedro Nunes, Coimbra, Portugal). This analysis was performed in a Poresizer 9320 (Micromeritics) in a pressure range of 3.5 ~ 200,000 kPa for a pore determination between 360 μm and 60 Å. The solid density of each adsorbent (R2030 and ACM-3mm) was determined by helium pycnometry (Instituto Pedro Nunes, Coimbra, Portugal).

For the samples HY2SEPS-AC and HY2SEPS -ZEO, the N_2 physisorption isotherms were measured at 77 K using an Autosorb-1 physisorption-chemisorption analyser (FORTH ICE-HT, Patras, Greece). The samples were degassed at 573 K for at least 2 hours before each measurement. The specific surface area, the pore volume and the pore size distribution of the samples were calculated using the following methods (FORTH ICE-HT, Patras, Greece): Brunauer-Emmett-Teller (BET), Langmuir, Barrer-Joyner-Halenda (BJH), V-t and Horvath-Kawazoe (HK). The mercury porosimetry was performed using a PoreMaster 60 Porosimeter (Quantachrome) (FORTH ICE-HT, Patras, Greece). The mercury intrusion-retraction was measured over a wide range of pressures (3.5 ~ 400,000 kPa). The pore size distribution of the carbon sample (HY2SEPS-AC) was calculated assuming that the macro/mesopores are uniform cylinders. On the other hand the pore size distribution of the zeolite sample (HY2SEPS-ZEO) was calculated assuming that the pore structure is represented by a network of pores and throats.

2.5.1 Activated carbon R2030

The mercury intrusion results and the adsorption isotherm of N_2 at 77 K for the activated carbon R2030 are shown in Figure 2.6. From the analysis of the N_2 by the BET model it was determined that the surface area of the sample is 700.3 $m^2 g^{-1}$, mostly composed by micropores. The results from mercury intrusion show that the transport to micropores is done by macropores with average diameter of 2.34 μm, confirming that the structure of the adsorbent is bidisperse. The properties of R2030 are summarized in Table 2.1.

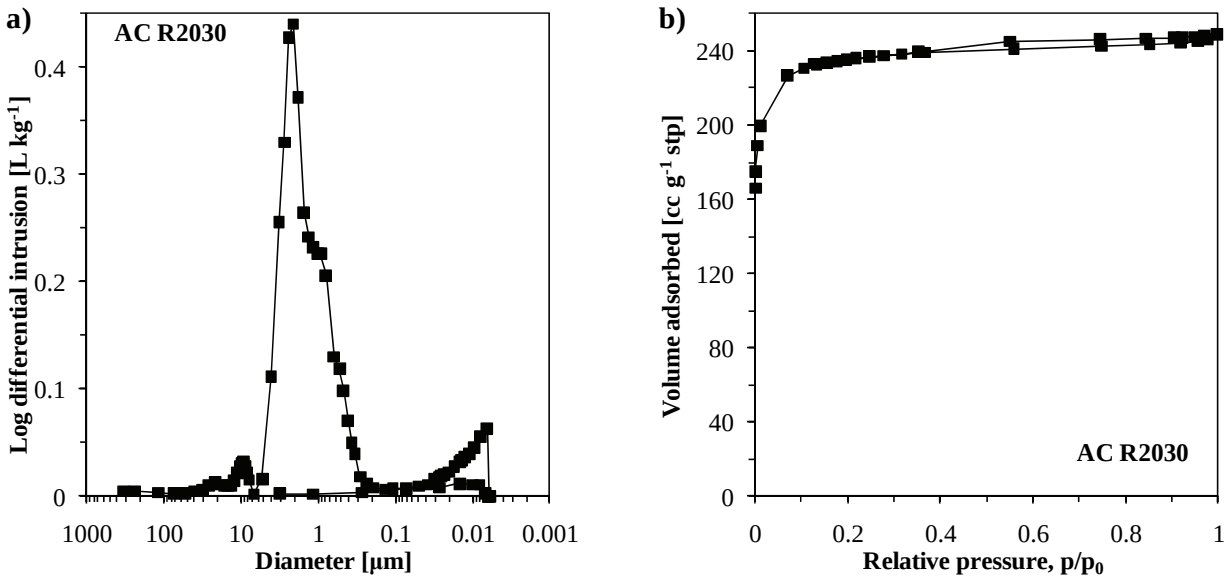


Figure 2.6: a) Pore size distribution by mercury intrusion of activated carbon R2030; b) Adsorption isotherm of nitrogen on R2030 at 77 K.

Table 2.1: Physical properties of activated carbon R2030 pellets.

Activated Carbon, AC	R2030
Surface area [$m^2 g^{-1}$]	700.3
Average pore diameter [μm]	2.34
Average pellet porosity	0.60
Particle density [kg m^{-3}]	874
Solid density [kg m^{-3}]	2162

2.5.2 Activated carbon ACM-3mm

The mercury intrusion results and the adsorption isotherm of N_2 at 77 K for activated carbon ACM-3mm are shown in Figure 2.7. As for activated carbon R2030, from the analysis of

the N_2 isotherm by the BET model the surface area of the sample was determined: 971.2 m^2 g^{-1} (mainly composed by micropores). The results from mercury intrusion on ACM-3mm show that the transport to micropores is done by macropores with average diameter of 2.55 μm. The properties of ACM-3mm are summarized in Table 2.2.

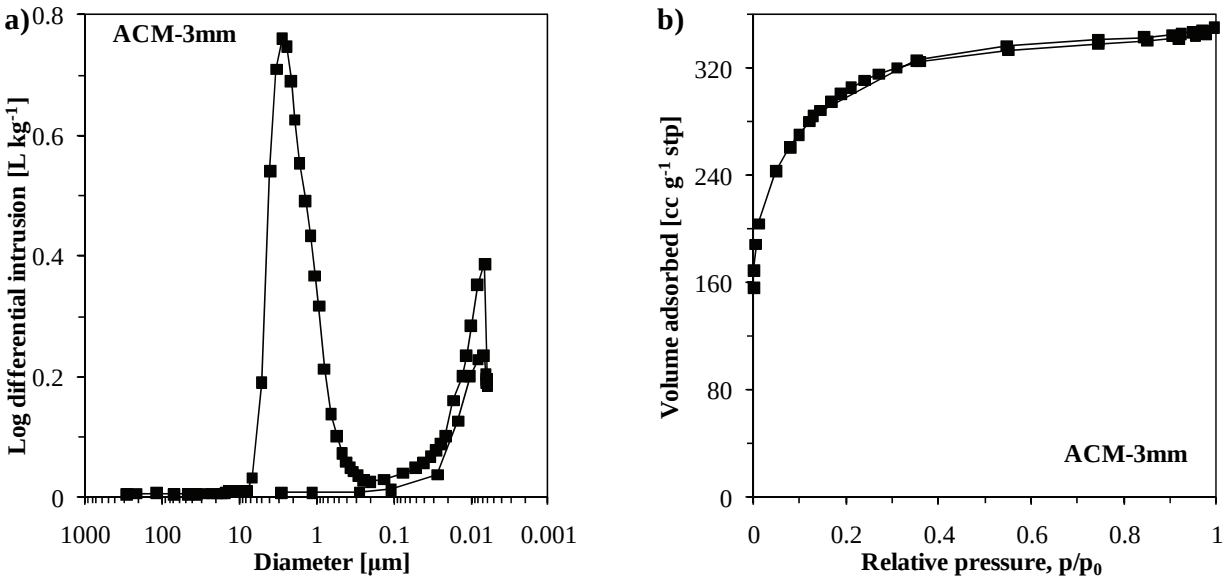


Figure 2.7: a) Pore size distribution by mercury intrusion of activated carbon ACM-3mm; b) Adsorption isotherm of nitrogen on ACM-3mm at 77 K.

Table 2.2: Physical properties of activated carbon ACM-3mm pellets.

Activated Carbon, AC	ACM-3mm
Surface area [m^2 g^{-1}]	971.2
Average pore diameter [μm]	2.55
Average pellet porosity	0.70
Particle density [kg m^{-3}]	649
Solid density [kg m^{-3}]	2140

2.5.3 Activated carbon HY2SEPS-AC

The mercury porosimetry was performed to determine the macropore structure of the HY2SEPS-AC extrudates. The pore size frequency distribution function is represented in Figure 2.8. The macroporous structure of the HY2SEPS-AC is widespread with macropores of several diameters. The average pore diameter distribution is 15.9 μm for the HY2SEPS-AC sample. Table 2.3 summarizes the data obtained in the analysis of the mercury porosimetry experiments. Nitrogen

adsorption isotherm at 77 K for HY2SEPS-AC is shown in Figure 2.8. The results show a high amount of micropores and only a small fraction of macropores. The micropore size distribution (calculated using the HK method) is represented in Figure 2.8. The activated carbon sample (HY2SEPS-AC) presents a wide distribution of micropores within 6 to 15 Å. The summary of the characterization values obtained with the N_2 physisorption experiment is shown in Table 2.3.

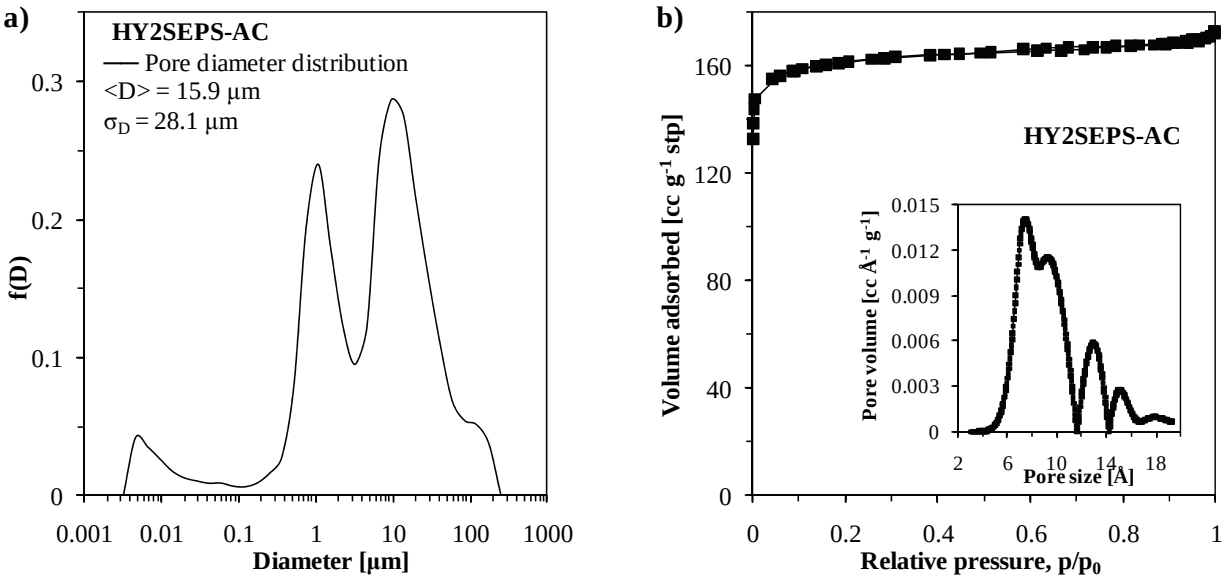


Figure 2.8: a) Pore size frequency distribution functions of the HY2SEPS-AC; b) adsorption isotherm of nitrogen on HY2SEPS-AC at 77 K with the pore size distribution of the HY2SEPS-AC calculated using the HK method.

Table 2.3: Specific surface area, total pore volume and average pore size of the HY2SEPS-AC sample estimated from the N_2 physisorption data and using mercury porosimetry.

	Method	Specific surface area [m^2 g^{-1}]	Pore volume [cc g^{-1}]	Average pore size [Å]
N_2 physisorption	BET Multipoint	480.8		
	Langmuir	729.9		
	BJH	806.8	0.243	< 9
	V-t micropore	401.4	0.208	
	V-t external	79.40		
	HK		0.248	7.4, 9.2, 12.95, 15.11
Mercury porosimetry		5.37	0.424	d1 < 10 d2 ~ 30 d3 ~ 1 × 10^3

2.5.4 Zeolite HY2SEPS-ZEO

The macropore structure of the HY2SEPS-ZEO extrudates was determined through mercury porosimetry. The respective pore and throat size frequency distribution function are represented in Figure 2.9. The macropore distribution within the zeolite is very narrow with a very well defined average at 4.25 μm.

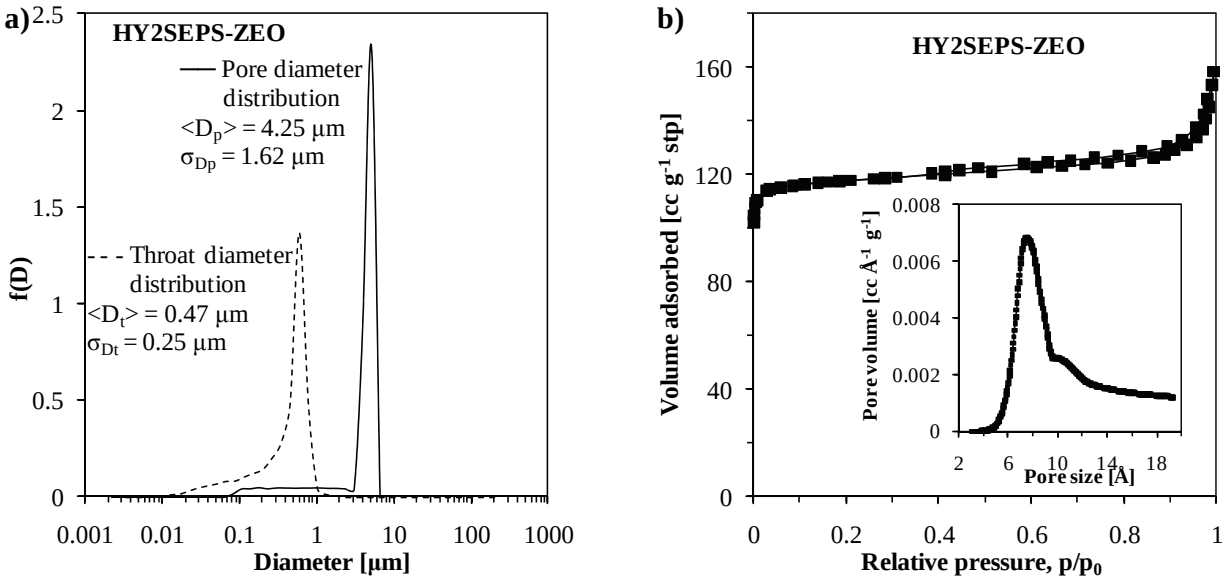


Figure 2.9: a) Pore (──) and throat (- - -) size frequency distribution functions of the HY2SEPS-ZEO; b) adsorption isotherm of nitrogen on HY2SEPS-ZEO at 77 K with the pore size distribution of the HY2SEPS-ZEO calculated using the HK method.

Table 2.4: Specific surface area, total pore volume and average pore size of the HY2SEPS-ZEO sample estimated from the N_2 physisorption data and using mercury porosimetry.

	Method	Specific surface area [m^2 g^{-1}]	Pore volume [cc g^{-1}]	Average pore size [Å]
N_2 physisorption	BET Multipoint	433.9		
	Langmuir	551.5		
	BJH	417.2	0.234	< 9
	V-t micropore	309.9	0.124	7 - 8
	V-t external	130		
	HK		0.1879	7.4, 10.2
Mercury porosimetry		13.04	0.259	d1 ~ 60 d2 ~ 1×10^4 d3 ~ 1×10^5

The average pore diameter distribution is 4.25 μm for the zeolite sample (HY2SEPS-ZEO). The data obtained in the analysis of the mercury porosimetry experiment for the HY2SEPS-ZEO is summarized in Table 2.4.

2.6 Adsorption equilibrium results

The fundamental property to be measured in a material that will be employed in an adsorption-based separation process is the adsorption equilibrium capacity of each of the pure gases employed. It was mentioned before that when adsorption equilibrium is to be measured in a gravimetric device, the correction for buoyancy effects has to be performed. The helium calibration was made at 303 ± 1 K in a pressure range of 0-50 bar for activated carbon R2030 and in a pressure range of 0-7 bar for the activated carbons ACM-3mm and HY2SEPS-AC and zeolite HY2SEPS-ZEO.

2.6.1 Activated carbon R2030

The results obtained for the helium calibration are represented in Figure 2.10. From the straight line obtained in the calibration, using equation (2.4) it was determined that the slope of Δm vs P was 2.6841×10^{-4} g bar^{-1}, giving a value of $(V_s + V_c) = 1.68023 \times 10^{-6}$ m^3. This value will be employed in the correction of buoyancy in all the experiments performed with AC R2030.

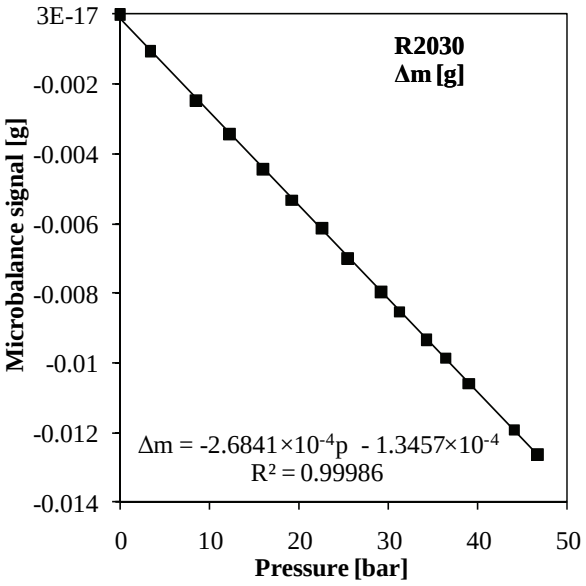


Figure 2.10: Helium measurements on R2030 at 303 K (■); —— the fitting of equation (2.4).

The value obtained from the gravimetric unit is called excess amount adsorbed, q_{exc}. In order to transform this value to the real amount adsorbed, buoyancy corrections with equation (2.2) were performed in all the experiments. As an example, Figure 2.11 shows the results obtained for CO_2 and H_2 at 303 K. In Figure 2.11 it can be seen that the influence of the buoyancy effects increase when pressure increases.

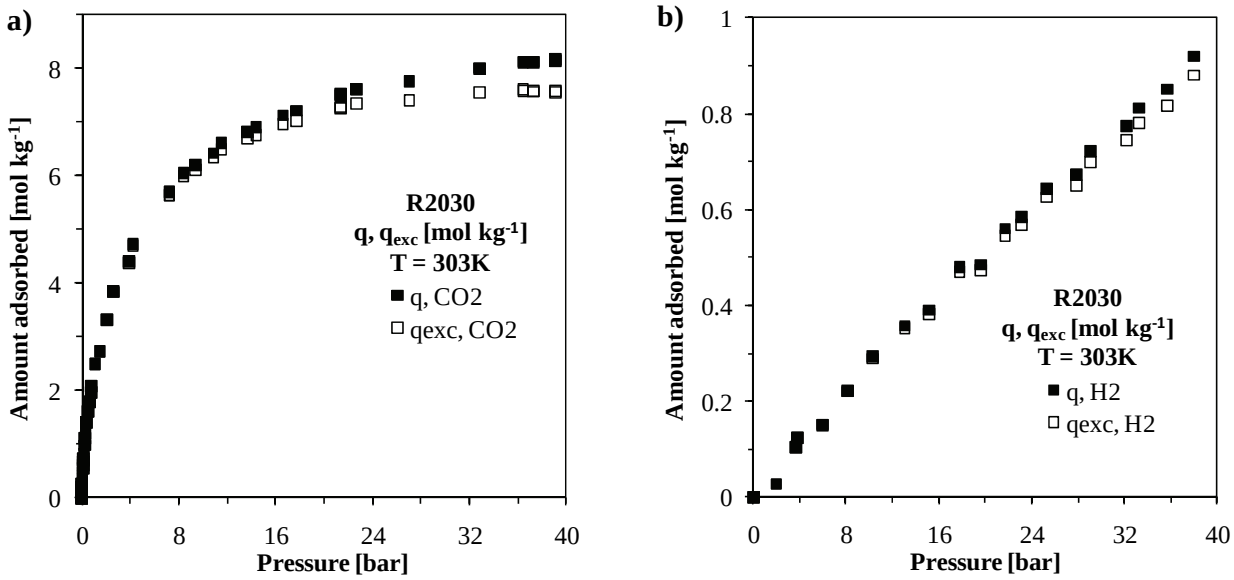


Figure 2.11: a) Excess (□) and absolute (■) amount of CO_2 (a) and H_2 (b) adsorbed on activated carbon R2030 at 303 K.

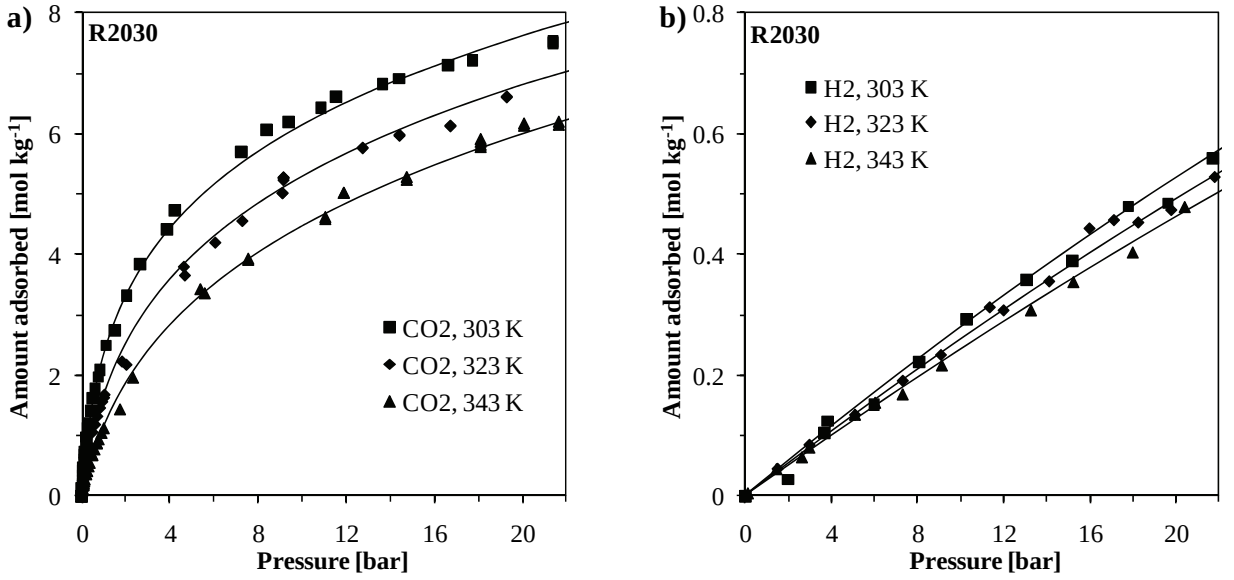


Figure 2.12: Amount of CO_2 (a) and H_2 (b) adsorbed on activated carbon R2030: experimental points at 303 (■), 323 (◆) and 343 K (▲) and —— Virial isotherm fitting.

Adsorption equilibrium of pure carbon dioxide and pure hydrogen were studied at 303, 323 and 343 K in the pressure range 0-22 bar. Once buoyancy corrections were performed, the absolute amount adsorbed was calculated as shown in Figure 2.12. The data obtained for CO_2 and H_2 are comparable with other values reported in literature [12, 15-16]. In Figure 2.13, the absolute amount adsorbed of methane, carbon monoxide and nitrogen are presented for 303, 323 and 343 K in the pressure range 0-18, 0-1 and 0-5 bar, respectively. Note that the pressure range measured for CO_2 and H_2 is much higher than for the other gases because these are the main components of the

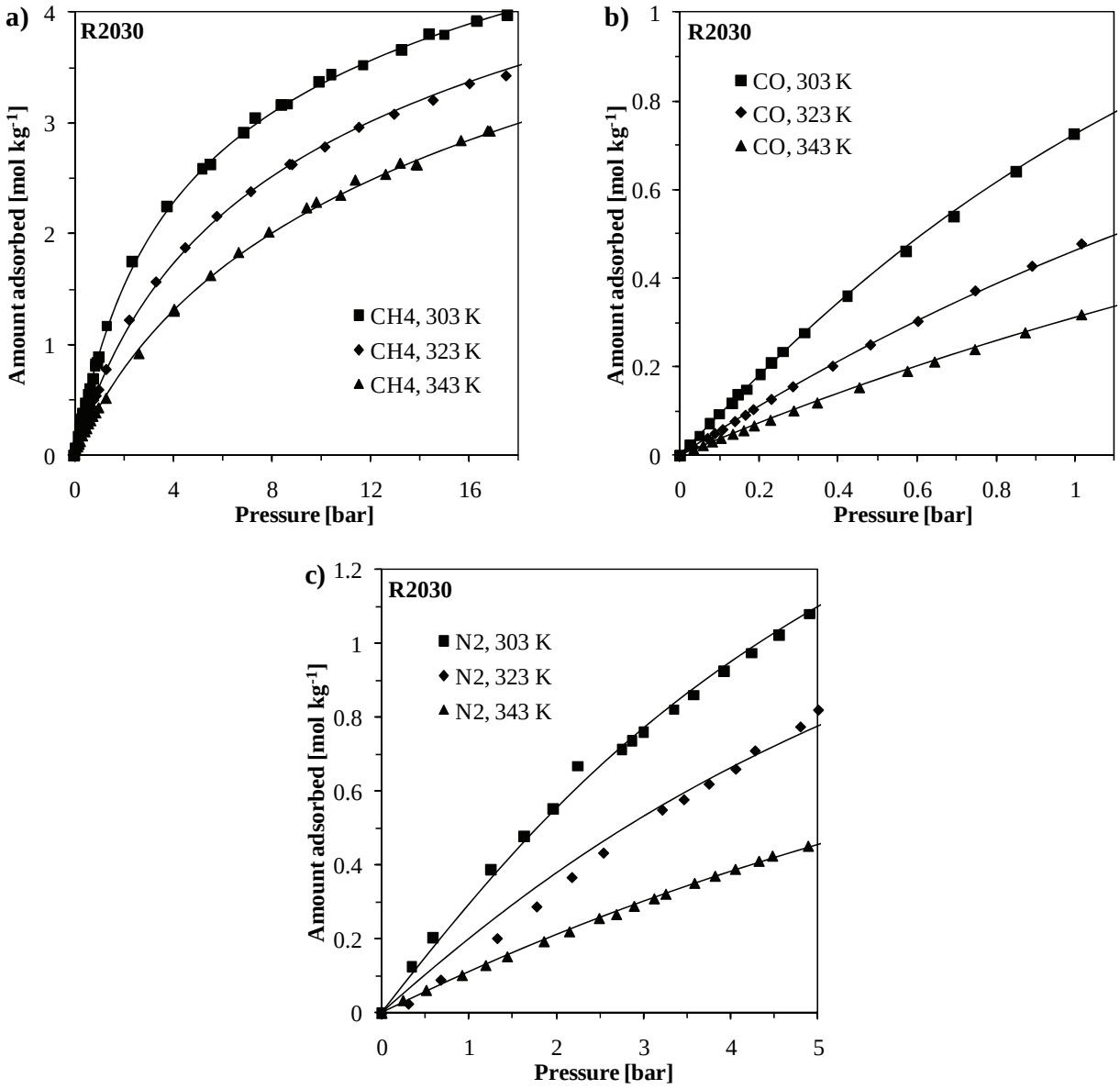


Figure 2.13: Amount of CH_4 (a), CO (b) and N_2 (c) adsorbed on activated carbon R2030: experimental points at 303 (■), 323 (◆) and 343 K (▲) and —— Virial isotherm fitting.

stream entering the PSA unit for H_2 purification.

The off-gases of a steam reformer contain large amounts of water. Normally before the PSA unit there exists a water separator, but the exiting stream is still saturated with water at the exit temperature. There are several approaches to remove water. Some processes use a separate unit containing normally alumina and other adsorbents to remove water before the H_2 PSA unit [8]. Other possibility is to remove water in the same unit, either by using alumina as a selective adsorbent [1-2] or by removing it in the initial layer of activated carbon [4]. To evaluate this last possibility, water adsorption equilibrium is shown at 303 K, until the saturation pressure, P_0 (0.042 bar). The results obtained were reported by Ribeiro *et al.* (2008) [27] and they are reported in Figure 2.14.

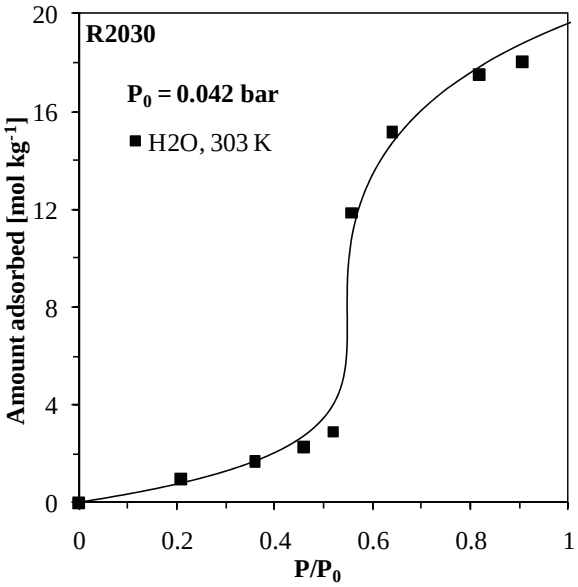


Figure 2.14: Amount of H_2O adsorbed on activated carbon R2030 at 303 K reported by Ribeiro *et al.* (2008) [27]: (■) experimental points and —— Virial isotherm fitting.

The experimental adsorption data determined for R2030 were fitted using the Virial isotherm (equation (2.5)) with the temperature dependence of the Virial coefficients truncated at the second term. The parameters obtained for CO_2, H_2 as well as for CH_4, CO, N_2 and H_2O are presented in Table 2.5. The fitting of the experimental data employing the Virial equation with the parameters reported in Table 2.5 can be observed above, in Figure 2.12, Figure 2.13 and Figure 2.14.

Table 2.5: Virial adsorption isotherm fitting parameters of CO_2, H_2, CH_4, CO, N_2 and H_2O on activated carbon R2030.

Species	K_∞ [mol kg^{-1} bar^{-1}]	$(-\Delta H)$ [kJ mol^{-1}]	$A_0 \times 10^{-5}$ [m^2 mol^{-1}]	$A_1 \times 10^{-6}$ [m^2 K mol^{-1}]	$B_0 \times 10^{-11}$ [m^4 mol^{-2}]	$B_1 \times 10^{-11}$ [m^4 K mol^{-2}]
CO_2	9.90×10^{-5}	27.870	-1.140	79.013	-0.021	-0.416
H_2	8.20×10^{-3}	3.192	0.418	-0.001	0.454	0.000
CH_4	1.04×10^{-3}	17.652	4.616	-121.43	-0.831	308.53
CO	4.62×10^{-4}	19.100	14.076	-422.77	0.264	299.25
N_2	2.54×10^{-3}	11.834	5.585	-163.77	3.385	-777.67
H_2O*	K_H [mol kg^{-1} bar^{-1}] = 76.56 ; $A \times 10^{-5}$ [m^2 mol^{-1}] = -0.896; $B \times 10^{-11}$ [m^4 mol^{-2}] = 0.027					

* obtained from the 303 K data

From these experiments we have observed the following order of adsorption (from the most adsorbed compound to the less adsorbed gas): $H_2O > CO_2 > CH_4 > CO > N_2 > H_2$. It can be also observed that the isotherm of CO_2 is non-linear as well as the isotherm of CH_4, while the isotherms of CO and N_2 are almost linear in the initial portion that corresponds to the concentration of the off-gas SMR streams.

It should be noted that each point of the H_2O isotherm took around one day to reach equilibrium. The isotherm is Type V (IUPAC classification) and is characterized by an initial unfavourable region followed by a steeper region and then a final plateau. It has to be noted that the amount of water adsorbed in R2030 is much higher than the other gases, reason why it is the most adsorbed compound: ~ 18 mol kg^{-1} at 303 K and with a saturation pressure of 0.042 bar. Besides, the initial unfavourable region of the adsorption isotherm makes easier the regeneration of the activated carbon.

It can be seen that a good fitting is obtained for all the gases in the whole pressure and temperature ranges studied. The Virial model showed great flexibility to fit the complete set of adsorption equilibrium data of the different gases with the additional advantage of direct prediction of multicomponent adsorption equilibrium, which is important to improve computation time of PSA process simulation. According to the fitting parameters, the heat of adsorption of CO_2 is much higher than the other gases, while CO heat of adsorption is slightly higher than the heat of adsorption of CH_4. The fitting of all isotherms was performed with a weight *SOR-ARE* parameter (*w*) equal to 0, to obtain good accuracy in the lower part of the isotherm. However changing this parameter significant differences in the results are not observed, even when it is equal to 1.

2.6.2 Activated carbon ACM-3mm

Adsorption equilibrium isotherms of CO_2 and H_2 were measured at 303, 323 and 343 K in the pressure range 0-7 bar. The excess amount adsorbed was obtained from the gravimetric unit and employing equation (2.2) the absolute amount adsorbed was calculated. For that, calibration with helium was initially performed and a value for the volume of cell and adsorbent was determined: $(V_s + V_c) = 2.14775 \times 10^{-6}$ m^3. The results for CO_2 and H_2 adsorption equilibrium on ACM-3mm are shown in Figure 2.15.

The experimental adsorption data determined for the activated carbon ACM-3mm were fitted using the multisite Langmuir model of Nitta (equation (2.10)). The parameters obtained for CO_2 and H_2 are presented in Table 2.6.

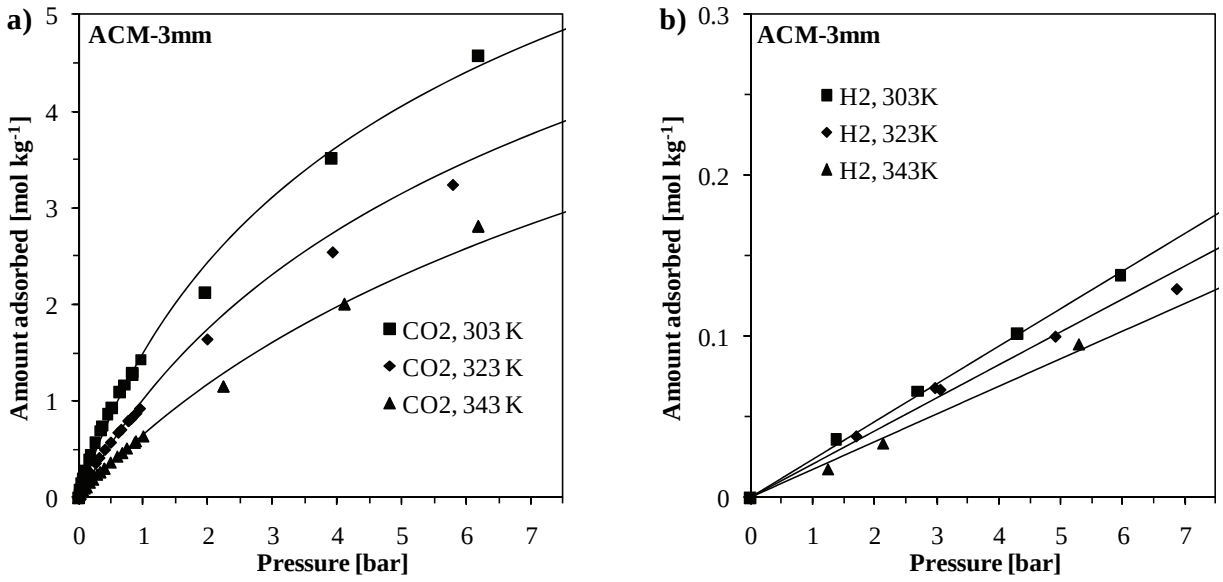


Figure 2.15: Amount of CO_2 (a) and H_2 (b) adsorbed on activated carbon ACM-3mm: experimental points at 303 (■), 323 (◆) and 343 K (▲) and —— multisite Langmuir isotherm fitting.

Table 2.6: Fitting parameters of the multisite Langmuir model for CO_2 and H_2 adsorption equilibrium on activated carbon ACM-3mm at 303, 323 and 343 K.

Species	q_{max} [mol kg^{-1}]	a_i [–]	$K_i^{\infty} \times 10^7$ [kPa^{-1}]	$(-\Delta H)$ [kJ mol^{-1}]
CO_2	13.125	2.5	3.7471	21.0
H_2	32.800	1.0	8.3322	5.43

Also on activated carbon ACM-3mm, the higher adsorption capability for carbon dioxide is obviously proved when compared to hydrogen and the maximum amount adsorbed for carbon dioxide and hydrogen is 4.6 and 0.15 mol kg^{-1}, respectively, for the pressure range 0-7 bar. As presented, good fitting with the multisite Langmuir model is obtained for all the temperature and pressure range studied for both CO_2 and H_2. The fitting was performed with a weight *SOR-ARE* parameter (w) of 0, since insignificant differences in the results were obtained for the all range of w ($0 \leq w \leq 1$). When carbon dioxide adsorption capacity on ACM-3mm is compared to R2030, the difference in the amount adsorbed is slightly lower for ACM-3mm. Therefore, the adsorption equilibrium of methane, carbon monoxide, nitrogen and water vapour were not studied on this commercial adsorbent due to the lower adsorption capacity of CO_2. As mentioned in the Introduction section, a first layer of activated carbon to completely remove H_2O and CO_2 and a second layer of zeolite to remove CH_4, CO and N_2 are generally used [10]. Thus, it is of our interest to study more in detail commercial activated carbons with higher adsorption capacity of carbon dioxide.

2.6.3 Activated carbon HY2SEPS-AC

For activated carbon HY2SEPS-AC, the calibration with helium was initially performed. The experimental results of Δm vs P show a linear curve that gives a slope of 3.8925×10^{-4} g bar^{-1} and using equation (2.4) 2.4517×10^{6} m^3 was the value obtained for the volumes of the cell and adsorbent ($V_s + V_c$). For all the experiments performed with HY2SEPS-AC, this value will be employed in the correction of buoyancy. Adsorption equilibrium of pure gases (carbon dioxide, hydrogen, methane, carbon monoxide and nitrogen) were studied at 303, 323 and 343 K in the pressure range 0-7 bar. In Figure 2.16, the CO_2 and H_2 absolute amount adsorbed are shown.

In Figure 2.17, the absolute amount adsorbed of CH_4, CO and N_2 are presented for the same pressure and temperature ranges. The adsorption equilibrium data of all the gases in HY2SEPS-AC were fitted using the multisite Langmuir model (equation (2.10); solid lines in Figure 2.16 and Figure 2.17). The parameters obtained for carbon dioxide, hydrogen, methane, carbon monoxide and nitrogen are presented in Table 2.7. The model was able to fit with reasonable accuracy the data within the temperature and pressure ranges studied for the five different pure gases on HY2SEPS-AC. This fitting was performed with a weight *SOR-ARE* parameter (w) of 0.

Analyzing the fitting of the experiments for the different pure gases in the Virial domain [41], small deviations for all isotherms can be seen. The Virial domain representation is the

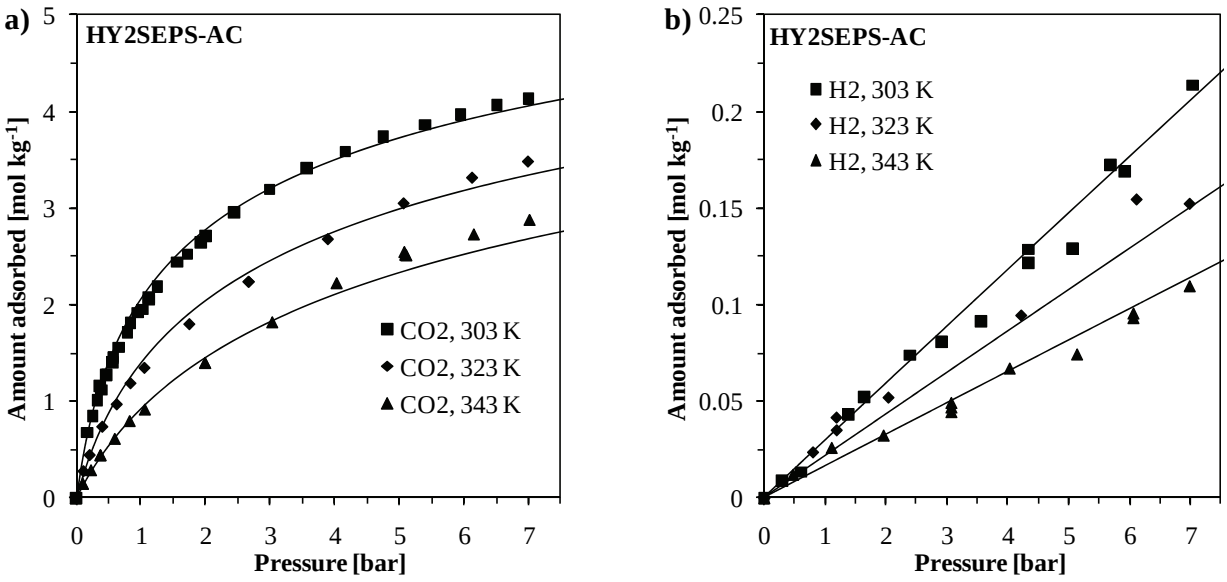


Figure 2.16: Amount of CO_2 (a) and H_2 (b) adsorbed on activated carbon HY2SEPS-AC: experimental points at 303 (■), 323 (◆) and 343 K (▲) and —— multisite Langmuir isotherm fitting.

isothermal data plotted in the form $\ln(P/q)$ versus q [34]. As can be seen in Figure 2.18, these small deviations of the fitting lead us to good predictions on multicomponent adsorption equilibrium.

Carbon dioxide is the most adsorbed gas followed by methane, carbon monoxide, nitrogen and then hydrogen is the less adsorbed compound observed in the HY2SEPS-AC sample.

In HY2SEPS-AC adsorbent, the amount adsorbed of carbon dioxide (at 303 K and 7 bar) is ~ 4.1 mol kg^{-1}. Other samples of activated carbons show relatively higher capacities at 7 bar; i.e, ~ 5.4 mol kg^{-1} [42] at 293 K, ~ 5.8 mol kg^{-1} [43] at 296 K and ~ 5.9 mol kg^{-1} [16], ~ 6.6 mol kg^{-1} [18] and ~ 6.7 mol kg^{-1} [44] at 298 K. This indicates that the CO_2 adsorption of the activated carbon studied (HY2SEPS-AC) has lower capacities than the materials found in the literature. However, for the HY2SEPS-AC, the ratio of adsorbed amounts for CO_2/H_2 (amount of CO_2/amount of H_2) is higher at 303 K and 7 bar (19.7) than the one obtained for the materials reported in the literature: ~ 17.1 [43] at 296 K and ~ 9.67 [16] and ~ 11 [44] at 298 K. Only in another activated carbon sample the CO_2/H_2 adsorbed amount ratio at 7 bar reaches so high values: ~ 19.3 [42] at 293 K.

Adsorption equilibrium of methane on the HY2SEPS-AC sample (at 303 K, 7 bar) is ~ 2.4 mol kg^{-1}. For carbon monoxide, the CO amount adsorbed on HY2SEPS-AC is ~ 2.0 mol kg^{-1} (at 303 K and 7 bar). The absolute amounts adsorbed of nitrogen on HY2SEPS-AC at the same

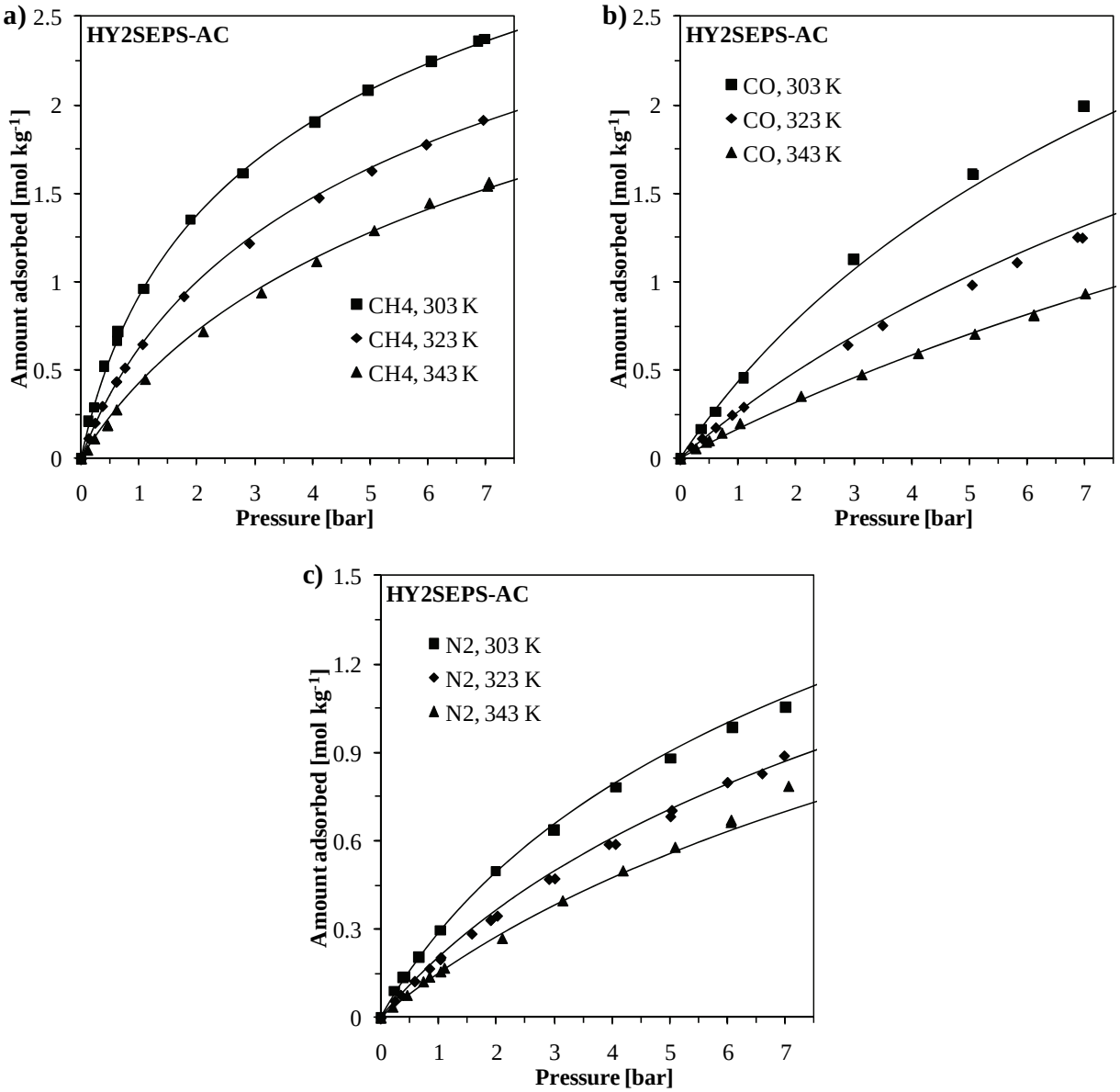


Figure 2.17: Amount of CH_4 (a), CO (b) and N_2 (c) adsorbed on activated carbon HY2SEPS-AC: experimental points at 303 (■), 323 (◆) and 343 K (▲) and —— multisite Langmuir isotherm fitting.

Table 2.7: Fitting parameters of the multisite Langmuir model for CO_2, H_2, CH_4, CO and N_2 adsorption equilibrium on HY2SEPS-AC at 303, 323 and 343 K.

Species	q_{max} [mol kg^{-1}]	a_i [–]	$K_i^{\infty} \times 10^8$ [kPa^{-1}]	$(-\Delta H)$ [kJ mol^{-1}]
CO_2	7.855	3.0	2.1278	29.1
H_2	23.57	1.0	7.6902	12.8
CH_4	6.733	3.5	7.9165	22.7
CO	9.063	2.6	2.6801	22.6
N_2	5.891	4.0	23.428	16.3

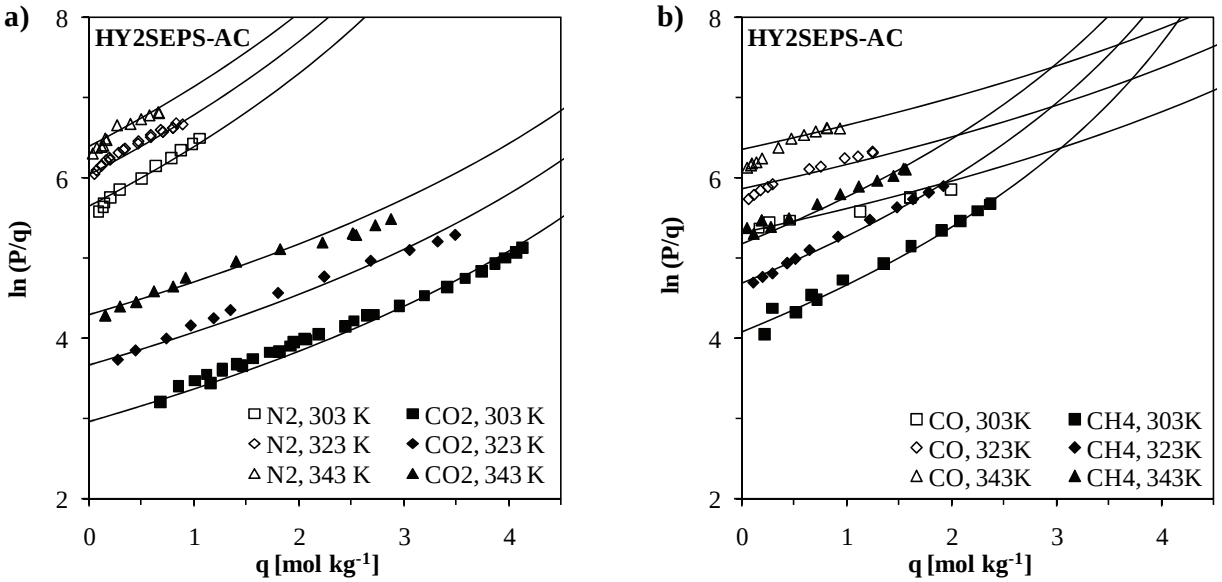


Figure 2.18: Virial domain plot of CO_2 and N_2 (a) and of CH_4 and CO (b) adsorption equilibrium on activated carbon HY2SEPS-AC: experimental points at 303 (■,□), 323 (◆,◇) and 343 K (▲,△) and —— multisite Langmuir isotherm fitting.

temperature and pressure is ~ 1.2 mol kg^{-1}. This is the less adsorbed contaminant and will be the first gas to breakthrough in the PSA column.

Hydrogen is the less adsorbed compound on HY2SEPS-AC. In this material, the amount adsorbed at 303 K for hydrogen is ~ 0.2 mol kg^{-1} (at 7 bar). The adsorption equilibrium capacities of hydrogen on other samples of activated carbons show results from ~ 0.1 mol kg^{-1} [45] to ~ 0.6 mol kg^{-1} [16, 44], increasing when the surface area of the adsorbent increases.

From the fitting parameters of the multisite Langmuir model shown in Table 2.7 it can be observed that the heat of adsorption of CO_2 is much higher than the other gases. The heat of adsorption of the different compounds follows the same order as the adsorption capacities (CO_2 > CH_4 > CO > N_2 > H_2). The variation of the single-component isosteric heat of adsorption was calculated using the Clausius-Clapeyron equation (Figure 2.19). These results are in agreement with the values obtained through the multisite Langmuir model.

As mentioned in section 2.6.1, the off-gases of a steam reformer contain large amounts of water and it is frequently used a water separator before the PSA unit. However, the exiting stream is still saturated with water at the exit temperature. As previously stated, the removal of water can be done in the same PSA unit. Therefore, adsorption equilibrium of water on HY2SEPS-AC was measured at 303 K to evaluate the possibility of water removal in the PSA unit. In Figure 2.20, the adsorption equilibrium isotherm is presented. As for the activated carbon R2030, each point of the

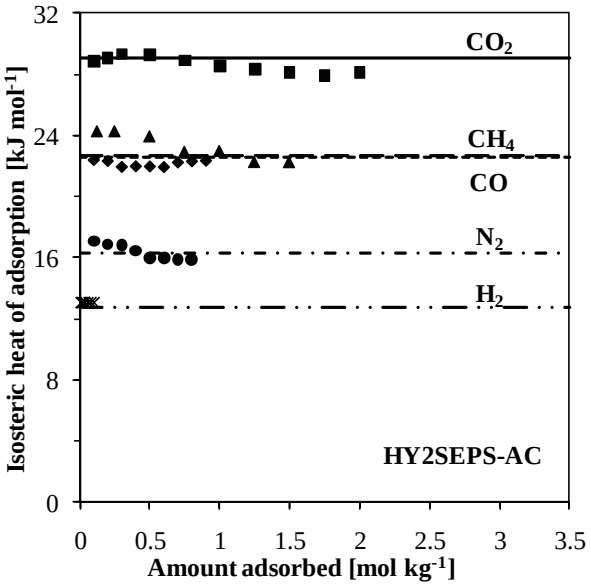


Figure 2.19: Single-component isosteric heats of adsorption on HY2SEPS-AC for CO_2 (■), CH_4 (▲), CO (◆), N_2 (●) and H_2 (×) as a function of equilibrium pressure in the temperature range of 303-343 K; Lines are the values obtained through the multisite Langmuir model.

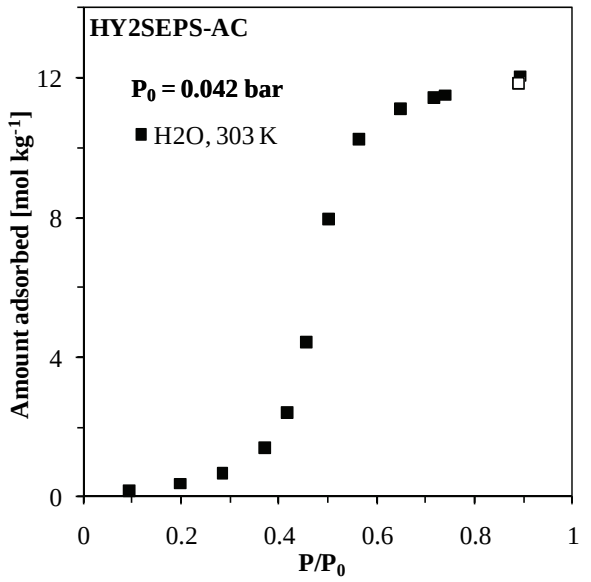


Figure 2.20: Amount of H_2O adsorbed on activated carbon HY2SEPS-AC at 303 K (■); open symbol (□) obtained from the analysis of the breakthrough experiment.

water adsorption equilibrium isotherm on HGYGEAR-AC took approximately one day to reach equilibrium. Once again, this H_2O isotherm is Type V, characterized by an initial unfavourable

region followed by a steeper region and then a final plateau. Water is the most adsorbed compound in HY2SEPS-AC, reaching approximately 12 mol kg^{-1} at 303 K and 0.042 bar of saturation pressure.

2.6.4 Zeolite HY2SEPS-ZEO

For zeolite HY2SEPS-ZEO extrudates, the calibration with helium was also initially performed. The experimental results of Δm vs P show a linear curve with a slope of 4.0444×10^{-4} g bar^{-1}. Using equation (2.4), the value obtained for the volumes of the cell and adsorbent ($V_s + V_c$) was 2.5473×10^{6} m^3 and it was employed in the correction of buoyancy for all the experiments performed with HY2SEPS-ZEO. Adsorption equilibrium of carbon dioxide, hydrogen, methane, carbon monoxide and nitrogen were studied at 303, 323 and 343 K and 0-7 bar of pressure. The absolute amount adsorbed of CO_2 and H_2 are shown in Figure 2.21. The CH_4, CO and N_2 absolute amount adsorbed are presented for the same pressure and temperature ranges in Figure 2.22.

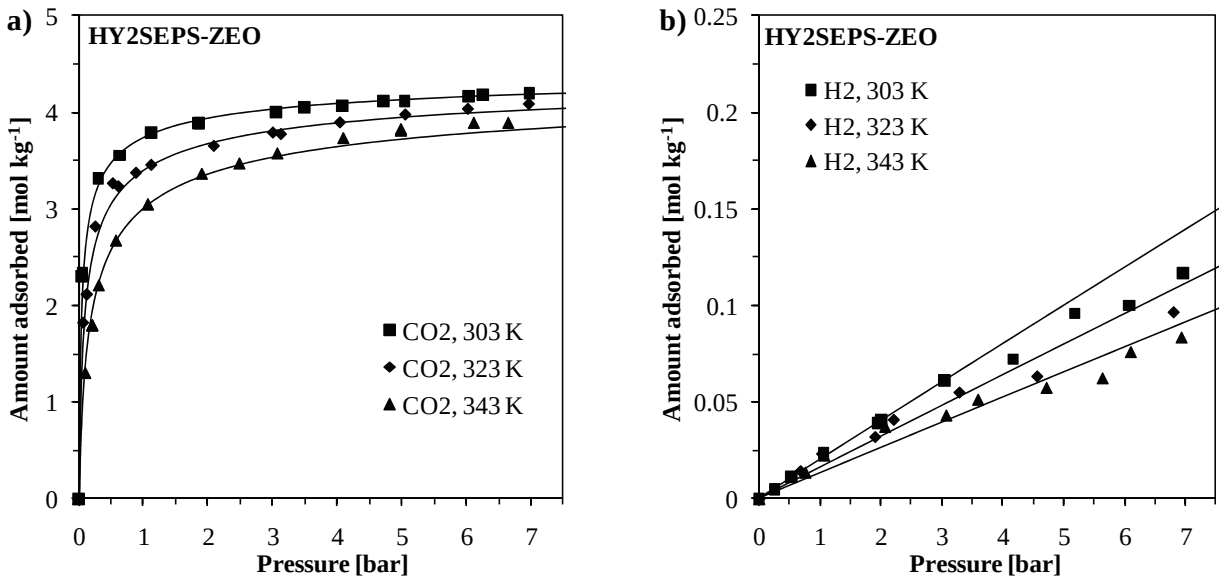


Figure 2.21: Amount of CO_2 (a) and H_2 (b) adsorbed on activated carbon HY2SEPS-ZEO: experimental points at 303 (■), 323 (◆) and 343 K (▲) and —— multisite Langmuir isotherm fitting.

The adsorption equilibrium data of all the gases in HY2SEPS-ZEO were fitted using the multisite Langmuir model (equation (2.10)). The corresponding results are shown in solid lines in

Figure 2.21 and Figure 2.22. The parameters obtained for CO_2, H_2 CH_4, CO and N_2 are presented in Table 2.8. As for the activated carbon HY2SEPS-AC, the model was able to fit the five different pure gases on HY2SEPS-ZEO with accurateness in all temperature and pressure ranges studied. This fitting was performed with a weight *SOR-ARE* parameter (*w*) of 0, taking more into consideration the smaller values of the amount adsorbed (*q*) and, consequently, fitting with higher accuracy at low pressures.

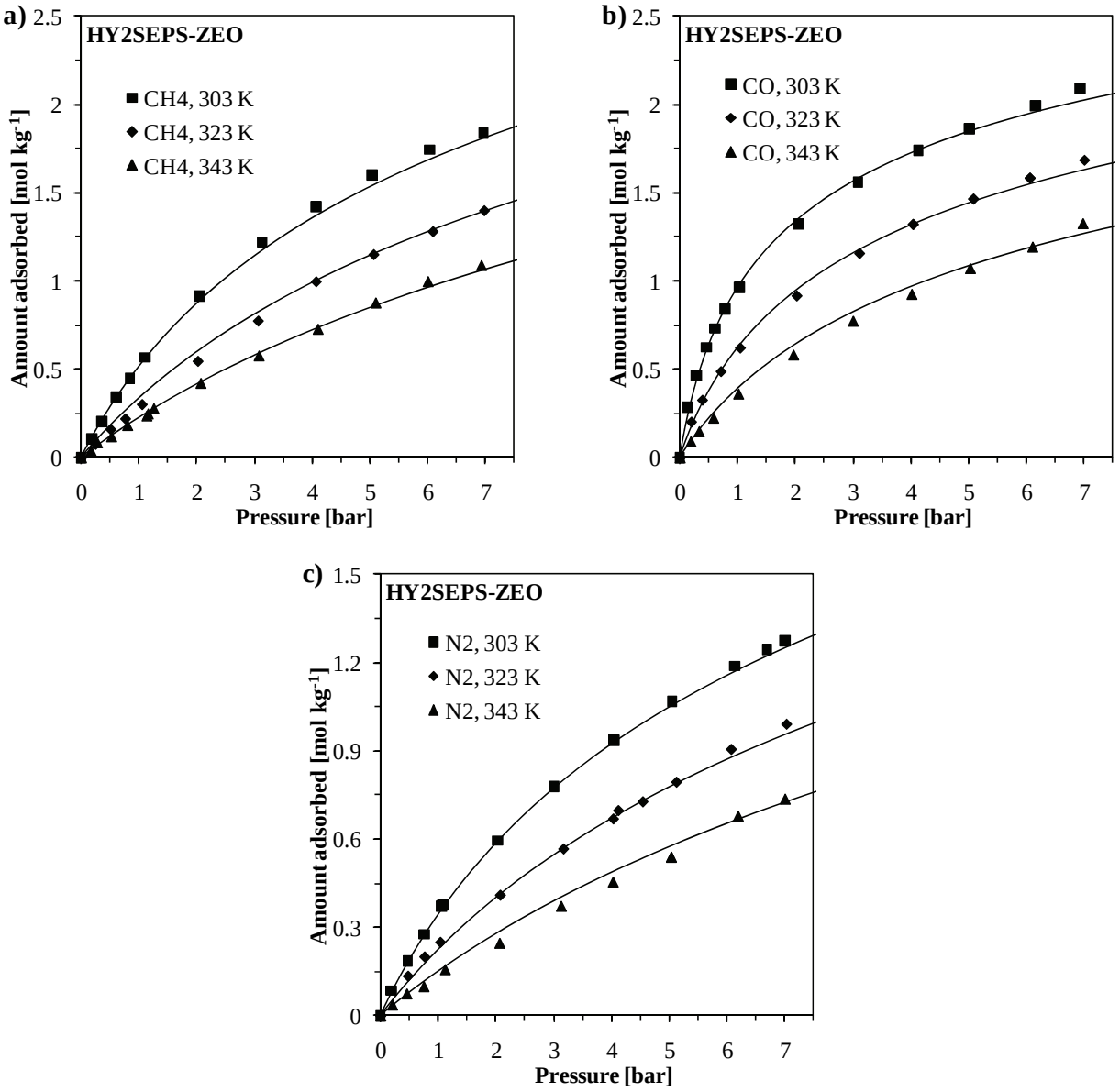


Figure 2.22: Amount of CH_4 (a), CO (b) and N_2 (c) adsorbed on activated carbon HY2SEPS-ZEO: experimental points at 303 (■), 323 (◆) and 343 K (▲) and —— multisite Langmuir isotherm fitting.

Table 2.8: Fitting parameters of the multisite Langmuir model for CO_2, H_2, CH_4, CO and N_2 adsorption equilibrium on HY2SEPS-ZEO at 303, 323 and 343 K.

Species	q_{max} [mol kg^{-1}]	a_i [–]	$K_i^{\infty} \times 10^8$ [kPa^{-1}]	$(-\Delta H)$ [kJ mol^{-1}]
CO_2	4.525	2.2	11.121	36.0
H_2	9.954	1.0	52.024	9.23
CH_4	4.976	2.0	17.793	20.6
CO	3.828	2.6	1.5164	29.8
N_2	4.148	2.4	12.851	20.4

Carbon dioxide is the most adsorbed gas followed by carbon monoxide, methane, nitrogen and hydrogen is the less adsorbed gas in the HY2SEPS-ZEO sample. Note that, for the activated carbon HY2SEPS-AC, methane was more adsorbed than carbon monoxide while for the zeolite HY2SEPS-ZEO is the reverse.

In HY2SEPS-ZEO extrudates, the CO_2 amount adsorbed is ~ 4 mol kg^{-1} (at 303 K and 7 bar) with a much higher steepness than in HY2SEPS-AC. The type of zeolite of the HY2SEPS-ZEO adsorbent cannot be disclosed due to the privacy politics of the European Project HY2SEPS [11]. Therefore the HY2SEPS-ZEO isotherms were compared to different types of zeolites, such as zeolites 4A and 13X. The data obtained is similar to reported values of zeolite 4A and it is slightly lower than for zeolite 13X at 298 K (~ 4.5 mol kg^{-1}) [44]. Other three samples of zeolite 13X showed higher capacities at 298 K and 7 bar: ~ 5.4 and ~ 5.7 mol kg^{-1} [16] and ~ 5.0 mol kg^{-1} [46].

At 303 K and 7 bar, the CH_4 amount adsorbed on HY2SEPS-ZEO sample is ~ 1.8 mol kg^{-1}. For carbon monoxide, the CO amount adsorbed on HY2SEPS-ZEO sample is ~ 2.1 mol kg^{-1} (at 303 K and 7 bar). Although the loading at high pressures is close, the capacity at low partial pressures is considerable larger for the HY2SEPS-ZEO than for HY2SEPS-AC. The absolute amount adsorbed of nitrogen on HY2SEPS-ZEO at 303 K and 7 bar is ~ 1.2 mol kg^{-1}. Once again, for HY2SEPS-ZEO this is the less adsorbed contaminant and will be the first gas to breakthrough in the PSA column.

On HY2SEPS-ZEO, the less adsorbed compound is hydrogen. At 303 K and 7 bar, the H_2 amount adsorbed for the HY2SEPS-ZEO sample is ~ 0.1 mol kg^{-1}. In the literature higher adsorption equilibrium capacities of hydrogen are reported on other samples of zeolites at the same conditions, i.e, ~ 0.2 mol kg^{-1} [16, 44].

In Table 2.8, the fitting parameters of the multisite Langmuir model show that the CO_2 heat of adsorption is much higher than the other gases. The heat of adsorption of the different

compounds follows the same order as the adsorption capacities (CO_2 > CO > CH_4 > N_2 > H_2). Using the Clausius-Clapeyron equation, the variation of the single-component isosteric heat of adsorption was calculated and it is reported in Figure 2.23. The single-component isosteric heat of adsorption values are in agreement with the results obtained through the multisite Langmuir model.

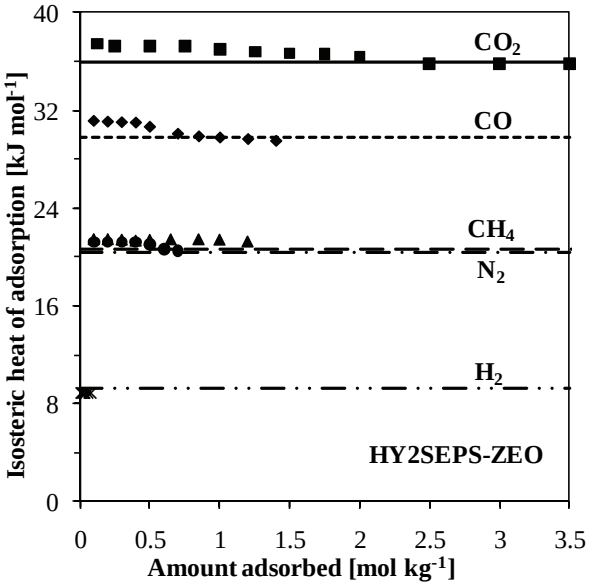


Figure 2.23: Single-component isosteric heats of adsorption on HY2SEPS-ZEO for CO_2 (■), CH_4 (▲), CO (◆), N_2 (●) and H_2 (×) as a function of equilibrium pressure in the temperature range of 303-343 K; Lines are the values obtained through the multisite Langmuir model.

Although it was not measured, the adsorption of water in the HY2SEPS-ZEO should be avoided because it is very strong and the adsorbent should be regenerated at high temperatures. Sircar and co-workers [47] reported the difficult water desorption from the zeolite (even at very low partial pressures), becoming a very energy intensive process.

2.7 Conclusions

Activated carbon R2030 was the first adsorbent studied. The adsorption equilibrium on this adsorbent was determined at 303, 323 and 343 K for H_2, CO_2, CH_4, CO and N_2. It was observed that the amount adsorbed was much higher for CO_2 than for H_2. The adsorption equilibrium of H_2O on this adsorbent at 303 K was also reported. The H_2O adsorption equilibrium isotherm showed an

initial dispersive part followed by a compressive shock indicating that regeneration of the adsorbent might be favourable. The following order of adsorption (from the most adsorbed compound to the less adsorbed gas) was observed in this sample of activated carbon: $H_2O > CO_2 > CH_4 > CO > N_2 > H_2$. The Virial isotherm equation was employed to fit the experimental data of H_2, CO_2, CH_4, CO, N_2 and H_2O on R2030 in the temperature range 303-343 K. It was found that this equation could describe the adsorption isotherms in the whole temperature and pressure range studied.

Activated carbon ACM-3mm was the second adsorbent studied. The adsorption equilibrium on this adsorbent was determined only for the two main gases (H_2 and CO_2) at 303, 323 and 343 K. The purpose of this study was to compare on different commercial samples of activated carbon the adsorption capacity of H_2 and CO_2. Once again it was observed that the amount adsorbed was much higher for CO_2 than for H_2, i.e., 4.6 and 0.15 mol kg^{-1}, respectively for the pressure range 0-7 bar. The multisite Langmuir model was employed to fit the experimental data of H_2 and CO_2 on ACM-3mm in the temperature range 303-343 K. Once more, adsorption equilibrium in the temperature and pressure ranges studied could be described by this model. However, for ACM-3mm adsorption equilibrium of CH_4, CO and N_2 were not performed due to lack of interest in this adsorbent since carbon dioxide adsorption capacity on ACM-3mm was slightly lower than for R2030. At 303 K and 6 bar, the CO_2 amount adsorbed on activated carbons R2030 and ACM-3mm was 5.3 and 4.5 mol kg^{-1}, respectively; the H_2 amount adsorbed on the same adsorbents was 0.17 and 0.15 mol kg^{-1}, respectively.

Experimental data of adsorption equilibrium of CO_2, H_2, CH_4, CO and N_2 were measured at three different temperatures (303, 323 and 343 K) for the activated carbon HY2SEPS-AC. Water adsorption equilibrium was also studied on this adsorbent at 303 K. The following order of adsorption (from the most adsorbed compound to the less adsorbed gas) $H_2O > CO_2 > CH_4 > CO > N_2 > H_2$ was observed in this sample of activated carbon. The multisite Langmuir model was employed to fit the experimental data of H_2, CO_2, CH_4, CO and N_2 on activated carbon HY2SEPS-AC at the three temperatures studied. This equation could describe the adsorption isotherms for the temperature and pressure ranges studied. However, this model could not be applied for the fitting of the H_2O experimental data, since this model is not able to fit isotherms of type V. No significant discrepancies were observed when comparing the single-component isosteric heat of adsorption obtained by the Clausius-Clapeyron equation and the values obtained by the multisite Langmuir model. The isosteric heats of adsorption for the HY2SEPS-AC obtained through the multisite Langmuir model were 29.1 (CO_2), 12.8 (H_2), 22.7 (CH_4), 22.6 (CO) and 16.3 kJ mol^{-1} (N_2).

Finally, CO_2, H_2, CH_4, CO and N_2 adsorption equilibrium data were reported for the zeolite HY2SEPS-ZEO at 303, 323 and 343 K and in the pressure range between 0 and 7 bar. In HY2SEPS-ZEO, the following order of adsorption was obtained: CO_2 > CO > CH_4 > N_2 > H_2, from the most adsorbed compound to the less adsorbed gas. Similar single-component isosteric heat of adsorption values were obtained by the Clausius-Clapeyron equation and the multisite Langmuir model. For this adsorbent, the isosteric heats of adsorption obtained through the multisite Langmuir model were 36.0 (CO_2), 9.23 (H_2), 20.6 (CH_4), 29.8 (CO) and 20.4 kJ mol^{-1} (N_2) .

The properties exhibited by the activated carbons R2030 and HY2SEPS-AC (CO_2 capacity and regenerability and water tolerance) indicate that one of these adsorbents should be employed as the first adsorbent in a layered PSA configuration. Within these adsorbents, water will be preferentially removed followed by CO_2 but methane and carbon monoxide will also be adsorbed. If a second layer of zeolite (e.g. HY2SEPS-ZEO) is employed, the remaining CH_4, CO and N_2 will be removed. According to the higher steepness of the CO_2 isotherms in the HY2SEPS-ZEO than in the activated carbons, it is important that all CO_2 should be removed within the activated carbon layer. Applying the HY2SEPS-ZEO as second layer in the PSA column, the N_2 adsorption capacity of the bed will increase; the capacity obtained for the activated carbons R2030 and HY2SEPS-AC at 1 bar (303 K) was ~ 0.30 and ~ 0.29 mol kg^{-1}, respectively, while the capacity in the zeolite HY2SEPS-ZEO was ~ 0.35 mol kg^{-1}. Also, considering that the density of the HY2SEPS-ZEO is higher, more adsorbent weight could be packed per volume of a fixed column, improving process productivity.

In this chapter adsorption equilibrium of the pure gases exiting a methane reformer on three activated carbons and one zeolite was provided. A total of fifty three isotherms were measured on several samples and it was confirmed that adsorption equilibrium of CO_2, H_2, CH_4, CO and N_2 are reversible both in activated carbons and in zeolites. The conditions used in these experiments were in accordance to a plant under operation for the H_2-CO_2 separation [11] but also covered a wide range of operating conditions of the PSA unit to reach a hydrogen stream with purity higher than 99.99%. The data reported in this chapter will contribute for the detailed design and simulation of a layered PSA unit for hydrogen purification.

2.8 Notation

Nomenclature

a_i	number of neighbouring sites occupied by adsorbate *i* molecule
A	Virial coefficients (m^2 mol^{-1})
B	Virial coefficients (m^4 mol^{-2})
K_H	Henry constant (mol kg^{-1} bar^{-1})
K_∞	adsorption constant at infinite temperature (mol kg^{-1} bar^{-1})
K_i	equilibrium constant of component *i* (Pa^{-1})
K_i^∞	equilibrium constant of compound *i* at infinite temperature (Pa^{-1})
m_{ads}	mass of adsorbed gas (kg)
m_s	mass of adsorbent (kg)
M_W	molecular weight of the gas (kg mol^{-1})
N	number of points of each isotherm
P	pressure (Pa)
P_0	saturation pressure (Pa)
$P_{\max}$	maximum pressure of each isotherm (Pa)
q	absolute adsorbed phase concentration (mol kg^{-1})
$q_{cal,T,P}$	calculated adsorbed phase concentration for each temperature *T* and pressure *P* (mol kg^{-1})
q_{exc}	excess adsorbed phase concentration (mol kg^{-1})
$q_{exp,T,P}$	experimental adsorbed phase concentration for each temperature *T* and pressure *P* (mol kg^{-1})
q_i	absolute adsorbed phase concentration of adsorbate *i* (mol kg^{-1})
$q_{i,\max}$	specific saturation adsorption capacity of adsorbate *i* (mol kg^{-1})
R_g	universal gas constant (J mol^{-1} K^{-1})
S	adsorbent specific area (m^2 kg^{-1})
T	temperature (K)
V_{ads}	volume of adsorbed phase (m^3)
V_c	volume of the cell where the adsorbent is located (m^3)
V_s	volume of the solid adsorbent (m^3)
w	weight *SOR-ARE* parameter, $0 \le w \le 1$

Greek letters

Δm	difference of weight between two measurements (kg)
(ΔZP)	difference of weight between two measurements of zero point (kg)
$(-\Delta H)$	isosteric heat of adsorption (kJ mol^{-1})
$(-\Delta H_i)$	isosteric heat of adsorption of component *i* (kJ mol^{-1})
ρ_g	density of the gas phase (kg m^{-3})
ρ_ℓ	density of the adsorbed phase (kg m^{-3})

2.9 References

[1] M.S.A. Baksh, M.W. Ackley, Pressure swing adsorption process for the production of hydrogen (2002) U.S. Patent 6,340,382.

[2] M.S.A. Baksh, C.E. Terbot, Pressure swing adsorption process for the production of hydrogen (2003) U.S. Patent 6,503,299.

[3] R. Kumar, Adsorption process for recovering two high purity gas products from multicomponent gas mixtures (1990) U.S. Patent 4,913,709.

[4] R.L. Le Bec, Method for purifying hydrogen-based gas mixtures using calcium X-zeolite (2005) U.S. Patent 6,849,106.

[5] A.E. Rodrigues, M.D. LeVan, D. Tondeur, Adsorption: Science and Technology, Kluwer, Boston, MA, 1989.

[6] S. Sircar, Separation of multicomponent gas mixtures (1979) U.S. Patent 4,171,206.

[7] S. Sircar, W.E. Waldron, M.B. Rao, M. Anand, Hydrogen production by hybrid SMR-PSA-SSF membrane system, Separation and Purification Technology. 17 (1999) 11-20.

[8] R.T. Yang, Gas separation by adsorption processes, Butterworths, Boston, 1987.

[9] M. Chlendi, D. Tondeur, Dynamic behaviour of layered columns in pressure swing adsorption, Gas Separation & Purification. 9 (1995) 231.

[10] J.-H. Park, J.-N. Kim, S.-H. Cho, J.-D. Kim, R.T. Yang, Adsorber dynamics and optimal design of layered beds for multicomponent gas adsorption, Chemical Engineering Science. 53 (1998) 3951-3963.

[11] HY2SEPS, Hybrid Hydrogen Carbon Dioxide Separation Processes, E.U. Res. Project 2005, Available from: http://hy2seps.iceht.forth.gr/.

[12] R.V. Siriwardane, M.-S. Shen, E.P. Fisher, J.A. Poston, Adsorption of CO_2 on molecular sieves and activated carbon, Energy & Fuels. 15 (2001) 279-284.

[13] F. Dreisbach, R. Seif, H.W. Lösch, Adsorption equilibria of CO/H_2 with a magnetic suspension balance - Purely gravimetric measurement, Journal of Thermal Analysis and Calorimetry. 71 (2003) 73-82.

[14] J. Yang, S. Han, C. Cho, C.-H. Lee, H. Lee, Bulk separation of hydrogen mixtures by a one-column PSA process, Separations Technology. 5 (1995) 239-349.

[15] R.V. Siriwardane, M.-S. Shen, E.P. Fisher, Adsorption of CO_2 on zeolites at moderate temperature, Energy & Fuels. 19 (2005) 1153-1159.

[16] R.V. Siriwardane, M.-S. Shen, E.P. Fisher, J.A. Poston, A. Shamsi, Adsorption and

desorption of CO_2 on solid sorbents, in Carbon Sequestration - First National Conference on Carbon Sequestration, Session 3B. Capture & Sequestration III: Adsorption Studies, 2001, NETL Publications.

[17] B.-U. Choi, D.-K. Choi, Y.-W. Lee, B.-K. Lee, Adsorption equilibria of methane, ethane, ethylene, nitrogen and hydrogen onto activated carbon, Journal of Chemical and Engineering Data. 48 (2003) 603-607.

[18] F. Dreisbach, R. Staudt, J.U. Keller, High pressure adsorption data of methane, nitrogen, carbon dioxide and their binary and ternary mixtures on activated carbon, Adsorption. 5 (1999) 215-227.

[19] J.A. Ritter, R.T. Yang, Equilibrium adsorption of multicomponent gas mixtures at elevated pressures, Industrial and Engineering Chemistry Research. 26 (1987) 1679-1686.

[20] K. Murata, J. Miyawaki, K. Kaneko, A simple determination method of the absolute adsorbed amount for high pressure gas adsorption, Carbon. 40 (2002) 425-428.

[21] S. Sircar, W.E. Waldron, M.B. Rao, M. Anand, Hydrogen production by hybrid SMR-PSA-SSF membrane system, Separation and Purification Technology. 17 (1999) 11-20.

[22] K. Murata, K. Kaneko, Nano-range interfacial layer upon high-pressure adsorption of supercritical gases, Chemical Physics Letters. 321 (2000) 342-348.

[23] R.C. Weast, Handbook of chemistry and physics, a ready-reference book of chemical and physical data, 54th Edition, The Chemical Rubber Co., 1973.

[24] R. Span, W. Wagner, A new equation of state for carbon dioxide covering the fluid region from the triple-point temperature to 1100 K at pressures up to 800 MPa, Journal of Physical and Chemical Reference Data. 25 (1996) 1509-1596.

[25] R.H. Perry, D.W. Green, Perry's Chemical Engineers' Handbook, 7th Edition, McGraw-Hill, 1997.

[26] S. Cavenati, Adsorptive processes for separation of $CH_4/CO_2/N_2$ mixtures, Ph.D. Dissertation, University of Porto, Porto, Portugal, 2005.

[27] A.M. Ribeiro, T.P. Sauer, C.A. Grande, R.F.P.M. Moreira, J.M. Loureiro, A.E. Rodrigues, Adsorption equilibrium and kinetics of water vapour on different adsorbents, Industrial and Engineering Chemistry Research. 47 (2008) 7019-7026.

[28] D.D. Do, Adsorption analysis: Equilibria and kinetics, Series on Chemical Engineering, Vol. 2, Imperial College Press, London, 1998.

[29] A.V. Kiselev, Vapor adsorption on zeolites considered as crystalline species adsorbents, Molecular Sieve Zeolites-II, ACS series. 102 (1971) 37-68.

[30] R.M. Barrer, Sorption in porous crystals: equilibria and their interpretation, Journal of Chemical Technology and Biotechnology. 31 (1981) 71-85.

[31] S.M. Taqvi, M.D. LeVan, Virial description of two-component adsorption on homogeneous and heterogeneous surfaces, Industrial and Engineering Chemistry Research. 36 (1997) 2197-2206.

[32] J.M. Prausnitz, R.N. Lichtenthaler, E.G. De Azevedo, Molecular thermodynamics of fluid-phase equilibria, Prentice Hall, Englewood Cliffs, NJ, 1996.

[33] T. Nitta, T. Shigetomi, M. Kuro-Oka, T. Katayama, An adsorption isotherm of multi-site occupancy model for homogeneous surface, Journal of Chemical Engineering of Japan. 17 (1984) 39-45.

[34] C.A. Grande, A.E. Rodrigues, Adsorption kinetics of propane and propylene in zeolite 4A, Chemical Engineering Research and Design. 82 (2004) 1604-1612.

[35] J.A.C. Silva, A.E. Rodrigues, Multisite Langmuir model applied to the interpretation of sorption of n-paraffins in 5A zeolite, Industrial and Engineering Chemistry Research. 38 (1999) 2434-2438.

[36] C.A. Grande, A.E. Rodrigues, Propane/propylene separation by pressure swing adsorption using zeolite 4A, Industrial and Engineering Chemistry Research. 44 (2005) 8815-8829.

[37] S. Sircar, Influence of adsorbate size and adsorbent heterogeneity on IAST, AIChE Journal. 41 (1995) 1135-1145.

[38] C.A. Grande, Propane/propylene separation by pressure swing adsorption, Ph.D. Dissertation, University of Porto, Porto, Portugal, 2005.

[39] S.S. Morgan, A comparison of simplex method algorithms, Ms Thesis, University of Florida, Florida, U.S.A., 1997.

[40] A. Malek, S. Farooq, Comparison of isotherm models for hydrocarbon adsorption on activated carbon, AIChE Journal. 42 (1996) 3191-3201.

[41] O. Talu, Needs, status, techniques and problems with binary gas adsorption experiments, Advances in Colloid and Interface Sience. 76-77 (1998) 227-269.

[42] J. Yang, C.-H. Lee, Adsorption dynamics of a layred bed PSA for H_2 recovery from coke oven gas, AIChE Journal. 44 (1998) 1325-1334.

[43] J.A. Ritter, R.T. Yang, Equilibrium adsorption of multicomponent gas mixtures at elevated pressures, Industrial and Engineering Chemistry Research. 26 (1987) 1679-1686.

[44] R.V. Siriwardane, M.-S. Shen, E.P. Fisher, J.A. Poston, Adsorption of CO_2 on molecular sieves and activated carbon, Energy & Fuels. 15 (2001) 279-284.

[45] B.-U. Choi, D.-K. Choi, Y.-W. Lee, B.-K. Lee, Adsorption equilibria of methane, ethane, ethylene, nitrogen and hydrogen onto activated carbon, Journal of Chemical and Engineering Data. 48 (2003) 603-607.

[46] R.V. Siriwardane, M.-S. Shen, E.P. Fisher, Adsorption of CO_2 on zeolites at moderate temperature, Energy & Fuels. 19 (2005) 1153-1159.

[47] S. Sircar, T.C. Golden, M.B. Rao, Activated carbon for gas separation and storage, Carbon. 34 (1996) 1-12.

3.

Adsorption kinetics of pure gases on commercial adsorbents[†]

3.1 Introduction

PSA is a dynamic separation process and thus it is important to measure the velocity of diffusion of the gases in the porous structure of the adsorbent. In several cases, the resistance to diffusion is so important that the PSA is kinetically controlled [1-2].

The kinetic properties of pure compounds in the adsorbent materials used in the separation unit are important information to acquire for the complete PSA process design. In this chapter, experimental data of carbon dioxide, hydrogen, methane, carbon monoxide, nitrogen and water on several commercial materials are presented. The adsorbent materials studied were the same analysed in chapter 2: the activated carbons R2030 (Norit, Holland), ACM-3mm (CECA, France) and HY2SEPS-AC and the zeolite HY2SEPS-ZEO. Note that activated carbon HY2SEPS-AC and zeolite HY2SEPS-ZEO were provided by an industrial partner within the framework of the European Project HY2SEPS [3]. Due to a confidential agreement with that partner, it is not

[†] The content of this chapter is part of the following articles:

C.A. Grande, F.V.S. Lopes, A.M. Ribeiro, J.M. Loureiro, A.E. Rodrigues, Adsorption of off-gases from steam methane reforming (H_2, CO_2, CH_4, CO and N_2) on activated carbon, Separation Science and Technology. 43 (2008) 1338-1364.

F.V.S. Lopes, C.A. Grande, A.M. Ribeiro, J.M. Loureiro, O. Evaggelos, V. Nikolakis, A.E. Rodrigues, Adsorption of H_2, CO_2, CH_4, CO, N_2 and H_2O in activated carbon and zeolite for hydrogen production, Separation Science and Technology. 44 (2009) 1045-1073.

possible to provide more detailed information about the structure of the adsorbent. Adsorption kinetics parameters of each gas were studied within the temperature range 303-343 K. Initially, the measurements of the diffusion coefficients of carbon dioxide, methane and carbon monoxide in the activated carbon R2030 were performed through zero length column (ZLC) technique. For the same adsorbent, also pulse experiments of methane, carbon monoxide and hydrogen were made as well as diluted breakthrough curves of carbon dioxide. For activated carbon ACM-3mm, ZLC experiments of carbon dioxide at 303, 323 and 343 K were performed. On the other hand, for the activated carbon HY2SEPS-AC and for the zeolite HY2SEPS-ZEO, the individual diffusivities of CO_2, H_2, CH_4, CO and N_2 were only estimated by measurements of breakthrough curves at the same temperatures (303, 323 and 343 K). Breakthrough experiments of water vapour were reported for the activated carbons R2030 and HY2SEPS-AC at 303 K employing a high relative humidity.

3.2 Experimental

Several techniques to measure the diffusion process were employed in this work to measure diffusion through adsorbent particles: zero length column [4-6], uptake curves [7-8] and perturbation chromatography (either pulse or step changes).

3.2.1 Zero length column (ZLC)

The ZLC experimental set-up employed in the measurements of adsorption kinetic properties of carbon dioxide, methane and carbon monoxide on different adsorbents (activated carbons R2030 and ACM-3mm) was build within the course of this thesis. The most important part of the system was the gas chromatograph (Varian GC CP-3800, Holland), shown in Figure 3.1. The adsorbent was placed in the ZLC cell mounted inside the GC, offering the possibility to perform experiments up to 673 K. The outlet stream of the ZLC cell exited directly to the TCD (thermal conductivity detector) where the concentration of the gas was measured. Although a FID (flame ionization detector) was installed in the unit, it was not employed in the determination of the adsorption kinetic parameters. Prior to the ZLC cell there was a multiport valve (Figure 3.1) to switch the inlet stream: mixture (helium + adsorbate) for saturation and pure helium for desorption. Following the equilibration step (saturation) the run was started by switching to a pure helium stream (at time zero). The concentration of the adsorbate specie is then followed continuously for a sufficiently long period (long time response) to ensure complete desorption of the sample. All connections were 1/16” and also the multiport valve was inside the gas chromatograph (GC) to



Figure 3.1: a) Varian gas chromatograph (Varian, Holland); b) Multiport valve and injector connected to the gas chromatograph.

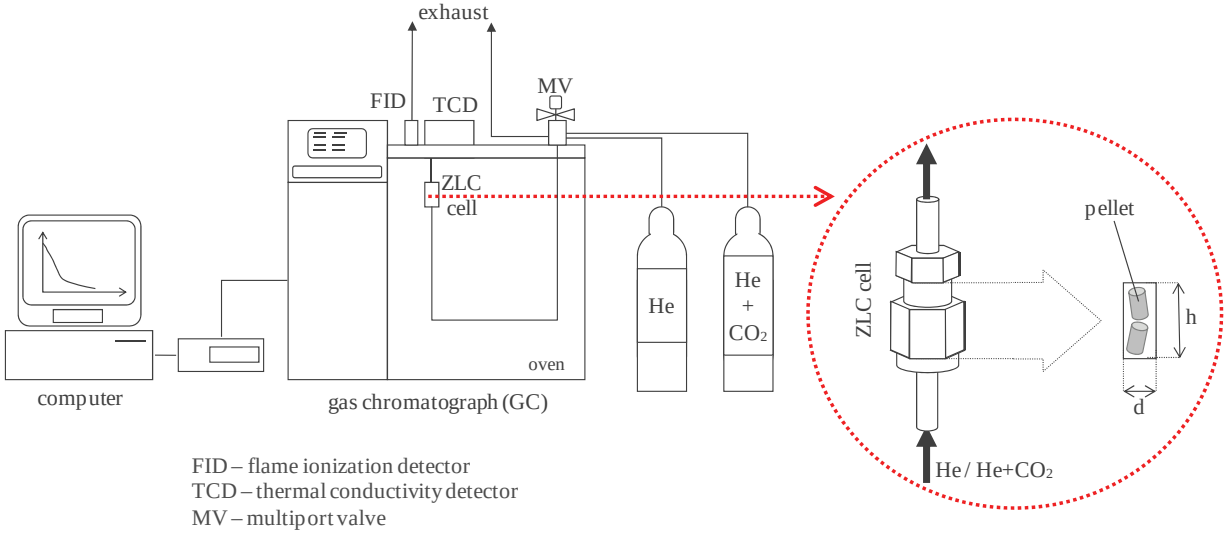


Figure 3.2: Zero length column (ZLC) experimental set-up with ZCL cell geometry description.

reduce dead volumes. All data (gas concentration histories) were recorded in a computer. The scheme of the system is shown in Figure 3.2.

ZLC experiments of carbon dioxide, methane and carbon monoxide in activated carbon R2030 were performed at 303, 323 and 343 K. For measurements of carbon dioxide, two different flow rates were employed: 2.42×10^{-7} and 6.25×10^{-7} m^3 s^{-1} (both measured at 298 K and 1 bar). The measurements with methane and carbon monoxide were performed with the lower flow rate (2.42×10^{-7} m^3 s^{-1}, measured at 298 K and 1 bar). Due to the toxicity of carbon monoxide only a set of experiments using long extrudates with the lower flow rate were performed. After passing the TCD detector, the mixture containing CH_4 and CO was burned in the FID to convert to CO_2

avoiding emissions of these two gases to the laboratory environment. In all experiments, the mixture helium + adsorbate employed for saturation had 0.5% of the adsorbate diluted in helium. A small quantity of the gas was diluted with helium in order to ensure that measurements are carried out in the linear (Henry) zone of the adsorption isotherm. Furthermore, by using diluted mixtures, it is possible to reduce velocity variations within the column and operate under isothermal conditions. To activate the adsorbents, a flow of helium of 6.25×10^{-7} m^3 s^{-1} (measured at 298 K and 1 bar) at 423 K was used overnight. The heating rate to reach this temperature was 1 K min^{-1}. All gases were provided by Air Liquide: carbon dioxide N24, methane N35, carbon monoxide N35 and helium N50 (purities greater than 99.4, 99.95, 99.95 and 99.999 %, respectively).

To prepare a diluted mixture (e.g. carbon dioxide balanced in helium), a mixture bottle B20 was used (Figure 3.3). Using a vacuum pump, the gas that was inside the bottle was removed. Helium was used to "clean" the remaining impurities inside the bottle. Connecting a sampling tank (Figure 3.3) to the CO_2 line (with purity greater than 99.4%), the carbon dioxide was inserted and closed in the sampling tank. Then, connected to the mixture bottle and passing helium through the structure, the sampling tank was opened and the carbon dioxide introduced. The bottle was filled up with helium (99.999% of purity) until the desired concentration. As a result, it is possible to adjust the amount of CO_2 (and other gases) to 0.5% balanced in He. An equivalent procedure was repeated for CH_4, CO and N_2.

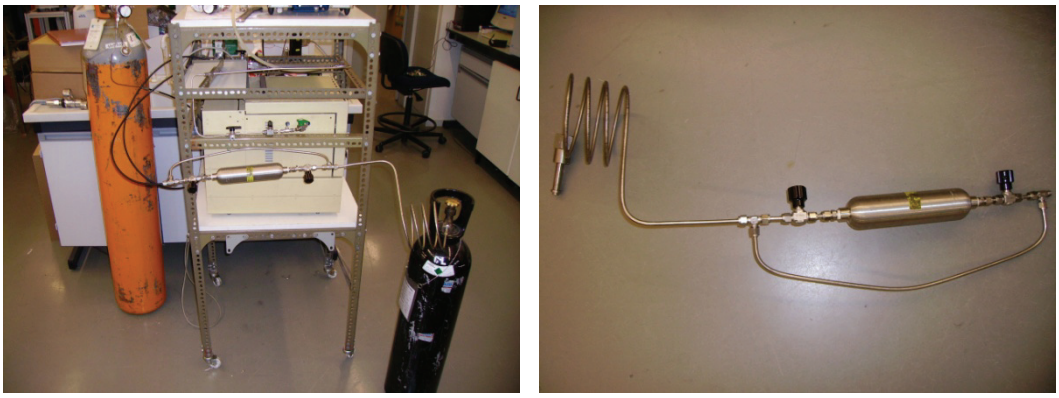


Figure 3.3: a) Gas mixture bottle set-up; b) Sampling tank to prepare gas mixtures

Experiments employing H_2 diluted in helium (considered as inert gas) showed that diffusion of H_2 is extremely fast to be measured by this technique: desorption curve approach equilibrium decay enhancing small oscillations in the flow rate and in the TCD signal when the streams were switched. Thus, the hydrogen diffusivity could not be measured in a reliable way by

ZLC technique. As a way to provide a diffusivity parameter of H_2 diffusion, it was measured the response of a H_2 pulse in a packed column.

3.2.2 Perturbation chromatography methods (pulses and breakthrough curves)

Activated carbons are porous solids with a wide pore size distribution. In ZLC experiments analyzed using the long time response, only the resistance in the smaller micropores will be accounted and then results of ZLC and pulses or breakthrough curves may give large differences [9]. For this reason perturbation chromatography methods were also considered [10].

Since it is important to provide a diffusivity parameter of H_2 diffusion, the response to a pulse of pure hydrogen on activated carbon R2030 was measured at 1 bar and 303 K. The experimental set-up employed in the pulse experiments was the same as for ZLC experiments (described in the previous section 3.2.1), where the ZLC cell was replaced by a much larger column containing the adsorbent. In the pulse experiments, the gas was injected into the inert gas stream in the injector very close to the column with a gas-tight syringe (see Figure 3.4), instead of using the multiport valve to switch to the gas mixture bottle. The experiments were performed with a volume of 5.0×10^{-7} m^3 of H_2 injected in the column and the reproducibility was tested. For comparison purposes with the ZLC experiments, also the responses to pulses of pure methane and carbon monoxide on activated carbon R2030 were measured at 303, 323 and 343 K. According to the higher sensitivity of the FID, very small amounts of CH_4 for pulse experiments were employed.

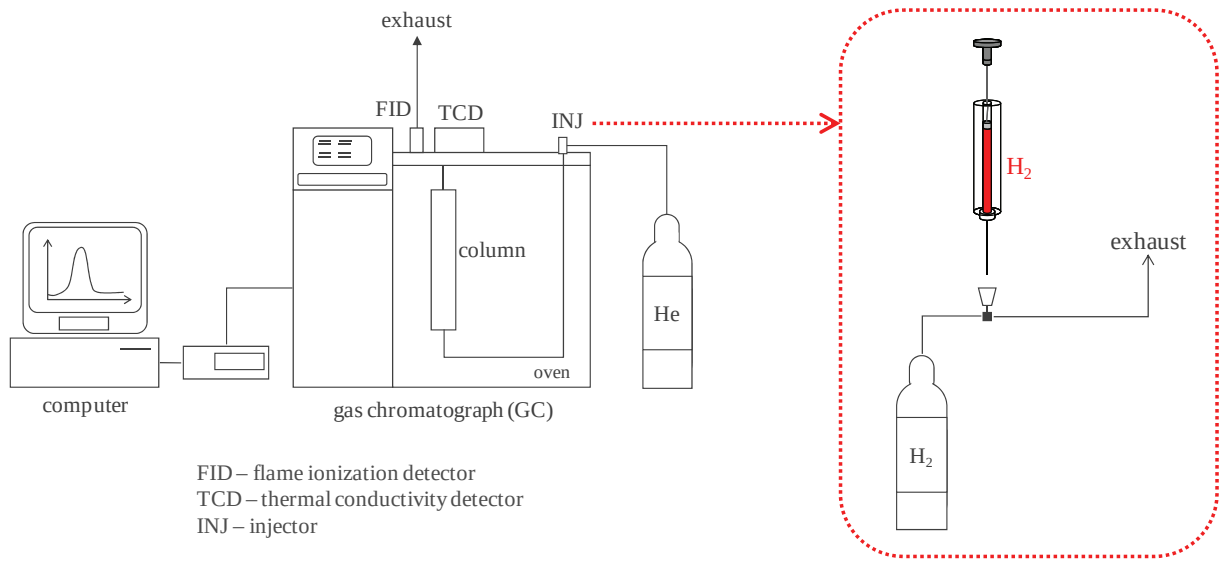


Figure 3.4: Pulse experimental set-up and the gas sample collection in a gas-tight syringe.

The experiments were performed with volumes of 1.0×10^{-8} m^3 of CH_4 and 1.0×10^{-8} m^3 of CO, respectively. Diluted concentrations of these gases were used to measure the diffusivities in the linear region of the isotherm. Note that the column used for H_2 experiments had to be larger to have reliable data of adsorption kinetics since hydrogen is a gas with little adsorption capacity at low partial pressures (together with very fast kinetics). The activation of the R2030 sample was performed heating at 1 K min^{-1} until 423 K and left overnight, under a continuous flow of helium (6.25×10^{-7} m^3 s^{-1}, measured at 298 K and 1 bar).

Diluted breakthrough curves of carbon dioxide (0.5% of CO_2 balanced in He) on activated carbon R2030 were measured at 303, 323 and 343 K. The experimental set-up employed in the breakthrough experiments was the same as for ZLC experiments, previously described in section 3.2.1 (the ZLC cell was replaced by a much larger column). Figure 3.5 shows the column in the gas chromatograph and the mixture bottle connected to the multiport valve. The breakthrough experimental set-up and the column geometry description are shown in Figure 3.6. The TCD was employed to measure the concentration of CO_2. Note that, a small quantity of CO_2 diluted with helium was used due to the same reasons explained in section 3.2.1.

The adsorption kinetics of water in activated carbon R2030 was evaluated by Ribeiro *et al.* (2008) [11] performing one breakthrough experiment. The breakthrough experimental set-up used and its scheme are shown in Figure 3.7 and Figure 3.8, respectively. The experiments were performed using a stainless steel column, containing the adsorbent sample, placed inside a convective oven to control the adsorption temperature. As in the case of the equilibrium determinations (Chapter 2), the residual humidity adsorbed during the setup assembling was removed by flowing dry helium at 453 K through the column overnight, and the adsorbate streams

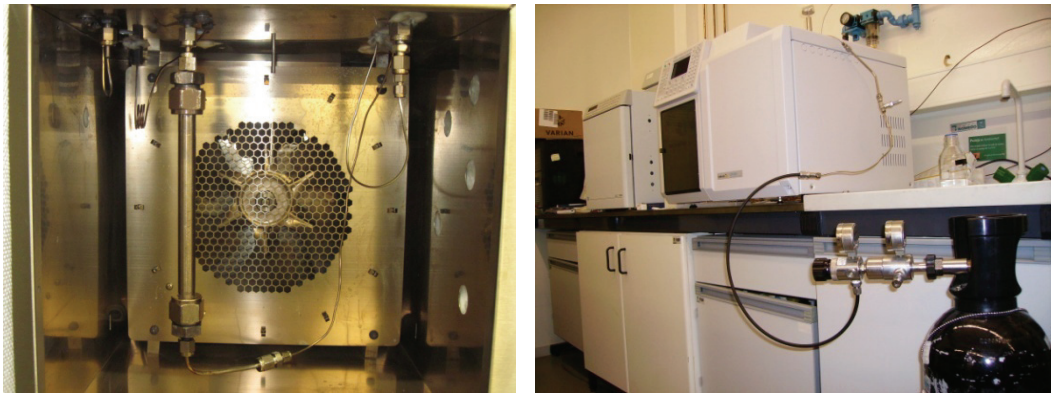


Figure 3.5: a) Column in the gas chromatograph (left); b) Mixture bottle connected to the multiport valve (right).

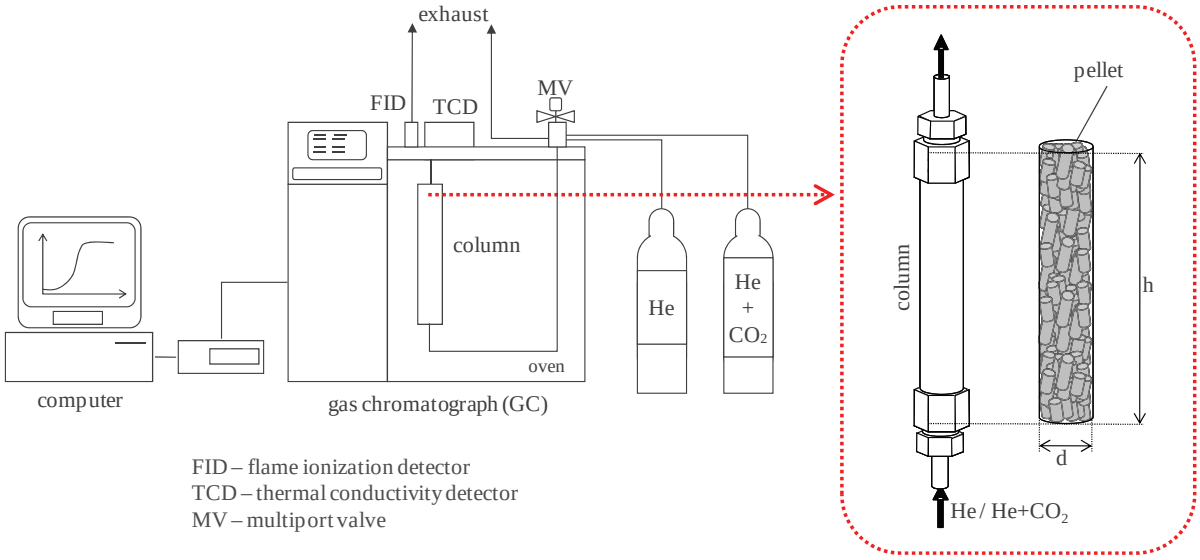


Figure 3.6: Diluted breakthrough experimental set-up with the column geometry description.



Figure 3.7: Breakthrough experimental set-up with generation of adsorbate vapours by flowing helium through glass bubblers filled with water.

entering the bed were also generated by adjusting a desired ratio between a saturated helium stream and a dry helium stream [11]. All the tubes were covered by heating tape kept 2-4 K above the experimental temperature to avoid condensation. The water compositions of the inlet and outlet gases were measured respectively by a thermo-hygrometer model T605-H1 (Testo, Germany) and a humidity sensor model SHT71 (Sensirion, Switzerland). Notice should be given to the fact that for activated carbon R2030, a high relative humidity was employed as this adsorbent is placed at the inlet end of the PSA process beds and contacts with high water vapour concentrations.

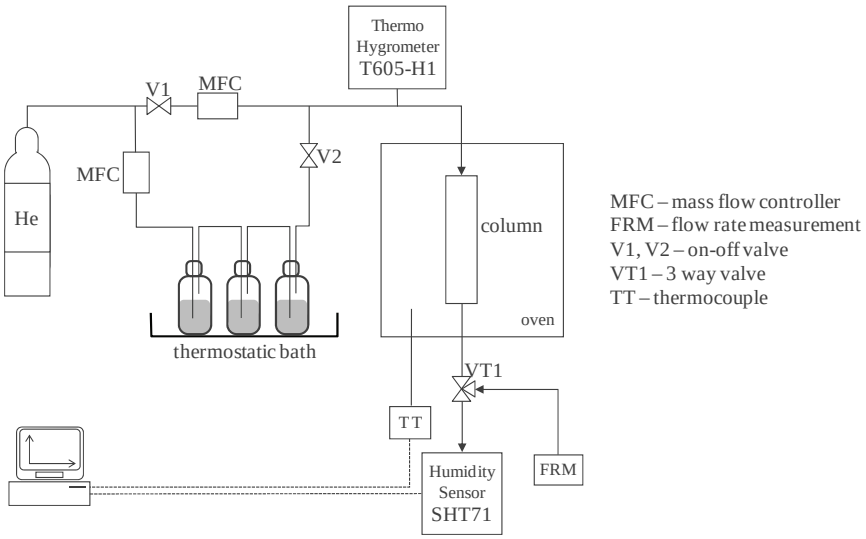


Figure 3.8: Schematic diagram of the experimental set-up for water vapour breakthrough measurements. Labelling: V1, V2, on-off valves; VT1, 3 port valve; VP, vacuum pump; PT, pressure transducer; TT, thermocouple.

For the activated carbon HY2SEPS-AC and zeolite HY2SEPS-ZEO, the individual diffusivities of carbon dioxide, hydrogen, methane, carbon monoxide and nitrogen were estimated by measurements of breakthrough curves. The TCD was employed to measure the concentration of CO_2, CO, N_2 and H_2, while the concentration of methane was detected by FID. The measurements with carbon dioxide, methane, carbon monoxide and nitrogen were performed with different flow rates measured at 298 K and 1 bar: 3.87×10^{-7} and 1.17×10^{-6} $m^3 s^{-1}$ for CO_2 experiments on HY2SEPS-AC and on HY2SEPS-ZEO, respectively; 2.42×10^{-7} $m^3 s^{-1}$ for CH_4, CO, N_2 and H_2 on both adsorbents. Due to the toxicity of carbon monoxide only a set of experiments was performed with this gas. The activation of the samples was performed heating at 1 K min^{-1} until 423 K (HY2SEPS-AC) or 593 K (HY2SEPS-ZEO) and left overnight, under a continuous flow of helium of 2.42×10^{-7} $m^3 s^{-1}$ (measured at 298 K and 1 bar). Note that, in the case of hydrogen, breakthroughs were performed with the pure gas while for CO_2, CH_4, CO and N_2, only a content of 0.5% of adsorbate diluted in helium was used. The small quantity of the gas (CO_2, CH_4, CO and N_2) diluted with helium was due to the same reasons explained in section 3.2.1. However, in the case of hydrogen, a higher concentration was employed reason why velocity variations were observed. Higher concentration was used because it was not possible to measure accurately at low partial pressure of H_2: the signal detected by TCD as well as the amount adsorbed of this gas were too low. Note that for hydrogen, the isotherms are linear within the entire pressure range employed for the measurements. The set-up employed for H_2 breakthrough curves was the same as for diluted

breakthrough runs mentioned before, where the mixture bottle was replaced by a pure hydrogen N60 bottle (purity greater than 99.9999%). The adsorption kinetics of water was also evaluated for HY2SEPS-AC by performing one breakthrough experiment. The experimental set-up used was the same for the measurement of H_2O breakthrough with activated carbon R2030. Again, a high relative humidity (89%) was employed since this adsorbent is placed at the inlet end of the PSA process beds and contacts with high water vapour concentrations.

Air Liquide provided all gases used: hydrogen N60, carbon dioxide N24, methane N35, carbon monoxide N35, nitrogen N45 and helium N50 (purities greater than 99.9999, 99.4, 99.95, 99.95, 99.995% and 99.999 %, respectively).

3.3 Theoretical

When temperature, partial pressure or any other equilibrium condition is changed, the molecules move to a new equilibrium state. After subjected to the induced net driving force, the gas phase molecules from the bulk phase start to move to inside the adsorbent. However, the molecules could be affected by several resistances from outside the particles (film mass transfer resistance [8]) to resistances inside the porous particles. When the molecules penetrate the structure of the adsorbent, they diffuse into the larger pores finding an ideal location to adsorb. This phenomenon is called macropore diffusion. Some adsorbents can have bidisperse pore structures: (1) micropores and macropores in the case of carbon materials; (2) crystals and macropores for the zeolitic materials. The definition of micropore or macropore in a carbon material corresponds to the size of the pore in the structure; in a zeolitic adsorbent, the macropores are the surrounding space between the crystals [8, 12]. Therefore, most of the molecules have to diffuse from the bulk gas phase to the adsorbent sites in the macropore and also to the adsorption sites in the zeolite crystals or microporous network (crystal or micropore diffusion) [8]. When the kinetic diameter of the molecules is close to the size of the micropore, the diffusion process can be very slow [8]. The rate of diffusion may also be very important in the design of an adsorption process.

3.3.1 Zero length column (ZLC)

The ZLC is a powerful technique for measurements of diffusivities of pure gases in porous solids [4]. The procedure is to saturate a small amount of adsorbent with a dilute mixture of adsorbate. Then the inlet is switched to an inert stream to clean the adsorbent. Plotting the desorption curve in a semi-logarithmic scale is possible to determine the diffusion coefficients

from the slope of the curve. This technique is not accurate to measure very small diffusivities because of serious difficulties to determine the slope of the curve [9]. Also when the diffusion is very fast, the inaccuracy of the technique is because the curve approximates to the equilibrium response [13].

In ZLC experiments, large flow rates are employed to ensure that film mass transfer resistance is minimized. The mass transfer control in bidisperse adsorbents is limited by macropore or micropore/crystal diffusion. Adsorbate concentrations employed in the experiments are low enough to describe adsorption equilibrium by the Henry law (linear isotherm) and to minimize heat generation ensuring isothermal operation. With these conditions, analytical expressions for the determination of diffusion parameters can be obtained. A general equation for infinite slabs, infinite cylinders and spheres is [13-15]:

$$\frac{C}{C_0} = 2L^* \sum_{j=1}^{\infty} \frac{\exp\left(-D_{ap}\beta_j^2 t / \ell^2\right)}{\beta_j^2 + L^*\left(L^* + 1 - n\right)} \tag{3.1}$$

where n = 0, 1 and 2 for slabs, cylinders and spheres respectively, C and C_0 are the instantaneous and initial gas phase concentration respectively, D_{ap} is the apparent diffusivity and K_{eq} is the dimensionless equilibrium constant, ℓ is the representative spatial dimension of the cell (radius for infinite cylinder and sphere; half length for infinite slab) and L^* is the ZLC parameter described by:

$$L^* = \frac{Q_p \ell^2}{(n+1) K^* V_s D_{ap}} \tag{3.2}$$

where Q_p is the purge flow rate, $K^*=\varepsilon_p+(1-\varepsilon_p)K_{eq}$ and V_s is the volume of adsorbent in the cell. The roots β_j are dependent of the adsorbent shape [14-15]:

$$\begin{aligned} &\beta_j J_1(\beta_j) - L^* J_0(\beta_j) = 0 && \text{for infinite cylinders} \\ &\beta_j \tan(\beta_j) - L^* = 0 && \text{for infinite slabs} \\ &\beta_j \cot(\beta_j) + L^* - 1 = 0 && \text{for spheres} \end{aligned} \tag{3.3}$$

where J_0 and J_1 are Bessel functions of first kind of order zero and one respectively.

For the case of micropore control, the apparent diffusivity in equation (3.1) has to be replaced by the crystal or micropore diffusivity (D_c) and the spatial coordinate is with respect to the crystal.

The long time response (LTR) is:

$$\ln\left(\frac{C}{C_0}\right) \cong \ln\left(\frac{2L^*}{\beta_1^2 + L^*\left(L^* + 1 - n\right)}\right) - \frac{\beta_1^2 D_{ap} t}{\ell^2} \tag{3.4}$$

Plotting equation (3.4) as $\ln(C/C_0)$ *versus* time a straight line is observed with slope

$-\beta_1^2 D_{ap}/\ell^2$ that can be employed for direct determination of the diffusivity coefficient. The approximation $\beta = \pi$ is valid for spherical particles and large values of the parameter L^*, although the ratio C/C_0 is still a function of L^* (which includes the purge flow rate) [15].

As mentioned before, the experiments were done on the Henry law region and thus the apparent diffusivity (D_{ap}) is related to the pore diffusivity (D_p) according to:

$$D_{ap} = \frac{\varepsilon_p D_p}{\varepsilon_p + (1-\varepsilon_p) K_{eq}} \tag{3.5}$$

where ε_p is the porosity of the particle and K_{eq} is the dimensionless equilibrium constant. The pore diffusivity (D_p) is related to the molecular diffusivity (D_m) and to the Knudsen diffusivity (D_k) by the Bosanquet equation:

$$\frac{1}{D_p} = \tau_p \left(\frac{1}{D_m} + \frac{1}{D_k} \right) \tag{3.6}$$

where τ_p is the pore tortuosity. The Knudsen diffusivity (D_k in $m^2\ s^{-1}$) is calculated by:

$$D_k = 97.0\, r_p \sqrt{\frac{T}{M_W}} \tag{3.7}$$

where r_p is the mean pore radius in meters, T is the pellet temperature in K and M_W is the molecular weight of the adsorbate in $g\ mol^{-1}$. The molecular diffusivity (D_m) for the mixture was approximated using the Wilke correlation (molecular diffusion coefficients) [16]:

$$D_m = \frac{1-y_i}{\sum_{\substack{j=1 \\ j \neq i}}^{n} \frac{y_i}{D_{ij}}} \tag{3.8}$$

where y_i is the molar fraction of component i and D_{ij} is the binary molecular diffusivity calculated (D_{ij} in $m^2\ s^{-1}$) with the Chapman-Enskog equation [17]:

$$D_{ij} = \frac{2.66 \times 10^{-2} T^{3/2}}{P\, M_{ij}^{1/2} \sigma_{ij}^2 \Omega_{D_{ij}}} \tag{3.9}$$

where T is the temperature in K, P is the pressure in Pa. M_{ij} is a function of the molecular weights of components i and j (M_i and M_j in $g\ mol^{-1}$) defined by:

$$M_{ij} = 2 \left[\frac{1}{M_i} + \frac{1}{M_j} \right]^{-1} \tag{3.10}$$

The Lennard-Jones parameter σ_{ij} (collision molecular diameter in Å) is defined by:

$$\sigma_{ij} = \frac{1}{2}\left(\sigma_i + \sigma_j\right) \tag{3.11}$$

The collision integral ($\Omega_{D_{ij}}$) is a dimensionless function of the temperature and the Lennard-Jones parameter ε_{ij}/k (maximum energy in K of interaction between molecular pairs). The following correlation was used for the calculation of the collision integral [17]:

$$\Omega_{D_{ij}} = \frac{A_1}{\omega^{A_5}} + \frac{A_2}{\exp\left(A_6\omega\right)} + \frac{A_3}{\exp\left(A_7\omega\right)} + \frac{A_4}{\exp\left(A_8\omega\right)}$$
$$A_1 = 1.06036 \quad A_2 = 0.193 \quad A_3 = 1.03587 \quad A_4 = 1.76474 \tag{3.12}$$
$$A_5 = 0.1561 \quad A_6 = 0.47635 \quad A_7 = 1.52996 \quad A_8 = 3.89411$$

with:

$$\omega = \frac{kT}{\varepsilon_{ij}} \quad , \quad \varepsilon_{ij} = \sqrt{\varepsilon_i\,\varepsilon_j} \tag{3.13}$$

where k is the Boltzmann's constant and T is the temperature in K.

The molecular weight of each compound and also the Lennard-Jones parameters σ_i and ε_i/k for each gas molecule are described in Table 3.1 [17].

Table 3.1: Molecular weight and Lennard-Jones parameters of each compound [17].

Species	M_i (g mol^{-1})	σ_i (Å)	ε_i/k (K)
He	4.003	2.576	10.2
H_2	2.016	2.915	38.0
CO_2	44.010	3.996	190
CH_4	16.043	3.780	154
CO	28.010	3.590	110
N_2	28.014	3.667	99.8
H_2O	18.015	2.641	809

3.3.2 Perturbation chromatography methods (pulses or breakthrough curves)

An alternative technique to estimate the kinetic parameters of the pure gases, that was also considered, is the packed column response to a pulse or a step function (breakthrough). The necessary equations are reported below, as well as equations to determine mass transfer parameters like axial dispersion and film mass transfer coefficients [8, 16-17].

The analyses of the pulse experiments were performed employing the moments theory [8], where the first moment (μ_1) and the variance (σ^2) are calculated from the experimental data by:

$$\mu_1 \equiv \frac{\int_0^\infty C\ t\ dt}{\int_0^\infty C\ dt} \tag{3.14}$$

$$\sigma^2 = \frac{\int_0^\infty C\left(t-\mu_1\right)^2 dt}{\int_0^\infty C\ dt} \tag{3.15}$$

For the diluted experiments carried out in this work, the first moment can also be calculated using the Henry constant (K_H) obtained through the isotherm. For that, the following equation is applied:

$$\mu_1 = \frac{L}{u_i}\left(1+\left(\frac{1-\varepsilon}{\varepsilon}\right)K_H \rho_p R_g T\right) \tag{3.16}$$

where L is the bed length, u_i is the interstitial velocity, ε is the porosity of the bed, ρ_g is the density of the gas phase, R_g is the universal gas constant and T is the temperature. The first moment is also known as stoichiometric time.

The ratio of the variance and two times the first moment square ($\sigma^2/2{\mu_1}^2$) of a pulse can be related with the sum of all diffusional resistances through the simplified equation (3.17) provided that $K_H >> \varepsilon_p$, which is usually true [8]:

$$\frac{\sigma^2}{2\mu_1^2} = \frac{D_{ax}}{u_i L} + \left(\frac{u_i}{L}\right)\left(\frac{\varepsilon}{1-\varepsilon}\right)\left(\frac{R_p}{2k_f} + \frac{R_p^2}{\Omega_p \varepsilon_p D_p} + \frac{r_c^2}{\Omega_c K_H \rho_p R_g T\, D_c}\right)\left(1+\frac{\varepsilon_p}{\left(1-\varepsilon_p\right)K_H \rho_p R_g T}\right)^{-2} \tag{3.17}$$

where Ω_p and Ω_c are the linear driving force (LDF) factors ($\Omega=(k_s+1)(k_s+3)$) of the particle and of the micropore or crystal, respectively. The geometrical factor of the particle or of the micropore or crystal (k_s) is 0 for slabs, 1 for cylinders or 2 for spheres. For strongly adsorbed species $\varepsilon_p/(1-\varepsilon_p)K_H$ is small and can be neglected. The axial dispersion (D_{ax}) and the film mass transfer coefficients (k_f) were calculated according to the following equations:

$$D_{ax} = \left(0.45+0.55\varepsilon\right)D_m + 0.35 R_p u_i \tag{3.18}$$

$$Sh = 2.0 + 1.1 Re^{0.6} Sc^{1/3} \tag{3.19}$$

where the dimensionless numbers (*Sh* is the Sherwood number, *Re* is the Reynolds number and *Sc* is the Schmidt number) are defined by:

$$Sh = \frac{2R_p k_f}{D_m} \tag{3.20}$$

$$\mathrm{Re} = \frac{2\rho_g u_0 R_p}{\mu} \tag{3.21}$$

$$Sc = \frac{\mu}{\rho_g D_m} \tag{3.22}$$

To calculate the viscosity of the gas mixture (μ), the multicomponent extension of the Chapman-Enskog theory can be used. Alternatively, the following semi-empirical equation can be applied [17]:

$$\mu = \sum_{i=1}^{n} \frac{y_i \mu_i}{\sum_{j=1}^{n} y_j \Phi_{ij}} \tag{3.23}$$

where y_i is the mole fraction of component i and μ_i is the viscosity of the component i defined in terms of the Lennard-Jones parameters by:

$$\mu_i = 2.669 \times 10^{-6} \frac{(M_i T)^{1/2}}{\sigma_i^2 \Omega_{\mu_i}} \tag{3.24}$$

where M_i is the molecular weight of components i in mol g^{-1} (see Table 3.1 [17]), T is the temperature in K and σ_i is the Lennard-Jones parameter corresponding to the collision molecular diameter (see Table 3.1 [17]). For the calculation of the dimensionless function of temperature and the Lennard-Jones parameter ε_{ij}/k, i.e., the collision integral of the viscosity ($\Omega_{\mu i}$), the following correlation was used [17]:

$$\begin{aligned} &\Omega_{\mu_i} = \frac{A_1}{\omega^{A_4}} + \frac{A_2}{\exp(A_5 \omega)} + \frac{A_3}{\exp(A_6 \omega)} \\ &A_1 = 1.16145 \quad A_2 = 0.52487 \quad A_3 = 2.16178 \\ &A_4 = 0.14874 \quad A_5 = 0.7732 \quad A_6 = 2.43787 \end{aligned} \tag{3.25}$$

with ω and ε_{ij} defined by equation (3.13).

In equation (3.23), the dimensionless quantities Φ_{ij} are:

$$\Phi_{ij} = \frac{1}{\sqrt{8}} \left(1 + \frac{M_i}{M_j}\right)^{-1/2} \left[1 + \left(\frac{\mu_i}{\mu_j}\right)^{1/2} \left(\frac{M_j}{M_i}\right)^{1/4}\right]^2 \tag{3.26}$$

where μ_i and μ_j are the viscosities of pure gases and M_i and M_j are the molecular weights of components i and j, respectively. Bird *et al.* (2002) [17] reported that equation (3.26) has been shown to reproduce measured values of the viscosity of mixtures within an average deviation of about 2%.

As mentioned before, the pore diffusivity (D_p) is related to the molecular diffusivity (D_m) and to the Knudsen diffusivity (D_k) by the Bosanquet equation (3.6). A tortuosity factor had to be assumed for the adsorbents to estimate the pore diffusivity. The Knudsen diffusivity (D_k) and the molecular diffusivity (D_m) are calculated by equations (3.7) and (3.8), respectively. Thus, having all the terms of equation (3.17), the term corresponding to micropore diffusivity (D_c) can be estimated.

The micropore diffusion is an activated process with exponential dependence with temperature according to:

$$\frac{D_c}{r_c^2} = \frac{D_c^0}{r_c^2} \exp\left(-\frac{E_a}{R_g T} \right) \tag{3.27}$$

where D_c^0/r_c^2 is the limiting diffusivity (divided by r_c^2) at infinite temperature and E_a is the activation energy.

To fit the experimental pulse data, the mathematical model described by equations (3.28) to (3.44) was employed [8]. For the pulse experiments, the adsorbate gas sample was inserted in a carrier gas flow of helium (considered as inert gas) through the injector placed in the GC. The velocity was considered constant within the bed, due to the low amount of gas adsorbed when compared to the total amount of gas injected. Besides, it was considered that the bed was packed with a bidisperse adsorbent (composed of macro and micropores or crystals). Thus, macropore and micropore or crystal resistances were considered. A film resistance in the external surface of the adsorbent particles was also considered. Axial dispersed plug flow was assumed. Moreover, isothermal process was considered. The equilibrium isotherm is given by:

$$q_i^* = K_i C_{m,i} \tag{3.28}$$

where q_i^* is the adsorbed phase concentration of component *i* in the micropore or crystal surface, K_i is the equilibrium constant of component *i* and $C_{m,i}$ is the concentration of component *i* in the macropores.

The mass balance in a differential element of the column for the component *i* can be described as:

$$\frac{\partial}{\partial z}\left(\varepsilon D_{ax} C_{g,T} \frac{\partial y_i}{\partial z} \right) - \frac{\partial}{\partial z}\left(u_0 C_{g,i} \right) - \varepsilon \frac{\partial C_{g,i}}{\partial t} - (1-\varepsilon)\rho_p \frac{\partial \langle \bar{q}_i \rangle}{\partial t} = 0 \tag{3.29}$$

with initial conditions:

$$\begin{aligned} &y_i = 0 \quad \text{for } i \neq inert \quad ; \quad y_{inert} = 1 \\ &C_{g,i} = 0 \quad \text{for } i \neq inert \quad ; \quad C_{g,inert} = C_{g,T} \end{aligned} \tag{3.30}$$

For the inert species, the last term in the left hand side of equation (3.29) is zero. The boundary conditions for feed inlet ($z = 0$) and product end ($z = L$), respectively:

$$\begin{aligned} u_{0\,inj} C_{inj,i} &= u_0 C_{g,i} - \varepsilon D_{ax} C_{g,T} \frac{\partial y_i}{\partial z} \quad \text{for} \quad t \in \left[0\,,\, t_{inj}\right] \\ 0 &= u_0 C_{g,i} - \varepsilon D_{ax} C_{g,T} \frac{\partial y_i}{\partial z} \quad \text{for} \quad t \in \left]t_{inj}\,,\, \infty\right[\end{aligned} \tag{3.31}$$

$$\frac{\partial C_{g,i}}{\partial z} = 0 \tag{3.32}$$

where y_i is the molar fraction of component i, $C_{g,i}$ is the molar concentration in the gas phase of component i, $C_{inj,i}$ is the molar concentration in the gas phase of adsorbate i injected, $\langle \overline{q}_i \rangle$ is the particle averaged adsorbed concentration of component i, q_i^* is the adsorbed concentration in equilibrium with $C_{m,i}$, t is the time, t_{inj} is the time of injection of adsorbate, z is the axial coordinate of the bed, ε is the bed porosity, ρ_p density of the adsorbent, D_{ax} is the axial dispersion coefficient, u_0 is the superficial velocity and u_{0inj} is the superficial velocity of the adsorbate injected.

The micropore or crystal averaged adsorbed phase concentration of component i ($\overline{q}_i$) and the particle averaged adsorbed phase concentration of component i ($\langle \overline{q}_i \rangle$) are defined by the following equations:

$$\overline{q}_i = \frac{k_s + 1}{r_c^{k_s+1}} \int_0^{r_c} q_i r^{k_s} dr \tag{3.33}$$

$$\left\langle \overline{q}_i \right\rangle = \frac{k_s + 1}{R_p^{k_s+1}} \int_0^{R_p} \overline{q}_i R^{k_s} dR \tag{3.34}$$

where q_i is the absolute adsorbed phase concentration of component i, r_c is the micropore or crystal radius, r is the radial coordinate of the micropore or crystal, R_p is the radius of the adsorbent particle, R is the radial coordinate of the particle and k_s is the geometrical factor of the particle or of the micropore or crystal (0 - slab; 1 - cylinder; 2 - sphere).

The Fickian description of diffusion in a micropore or crystal for each component is represented by:

$$\frac{\partial q_i}{\partial t} = \frac{1}{r_c^{k_s}} \frac{\partial}{\partial r} \left(D_{c,i} r^{k_s} \frac{\partial q_i}{\partial r} \right) \tag{3.35}$$

with initial condition:

$$q_i = 0 \tag{3.36}$$

and boundary conditions for the pore centre ($r = 0$) and for the pore wall ($r = r_c$), respectively:

$$\frac{\partial q_i}{\partial r} = 0 \quad ; \quad r = 0 \tag{3.37}$$

$$q_i = q_i^* \quad ; \quad r = r_c \tag{3.38}$$

where $D_{c,i}$ is the micropore/crystal diffusivity of component *i*. The adsorption equilibrium at the micropore or crystal surface is described by equation (3.38).

The mass balance in a volume element of the adsorbent particle is represented by:

$$\frac{\partial C_{m,i}}{\partial t} + \rho_p \left(\frac{1-\varepsilon_p}{\varepsilon_p} \right) \frac{\partial \overline{q}_i}{\partial t} = \frac{1}{R_p^{k_s}} \frac{\partial}{\partial R} \left(D_{p,i} R^{k_s} \frac{\partial C_{m,i}}{\partial R} \right) \tag{3.39}$$

with initial condition:

$$C_{m,i} = 0 \quad \text{for } i \neq inert \quad ; \quad C_{m,inert} = C_{g,T} \tag{3.40}$$

and boundary conditions for the centre of the particle ($R = 0$) and for the particle wall ($R = R_p$), respectively:

$$\left. \frac{\partial C_{m,i}}{\partial R} \right|_{R=0} = 0 \tag{3.41}$$

$$\varepsilon_p D_{p,i} \left. \frac{\partial C_{m,i}}{\partial R} \right|_{R=R_p} = k_f \left(C_{g,i} - C_{m,i}\big|_{R=R_p} \right) \tag{3.42}$$

where $C_{m,i}$ is the concentration of component *i* in the macropores, $C_{g,i}$ is the component *i* molar concentration in the gas phase, $\overline{q}_i$ is the micropore or crystal averaged adsorbed phase concentration of component *i*, *t* is the time, *R* is the radial coordinate of the particle, ρ_p density of the adsorbent, ε_p is the particle porosity, R_p is the radius of the adsorbent, $D_{p,i}$ is the macropore diffusivity of component *i* and k_f is the film mass transfer coefficient.

The pressure and the concentration in the gas phase are related by the ideal gas equation. In the macropores, the pressure and the concentration are related by the same ideal gas equation:

$$P_{g,i} = C_{g,i} R_g T \tag{3.43}$$

$$P_{m,i} = C_{m,i} R_g T \tag{3.44}$$

where $P_{g,i}$ and $P_{m,i}$ are the pressure of the adsorbate *i* in the gas phase and in the pores of the adsorbent, respectively, R_g is the universal gas constant and *T* is the temperature.

The numerical solution of the mathematical model described in equations (3.28) to (3.44) was performed by gPROMS (PSE Enterprise, UK) using the orthogonal collocation on finite elements (OCFEM). The number of elements used was 25 with two interior collocation points (third order polynomials) in each element of the adsorption bed. The simulations were performed

with an absolute and relative tolerance of 1×10^{-5}.

Equations (3.14) to (3.27) and also equations (3.6) to (3.13) were employed for the analyses of pulse experiments. For the analyses of the breakthrough experiments, these equations can be employed after calculation of the derivative of the breakthrough curve. The breakthrough experiments used mixtures of 0.5% of adsorbate balanced in helium (inert). Due to the low amount of gas adsorbed when compared to the total amount of gas fed, constant velocity within the bed was assumed. It was also assumed that mass transfer is present in macropore and micropore or crystal resistances (a bidisperse adsorbent composed of macro and micropores or crystals was used to pack the bed) and a film resistance in the external surface of the adsorbent particles. Finally, axial dispersed plug flow and isothermal process was assumed. To fit these breakthrough curves it was employed the mathematical model previously described for the pulse experiments by equations (3.28) to (3.44). Only the boundary conditions for the mass balance in a differential element of the column (equation (3.31)), were changed to (feed inlet ($z = 0$) and product end ($z = L$), respectively):

$$u_{0\,inlet} C_{inlet,i} = u_0 C_{g,i} - \varepsilon D_{ax} C_{g,T} \frac{\partial y_i}{\partial z} \tag{3.45}$$

$$\frac{\partial C_{g,i}}{\partial z} = 0 \tag{3.46}$$

where $C_{g,i}$ is the bulk molar concentration in the gas phase, z is the axial coordinate of the bed, D_{ax} is the axial dispersion coefficient and u_0 is the superficial gas velocity.

Once again, the numerical solution of the mathematical model was performed by gPROMS (PSE Enterprise, UK) using the orthogonal collocation on finite elements (OCFEM). Twenty five elements with two interior collocation points (third order polynomials) in each element of the adsorption bed were used with an absolute and relative tolerance of 1×10^{-5}.

3.4 Adsorption kinetic results

For the design of a PSA unit for hydrogen purification, the transport mechanism and diffusivity parameters of the gases exiting the SMR reactor in different adsorbents were studied. These diffusivity parameters were obtained for pure gases (carbon dioxide, hydrogen, methane, carbon monoxide, nitrogen and water) through the ZLC technique, the response to a pulse and/or breakthrough curves. The adsorbents studied were the activated carbons R2030, ACM-3mm and HY2SEPS-AC and the zeolite HY2SEPS-ZEO.

3.4.1 Activated carbon R2030

Adsorption kinetics of pure carbon dioxide, methane and carbon monoxide in activated carbon R2030 were determined by ZLC experiments. The experimental conditions used in the ZLC measurements of CO_2, CH_4 and CO in R2030 are reported in Table 3.2. The ZLC results in activated carbon R2030 are shown in Figure 3.9 a, b and c for carbon dioxide, methane and carbon monoxide, respectively. For all the gases the experiments were carried at three temperatures (303, 323 and 343 K). Figure 3.9 shows the straight lines in the long time response with the intercept and slope for all temperatures. A summary of the intercepts and slopes of all the experiments of the different gases is shown in Table 3.3.

Table 3.2: Experimental conditions used on the ZLC measurements of CO_2, CH_4 and CO in activated carbon R2030 at 1 bar of total pressure.

Adsorbate	CO_2	CH_4, CO
Adsorbate partial pressure [bar]	0.005	
Mass adsorbent × 10^3 [kg]	0.07445	
Flow rate × 10^7 [m^3 s^{-1}]*	2.42; 6.25	2.42
Temperatures [K]	303, 323, 343	
Cell height × 10^2 [m]	1.65	
Cell volume × 10^7 [m^3]	2.34	
Cell porosity, ε	0.636	
Adsorbent	R2030	
Type	extrudates	
Average pellet diameter × 10^3 [m]	2.90	
Average pellet length × 10^3 [m]	6.45	
Pellet porosity, ε_p	0.600	
Adsorbent density, ρ_p [kg m^{-3}]	874	
Solid density, ρ_s [kg m^{-3}]	2162	

* measured at 298 K and 1 bar

Applying the set of equations (3.1) to (3.8) assuming macropore control, extremely large values of tortuosity were obtained (over 10000) indicating that the control mechanism of diffusion is not within the macropore network. For this reason, the micropore model was applied to determine the diffusivities of the three gases (CO_2, CH_4 and CO).

The micropore diffusivities (divided by r_c^2) of CO_2, CH_4 and CO are reported in Table 3.3.

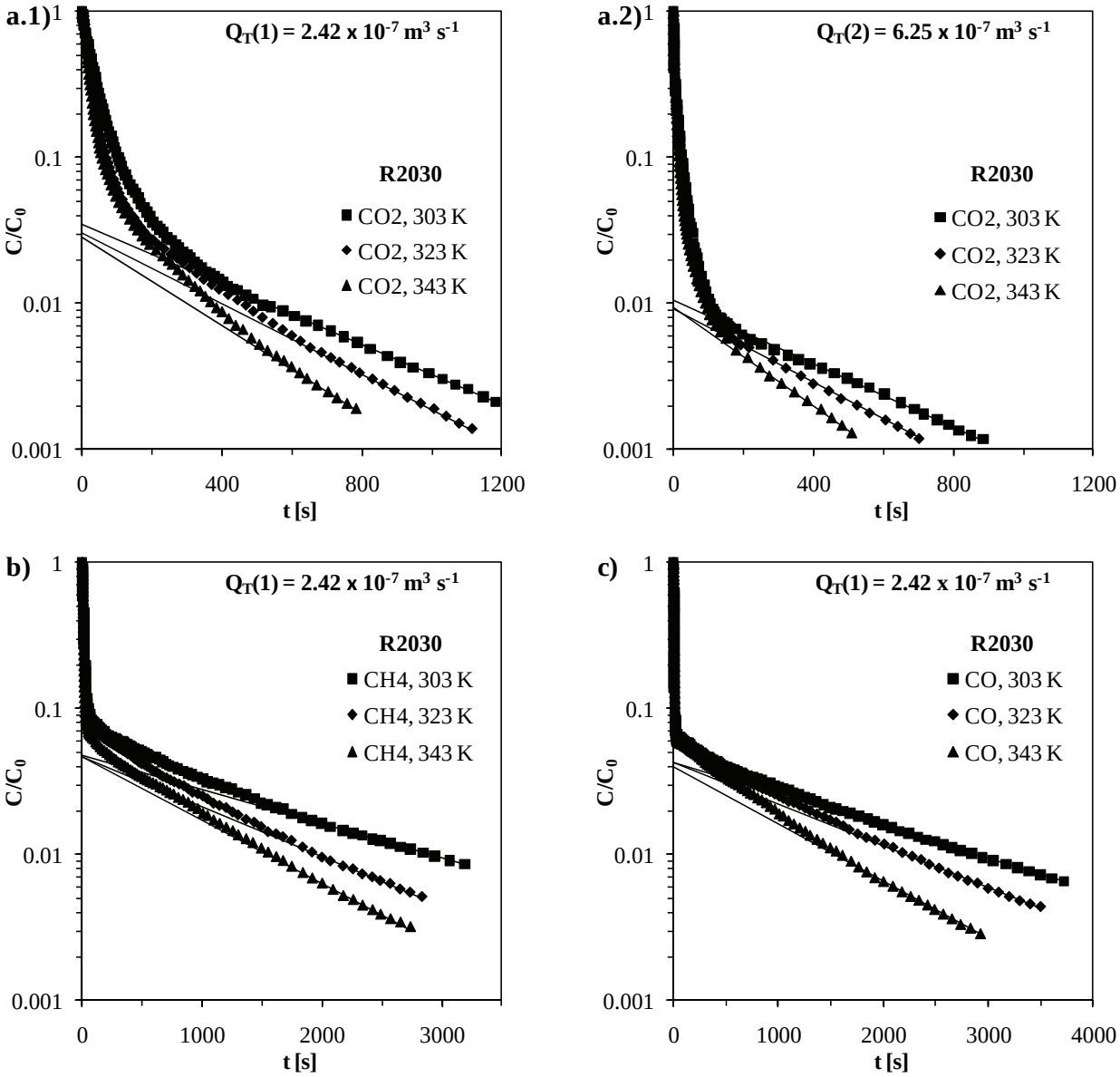


Figure 3.9: ZLC curves for CO_2 (a), CH_4 (b) and CO (c) on R2030 at three different temperatures: 303 (■), 323 (◆) and 343 K (▲); flow rate $Q_T(1)$ of 2.42×10^{-7} m^3 s^{-1} (measured at 298 K and 1 bar); flow rate $Q_T(2)$ of 6.25×10^{-7} m^3 s^{-1} (measured at 298 K and 1 bar); experimental conditions are detailed in Table 3.2.

The results obtained for the micropore diffusivities of all these gases were within the same order of magnitude. The higher diffusivities were the ones of CO_2 followed by CO and CH_4 was the slowest molecule to diffuse. This is coincident with the kinetic molecular diameter of the different gases (3.3, 3.76 and 3.8 Å for CO_2, CO and CH_4, respectively) [18]: the largest molecule (CH_4) should be the one that founds more difficulties to move within the micropore network of the

adsorbent. As mentioned in section 3.3.2, the micropore diffusion is an activated process with exponential dependence with temperature according to equation (3.27). Also the parameters to describe micropore diffusion coefficients within the temperature range of 303-343 K covered in this study are reported in Table 3.3.

Table 3.3: Micropore diffusivity (divided by r_c^2) obtained through ZLC experiments for CO_2, CH_4 and CO in R2030 within 303-343 K at infinite dilution.

Species	Flow rate [$m^3\ s^{-1}$]*	Temp. [K]	slope [s^{-1}]	intercept	D_c/r_c^2 [s^{-1}]	D_c^0/r_c^2 [s^{-1}]	E_a [kJ mol^{-1}]
CO_2	2.42×10^{-7}	303	2.36×10^{-3}	0.0346	4.14×10^{-4}	2.01×10^{-6}	9.79
		323	2.79×10^{-3}	0.0307	4.89×10^{-4}		
		343	3.81×10^{-3}	0.0285	6.67×10^{-4}		
	6.25×10^{-7}	303	2.49×10^{-3}	0.0105	4.36×10^{-4}		
		323	2.89×10^{-3}	0.0093	5.06×10^{-4}		
		343	3.87×10^{-3}	0.0097	6.76×10^{-4}		
CH_4	2.42×10^{-7}	303	5.24×10^{-4}	0.0457	9.48×10^{-5}	1.04×10^{-6}	11.8
		323	7.35×10^{-4}	0.0412	1.32×10^{-4}		
		343	9.10×10^{-4}	0.0378	1.63×10^{-4}		
CO	2.42×10^{-7}	303	5.09×10^{-4}	0.0433	9.19×10^{-5}	1.10×10^{-6}	12.1
		323	6.38×10^{-4}	0.0403	1.15×10^{-4}		
		343	8.98×10^{-4}	0.0396	1.62×10^{-4}		

* measured at 298 K and 1 bar

In Figure 3.10, the straight lines are the complete ZLC model results obtained from the analytical solution of equations (3.1) to (3.3) using the kinetic parameters previously determined in the long time response (LTR) region.

The response to a pulse of pure hydrogen on R2030 was measured at 1 bar and 303 K to provide a diffusivity parameter of H_2 diffusion. The experimental conditions used on the H_2 pulse are reported in Table 3.4. The H_2 pulse at 303 K in activated carbon R2030 is shown in Figure 3.11. Also the responses to pulses of pure methane and carbon monoxide on R2030 at 303, 323 and 343 K were measured for comparison purposes with the CH_4 and CO diffusivity parameters obtained through the ZLC experiments. Table 3.4 shows the experimental conditions used on the pulse experiments and Figure 3.11 shows the pulse experimental results obtained for pure CH_4 and

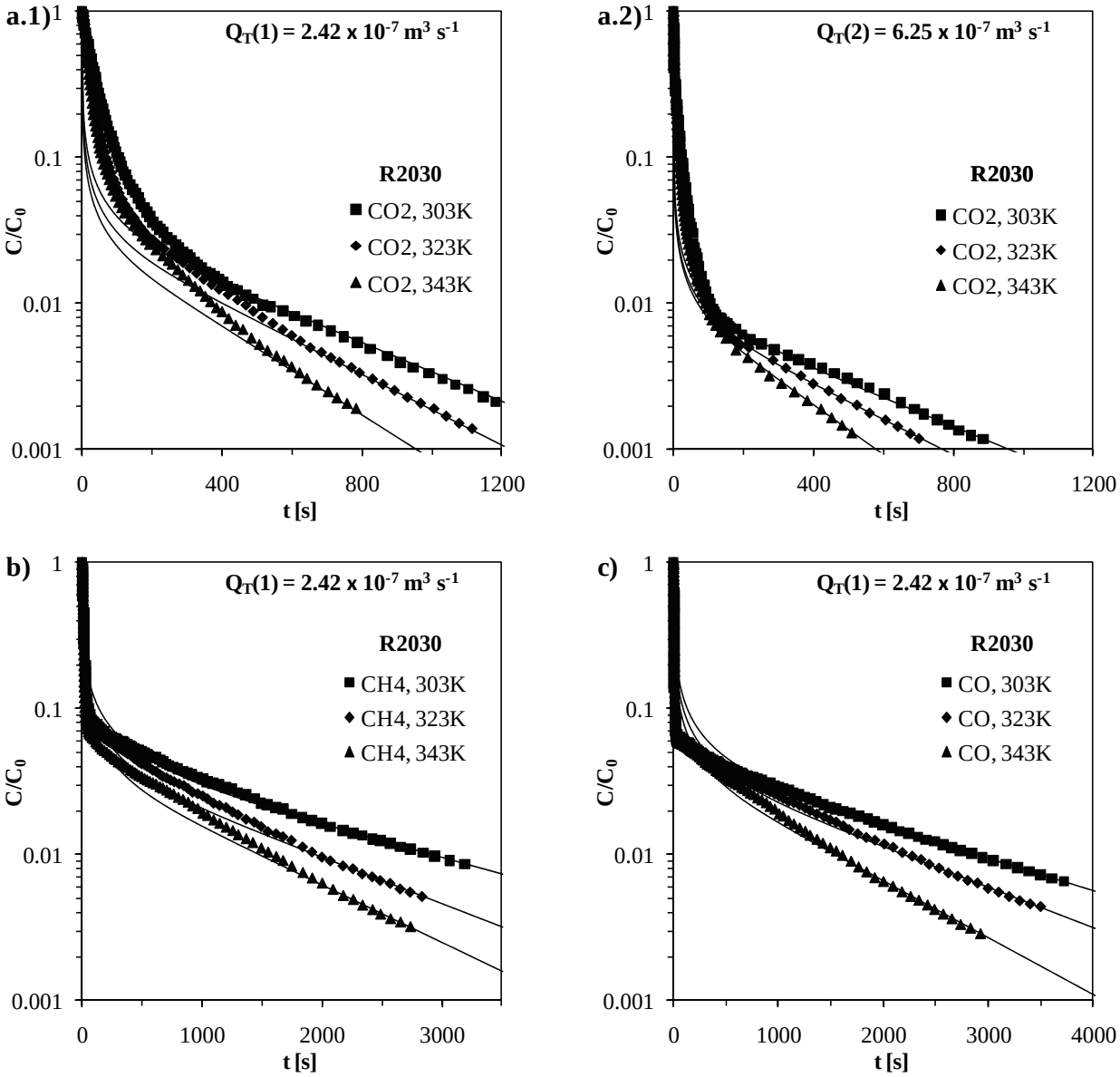


Figure 3.10: ZLC curves for CO_2 (a), CH_4 (b) and CO (c) on R2030 at three different temperatures: 303 (■), 323 (◆) and 343 K (▲); straight lines (——) are the complete ZLC model results using the parameters from LTR; experimental conditions are detailed in Table 3.2.

CO on R2030 at 303, 323 and 343 K. To measure the diffusivities in the linear region of the isotherm, diluted concentrations of CH_4 and CO were used. As mentioned in section 3.2.2, note that the column used for H_2 experiments had to be larger to have reliable data of adsorption kinetics due to the H_2 fast kinetics and the low H_2 adsorption capacity at low partial pressures.

It should be pointed out that the experimental error associated to the measurement of the peak of hydrogen was considerable because of the small difference of thermal conductivities

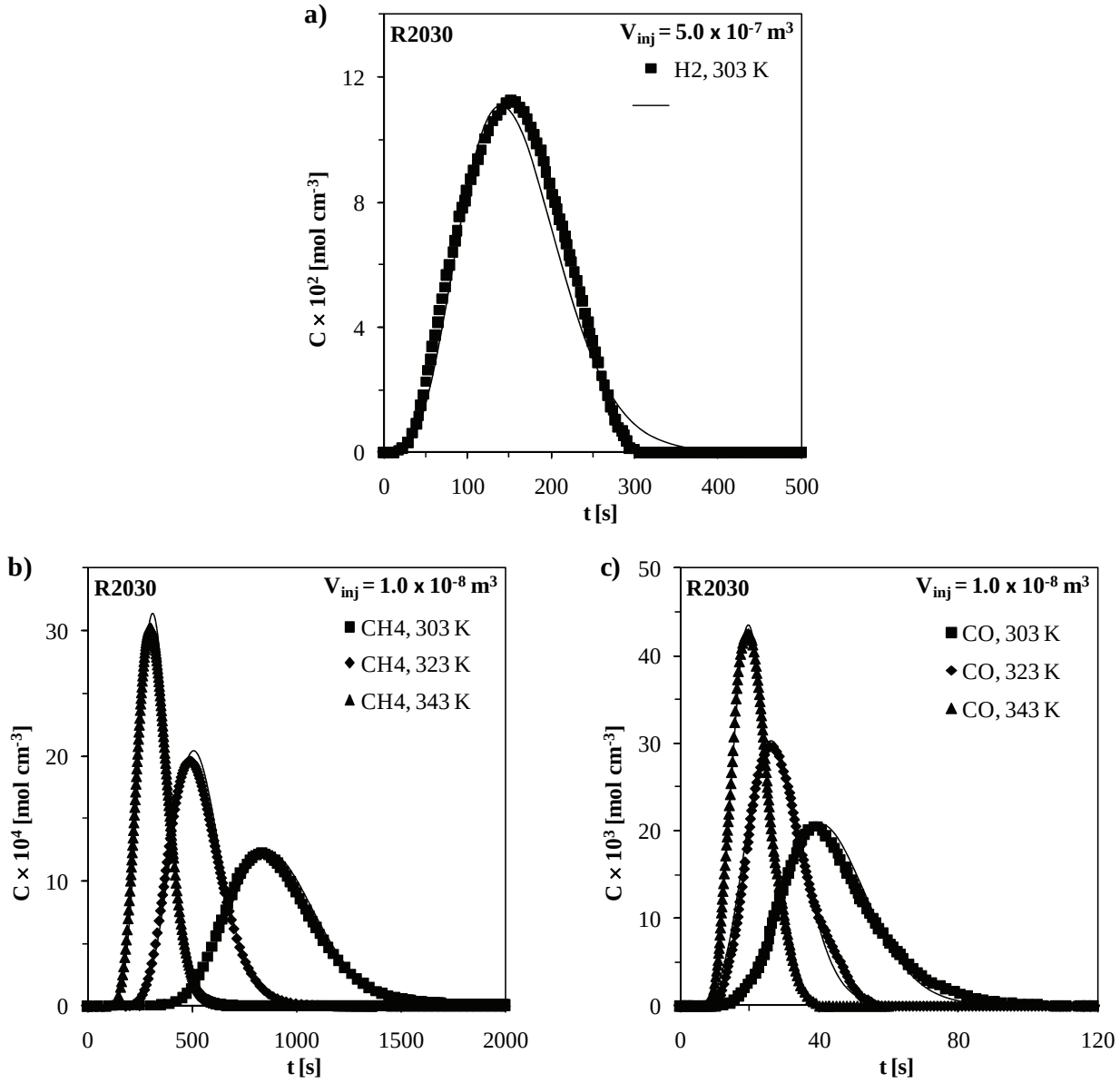


Figure 3.11: Pulse experiments of H_2 (a), CH_4 (b) and CO (c) on R2030 at three different temperatures: 303 (■), 323 (◆) and 343 K (▲); —— simulation with the kinetic parameters obtained; experimental conditions are detailed in Table 3.4.

between helium (inert gas employed for pre-conditioning of the column) and hydrogen. From each pulse experiment of H_2, CH_4 and CO, the first moment and the variance were calculated according to equations (3.14) and (3.15), respectively. The stoichiometric times (first moments) are coincident (within experimental error) to the values obtained from the isotherms. The procedure to calculate diffusional resistances was as follows: axial dispersion and film mass transfer coefficient were calculated from equation (3.18) to (3.19). Having all the terms, the term corresponding to the micropore diffusivity was calculated. The results obtained of all calculations are shown in

Table 3.4: Experimental conditions used on the pulse experiments of H_2, CH_4 and CO in R2030 at 1 bar of pressure.

Adsorbate	H_2	CH_4, CO
Pressure [bar]	1	
Mass adsorbent × 10^3 [kg]	111.6	5.0916
He flow rate × 10^7 [m^3 s^{-1}]*	11.7	6.25
Volume injected × 10^7 [m^3]	5.0	0.10
Temperatures [K]	303	303, 323, 343
Bed height [m]	0.254	0.167
Bed volume × 10^6 [m^3]	200	9.48
Bed porosity, ε	0.363	0.385
Adsorbent	R2030	
Type	extrudates	
Average pellet diameter × 10^3 [m]	2.90	
Average pellet length × 10^3 [m]	6.45	
Pellet porosity, ε_p	0.600	
Adsorbent density, ρ_p [kg m^{-3}]	874	
Solid density, ρ_s [kg m^{-3}]	2162	

* measured at 298 K and 1 bar

Table 3.5: Pulse experimental results obtained for H_2, CH_4 and CO in R2030 at 1 bar and 303-343 K.

Adsorbate	H_2	CH_4			CO		
Temperature [K]	303	303	323	343	303	323	343
Flow rate × 10^7 [m^3 s^{-1}]*	11.7	6.25			6.25		
μ_1 × 10^3 [s]	152.2	903.4	528.0	322.9	44.54	29.09	20.93
σ^2 × 10^3 [s^2]	2962	52792	16596	6030	200.5	67.6	27.4
D_{ax} × 10^5 [m^2 s^{-1}]	6.18	4.37	4.64	4.93	4.49	4.77	5.07
D_m × 10^5 [m^2 s^{-1}]	16.1	6.96	7.74	8.56	7.30	8.12	8.96
D_k × 10^4 [m^2 s^{-1}]	14.0	4.94	5.10	5.25	3.73	3.85	3.97
D_p × 10^5 [m^2 s^{-1}]	2.40	3.05	3.36	3.68	3.05	3.35	3.66
k_f [m s^{-1}]				0.1184			
D_c/r_c^2 × 10^2 [s^{-1}]	13.5	1.55	3.01	5.04	13.8	21.8	24.0
D_c^0/r_c^2 [s^{-1}]	—		391.2			17.7	
E_a [kJ mol^{-1}]	—		25.5			12.1	

* measured at 298 K and 1 bar

Table 3.5. It was observed that from all the possible resistances in the packed bed for the H_2 pulse experiment, the most important term corresponds to the axial dispersion (accounting for 92% of all resistances). From the other resistances it can be observed that the film mass transfer term is negligible when compared to pore and micropore resistances. From this analysis a H_2 micropore diffusion coefficient in R2030 at 303 K was evaluated and is reported in Table 3.5. The fast diffusion, together with a very small amount adsorbed, make that measurements of hydrogen diffusivity have large sources of error: in this case, the axial dispersion is more important than all diffusional resistances. The CH_4 and CO micropore diffusion coefficients in R2030 at 303, 323 and 343 K were evaluated and are reported in Table 3.5. Note that the film mass transfer term is negligible when compared to pore and micropore resistances for both methane and carbon monoxide and a tortuosity factor of 2 was assumed for R2030. The pulses were fitted with the kinetic parameters obtained.

Diluted breakthrough curves for carbon dioxide (0.5% of CO_2 balanced in He) on activated carbon R2030 were measured at 303, 323 and 343 K for comparison purposes with the CO_2 diffusivity parameters obtained through the ZLC experiments. The experimental conditions used on the diluted breakthrough experiments of CO_2 on R2030 are reported in Table 3.6. Figure 3.12 reports the three diluted breakthrough curves.

Table 3.6: Experimental conditions used on the dilute breakthrough experiments of CO_2 in R2030 at 1 bar of pressure.

Adsorbate	CO_2
Adsorbate partial pressure [bar]	0.005
Mass adsorbent × 10^3 [kg]	5.0916
Flow rate × 10^7 [m^3 s^{-1}]*	6.25
Temperatures [K]	303, 323, 343
Bed height [m]	0.167
Bed volume × 10^6 [m^3]	9.48
Bed porosity, ε	0.385
Adsorbent	**R2030**
Type	extrudates
Average pellet diameter × 10^3 [m]	2.90
Average pellet length × 10^3 [m]	6.45
Pellet porosity, ε_p	0.600
Adsorbent density, ρ_p [kg m^{-3}]	874
Solid density, ρ_s [kg m^{-3}]	2162

* measured at 298 K and 1 bar

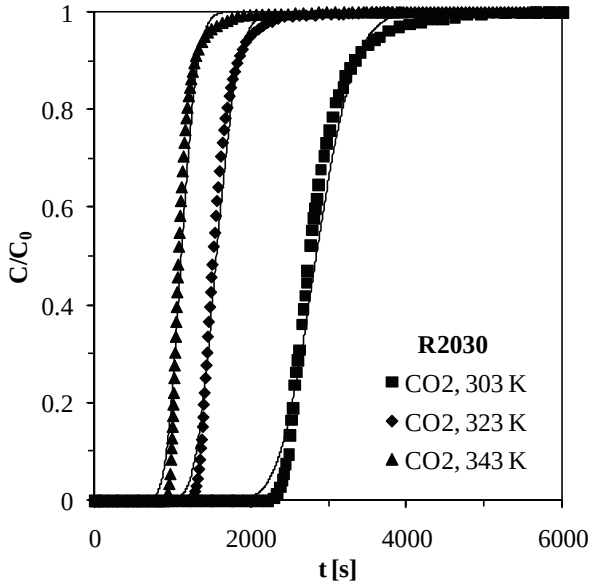


Figure 3.12: Dilute breakthrough curves of carbon dioxide on R2030 at three different temperatures: 303 (■), 323 (◆) and 343 K (▲); —— simulation with the kinetic parameters obtained; experimental conditions are detailed in Table 3.6.

By determining the first moment (equation (3.14)) and the variance (equation (3.15)) with the results obtained in this set of experiments, the kinetic properties were determined with equation (3.17). As for the pulse experiments, also in the breakthrough analysis the axial dispersion and film mass transfer coefficient were calculated from equations (3.18) and (3.19). The pore diffusivity coefficient was estimated by the Bosanquet equation (equation (3.6)) considering a tortuosity factor for R2030 of 2. The analyses of the diluted breakthrough curves on R2030 obtained for carbon dioxide are shown in Table 3.7. Figure 3.12 shows that, employing the mathematical model reported in equations (3.28) to (3.46) of Section 3.3.2, the simulations (solid lines) are able to predict the experimental results of the CO_2 breakthrough curves.

According to the full set of experiments it was determined that micropore resistances control diffusion for all the gases studied (CO_2, H_2, CH_4 and CO). At 303 K, the faster species is CO_2 while diffusion of CO is faster at higher temperatures. This indicates that the activation energy of diffusion is higher for CO (12.1 kJ mol^{-1}) than for CO_2 (9.75 kJ mol^{-1}). For CH_4, the larger molecule in this system, the energy of activation of micropore diffusion is 25.5 kJ mol^{-1}. This order does follow the expected order according to the size of the molecules (CO_2 < CO < CH_4) [18]. Diffusion of hydrogen was very fast in this material, in fact, its measurement is very difficult and the value reported in Table 3.5 is indicative of the order of magnitude of the micropore diffusion

Table 3.7: Diluted breakthrough experimental results obtained for CO_2 in R2030 at 1 bar and 303-343 K.

Adsorbate		CO_2	
Temperature [K]	303	323	343
Flow rate × 10^7 [m^3 s^{-1}]*		6.25	
$\mu_1 \times 10^3$ [s]	2852	1570	1118
$\sigma^2 \times 10^3$ [s^2]	182133	59289	33191
$D_{ax} \times 10^5$ [m^2 s^{-1}]	4.03	4.27	4.51
$D_m \times 10^5$ [m^2 s^{-1}]	5.98	6.66	7.37
$D_k \times 10^4$ [m^2 s^{-1}]	2.97	3.07	3.17
$D_p \times 10^5$ [m^2 s^{-1}]	2.49	2.74	2.99
k_f [m s^{-1}]		0.1184	
$D_c/r_c^2 \times 10^2$ [s^{-1}]	4.27	6.13	6.67
D_c^0/r_c^2 [s^{-1}]		2.13	
E_a [kJ mol^{-1}]		9.75	

* measured at 298 K and 1 bar

coefficient. In equation (3.17) almost 80% of the resistance was in the axial dispersion term, being only 20% the resistance within the micropores.

The results obtained through the ZLC experiments and by the pulse or breakthrough experiments of methane, carbon monoxide and nitrogen were compared. The micropore diffusivity (divided by r_c^2) obtained through ZLC experiments and pulse or breakthrough experiments for CH_4, CO and CO_2 in R2030 within 303-343 K at infinite dilution are shown in Table 3.8.

It can be observed from these experiments that a large difference between the values obtained from ZLC and pulse or breakthrough curves analysis were obtained: the diffusivity coefficients obtained in pulse or breakthrough experiments are much higher than the ones obtained by ZLC. As it was mentioned before, this is due to the distribution of micropore sizes (see section 3.2.2). In the ZLC experiments, the larger resistances of the smaller pores (small value of diffusivity) are detected in the long time response while in the diluted breakthrough curves and pulse response analysis, a more representative response is obtained. These smaller micropores are the ones with higher resistance resulting in small diffusivity coefficients. When diluted breakthrough curves (isothermal behaviour, constant velocity over the column and linear isotherm) are analyzed, the results obtained also accounts the distribution of micropore sizes: steeper breakthrough due to fast diffusion in larger micropores and then low approach to the concentration corresponding to the smaller micropores. For this reason, the values of diffusivity obtained by

Table 3.8: Micropore diffusivity (divided by r_c^2) obtained through ZLC experiments and pulse or breakthrough experiments for CH_4, CO and CO_2 in R2030 within 303-343 K at infinite dilution.

Species	ZLC experiments			Pulse or breakthrough experiments		
	Flow rate $[m^3\ s^{-1}]^*$	Temp. [K]	D_c/r_c^2 $[s^{-1}]$	Flow rate $[m^3\ s^{-1}]^*$	Temp. [K]	D_c/r_c^2 $[s^{-1}]$
CH_4	2.42×10^{-7}	303	9.48×10^{-5}	6.25×10^{-7}	303	1.55×10^{-2}
		323	1.32×10^{-4}		323	3.01×10^{-2}
		343	1.63×10^{-4}		343	5.04×10^{-2}
CO	2.42×10^{-7}	303	9.19×10^{-5}	2.42×10^{-7}	303	1.38×10^{-1}
		323	1.15×10^{-4}		323	2.18×10^{-1}
		343	1.62×10^{-4}		343	2.40×10^{-1}
CO_2	2.42×10^{-7}	303	4.14×10^{-4}	—	—	—
		323	4.89×10^{-4}		—	—
		343	6.67×10^{-4}		—	—
	6.25×10^{-7}	303	4.36×10^{-5}	6.25×10^{-7}	303	4.27×10^{-2}
		323	5.06×10^{-4}		323	6.13×10^{-2}
		343	6.76×10^{-4}		343	6.67×10^{-2}

* measured at 298 K and 1 bar

breakthrough curves and pulse response analysis were considered more representative of the overall resistance of the activated carbon R2030 extrudates than the ones previously reported from ZLC experiments and are more reliable to be employed in the prediction of PSA experiments.

3.4.2 Activated carbon ACM-3mm

Adsorption kinetics of pure carbon dioxide in activated carbon ACM-3mm was studied by ZLC experiments. The experimental conditions used on the ZLC measurements of CO_2, CH_4 and CO in R2030 are reported in Table 3.9. Figure 3.13 shows the ZLC results for carbon dioxide in activated carbon ACM-3mm. These experiments were carried at 303, 323 and 343 K.

Initially it was decided to study the micropore diffusivities of all gases through ZLC experiments. It can be observed from these experiments that the diffusivity coefficients cannot be estimated using the ZLC curves. The same kind of behaviour was previously observed by Grande *et al.* (2003) [19] in another system employing carbonaceous adsorbents. In the analysis of these ZLC curves, it can be observed that the gas desorbs from the larger micropores very fast and using the long time response to determine the diffusivity coefficients, only the resistance of these larger

Table 3.9: Experimental conditions used on the ZLC measurements of CO_2 in ACM-3mm at 1 bar of pressure.

Adsorbate	CO_2
Adsorbate partial pressure [bar]	0.005
Mass adsorbent × 10^3 [kg]	0.05570
Flow rate × 10^7 [m^3 s^{-1}]*	2.42; 6.25
Temperatures [K]	303, 323, 343
Cell height × 10^2 [m]	1.65
Cell volume × 10^7 [m^3]	2.34
Cell porosity, ε	0.633
Adsorbent	**ACM-3mm**
Type	extrudates
Average pellet diameter × 10^3 [m]	3.00
Average pellet length × 10^3 [m]	4-5
Pellet porosity, ε_p	0.700
Adsorbent density, ρ_p [kg m^{-3}]	649
Solid density, ρ_s [kg m^{-3}]	2140

* measured at 298 K and 1 bar

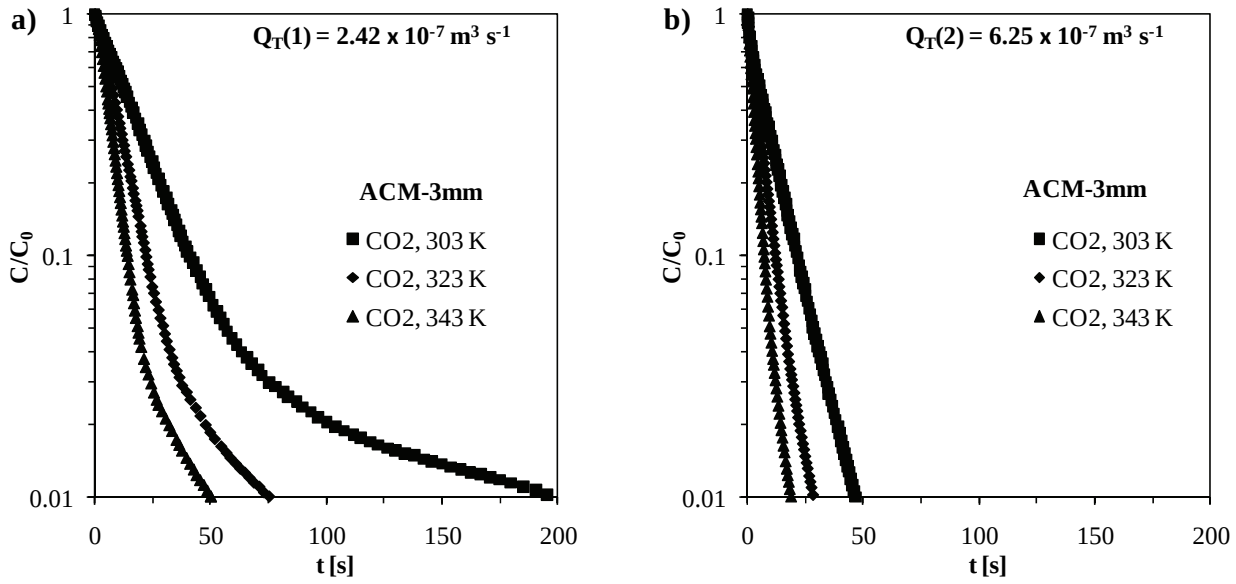


Figure 3.13: ZLC curves for CO_2 on ACM-3mm at three different temperatures: 303 (■), 323 (◆) and 343 K (▲); a) flow rate $Q_T(1)$ of 2.42 × 10^{-7} m^3 s^{-1} (measured at 298 K and 1 bar); b) flow rate $Q_T(2)$ of 6.25 × 10^{-7} m^3 s^{-1} (measured at 298 K and 1 bar); experimental conditions are detailed in Table 3.9.

micropores was accounted and the curves approximate to the equilibrium responses [13].

For ACM-3mm diluted breakthrough curves were not performed. According to the results obtained in chapter 2, the CO_2/H_2 equilibrium selectivity on this adsorbent was lower than the selectivity shown by activated carbon R2030. Also, at 303 K and 1 bar, the selectivity increased more significantly for activated carbon R2030 than for ACM-3mm (77 and 58, respectively). At that particular time, to fulfill the objectives of the HY2SEPS project it was necessary only to select one commercial adsorbent and it was decided to leave the measurements on ACM-3mm.

3.4.3 Activated carbon HY2SEPS-AC

Adsorption kinetics of pure gases (CO_2, H_2, CH_4, CO and N_2) in HY2SEPS-AC was determined by breakthrough experiments. In the case of CO_2, CH_4, CO and N_2, the experiments were performed using a small amount of the gas diluted in helium (see Table 3.10 for detailed experimental conditions). The breakthrough curves obtained for these gases are shown in Figure 3.14. The solid lines in Figure 3.14 correspond to the simulations using the mathematical model reported in Section 3.3.2 (equations (3.28) to (3.46)).

Table 3.10: Experimental conditions used on the measurement of the breakthrough curves of CO_2, CH_4, CO, N_2, H_2 and H_2O on HY2SEPS-AC at 1 bar of pressure.

Adsorbate	CO_2, CH_4, CO, N_2; H_2	H_2O
Adsorbate partial pressure [bar]	0.005; 1*	0.0374
Mass Adsorbent × 10^3 [kg]	6.3554	2.6258
Temperatures [K]	303, 323, 343	303
Bed height [m]	0.165	0.085
Bed volume × 10^5 [m^3]	1.245	0.5053
Bed porosity, ε	0.394	0.383
Adsorbent	HY2SEPS-AC	
Type	extrudates	
Average pellet diameter × 10^3 [m]	2.35	
Average pellet length × 10^3 [m]	3-4	
Pellet porosity, ε_p	0.566	
Adsorbent density, ρ_p [kg m^{-3}]	842	
Solid density, ρ_s [kg m^{-3}]	1939	

* The adsorbate partial pressure is 1 bar for H_2; for the other gases is 0.005 bar

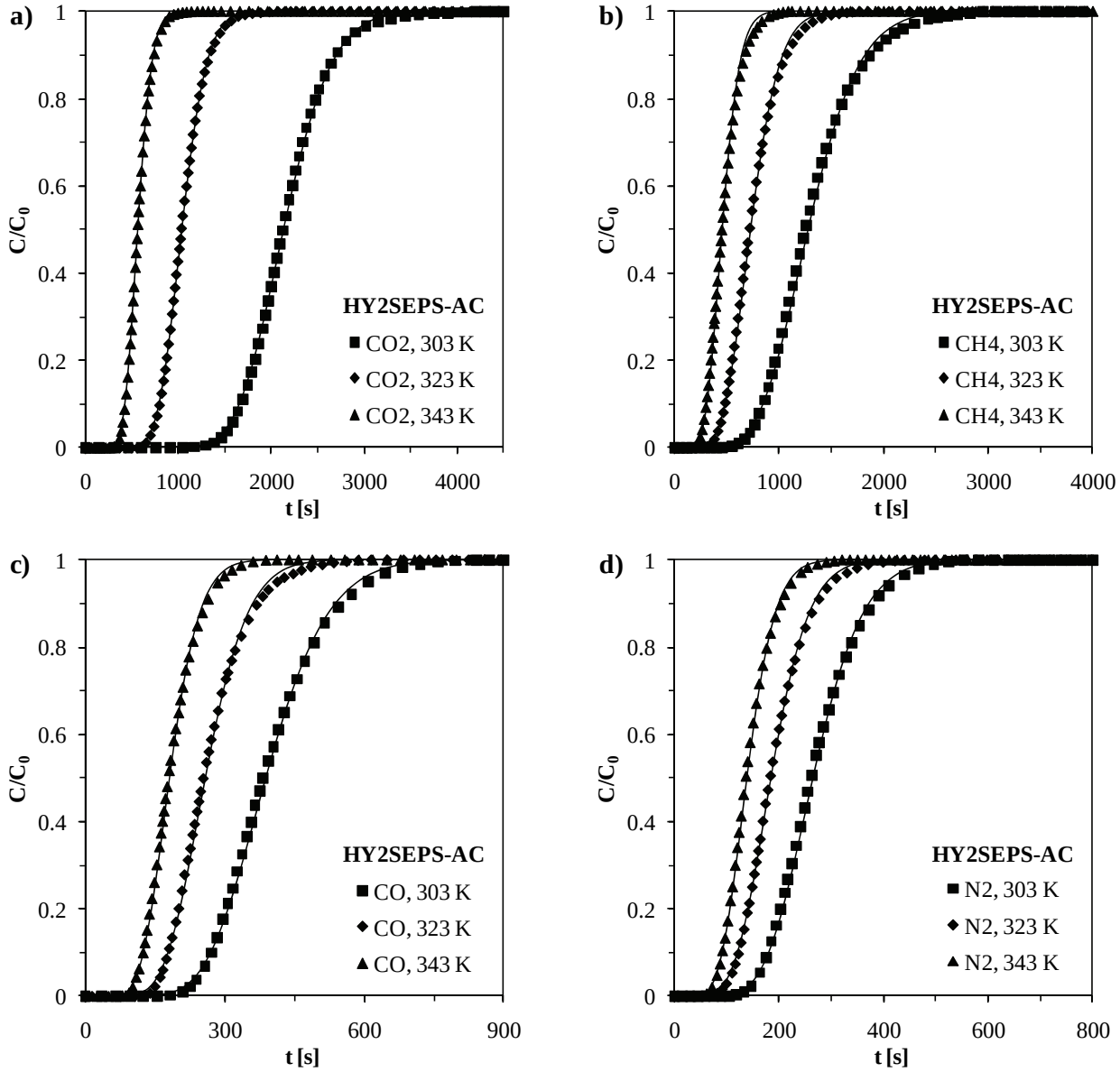


Figure 3.14: Diluted breakthrough curves of CO_2 (a), CH_4 (b), CO (c) and N_2 (d) on HY2SEPS-AC at 303 (■), 323 (◆) and 343 K (▲); 1 bar of total pressure; —— simulation with the kinetic parameters obtained; experimental conditions are detailed in Table 3.10.

Breakthrough curves of hydrogen on HY2SEPS-AC were performed using pure hydrogen. The reason for using pure hydrogen breakthrough curves is because H_2 is weakly adsorbed at low partial pressures and also due to the extremely fast H_2 diffusion (extremely fast breakthrough with a very small signal). The breakthrough curves of pure hydrogen on HY2SEPS-AC are reported in Figure 3.15. The experimental conditions are detailed in Table 3.10.

The breakthrough curves present several resistances to mass transfer: axial dispersion, film in the outer layer of the extrudates, macropore diffusion and micropore diffusion. To employ these

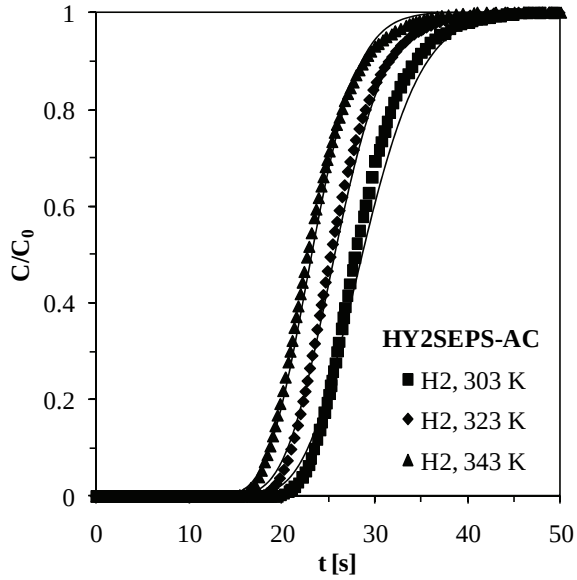


Figure 3.15: Breakthrough curves of pure H_2 on HY2SEPS-AC at 303 (■), 323 (◆) and 343 K (▲); 1 bar of total pressure; —— simulation with the kinetic parameters obtained; experimental conditions are detailed in Table 3.10.

breakthrough curve experiments to fit the diffusivity parameters, the axial dispersion and film mass transfer were estimated. According to the values from the mercury porosimetry, the pore radius of the macropore structure was large enough to neglect Knudsen diffusion (larger than the mean molecular path: e.g., for CO_2 at 297 K and 0.4-2.8 bar is 314-116 Å [20]), reason why pore diffusion was only calculated using molecular diffusion [21].

To determine the relative importance of all the resistances, the moment analysis was performed. The results obtained for the contributions of the axial dispersion term, film mass transfer term, pore resistance term and micropore resistance term to the variance obtained for CO_2, CH_4, CO, N_2 and H_2 in HY2SEPS-AC at 303, 323 and 343 K are reported in Table 3.11. Using the derivative of the breakthrough curves, the first moment give us the capacity of the adsorbent. The ratio of the variance and two times the first moment square ($\sigma^2/2\mu_1^2$) can be related with the sum of all the resistances to mass transfer through equation (3.17). At the experimental conditions employed it was observed that the film mass transfer resistance can be neglected having a very small effect. Assuming a tortuosity value of 2 it was also observed that the macropore resistance was smaller than 3% in all the cases (Table 3.11). In all the breakthrough curves, the important dispersive mechanisms were the axial dispersion and also the micropore mass transfer resistance. The axial dispersion was estimated using the equation (3.18) (valid for low Reynolds numbers) and depends on the molecular diffusion and also on the velocity employed in the experiments. It was

Table 3.11: Contributions of the axial dispersion term, film mass transfer term, pore resistance term and micropore resistance term for CO_2, H_2, CH_4, CO and N_2 in HY2SEPS-AC at 303, 323 and 343 K.

Species	Temp. [K]	Term contribution [%]			
		Axial Disp.	Film Res.	Pore Res.	Microp. Res.
CO_2	303	69.9	2.7	2.8	24.6
	323	64.3	2.2	2.4	31.1
	343	60.6	1.9	2.0	35.5
H_2	303	72.76	0.05	0.05	27.14
	323	78.54	0.03	0.03	21.40
	343	81.48	0.03	0.03	18.46
CH_4	303	45.4	0.6	0.6	53.4
	323	46.6	0.5	0.5	52.4
	343	48.6	0.5	0.5	50.4
CO	303	60.4	0.6	0.7	38.3
	323	55.3	0.5	0.5	43.7
	343	59.5	0.5	0.5	39.5
N_2	303	55.1	0.6	0.6	43.7
	323	47.7	0.4	0.4	51.5
	343	51.3	0.4	0.4	47.9

$$\frac{\sigma^2}{2\mu_1^2} = \left\{\begin{matrix}\text{Axial}\\ \text{Disp.}\end{matrix}\right\} + \left(\frac{u_i}{L}\right)\left(\frac{\varepsilon}{1-\varepsilon}\right)\left(\left\{\begin{matrix}\text{Film}\\ \text{Res.}\end{matrix}\right\} + \left\{\begin{matrix}\text{Pore}\\ \text{Res.}\end{matrix}\right\} + \left\{\begin{matrix}\text{Microp.}\\ \text{Resist.}\end{matrix}\right\}\right)\left(1 + \frac{\varepsilon_p}{(1-\varepsilon_p)K_H \rho_p R_g T}\right)^{-2}$$

concluded that in HY2SEPS-AC extrudates (bidisperse adsorbent), the controlling resistance to mass transfer of all gases within the particles is the micropore diffusion.

The micropore diffusion was thus estimated using the variance calculated from the derivatives of the breakthrough curves. The specific values obtained from all the derivatives of the breakthrough curves and the exponential dependence with temperature of micropore diffusion are detailed in Table 3.12. It can be observed that in HY2SEPS-AC hydrogen (the smaller molecule) is the one where higher diffusion rate is observed. The diffusion of the whole set of molecules follow the trend that can be predicted from the molecular diameters of the molecules: larger molecules have smaller diffusion coefficients. As an example, the macropore diffusivities of the five gases for HY2SEPS-AC at 303 K are: 7.21×10^{-5} (H_2) > 3.55×10^{-5} (CO) > 3.49×10^{-5} (N_2) > 3.42×10^{-5} (CH_4) > 2.91×10^{-5} m^2 s^{-1} (CO_2). For HY2SEPS-AC at 303 K the micropore diffusivity (divided by r_c^2) have the following order: 2.31×10^{-1} (H_2) > 6.44×10^{-2} (N_2) > 5.79×10^{-2} (CO) >

Table 3.12: Micropore diffusivity (divided by r_c^2) and the parameters to describe temperature dependence of micropore diffusion of CO_2, H_2, CH_4, CO and N_2 in HY2SEPS-AC within 303-343 K at infinite dilution.

Species	T [K]	D_c/r_c^2 [s^{-1}]	D_c^0/r_c^2 [s^{-1}]	E_a [kJ mol^{-1}]
CO_2	303	3.35×10^{-2}	17.5	15.8
	323	4.74×10^{-2}		
	343	6.97×10^{-2}		
H_2	303	2.31×10^{-1}	14.8	10.4
	323	3.17×10^{-1}		
	343	3.73×10^{-1}		
CH_4	303	9.41×10^{-3}	81.5	22.8
	323	1.64×10^{-3}		
	343	2.71×10^{-2}		
CO	303	5.79×10^{-2}	59.2	17.5
	323	8.08×10^{-2}		
	343	1.31×10^{-1}		
N_2	303	6.44×10^{-2}	0.995	7.03
	323	6.47×10^{-2}		
	343	8.98×10^{-2}		

3.35×10^{-2} (CO_2) > 9.41×10^{-3} s^{-1} (CH_4).

Several studies have determined diffusion constants of these gases in activated carbons. Most of the data is expressed as LDF (linear driving force) coefficients (K_{LDF}) which correspond to $K_{LDF} = 3D_c/r_c^2$ for activated carbons. In this study, the LDF coefficients of CO_2 (~ 0.1 s^{-1}), H_2 (~ 0.7 s^{-1}), CO (~ 0.17 s^{-1}) and N_2 (~ 0.19 s^{-1}) are of the same order of magnitude of the values reported by Park *et al.* (1998) [22] and Jee *et al.* (2001) [23]. However, the same authors presented a LDF coefficient of CH_4 for activated carbon much higher than the value obtained for HY2SEPS-AC; the result obtained was ~ 0.03 s^{-1} and in the literature are reported ~ 0.195 s^{-1} [23] and ~ 0.4 s^{-1} [22]. Warmuziński and Tańczyk (1997) [24] reported a LDF coefficient of CH_4 of ~ 0.068 s^{-1} (the same order of magnitude of the value obtained in this study). The difference in the results with the literature indicates the specific interactions of the CH_4 molecules with the surface of activated carbon HY2SEPS-AC.

A water vapour breakthrough experiment in HY2SEPS-AC extrudates was also performed at 303 K using an inlet humidity percentage of 89%. The exit concentration as a function of time is reported in Figure 3.16. The obtained breakthrough curve is composed of two parts as a result of

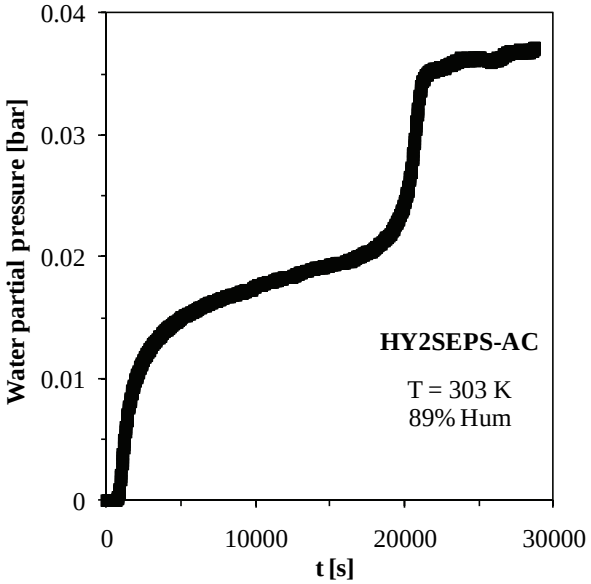


Figure 3.16: Water vapour breakthrough curve on activated carbon at 303 K (■) obtained with activated carbon for 89% of humidity; experimental conditions are detailed in Table 3.10.

the shape of the isotherm. The first part is dispersive as a result of the unfavourable part of the isotherm and the second part is a compressive front or shock that results from the second (favourable) portion of the isotherm. In this second part of the breakthrough curve, a steep rise in the outlet concentration is observed, indicating that the dispersive effects are small, that is, that mass transfer resistances are low. One of the advantages of using activated carbon is that during the regeneration of the adsorbent at low pressures, the concentration front becomes compressive and the water vapour removal is favourable.

3.4.4 Zeolite HY2SEPS-ZEO

Breakthrough experiments of CO_2, H_2, CH_4, CO and N_2 in HY2SEPS-ZEO were performed to determine adsorption kinetics of pure gases. For CO_2, CH_4, CO and N_2, the experiments were performed using a small amount of the gas diluted in helium. The experimental conditions are detailed in Table 3.13. The experimental data of the breakthrough curves obtained for these gases and the simulations (solid lines) using the mathematical model reported in Section 3.3.2 equations (3.28) to (3.46) are shown in Figure 3.17.

Breakthrough curves of hydrogen on HY2SEPS-ZEO were performed using pure hydrogen as previously explained for HY2SEPS-AC in section 3.4.3. Figure 3.18 and Table 3.13 show the

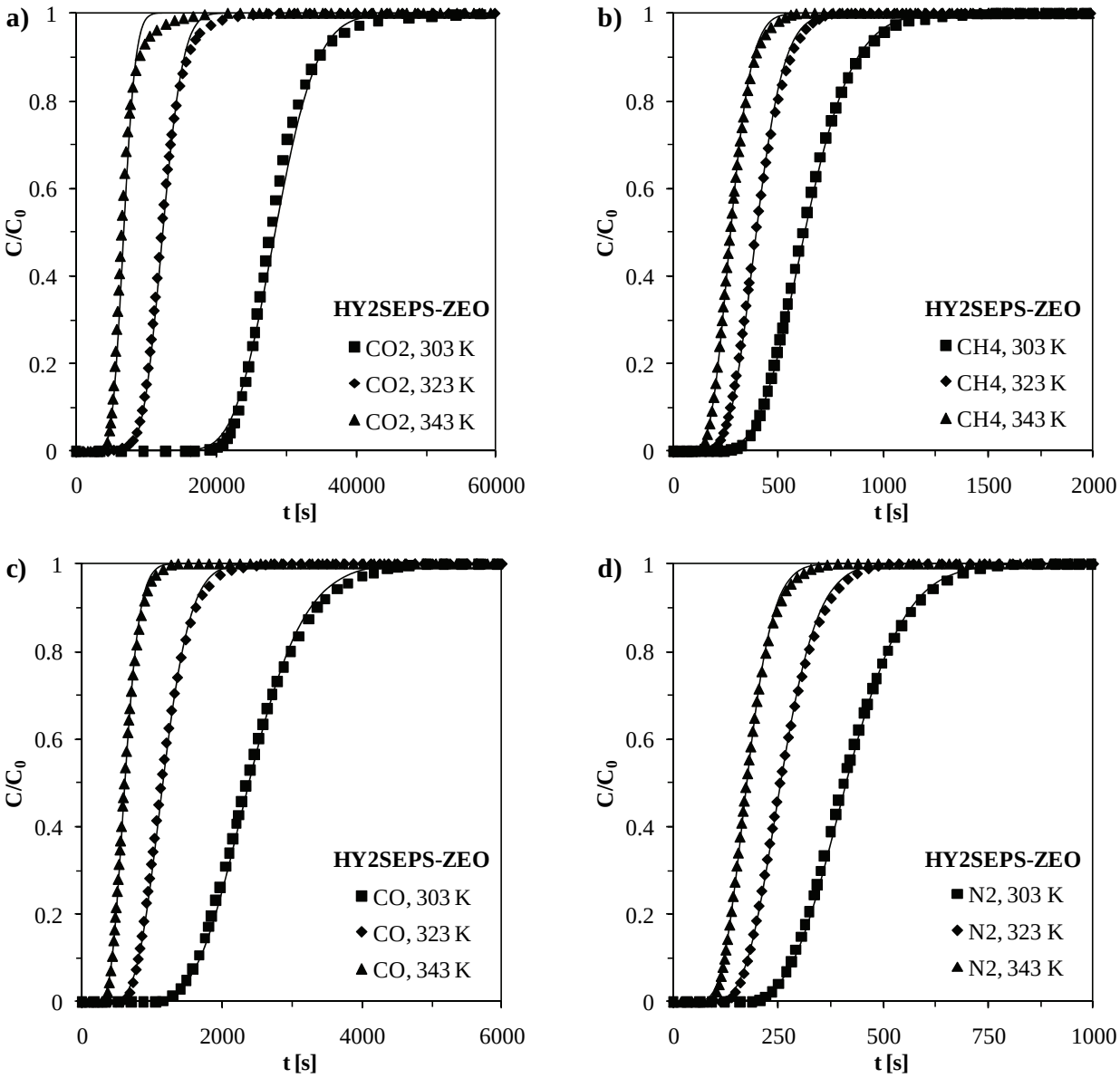


Figure 3.17: Diluted breakthrough curves of CO_2 (a), CH_4 (b), CO (c) and N_2 (d) on HY2SEPS-ZEO at 303 (■), 323 (◆) and 343 K (▲); 1 bar of total pressure; —— simulation with the kinetic parameters obtained; experimental conditions are detailed in Table 3.13.

breakthrough curves of pure hydrogen on HY2SEPS-ZEO and the detailed experimental conditions, respectively.

The axial dispersion, film in the outer layer of the extrudates, macropore diffusion and crystal diffusion are several resistances to mass transfer in these breakthrough curves. Axial dispersion and film mass transfer were estimated to fit the diffusivity parameters. The pore diffusion was only calculated using molecular diffusion (see section 3.4.3).

Table 3.13: Experimental conditions used on the measurement of the breakthrough curves of CO_2, CH_4, CO, N_2, H_2 and H_2O on HY2SEPS-ZEO at 1 bar of pressure.

Adsorbate	CO_2, CH_4, CO, N_2; H_2
Adsorbate partial pressure [bar]	0.005; 1*
Mass Adsorbent × 10^3 [kg]	8.5315
Temperatures [K]	303, 323, 343
Bed height [m]	0.165
Bed volume × 10^5 [m^3]	1.245
Bed porosity, ε	0.391
Adsorbent	**HY2SEPS-ZEO**
Type	extrudates
Average pellet diameter × 10^3 [m]	1.70
Average pellet length × 10^3 [m]	4-6
Pellet porosity, ε_p	0.503
Adsorbent density, ρ_p [kg m^{-3}]	1126
Solid density, ρ_s [kg m^{-3}]	2267

* The adsorbate partial pressure is 1 bar for H_2; for the other gases is 0.005 bar

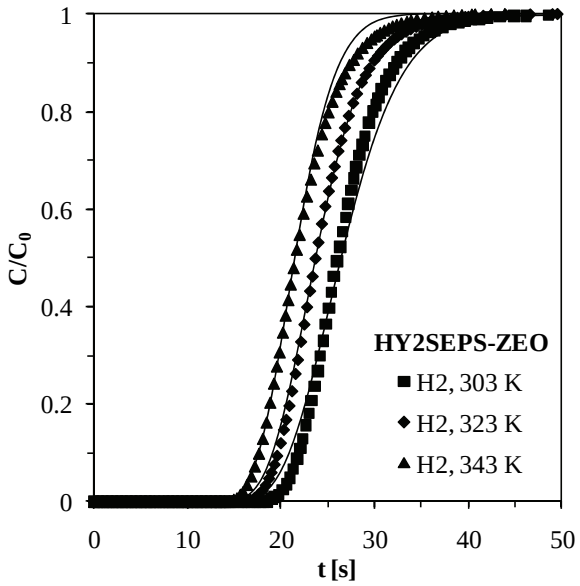


Figure 3.18: Breakthrough curves of pure H_2 on HY2SEPS-ZEO at 303 (■), 323 (◆) and 343 K (▲); 1 bar of total pressure; —— simulation with the kinetic parameters obtained; experimental conditions are detailed in Table 3.13.

The moment analysis was performed to determine the relative importance of all the resistances. Table 3.14 shows the contributions of the axial dispersion term, film mass transfer term, pore resistance term and crystal resistance term to the variance obtained for CO_2, CH_4, CO, N_2 and H_2 in HY2SEPS-ZEO at 303, 323 and 343 K. The first moment was determined using the derivative of the breakthrough curves. Therefore, the ratio of the variance and two times the first moment square ($\sigma^2/2\mu_1^2$) was related through equation (3.17) with the sum of all the resistances to mass transfer. The film mass transfer resistance for the experimental conditions employed can be neglected since its effect is insignificant. Table 3.14 shows that the macropore resistance was smaller than 3% in all the cases for a tortuosity value of 2. The axial dispersion and the crystal mass transfer resistance were the most important dispersive mechanisms. It was also concluded that in bidisperse HY2SEPS-ZEO extrudates, the crystal diffusion is the controlling resistance to mass transfer of CO_2, H_2, CH_4, CO and N_2 within the particles.

Table 3.14: Contributions of the axial dispersion term, film mass transfer term, pore resistance term and crystal resistance term for CO_2, H_2, CH_4, CO and N_2 in HY2SEPS-ZEO at 303, 323 and 343 K.

Species	Temp. [K]	Term contribution [%]			
		Axial Disp.	Film Res.	Pore Res.	Crystal Res.
CO_2	303	33.2	4.6	6.5	55.7
	323	29.3	3.8	5.4	61.5
	343	24.9	3.1	4.3	67.7
H_2	303	73.68	0.02	0.03	26.27
	323	78.18	0.02	0.02	21.78
	343	82.74	0.02	0.02	17.22
CH_4	303	49.1	0.3	0.4	50.2
	323	58.4	0.3	0.4	40.9
	343	52.8	0.3	0.3	46.6
CO	303	58.4	0.4	0.4	40.8
	323	56.5	0.3	0.4	42.8
	343	60.6	0.3	0.4	38.7
N_2	303	60.0	0.4	0.4	39.2
	323	59.7	0.3	0.4	39.6
	343	58.8	0.3	0.3	40.6

$$\frac{\sigma^2}{2\mu_1^2} = \left\{\begin{matrix}\text{Axial}\\ \text{Disp.}\end{matrix}\right\} + \left(\frac{u_i}{L}\right)\left(\frac{\varepsilon}{1-\varepsilon}\right)\left(\left\{\begin{matrix}\text{Film}\\ \text{Res.}\end{matrix}\right\} + \left\{\begin{matrix}\text{Pore}\\ \text{Res.}\end{matrix}\right\} + \left\{\begin{matrix}\text{Crystal}\\ \text{Resist.}\end{matrix}\right\}\right)\left(1 + \frac{\varepsilon_p}{(1-\varepsilon_p)K_H \rho_p R_g T}\right)^{-2}$$

Using the variance calculated from the derivatives of the breakthrough curves, the crystal diffusion was thus estimated. Table 3.15 shows the specific values obtained from all the derivatives of the breakthrough curves and the exponential dependence with temperature of micropore diffusion. In HY2SEPS-ZEO, it was concluded that smaller molecules have higher diffusion coefficients, as for the activated carbon HY2SEPS-AC. Therefore, the smaller molecule (hydrogen) was the molecule where higher diffusion rate was observed. The macropore diffusivity of hydrogen (7.56×10^{-5} m^2 s^{-1}) was higher than for carbon monoxide (3.30×10^{-5} m^2 s^{-1}), followed by nitrogen (3.25×10^{-5} m^2 s^{-1}), then methane (3.24×10^{-5} m^2 s^{-1}) and finally carbon dioxide (2.69×10^{-5} m^2 s^{-1}).

Table 3.15: Crystal diffusivity (divided by r_c^2) and the parameters to describe temperature dependence of crystal diffusion of CO_2, H_2, CH_4, CO and N_2 in HY2SEPS-ZEO within 303-343 K at infinite dilution.

Species	T [K]	D_c/r_c^2 [s^{-1}]	D_c^0/r_c^2 [s^{-1}]	E_a [kJ mol^{-1}]
CO_2	303	3.41×10^{-4}	0.268	18.0
	323	5.17×10^{-4}		
	343	7.84×10^{-4}		
H_2	303	4.97×10^{-2}	9.33	11.6
	323	6.40×10^{-2}		
	343	8.53×10^{-2}		
CH_4	303	5.05×10^{-3}	36.9	20.6
	323	1.13×10^{-2}		
	343	1.29×10^{-2}		
CO	303	2.34×10^{-3}	368	28.7
	323	4.20×10^{-3}		
	343	8.85×10^{-3}		
N_2	303	1.13×10^{-2}	7.86	14.9
	323	1.66×10^{-2}		
	343	2.24×10^{-2}		

From Table 3.14, it can be concluded that for HY2SEPS-ZEO, the crystal diffusivity is also the limiting mass transfer resistance for all gases. In addition, it is observed that the highest contribution to the dispersive effects results again from the axial dispersion term, except in the case of carbon dioxide where the overall major contribution is due to the crystal resistance.

As for activated carbons, several studies have also determined diffusion constants of CO_2, H_2, CH_4, CO and N_2 in zeolites. LDF coefficients (which correspond to $K_{LDF} = 15D_c/r_c^2$ for zeolites) is the most common way that the results are presented in the literature. The LDF coefficients for zeolite materials are reported by the same authors mentioned for HY2SEPS-AC: Park *et al.* (1998) [22] and Jee *et al.* (2001) [23]. These coefficients of H_2 (~ 0.7 s^{-1}), CO (~ 0.03 s^{-1}) and N_2 (~ 0.17 s^{-1}) for HY2SEPS-ZEO are in agreement with the values reported [22-23]. The LDF coefficient of CH_4 for HY2SEPS-ZEO is ~ 0.08 s^{-1} and it is two times smaller than ~ 0.14 s^{-1} [23] or ~ 0.2 s^{-1} [22]. The difference in the results with the literature indicates the specific interactions of the CH_4 molecules with the surface of both adsorbent materials. As mentioned in section 3.4.3, the difference in the results obtained for the LDF coefficients of methane with the literature can be explained with specific interactions of the CH_4 molecules with the surface of the zeolite HY2SEPS-ZEO.

Water vapour breakthrough experiments in HY2SEPS-ZEO extrudates were not measured. As mentioned in chapter 2, it should be avoided because the adsorption of water in a zeolite is very strong and to regenerate the adsorbent it should be made at high temperatures becoming a very energy intensive process [25].

3.5 Conclusions

Activated carbon R2030 was the first adsorbent studied. Adsorption kinetics of five different pure gases (H_2, CO_2, CH_4, CO, H_2O) were evaluated in a commercial sample of activated carbon R2030. Initially, adsorption kinetics of CO_2, CH_4, CO were determined by ZLC at three different temperatures (303, 323 and 343 K). The adsorption kinetic results obtained by ZLC for the pure gases indicate that in all cases the diffusion was controlled within the micropore structure of the activated carbon R2030. Carbon dioxide has the higher diffusivity coefficients followed by carbon monoxide and methane, which is coincident with the kinetic molecular diameter of the molecules (CO_2, CO and CH_4 kinetic diameters: 3.3, 3.76 and 3.8 Å, respectively). Diffusion of hydrogen was very fast and hard to measure by any macroscopic technique, especially ZLC. Therefore, diffusivity of H_2 was determined by pulse experiments. Diffusivities of CH_4 and CO were also determined by pulse experiments and the diffusivity of CO_2 determined by diluted breakthrough experiments. The results obtained were compared to the values determined by ZLC technique. It was concluded that the diffusivity coefficients obtained from pulse or breakthrough experiments were more representative of the overall resistance of the activated carbon extrudates

than the results reported from ZLC experiments. The influence of H_2 diffusivity is much smaller than the axial dispersion contribution reason why the reliability of the diffusivity coefficient is limited only to the order of magnitude.

Activated carbon ACM-3mm was the second adsorbent studied. ZLC experiments were performed to evaluate the adsorption kinetics of CO_2 in a commercial sample of activated carbon ACM-3mm. However, from the ZLC experiments it was observed that CO_2 desorbed from the larger micropores very fast and so the diffusivity coefficients could not be estimated using the long time response of those curves (the curves approximate to the equilibrium responses).

Adsorption kinetics of CO_2, CH_4, CO and N_2 in the activated carbon HY2SEPS-AC were measured by diluted breakthrough experiments with 0.5% of the adsorbate balanced by helium at 303, 323 and 343 K. Breakthrough experiments were performed to measure adsorption kinetics of H_2 at the same temperatures and adsorption kinetics of H_2O at 303 K. From the analysis of the moments of CO_2, CH_4, CO, N_2 and H_2 breakthrough curves, it was observed that the contributions of film and macropore mass transfer resistances to the total dispersion were very small and also that the mechanism controlling mass transfer is micropore diffusion. The micropore diffusivities in HY2SEPS-AC of all five gases at 303 K differ in one order of magnitude having the following order from the fastest to the slowest species: $H_2 > N_2 > CO > CO_2 > CH_4$.

Also for the zeolite HY2SEPS-ZEO, adsorption kinetics of CO_2, CH_4, CO and N_2 were measured by diluted breakthrough experiments with 0.5% of the adsorbate balanced by helium at 303, 323 and 343 K. For the same temperatures, pure H_2 breakthrough experiments were performed to measure adsorption kinetics of hydrogen. The results obtained show that crystal diffusion is the controlling mass transfer mechanism and also that the contributions to the total dispersion of film and macropore mass transfer resistances were very small. In the case of HY2SEPS-ZEO, the values of the crystal diffusivity vary two orders of magnitude and with a diffusivity order of $H_2 > N_2 > CH_4 > CO > CO_2$ (from the fastest to the slowest gas).

In this chapter the adsorption kinetics of the pure gases exiting a methane reformer on three activated carbons and one zeolite was measured. A total of fifty nine experiments (ZLC, pulses or breakthroughs) were performed and its reproducibility was verified and confirmed. The data reported in this chapter together with the adsorption equilibrium data measured in the previous chapter, allow the development of mathematical models to design and simulate a normal or layered PSA unit for hydrogen purification.

3.6 Notation

Nomenclature

C	concentration (mol m^{-3})
C_0	initial gas phase concentration (mol m^{-3})
$C_{g,i}$	molar concentration of component *i* in the gas phase (mol m^{-3})
$C_{g,T}$	total gas phase concentration (mol m^{-3})
$C_{m,i}$	concentration of component *i* in the macropores (mol m^{-3})
$C_{m,T}$	total concentration in the macropores (mol m^{-3})
D_{ap}	apparent diffusivity (m^2 s^{-1})
D_{ax}	axial dispersion coefficient (m^2 s^{-1})
D_c	micropore/crystal diffusivity (m^2 s^{-1})
D_c^0	limiting diffusivity at infinite temperatures (m^2 s^{-1})
D_{ij}	binary molecular diffusivity (m^2 s^{-1})
D_k	Knudsen diffusivity (m^2 s^{-1})
D_m	molecular diffusivity (m^2 s^{-1})
D_p	macropore diffusivity (m^2 s^{-1})
E_a	activation energy of micropore/crystal diffusion (kJ mol^{-1})
J_{0p} , J_1	Bessel functions
k	Boltzmann's constant (J K^{-1})
k_f	film mass transfer coefficient (m s^{-1})
k_s	geometrical factor of the particle or of the micropore or crystal: 0 - slab; 1 - cylinder; 2 – sphere
K_{eq}	dimensionless equilibrium constant
K_i	equilibrium constant (m^3 kg^{-1})
K_{LDF}	linear driving force (LDF) coefficient (s^{-1})
K_H	Henry constant (mol kg^{-1} bar^{-1})
ℓ	representative spatial dimension of the cell: radius – infinite cylinder and sphere; half length – slab
L	column length (m)
L^*	zero length column (ZLC) parameter
M_i	molecular weight of adsorbate *i* (kg mol^{-1})
M_j	molecular weight of adsorbate *j* (kg mol^{-1})

M_{ij}	molecular weight of the gas mixture (kg mol^{-1})
M_W	molecular weight of the gas (kg mol^{-1})
n	ZLC geometrical factor of the adsorbent: 0 - slab; 1 - cylinder; 2 – sphere
$P_{g,i}$	pressure of the adsorbate *i* in the gas phase (Pa)
$P_{m,i}$	pressure of the adsorbate *i* in the pores of the adsorbent (Pa)
q_i	absolute adsorbed phase concentration of component *i* (mol kg^{-1})
$\bar{q}_i$	micropore or crystal averaged adsorbed phase concentration of component *i* (mol kg^{-1})
$\langle \bar{q}_i \rangle$	particle averaged adsorbed phase concentration of component *i* (mol kg^{-1})
q_i^*	adsorbed concentration in equilibrium with $C_{m,i}$ (mol kg^{-1})
Q_p	purge flow rate (m^3 s^{-1})
r	radial coordinate of the micropore or crystal (m)
r_c	micropore or crystal radius (m)
r_p	mean pore radius (m)
R	radial coordinate of the particle (m)
R_g	universal gas constant (J mol^{-1} K^{-1})
R_p	radius of the adsorbent extrudates (m)
Re	Reynolds number
Sc	Schmidt number
Sh	Sherwood number
t	time (s)
T	temperature (K)
u_0	superficial velocity (m s^{-1})
u_i	interstitial velocity (m s^{-1})
V_{inj}	volume of the solid adsorbent (m^3)
V_s	volume of the solid adsorbent (m^3)
y_i	molar fraction of component *i*
z	partition of the column length *L* (m)

Greek letters

β_j	ZLC roots dependent of the adsorbent shape
ε	bed porosity
ε_p	particle porosity
ε_{ij}/k	maximum energy of interaction between molecular pairs (K)

ε_i	Lennard-Jones parameter of adsorbate *i* (J^{-1})
ε_j	Lennard-Jones parameter of adsorbate *j* (J^{-1})
ε_{ij}	Lennard-Jones parameter of the mixture (J^{-1})
Φ_{ij}	dimensionless quantity of viscosity
μ	gas viscosity (Pa s)
μ_i	gas viscosity of component *i* (Pa s)
μ_j	gas viscosity of component *j* (Pa s)
μ_1	first moment (s)
ρ_g	density of the gas phase (kg m^{-3})
ρ_p	density of the adsorbent (kg m^{-3})
σ^2	variance (s^2)
σ_i	collision molecular diameter between molecules *i* (Å)
σ_j	collision molecular diameter between molecules *j* (Å)
σ_{ij}	collision molecular diameter between molecules *i* and *j* (Å)
τ_p	pore tortuosity
ω	dimensionless temperature in the diffusion collision integral
Ω_c	linear driving force (LDF) factor of the micropore or crystal: $\Omega_c = (k_s + 1)(k_s + 3)$
Ω_{Dij}	dimensionless collision integral of the diffusivity
Ω_p	linear driving force (LDF) factor of the particle: $\Omega_p = (k_s + 1)(k_s + 3)$
$\Omega_{\mu i}$	dimensionless collision integral of the viscosity

3.7 References

[1] A. Jayaraman, A.S. Chiao, J. Padin, R.T. Yang, C.L. Munson, Kinetic separation of methane/carbon dioxide by molecular sieve carbons, Separation Science and Technology. 37 (2002) 2505 -2528.

[2] R.P. Marathe, K. Mantri, M.P. Srinivasan, S. Farooq, Effect of ion exchange and dehydration temperature on the adsorption and diffusion of gases in ETS-4, Industrial and Engineering Chemistry Research. 43 (2004) 5281-5290.

[3] HY2SEPS, Hybrid Hydrogen Carbon Dioxide Separation Processes, E.U. Res. Project 2005, Available from: http://hy2seps.iceht.forth.gr/.

[4] M. Eic, D.M. Ruthven, New experimental technique for measurement of intracrystalline diffusivity, Zeolites. 8 (1988) 40-45.

[5] J.A.C. Silva, F.A. Da Silva, A.E. Rodrigues, Sorption and diffusion of propane, propylene, pentane and hexane in pellets of 13X and 5A zeolites studied by the gravimetric and ZLC techniques, in 12th International Zeolite Conference, 1999, Baltimore, Maryland, USA, Materials Research Society.

[6] J.A.C. Silva, A.E. Rodrigues, Analysis of ZLC technique for diffusivity measurements in bidisperse porous adsorbent pellets, Gas Separation & Purification. 10 (1996) 207-224.

[7] D.D. Do, Adsorption analysis: Equilibria and kinetics, Series on Chemical Engineering, Vol. 2, Imperial College Press, London, 1998.

[8] D.M. Ruthven, Principles of adsorption and adsorption processes, John Wiley & Sons, New York, 1984.

[9] C.A. Grande, A.E. Rodrigues, Adsorption kinetics of propane and propylene in zeolite 4A, Chemical Engineering Research and Design. 82 (2004) 1604-1612.

[10] C.J. Glover, W.R. Lau, Determination of multicomponent sorption equilibria using perturbation gas chromatography, AIChE Journal. 29 (1983) 73-79.

[11] A.M. Ribeiro, T.P. Sauer, C.A. Grande, R.F.P.M. Moreira, J.M. Loureiro, A.E. Rodrigues, Adsorption equilibrium and kinetics of water vapour on different adsorbents, Industrial and Engineering Chemistry Research. 47 (2008) 7019-7026.

[12] M. Suzuki, Adsorption engineering, Elsevier Science, Inc., New York, 1990.

[13] J.R. Hufton, D.M. Ruthven, Diffusion of light alkanes in silicalite studied by the zero length column method, Industrial and Engineering Chemistry Research. 32 (1993) 2379-2386.

[14] S. Brandani, D.M. Ruthven, Analysis of ZLC desorption curves for gaseous systems,

Adsorption. 2 (1996) 133-143.

[15] C.A. Grande, Propane/propylene separation by pressure swing adsorption, Ph.D. Dissertation, University of Porto, Porto, Portugal, 2005.

[16] C.R. Wilke, Diffusional properties of multicomponent gases, Chemical Engineering Progress. 46 (1950) 95-104.

[17] R.B. Bird, W.E. Stewart, E.N. Lightfoot, Transport phenomena, 2nd Edition, Wiley International, Singapore, 2002.

[18] D.W. Breck, Zeolite molecular sieves, R. E. Krieger Publishing, Malabar, FL, 1998.

[19] C.A. Grande, V.M.T.M. Silva, C. Gigola, A.E. Rodrigues, Adsorption of propane and propylene onto carbon molecular sieve, Carbon. 41 (2003) 2533-2545.

[20] E. Taketomo, M. Fujiura, Porous materials for concentration and separation of hydrogen or helium, and process therewith for the separation of the gas (1984) U.S. Patent 4,482,360.

[21] R.T. Yang, Gas Separation by Adsorption Processes, Butterworths, Boston, 1987.

[22] J.-H. Park, J.-N. Kim, S.-H. Cho, J.-D. Kim, R.T. Yang, Adsorber dynamics and optimal design of layered beds for multicomponent gas adsorption, Chemical Engineering Science. 53 (1998) 3951-3963.

[23] J.-G. Jee, M.-B. Kim, C.-H. Lee, Adsorption characteristics of hydrogen mixtures in a layered bed: binary, ternary, and five-component mixtures, Industrial and Engineering Chemistry Research. 40 (2001) 868-878.

[24] K. Warmuziński, M. Tańczyk, Multicomponent pressure swing adsorption Part I. Modelling of large-scale PSA installations, Chemical Engineering and Processing. 36 (1997) 89-99.

[25] S. Sircar, T.C. Golden, M.B. Rao, Activated carbon for gas separation and storage, Carbon. 34 (1996) 1-12.

4.

Large scale preparation of adsorbents for CO_2 and N_2 separations[‡]

4.1 Introduction

To improve the performance of the PSA units, materials with enhanced capacity towards contaminants are required. The PSA columns for H_2 purification from SMR off-gases are packed by two different layers of adsorbents: the first one should remove the heavier contaminants while the second should remove the lighter compounds. These adsorbents are normally activated carbons and zeolites, respectively [1-3].

In this work, a commercial activated carbon (R2030, Norit, Holland) and a zeolite 13X (Na-form) were used for the preparation of two materials with enhanced capacity toward contaminants, with special focus to CO_2 (most abundant impurity) and N_2 (first impurity to break through the column).

[‡] The content of this chapter is part of the work published in the following articles:

F.V.S. Lopes, C.A. Grande, A.M. Ribeiro, E.L.G. Oliveira, J.M. Loureiro, A.E. Rodrigues, Enhancing capacity of activated carbons for hydrogen production, Industrial and Engineering Chemistry Research. 48 (2009) 3978-3990.

F.V.S. Lopes, C.A. Grande, A.M. Ribeiro, V.J.P. Vilar, J.M. Loureiro, A.E. Rodrigues, Effect of ion exchange on the adsorption of SMR off-gases on zeolite 13X, Journal of Chemical and Engineering Data. 55 (2010) 184-195.

4.2 Modification of activated carbons for enhanced CO_2 capacity

4.2.1 Routes for enhanced CO_2 adsorption

High adsorptive capacities of activated carbons are mainly associated with their textural properties such as functional surface groups, high surface area, pore volume and pore size distribution [4]. The textural properties of the activated carbons are highly influenced by the preparation conditions of these adsorbents [5] and by the nature of the precursor (coal, peat, coconut shell, etc) [6-7].

The main processes for the preparation of activated carbons are chemical and physical activations or a combination of chemical followed by physical activation. The chemical activation consists of a carbonization step at a specific temperature in the presence of chemical agents, for instance KOH, NaOH, NH_4Cl, H_3PO_4, $ZnCl_2$, and so forth [7-8]. The physical activation is carried out after the carbonization process with a suitable oxidizing agent, generally carbon dioxide or steam [4, 9]. This activation with a mild oxidant may enhance the pore volume, enlarge the diameters of the pores or create new porosity [10-12]. In the literature it is reported that higher development of microporosity by physical activation is obtained with carbon dioxide as activating agent and the widening of porosity with steam [7, 10, 13-15]. Feng and Bhatia (2003) [16] reported that the surface area and the volume of the small micropores increase dramatically with the physical activation process using carbon dioxide. The resulting removal of carbon atoms initially increases the number of open micropores and their sizes going through maxima [17]. In this process, the adsorbent could be modified under different flows of activating agent, using different activation temperatures, activation times or pressures. The use of different experimental conditions affects the porosity of the product and optimum conditions should be found for a desired application.

Several authors discussed the importance of the possibility of modifying the activation process to create pores of a particular size on the activated carbons, tailored to adsorb a group of specific molecules [18-20]. It was reported by Maciá-Agulló *et al.* (2004) [21] that the chemical activation uses more expensive activating agents in comparison to the physical activation. Hydroxides are very corrosive and it is necessary to apply an additional washing stage in the chemical activation process.

This work was focused on the production of large amounts of a material with enhanced capacity toward carbon dioxide starting from a commercial activated carbon – R2030 (Norit, Holland) – studied by Grande *et al.* (2008) [22]. The objective was to determine operating

conditions to enhance CO_2 capacity without affecting its diffusion rate or the regenerability of the adsorbent. This protocol should provide a simple routine to increase the capacity of a commercial activated carbon to boost the performance of a plant already under operation. With the purpose of increasing the microporosity of the sample without a significant reduction in the size of the micropores, activation with CO_2 using different operating conditions was performed. Once the protocol that achieved the maximum amount of micropores was obtained, operating conditions were adapted to produce four hundred grams of the new material.

The final characterization of the modified samples included the comparison between the adsorption equilibrium isotherms of CO_2 and other gases (H_2, CH_4, CO and N_2) with those obtained in the original activated carbon R2030 [22]. Equilibrium and kinetic experiments were performed at 303 and 323 K within a pressure range of 0-7 bar. These conditions can be employed in a PSA unit for the production of hydrogen with high purity (>99.99%) integrating a CO_2 capture technology [23]. The adsorption equilibrium of all gases was fitted with the Virial isotherm equation [24-25] that allows direct prediction of multicomponent adsorption [26].

4.2.2 Adsorbents preparation and characterization

4.2.2.1 Preparation protocol for physical activation

The first task in the preparation of new samples of activated carbons was the determination of suitable activating conditions. In order to identify the effect of some important operating variables (T, P, gas flow rate) several small-scale experiments were carried out. All samples of modified activated carbons were prepared from a commercially available activated carbon material (R2030) by physical activation with carbon dioxide. Experiments were performed in a vertical furnace under different flows of activating agent and at different temperatures, pressures and activation times. The activation protocol consists of an initial stage of heating of the sample under a flow of nitrogen (2.5×10^{-7} m^3 s^{-1}, measured at 298 K and 1 bar) until the desired temperature using a heating rate of 5 K min^{-1}. Once the desired temperature is reached, the inlet flow is switched to a pure stream of carbon dioxide with a specific flow rate and pressure for a desired period of time. Samples were held at the desired temperature for different activation times of 1200, 2400 and 3600 s. Once the activation time is completed, the cooling was also performed under flow of nitrogen (2.5×10^{-7} m^3 s^{-1}, measured at 298 K and 1 bar). The experimental set-up and the schematic diagram of the experimental set-up for the activated carbon modification by physical activation are shown in Figure 4.1 and Figure 4.2, respectively. Five different samples (AC1-AC5)



Figure 4.1. Experimental set-up for the activated carbon modification by physical activation.

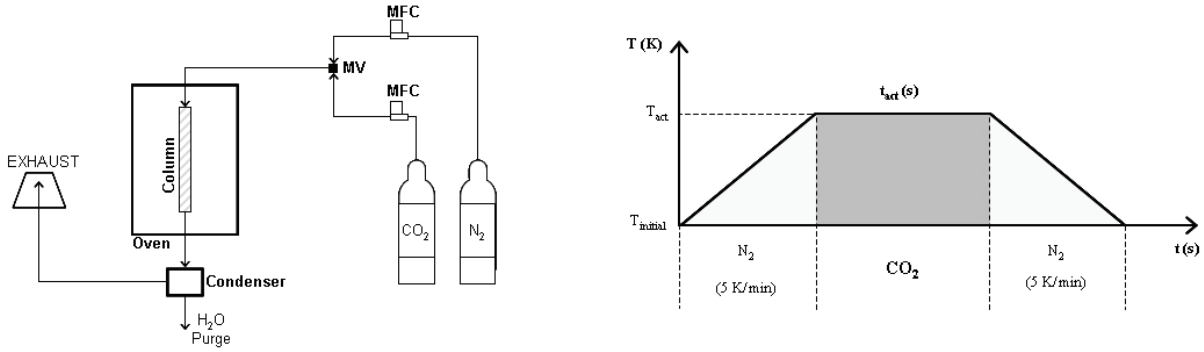


Figure 4.2. Schematic diagram of the experimental set-up for the activated carbon modification by physical activation.

Table 4.1. Conditions of the activation process.

Sample	Activation temp. [K]	CO_2 flow rate [$m^3\ s^{-1}$]*	Pressure [bar]	Activation time [s]
AC1	1098	2.5×10^{-7}	1	1200
AC2	1173	2.5×10^{-7}	1	2400
AC3	1023	1.0×10^{-7}	1	3600
AC4	1173	1.0×10^{-6}	3	2400
AC5	1173	5.0×10^{-7}	1	2400

Initial temperature of 298 K and N_2 flow rate of 2.5×10^{-7} $m^3\ s^{-1}$ #;
Original AC (R2030) surface area of 700.3 $m^2\ g^{-1}$

*, # CO_2 and N_2 flow rates measured at 298 K and 1 bar

were prepared changing pressure, activation temperature, activation times and carbon dioxide flow rate. The operating conditions employed in the preparation of the modified samples are reported in Table 4.1. The characteristics of the column and the adsorbent physical properties are shown in Table 4.2. The amount of sample employed in each run for the determination of the operating conditions was around one gram of activated carbon extrudates.

Table 4.2. Characteristics of the column employed in the activation process; adsorbent physical properties.

Column characteristics	First test column
Bed diameter [m]	4.3×10^{-3}
Bed porosity, ε	0.55
Flow rate [$m^3\ s^{-1}$]*	5.00×10^{-7}
Mass of adsorbent [g]	~ 1
Adsorbent (R2030) physical properties	
Pellet porosity, ε_p	0.601
Adsorbent density, ρ_p [kg m^{-3}]	841
Solid density, ρ_s [kg m^{-3}]	2110
Average pellet radius, R_p [m]	1.45×10^{-3}

* measured at 298 K and 1 bar

4.2.2.2 Sample characterization and reproducibility

For each sample of modified activated carbon, the nitrogen adsorption isotherm at 77 K was measured to determine the surface area and find out in which sample the macropore, mesopore or micropore volumes were increased (Table 4.3). The modified activated carbon with the largest microporosity was chosen for scale-up tests and to analyze the reproducibility of the experiments. An intermediate scale-up for approximately 10 g/batch (sample "I") and a final scale-up for approximately 400 g/batch (*King size* sample "KS") were performed using the operating conditions established in the initial tests (see Figure 4.3 and Table 4.3). The final objective was to produce around four kilograms of activated carbon to supply to one industrial partner within the framework of the EU project HY2SEPS. The sample was sent to Hygear B.V. (Holland) to be employed in a prototype PSA unit. A image of the 4-column PSA prototype is shown in Figure 4.4. Scale-up was limited to 400 g because it was the maximum amount of sample that could be accommodated in the vertical oven used for activation. The specifications of the different columns employed in the successive scale-up preparations are reported in Table 4.4.

Table 4.3. Conditions and results of the activation process.

Sample	Activation temp. [K]	CO_2 flow rate [$m^3\ s^{-1}$]*	Pressure [bar]	Activation time [s]	BET surface area [$m^2\ g^{-1}$]	Burn-off [%]
AC1	1098	2.5×10^{-7}	1	1200	872	5
AC2	1173	2.5×10^{-7}	1	2400	907	10
AC3	1023	1.0×10^{-7}	1	3600	814	12
AC4	1173	1.0×10^{-6}	3	2400	—	20
AC5	1173	5.0×10^{-7}	1	2400	1004	10
AC5-I	1173	2.0×10^{-6}	1	2400	1061	11
AC5-KS	1173	1.14×10^{-4}	1	2400	971	10
AC5-KS-2					987	10
AC5-KS-3	1173	1.14×10^{-4}	1	2400	1094	10
AC5-KS-4					932	10
Initial temperature of 298 K and N_2 flow rate of 2.5×10^{-7} $m^3\ s^{-1}$ #; Original AC (R2030) surface area of 700.3 $m^2\ g^{-1}$						

*, # CO_2 and N_2 flow rates measured at 298 K and 1 bar

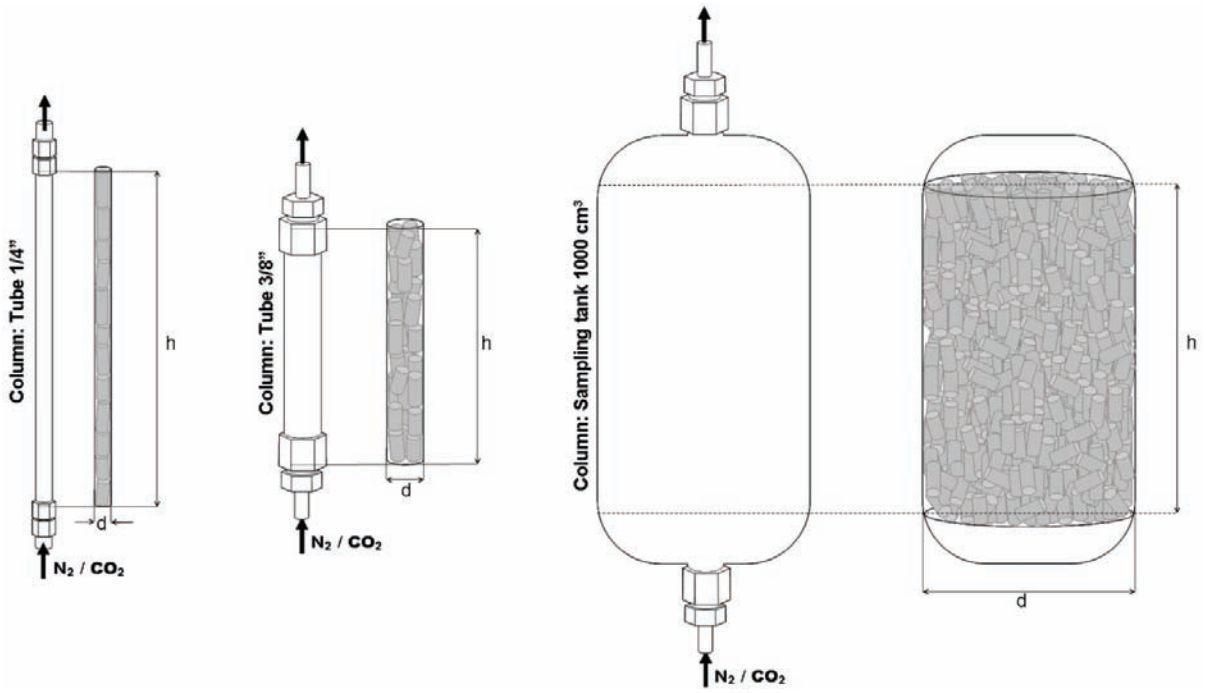


Figure 4.3. Schematic diagram of the different columns employed in the activation process to enhance adsorption properties of activated carbon extrudates.

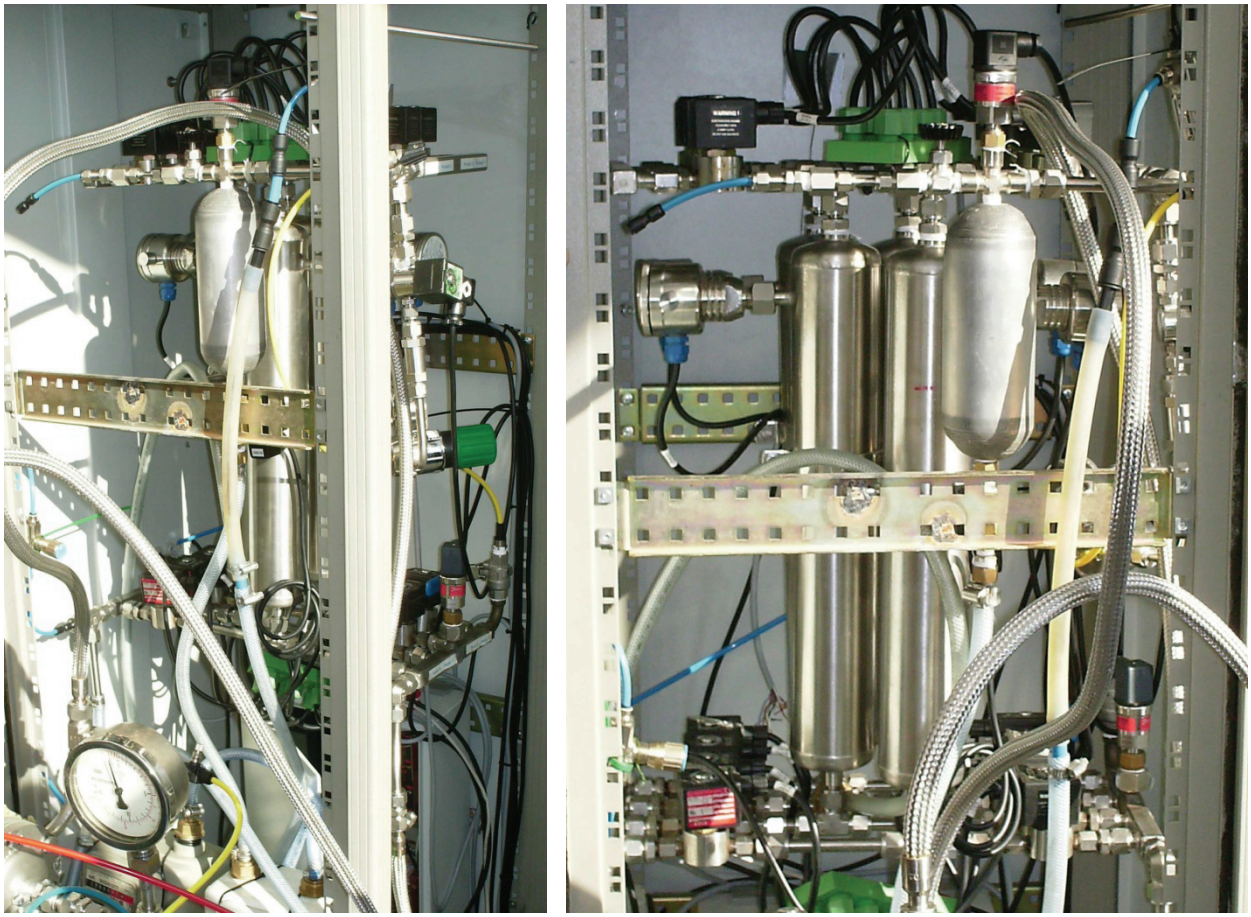


Figure 4.4. The 4-column PSA prototype for H_2 purification developed within the European Project HY2SEPS [23] by Hygear B.V.; Courtesy of Hygear B.V.

Table 4.4. Characteristics of the different columns employed in the activation process.

Column characteristics	First test column	Scale-up columns	
		intermediate	final
Bed diameter [m]	4.3×10^{-3}	9.5×10^{-3}	7.97×10^{-2}
Bed porosity, ε	0.55	0.45	0.40
Flow rate [$m^3\ s^{-1}$]*	5.00×10^{-7}	2.00×10^{-6}	1.14×10^{-4}
Mass of adsorbent [g]	~ 1	~ 10	~ 400

* measured at 298 K and 1 bar

4.2.2.3 Results

Five different samples of modified activated carbons were prepared by changing activation temperature, pressure and time as well as carbon dioxide flow rate. These samples were termed AC1 to AC5 and the full set of operating conditions employed is reported in Table 4.1.

In the experiment using carbon dioxide at 3 bar for activation (AC4) at 1173 K, the extrudates were partially destroyed at the end of the preparation time. The structure of this sample was not determined because the mechanical resistance of the pellets was seriously damaged and it will not be desirable to work with this material in any adsorption-based process, especially PSA, where the particles are submitted to considerable mechanical stress due to the pressure variations.

The extrudates of the samples AC1, AC2, AC3 and AC5 kept the shape and size of the original R2030 pellets. For these samples and also for R2030, the nitrogen adsorption isotherms at 77 K were measured to determine surface area (Table 4.3). The results obtained are shown in Figure 4.5. The weight losses (burn-off) and the BET surface areas of the samples AC1, AC2, AC3 and AC5 as well as values for R2030 are reported in Table 4.3. According to the results obtained, we could determine that by increasing the activation temperature, the surface area increases if the contact time (activation time) is 2400 s. For longer activation times, the surface area is reduced and is also accompanied by the presence of larger mesopores (see Figure 4.5). Ismadji *et al.* (2005) [6] also observed a significant effect of the activation time on the pore structure of the resulting carbons. The flow rate of carbon dioxide also seems to have an important effect which indicates that the reaction-controlled regime was not fully achieved; in the complete reaction-controlled

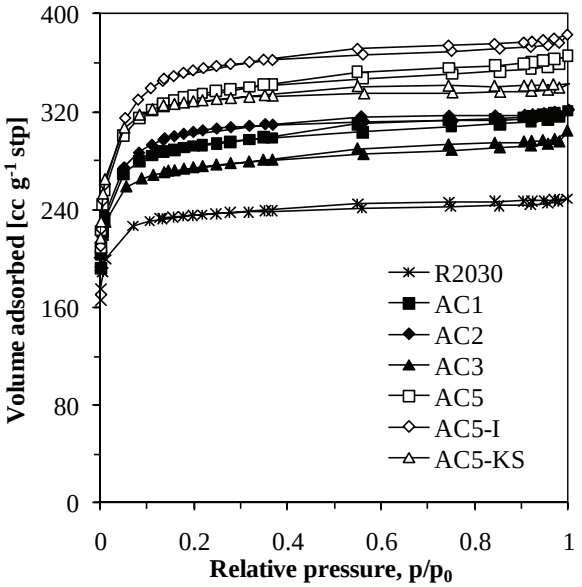


Figure 4.5. Nitrogen adsorption isotherms for the original activated carbon R2030 (-∗-; Grande et al., 2008) and for the modified activated carbon samples AC1 (-■-), AC2 (-◆-), AC3 (-▲-), AC5 (-□-), AC5-I (-◇-) and AC5-KS (-△-).

regime, we would be able to change the flow rate of the activating agent without significantly affecting the result.

The burn-off of AC1, AC2, AC3 and AC5 is between 5-15% and for AC4 it is around 20%. The nitrogen adsorption isotherms show a larger amount of micropores in the modified activated carbon AC5 than in AC1, AC2, AC3 and in the original activated carbon R2030. Thus, the operating conditions employed in the preparation of modified activated carbon AC5 were chosen for scale-up tests: intermediate scale-up sample AC5-I and a final scale-up sample AC5-KS (Table 4.3). The key parameter of the two scale-up processes was constant velocity during the activation. For that, and according to the different columns used, the flow rate of carbon dioxide increased with the increase of the column diameter to keep the velocity constant (Table 4.3). However, Figure 4.5 shows smaller adsorption capacity for nitrogen in AC5-KS than in AC5 due to the lower flow rate used, a consequence of the experimental limitations in the mass flow controllers.

The nitrogen adsorption isotherms at 77 K for the two scale-up samples AC5-I and AC5-KS are also shown in Figure 4.5. The shape of the nitrogen adsorption isotherms at 77 K shows the same micropore volume for the samples AC5, AC5-I and AC5-KS. The mesopores vary slightly in the three samples mentioned before. The BET surface areas for the samples AC5-I and AC5-KS are reported in Table 4.3. The burn-off of the intermediate scale-up sample AC5-I and the burn-off of the final scale-up sample AC5-KS are in the same range of the sample AC5 (approximately 10%). The BET surface areas of both scale-up samples (AC5-I and AC5-KS) are approximately the same of the AC5 BET surface area.

For the four scale-up samples AC5-KS, AC5-KS-2, AC5-KS-3 and AC5-KS-4, the nitrogen adsorption isotherms at 77 K are shown in Figure 4.6. The BET surface area and the burn-off of each of these samples are reported in Table 4.3. The BET surface areas of all these scale-up samples are approximately the same and the shape of the curves shows an equivalent increase of microporosity for all of them. Since the reproducibility of the scale-up experimental tests were verified, approximately four kilograms of activated carbon AC5-KS-Mix (mixture of 400 g batches of AC5-KS) was produced to supply to one industrial partner of the HY2SEPS project (Figure 4.7).

The mercury porosimetry intrusion curves obtained for the two activated carbons (AC5-KS and original activated carbon R2030) are shown in Figure 4.8. It can be observed that in the modified sample, the fraction with pore diameters smaller than 1 μm was increased; that is, we have succeeded in the opening of new porosity.

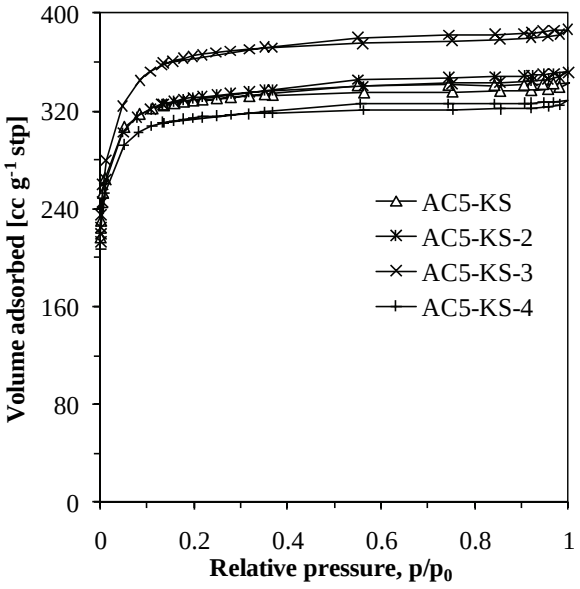


Figure 4.6. Nitrogen adsorption isotherms for the modified activated carbon samples AC5-KS (-△-), AC5-KS-2 (-✳-), AC5-KS-3 (-×-) and AC5-KS-4 (-+-).



Figure 4.7. Preparation of approximately four kilograms of AC5-KS-Mix through physical activation of the activated carbon R2030.

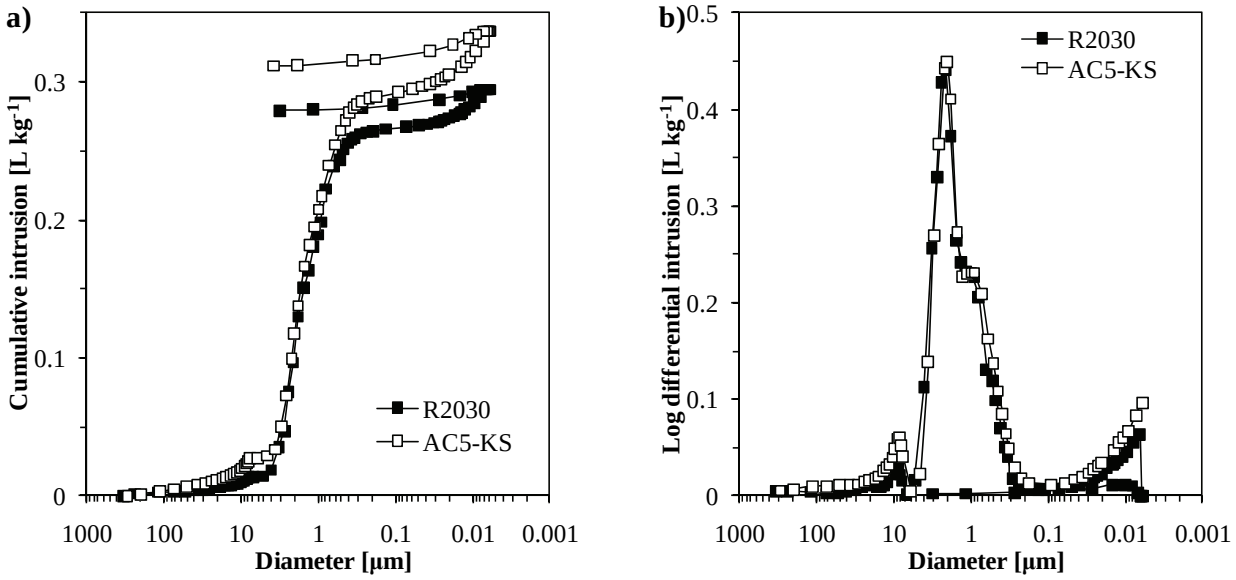


Figure 4.8. Pore size distribution of the original activated carbon R2030 (-■-; Grande et al., 2008) and of the modified activated carbon AC5-KS (-□-) obtained from mercury porosimetry intrusion.

4.2.3 Adsorption equilibrium and kinetics of pure gases

4.2.3.1 Experimental

The adsorption equilibrium isotherms of all gases (CO_2, CH_4, CO, N_2 and H_2) were measured at 303 and 323 K in a magnetic suspension microbalance (Rubotherm, Germany) within the pressure range of 0-7 bar. The experimental set-up is detailed in chapter 2, where is also reported how the corrections of the buoyancy effects in the equilibrium measurements were taken into account. Degassing of all the samples was carried out with a heating rate of 1 K min^{-1} under vacuum (< 10^{-7} bar) at 423 K overnight. The reversibility of each isotherm was confirmed with adsorption and desorption measurements.

To determine the rate of diffusion of pure carbon dioxide, methane, carbon monoxide and nitrogen, breakthrough experiments were performed using 0.5% of adsorbate diluted in helium. In the case of H_2, breakthrough experiments of pure gas were made to avoid the high degree of uncertainty at low partial pressure of hydrogen. This is due to the low amount adsorbed of this gas as well as the low signal detected by the thermal conductivity detector (TCD). The experimental set-up is detailed in chapter 3. The activation of the sample was performed heating at 1 K min^{-1} until 423 K and left overnight, under a continuous flow of helium of 2.42×10^{-7} m^3 s^{-1} (measured at 298 K and 1 bar). The dimensions of the columns used and experimental conditions are displayed

Table 4.5. Experimental conditions used in the measurement of the breakthrough curves (single component) on the modified activated carbon sample AC5-KS.

Breakthrough curves (BT)	Single component mixtures	
Adsorbate (Ads)	CO_2, CH_4, CO, N_2*	H_2
Ads partial pressure [bar]	0.005*	1
Mass of Adsorbent [kg]	5.9309×10^{-3}	
Bed height [m]	0.165	
Bed volume [m^3]	1.245×10^{-5}	
Bed porosity, ε	0.394	
Temperatures [K]	303, 323	
Pressure [bar]	1	
Adsorbent (AC5-KS) physical properties		
Pellet porosity, ε_p	0.627	
Adsorbent density, ρ_p [kg m^{-3}]	786	
Solid density, ρ_s [kg m^{-3}]	2110	
Average pellet radius, R_p [m]	1.45×10^{-3}	

* The adsorbate partial pressure is 0.005 bar balanced in He;

in Table 4.5.

All gases used in this work were provided by Air Liquide: hydrogen N50, carbon dioxide N24, methane N35, carbon monoxide N47, nitrogen N45 and helium N50 (purities greater than 99.999, 99.4, 99.95, 99.997, 99.995 and 99.999 %, respectively).

4.2.3.2 Theoretical

The Virial adsorption isotherm [24-25] was the mathematical model used to describe adsorption equilibrium of pure gases on the original activated carbon (described in the previous section 3.2.1 and summarized in Table 4.6 [24-25]) and on the modified activated carbon previously chosen.

As previously stated, this model is able to fit adsorption isotherms of different gases over a wide range of temperatures and pressures, satisfying thermodynamic constraints. The Virial adsorption isotherm model is generically reported in Table 4.6 [24-25]. The fitting was performed using MATLAB (The MathWorks, Inc.), by minimization of an error function with a precision of 10^{-9} for all the variables involved.

To estimate the kinetic parameters of the pure gases, fixed-bed experiments and the moments theory were once again employed [27]. It was assumed that the process is isothermal and

Table 4.6. Virial adsorption isotherm model.

The Virial isotherm	$P = \frac{q}{K_H}\exp\left(\frac{2}{S}Aq + \frac{3}{2S^2}Bq^2 + \ldots\right)$
Virial coefficients	$A = \sum_{m=0}^{\infty}\frac{A_m}{T^m} \quad , \quad B = \sum_{m=0}^{\infty}\frac{B_m}{T^m}$
Van't Hoff equation	$K_H = K_\infty \exp\left(\frac{-\Delta H}{R_g T}\right)$
error function	$ERR = \frac{(1-w)}{N}\sum_T\sum_q\left(\frac{P_{exp,T,q} - P_{cal,T,q}}{P_{exp,T,q}}\right)^2 + \frac{w}{N}\sum_T\sum_q\left(P_{exp,T,q} - P_{cal,T,q}\right)^2$

Table 4.7. Moment analysis based on the derivative of diluted breakthrough curves and correlations used to estimate the diffusivity constants.

First moment	$\mu_1 = \frac{L}{u_i}\left(1 + \left(\frac{1-\varepsilon}{\varepsilon}\right)K_H\rho_p R_g T\right)$
Ratio of the variance and 2 times the first moment square	$\frac{\sigma^2}{2\mu_1^2} = \frac{D_{ax}}{u_i L} + \left(\frac{u_i}{L}\right)\left(\frac{\varepsilon}{1-\varepsilon}\right)\left(\frac{R_p}{2k_f} + \frac{R_p^2}{\Omega_p\varepsilon_p D_p} + \frac{r_c^2}{\Omega_c K_H\rho_p R_g T\, D_c}\right)\times$ $\times\left(1 + \frac{\varepsilon_p}{(1-\varepsilon_p)K_H\rho_p R_g T}\right)^{-2}$ with $K_H >> \varepsilon_p$ For the activated carbon $\Omega_p = 8$ (cylinder particles) and $\Omega_c = 3$ (slab micropores)
Axial dispersion	$D_{ax} = (0.45 + 0.55\varepsilon)D_m + 0.35R_p u_i$
Film mass transfer	$Sh = 2.0 + 1.1Re^{0.6}Sc^{1/3}$ with $Sh = 2R_p k_f / D_m$, $\mathrm{Re} = 2\rho_g u_0 R_p/\mu$ and $Sc = \mu/\rho_g D_m$
Bosanquet equation	$\frac{1}{D_p} = \tau_p\left(\frac{1}{D_m} + \frac{1}{D_k}\right)$
Wilke correlation (molecular diffusion coefficients)	$D_m = \frac{1-y_i}{\sum_{\substack{j=1\\ j\neq i}}^{n}\frac{y_i}{D_{ij}}}$
Knudsen diffusivity ($m^2\ s^{-1}$)	$D_k = 97.0\, r_p\sqrt{\frac{T}{M_W}}$ with r_p in meters
Micropore diffusivity	$\frac{D_c}{r_c^2} = \frac{D_c^0}{r_c^2}\exp\left(-\frac{E_a}{R_g T}\right)$

that velocity in the column is constant. The necessary equations are reported in Table 4.7, as well as equations to determine mass transfer parameters like axial dispersion and film-mass transfer coefficients [27-29]. The equation of the ratio of the variance and two times the first moment square ($\sigma^2/2\mu_1^2$) of a pulse was employed after calculation of the derivative of breakthrough curves. To fit the breakthrough curves the mathematical model described in chapter 2 was employed and is now summarized in Table 4.8. The numerical solution of the mathematical model was performed using gPROMS (PSE Enterprise, UK) using orthogonal collocation on finite elements with an absolute and relative tolerance of 1×10^{-5}. In each element of the adsorption bed, 25 elements were used with two interior collocation points (third order polynomials).

Table 4.8. Mathematical model used for fixed-bed experiments of CO_2-H_2-CH_4 multicomponent mixtures.

System of partial differential equations		
mass balance in a differential element of the column	$\frac{\partial}{\partial z}\left(\varepsilon D_{ax} C_{g,T} \frac{\partial y_i}{\partial z}\right) - \frac{\partial}{\partial z}\left(u_0 C_{g,i}\right) - \varepsilon \frac{\partial C_{g,i}}{\partial t} - (1-\varepsilon)\rho_p \frac{\partial \langle \overline{q}_i \rangle}{\partial t} = 0$	
mass balance in a volume element of the adsorbent particle	$\frac{\partial C_{m,i}}{\partial t} + \rho_p \left(\frac{1-\varepsilon_p}{\varepsilon_p}\right) \frac{\partial \overline{q}_i}{\partial t} = \frac{1}{R_p^{k_s}} \frac{\partial}{\partial R}\left(D_{p,i} R^{k_s} \frac{\partial C_{m,i}}{\partial R}\right)$	
Fickian description of diffusion in a micropore or crystal	$\frac{\partial q_i}{\partial t} = \frac{1}{r_c^{k_s}} \frac{\partial}{\partial r}\left(D_{c,i} r^{k_s} \frac{\partial q_i}{\partial r}\right)$	
particle and micropore / crystal averaged adsorbed phase concentrations	$\langle \overline{q}_i \rangle = \frac{k_s+1}{R_p^{k_s+1}} \int_0^{R_p} \overline{q}_i R^{k_s} dR \quad ; \quad \overline{q}_i = \frac{k_s+1}{r_c^{k_s+1}} \int_0^{r_c} q_i r^{k_s} dr$	
Initial Conditions		
$y_i = C_{m,i} = q_i = 0$ for $i \neq inert$; $y_{inert} = 1$ and $C_{m,inert} = C_{g,inert} = C_{g,T}$		
Boundary conditions		
column	particle	micropore/crystal
$(z = 0)$	$(R = 0)$	$(r = 0)$
$u_{0inlet} C_{inlet,i} = u_0 C_{g,i} - \varepsilon D_{ax} C_{g,T} \frac{\partial y_i}{\partial z}$	$\frac{\partial C_{m,i}}{\partial R} = 0$	$\frac{\partial q_i}{\partial r} = 0$
$(z = L)$	$(R = R_p)$	$(r = r_c)$
$\frac{\partial C_{g,i}}{\partial z} = 0$	$\varepsilon_p D_{p,i} \left.\frac{\partial C_{m,i}}{\partial R}\right\|_{R=R_p} = k_f \left(C_{g,i} - C_{m,i}\big\|_{R=R_p}\right)$	$q_i = q_i^*$

4.2.3.3 Results

Adsorption equilibria of carbon dioxide on the selected modified activated carbon were studied at 303 and 323 K in the pressure range 0-7 bar. The CO_2 absolute amount adsorbed on the samples of AC5-I and AC5-KS is shown in Figure 4.9. The extrudates used in the measurements were selected after randomly mixing the entire 400 g sample. The reproducibility of the experiments was verified and also the viability of the scale-up experimental protocol since the results obtained for AC5-I and AC5-KS within experimental error were approximately the same, that is, no significant variations were observed. In Figure 4.9, the results on the original activated carbon R2030 reported by Grande *et al.* (2008) [22] are also shown for comparison. At 303 K and 7 bar, the amount adsorbed of carbon dioxide on the modified activated carbon AC5-KS is ~ 6.7 mol kg^{-1} and this is ~ 1 mol kg^{-1} (17.5%) more than the CO_2 amount adsorbed on R2030 (~ 5.7 mol kg^{-1}). At 303 K and 1 bar, the difference between the CO_2 amount adsorbed on the modified activated carbon AC5-KS and on R2030 is ~ 0.1 mol kg^{-1}. However, the density of the modified adsorbent is slightly smaller than the original activated carbon ($\rho_{p,\text{AC5-KS}}$ = 786 kg m^{-3}; $\rho_{p,\text{R2030}}$ = 841 kg m^{-3}). Figure 4.9 shows the non-linearity of the CO_2 isotherms on the original activated carbon R2030 and the small decrease of the steepness of the CO_2 isotherms on the AC5-KS sample.

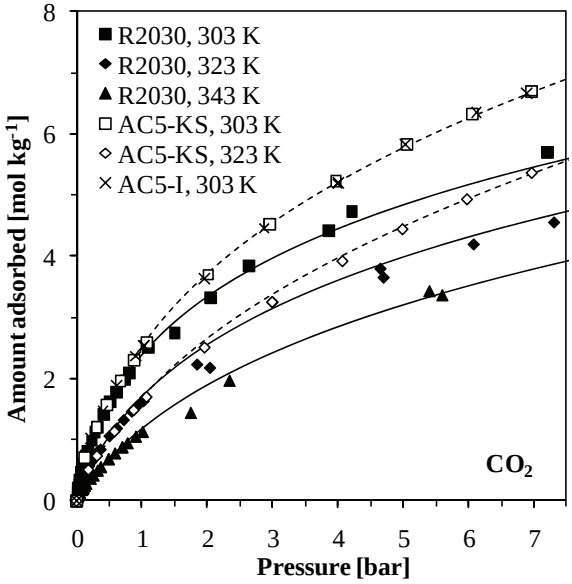


Figure 4.9. Amount adsorbed of CO_2 on the original AC (closed symbols; Grande et al., 2008), on the modified AC5-I and AC5-KS (open symbols): experimental points at 303 (■,×,□), 323 (◆,◇) and 343 K (▲). Fitting with the Virial isotherm model of the original AC (—) and of the AC5-KS (- - -).

Adsorption equilibria of hydrogen, methane, carbon monoxide and nitrogen on the selected modified activated carbon AC5-KS were also studied at 303 and 323 K in the pressure range 0-7 bar. The experimental adsorption data of these gases are reported in Figure 4.10. Improvements on the adsorption capacities of the modified adsorbent for hydrogen, methane and nitrogen were obtained: ~ 0.04 mol kg^{-1} for H_2 and ~ 0.5 mol kg^{-1} for CH_4 (at 303 K and 7 bar) and ~ 0.14 mol kg^{-1} for N_2 (at 303 K and 5 bar).

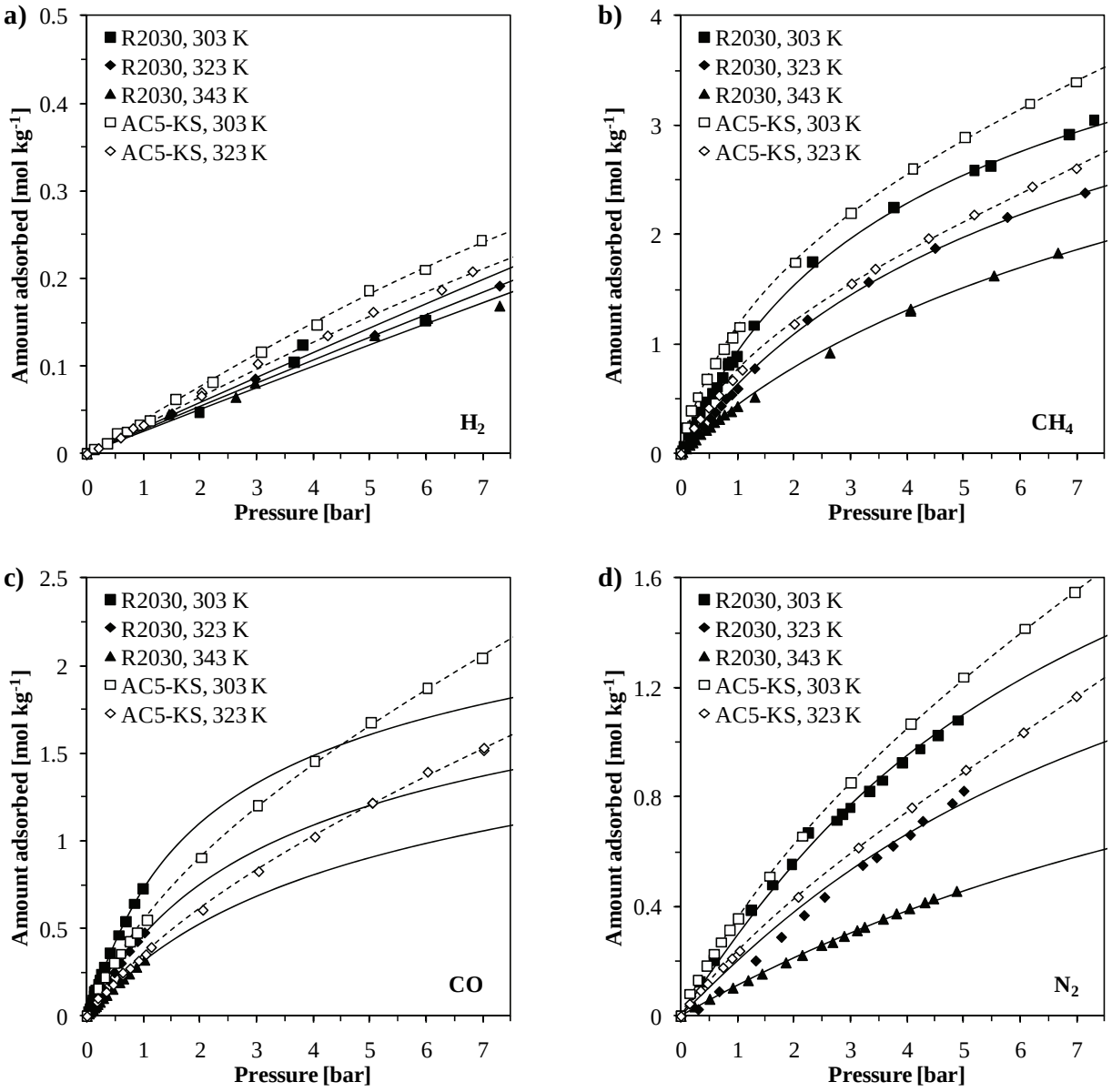


Figure 4.10. Amount adsorbed of H_2 (a), CH_4 (b), CO (c) and N_2 (d) on the original AC (closed symbols; Grande et al., 2008) and on the modified AC5-KS (open symbols): experimental points at 303 (■,□), 323 (◆,◇) and 343 K (▲). Fitting with the Virial isotherm model of the original AC (—) and of the AC5-KS (- - -).

The results obtained for the five gases (CO_2, CH_4, CO, N_2 and H_2) were fitted using the Virial isotherm and the parameters are detailed in Table 4.9. As reported in Figure 4.9 and Figure 4.10, a good fitting is obtained for all gases in the whole pressure and temperature range studied.

Table 4.9. Virial adsorption isotherm fitting parameters of CO_2, H_2, CH_4, CO and N_2 for the modified activated carbon AC5-KS at 303-323 K.

Species	K_∞ [mol kg^{-1} bar^{-1}]	$(-\Delta H)$ [kJ mol^{-1}]	$A_0 \times 10^{-5}$ [m^2 mol^{-1}]	$A_1 \times 10^{-6}$ [m^2 K mol^{-1}]	$B_0 \times 10^{-11}$ [m^4 mol^{-2}]	$B_1 \times 10^{-11}$ [m^4 K mol^{-2}]
CO_2	8.06×10^{-5}	28.02	0.081	45.31	-0.365	92.247
H_2	2.12×10^{-3}	7.26	-1.917	0.1994-	-4.015	7315.4
CH_4	2.29×10^{-4}	23.18	12.808	-294.44	-6.101	1745.7
CO	7.63×10^{-5}	23.23	-0.149	-105.46	-2.407	528.18
N_2	3.06×10^{-4}	18.27	11.989	-278.79	-13.758	3988.6

The results confirm the increase of the adsorption capacities of the modified adsorbent AC5-KS for carbon dioxide, methane and nitrogen in comparison to the original activated carbon. It can be concluded that the new material (AC5-KS) prepared will provide a higher capacity to a PSA column since it increases the adsorption capacity of the main contaminants. According to the objectives proposed, the new material with enhanced capacity toward contaminants was produced with a very considerable scale up of four hundred grams.

The diluted breakthrough experiments performed with a diluted stream of carbon dioxide in the column packed with the modified activated carbon AC5-KS are shown in Figure 4.11. The objective of these experiments was to determine if the diffusion rate is modified in this new sample. A diluted stream (CO_2 partial pressure of 0.005 bar) was employed to avoid the effect of isotherm non-linearity. At 303 K, the diffusion rate of carbon dioxide in the modified carbon AC5-KS is approximately the same. The micropore diffusivity divided by r_c^2 (D_c/r_c^2) for the original activated carbon and for the modified activated carbon obtained at 303 K is 4.27×10^{-2} [22] and 3.70×10^{-2} s^{-1} [30], respectively, (Table 4.10).

The contribution of the axial dispersion term is approximately 90%, showing that it is the most relevant dispersive mechanism.

The transport kinetics of methane, carbon monoxide and nitrogen on the modified AC5-KS were also studied by diluted breakthrough curves (0.5% of adsorbate balanced with helium) at the same temperatures (see Figure 4.12). With these mixtures, the effect of the isotherm non-linearity

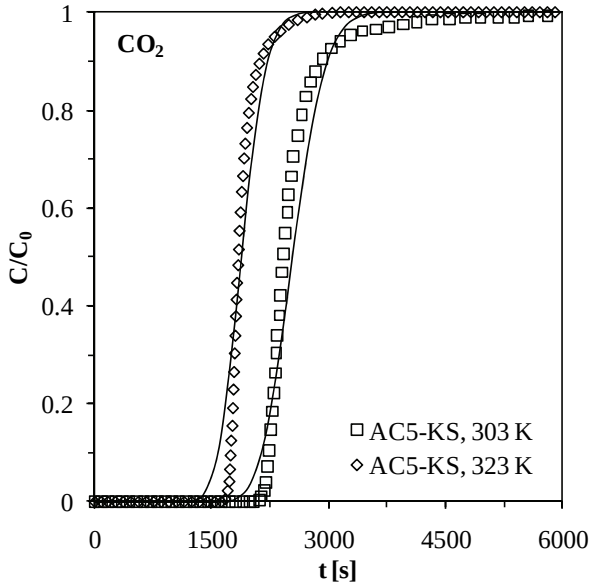


Figure 4.11. Diluted breakthrough curves of CO_2 (0.5% of CO_2 balanced with He) on the modified activated carbon AC5-KS at 303 (□) and 323 K (◇); Total pressure of 1 bar; Flow rate of 6.25×10^{-7} m^3 s^{-1} (measured at 298 K and 1 bar); —— Simulation with the kinetic parameters obtained.

Table 4.10. Micropore diffusivity (divided by r_c^2) and activation energy of CO_2, H_2, CH_4, CO and N_2 in the original and modified activated carbons.

Species	T [K]	Original AC		AC5-KS	
		(D_c/r_c^2) [s^{-1}]	E_a [kJ mol^{-1}]	(D_c/r_c^2) [s^{-1}]	E_a [kJ mol^{-1}]
CO_2	303	4.27×10^{-2}	25.5	3.70×10^{-2}	17.6
	323	6.13×10^{-2}		4.73×10^{-2}	
	343	6.67×10^{-2}		—	
H_2	303	1.35×10^{-1}	—	8.130	8.51
	323	—		10.04	
CH_4	303	1.55×10^{-2}	9.75	7.56×10^{-2}	26.4
	323	3.01×10^{-2}		1.44×10^{-1}	
	343	5.04×10^{-2}		—	
CO	303	1.38×10^{-1}	12.1	3.59×10^{-1}	10.8
	323	2.18×10^{-1}		5.06×10^{-1}	
	343	2.40×10^{-1}		—	
N_2	303	—	—	7.16×10^{-1}	19.8
	323	—		11.7×10^{-1}	

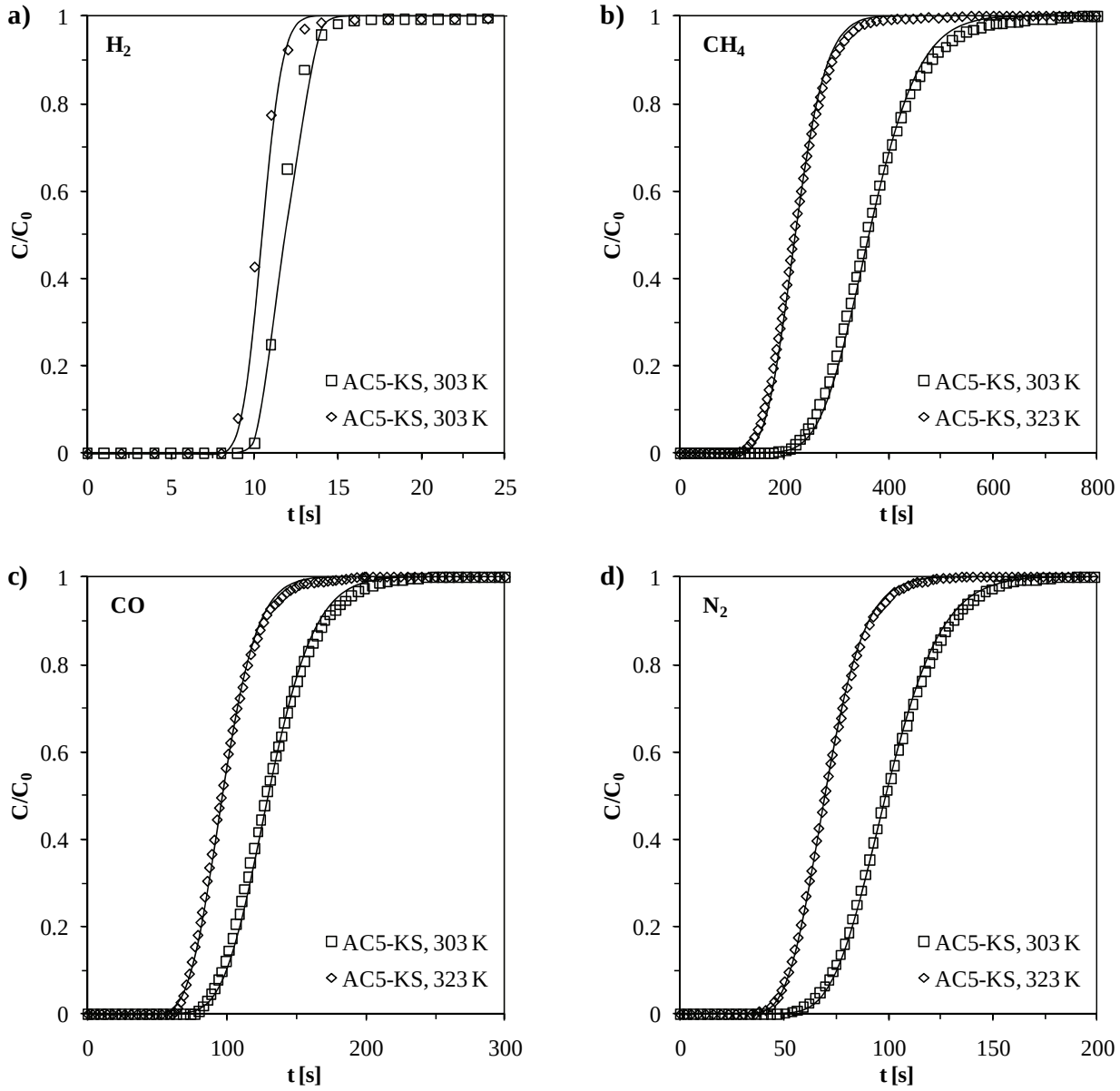


Figure 4.12. Breakthrough curves of pure H_2 (a) and diluted breakthrough curves of CH_4 (b), CO (c) and N_2 (d) (0.5% of adsorbate balanced with He) on the modified activated carbon AC5-KS at 303 (□) and 323 K (◇); Total pressure of 1 bar; Flow rates (measured at 298 K and 1 bar) of 8.67×10^{-7} (a), 9.00×10^{-7} (b, c) and 6.67×10^{-7} $m^3 s^{-1}$ (d); —— Simulation with the kinetic parameters obtained.

was once again avoided. Experiments employing hydrogen diluted in helium show that H_2 diffusion is extremely fast and H_2 is weakly adsorbed at low partial pressures making the measurements of the kinetic parameters difficult. Thus and also since hydrogen isotherms are linear in the pressure range 0-1 bar, breakthrough curves of pure H_2 were performed for the same

temperature values. The breakthrough experiments were performed to determine the diffusion coefficients in this new sample (Table 4.10). According to the analysis of the derivative of each breakthrough curve, hydrogen has the highest micropore diffusivity followed by nitrogen, carbon monoxide, methane and finally carbon dioxide. This is coincident with the molecular diameter of the different gases, except for the case of CO_2. The diffusion of carbon dioxide within the micropore structure is slower because of its stronger interactions with the activated carbon surface. The set of experiments performed indicates that micropore resistances control diffusion within the extrudates. However, measurements of hydrogen diffusion were extremely difficult since its diffusion is very fast and the breakthrough behaviour was dominated by axial dispersion. The very fast diffusion of hydrogen is important in PSA applications.

4.3 Ion exchange of zeolites for enhanced N_2 capacity

4.3.1 Routes for enhanced N_2 adsorption

Zeolites are microporous crystalline solids with neutral SiO_2 groups and negatively charged $(AlO_2)^-$ compensated by a non-framework cation (Na^+, Li^+, Ba^{2+} and/or Ca^{2+}) [31-33]. These cations interact with the gas molecules that we want to separate and are responsible for the selectivity of the material [31, 33]. These charge-balancing cations can be permuted through ion exchange [34]. To reach total or high exchange levels with simplicity and reproducibility, this method should be repeated several times (it essentially depends on the amount of cations present in solution), involving handling and recycling of large volumes of solution [35]. Another procedure to reach high levels of exchange is to pass a continuous flow of calcium solution through a column packed with zeolite until the exchange is completed.

As shown in the previous chapters, in many adsorbents used for H_2 purification by PSA, nitrogen is the lighter contaminant and the first one to break through. This is the reason why improving the capacity of the adsorbents towards this gas will increase the productivity of the unit. When N_2 is not present, the extent of the feed step is determined by CH_4 and CO [36]. Many authors reported different types of ion exchange of a zeolite to allow the enhancement of the nitrogen selectivity [36-39]. Calcium and barium were employed for this purpose [36]. Significant enhancements were reported for zeolites with more than 50% of exchanged calcium ions [39]. Different types of lithium exchanged zeolite X with different ion exchange ratios were also suggested in the literature due to their higher adsorption capacities for nitrogen and carbon monoxide. It was reported that a binary ion exchanged zeolite of type X with lithium and calcium

(85% of Li^+ and 15% of Ca^{2+}; instead of calcium it could also be strontium) had the best performance to enhance the N_2 adsorption capacity [37]. Moreover, Plee (2002) [38] mentioned that a binary lithium and calcium ion exchanged zeolite for a $Li/(Li + Ca)$ ratio higher than 0.7 is preferable for nitrogen adsorption.

The purpose of this work is to provide fundamental adsorption data of SMR off-gases (CO_2, H_2, CH_4, CO and N_2) on ion exchange zeolite 13X with enhanced adsorption capacity toward nitrogen. Three samples of exchanged zeolites were prepared starting from a commercial zeolite 13X and then characterized. Diffusion parameters of nitrogen in zeolite 13X and the three exchanged zeolites at 303 and 323 K were determined. A selection of the "best" adsorbent for N_2 adsorption was based on the difference between the amount of gas adsorbed at the highest and lowest adsorbate partial pressures, which in this case are 0.25 and 0.01 bar. The difference between these amounts will be termed as "useful capacity". The adsorbent chosen was the one with the "best" performance (higher adsorption capacity): 13X-Ca. Adsorption equilibrium and kinetics of N_2, CO_2, CH_4, CO and H_2 on the 13X-Ca were studied at 0-7 bar and 303 and 323 K.

4.3.2 Adsorbents preparation and characterization

4.3.2.1 Preparation protocol for ion exchange

Three different samples were prepared by exchanging 10.0 g ($\pm 10^{-5}$ g) of zeolite 13X extrudates (Trade/Shanli, China) with lithium, calcium and barium. To exchange the samples with Li^+, Ca^{2+} or Ba^{2+} ions with a proportion of 20.0 $mL_{solution}/g_{zeolite}$, three 1 N solutions of 200 mL ($\pm$ 0.10 mL) were prepared in deionised water: one with LiCl, a second with $Ca(NO_3)_2$ and another with $BaCl_2$. Each sample was introduced into an Erlenmeyer with 50 mL ($\pm$ 0.05 mL) of the respective cationic solution. The three Erlenmeyer flasks were placed in a shaker for 12 h, at 313 K ($\pm$ 0.1 K). The solid and liquid phases present in the flasks were separated by filtration. This procedure was repeated three more times to reach the 200 mL of cationic solution used in each sample. At the end of the fourth batch, the two phases present in the Erlenmeyers were separated by filtration and then the samples (solid phase) were dried in an oven at 373 K ($\pm$ 0.1 K) for 1 day.

4.3.2.2 Sample characterization and reproducibility

For the zeolite 13X and for three samples of exchanged zeolites 13X (13X-Li, 13X-Ba and 13X-Ca), the morphology of the particles were observed by scanning electron microscopy (SEM). Semi-quantitative elemental composition was determined by energy dispersive X-ray (EDX).

A scale-up protocol to exchange 80 g/batch (± 10^{-5} g/batch) of exchanged zeolite 13X sample with the highest performance for nitrogen (adsorbent with higher N_2 adsorption capacity) was performed using similar experimental conditions as detailed previously. In the scale-up protocol, 400 mL (± 0.30 mL) of 1 N cationic solution was used in the four exchange batches. During the scale-up procedure, the concentration history of the Na^+ cations in the supernatants was determined by atomic absorption spectrometry (GBC 932 Plus Atomic Absorption Spectrometer). The working current/wavelength was adjusted to 5.0 mA/330.2 nm, giving a detection limit of 4 mg L^{-1}. The instrument response was periodically checked with Na^+ solution standards. This procedure allowed the calculation of the final total concentration of exchanged cations on the structure of the modified zeolite material.

4.3.2.3 Results

The scanning electron microscopy (SEM) images used to determine the morphology of the particles of the samples of zeolite 13X and of the three ion exchanged samples (13X-Li, 13X-Ba and 13X-Ca) are shown in Figure 4.13. The dimensions of the crystals determined by SEM are ~ 3 µm. It was observed that the crystals were not damaged or destroyed after the ion exchange.

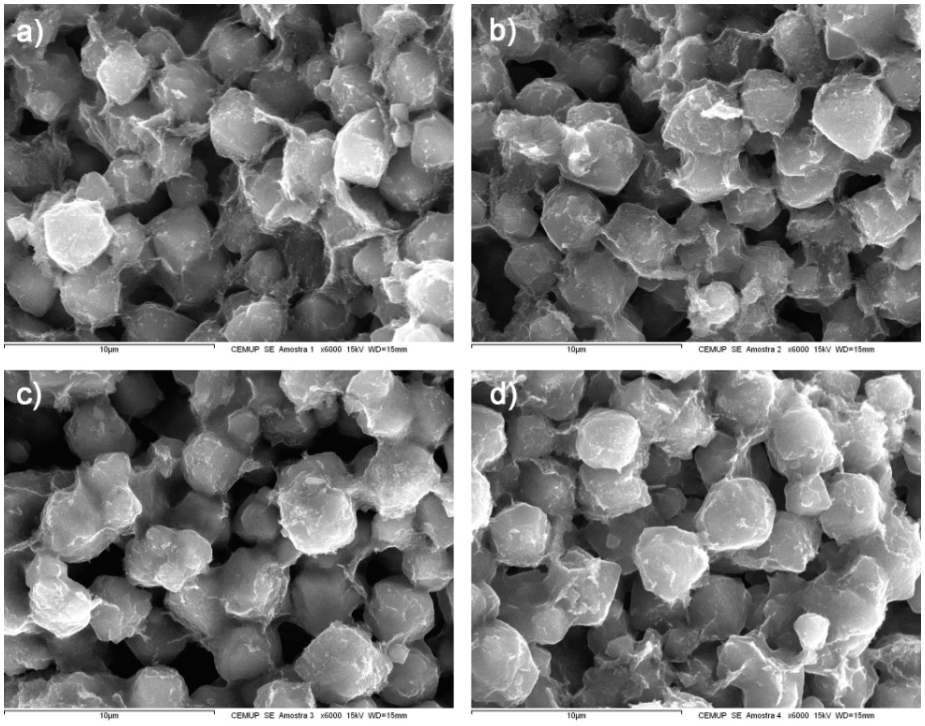


Figure 4.13. Scanning electron microscopy (SEM) image of zeolite 13X (a) and ion exchanged zeolites 13X-Li (b), 13X-Ba (c) and 13X-Ca (d).

Energy dispersive X-ray (EDX) analyses of the four zeolite samples (13X, 13X-Li, 13X-Ba and 13X-Ca) were performed to observe the effects of ion exchange. The EDX patterns are shown in Figure 4.14. All the exchanged samples show a significant reduction of the amount of sodium in the zeolite structure when compared to the original sample. Due to the detection limitation to lower atomic elements, i.e., the X-ray energy of lithium is too low (54.75 eV) [40], the Li presence is not detected by EDX analysis (see Figure 4.14 b).

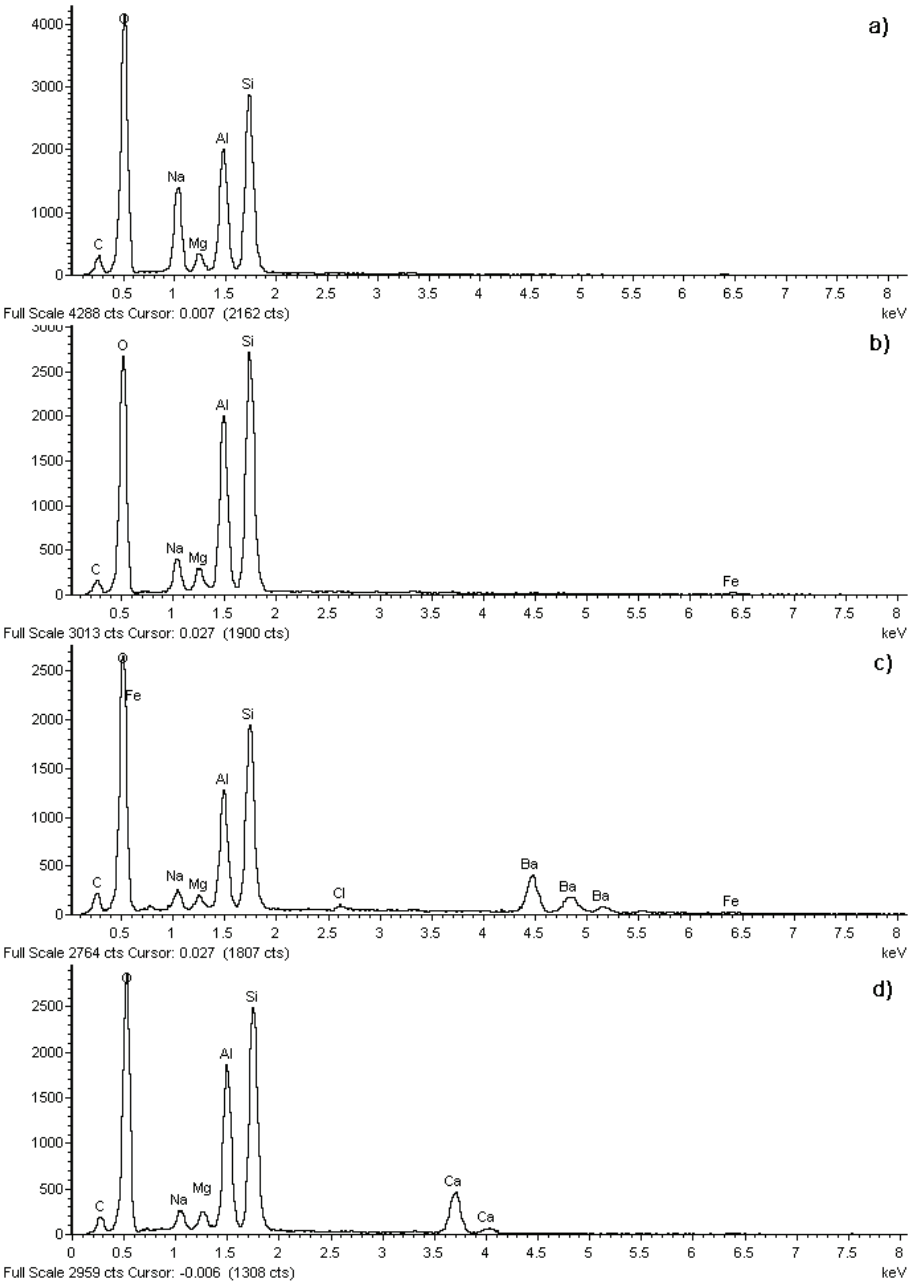


Figure 4.14. Energy dispersive X-ray (EDX) pattern of zeolite 13X (a) and ion exchanged zeolites 13X-Li (b), 13X-Ba (c) and 13X-Ca (d).

For the scale-up sample of zeolite 13X-Ca, the obtained evolution of Na^+ concentration for each exchange was determined by atomic absorption (Figure 4.15). It is observed that the equilibrium is reached after ~ 250 min. The determined Na^+ concentrations in solution are respectively 11.4, 3.7, 1.5 and 0.9 g L^{-1} at the end of each exchange. The ion exchange results in a final total concentration of 0.076 $g_{calcium}/g_{material}$ on the structure of the modified zeolite material.

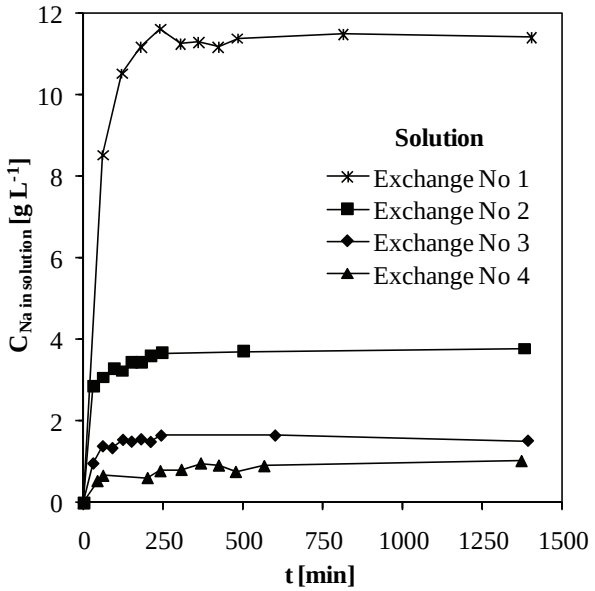


Figure 4.15. Concentration history of the Na^+ cations exchange in zeolite 13X using 400 mL of 1N Ca^{2+} solutions and 80 g of zeolite: Exchange no 1 (-✳-), 2 (-■-), 3 (-◆-) and 4 (-▲-).

4.3.3 Nitrogen adsorption on ion exchanged zeolites

4.3.3.1 Experimental

The adsorption equilibrium of pure nitrogen on the samples of zeolites 13X, 13X-Li, 13X-Ba and 13X-Ca were studied by chromatographic technique measurements of two sets of breakthrough curves at 303 and 323 K (± 0.1 K) and atmospheric pressure: one set with mixtures of 1.0% of nitrogen and another of 25.0% of nitrogen, both balanced with helium. The experimental conditions used in these measurements and the dimensions of the column are given in Table 4.11.

The breakthrough experiments performed with the mixture of 1.0% N_2 balanced in He were also used to determine the transport kinetics of nitrogen in the four samples through moment analysis of the pulse response, i.e., derivative of the diluted breakthrough curve. The crystal

diffusivities were calculated based on the experimental values of the moments together with estimated values of axial dispersion coefficients, molecular and macropore diffusivities. These values were estimated according to the correlations reported in chapter 3 and also summarized in Table 4.7 [27-29]). Note that for the zeolite $\Omega_p = 8$ (cylinder particles) and $\Omega_c = 15$ (spherical crystals). Employing this highly diluted mixture (N_2 partial pressure of 0.01 bar), we will not have the effect of isotherm non-linearity and we ensure isothermal conditions with an almost constant flow rate.

Table 4.11. Experimental conditions used on the measurement of the breakthrough curves of N_2 (1.0% and 25.0% of N_2 balanced in He) in zeolites 13X, 13X-Li, 13X-Ba and 13X-Ca at 303 and 323 K and 1 bar of total pressure.

Adsorbate	N_2			
Partial pressure [bar]	0.010, 0.250			
Adsorbent	13X	13X-Li	13X-Ba	13X-Ca
Mass of Adsorbent × 10^3 [kg]	9.118	6.948	8.597	7.863
Bed height [m]	0.165	0.134	0.139	0.139
Bed volume × 10^5 [m^3]	1.245	1.012	1.048	1.048
Bed porosity, ε	0.396	0.397	0.395	0.395
Pellet porosity, ε_p	0.394	0.431	0.322	0.380
Adsorbent density, ρ_p [kg m^{-3}]	1212	1138	1356	1241
Solid density, ρ_s = 2000 kg m^{-3}; Crystal radius, r_c = ~ 1.5 μm; Average pellet radius, $R_p = 8.5 \times 10^{-4}$ m; Average pellet length, L_p = ~ 5×10^{-3} m				

To degass the sample of zeolite 13X and the ion exchanged samples of zeolite 13X, a helium flow of 6.25×10^{-7} m^3 s^{-1} (measured at 298 K and 1 bar) was used overnight at 593 K (± 0.1 K), after heating at 1 K min^{-1} (± 0.1 K min^{-1}) from 298 K.

4.3.3.2 Results

Breakthrough curves of nitrogen in the all the zeolites 13X, 13X-Li, 13X-Ba and 13X-Ca are reported in Figure 4.16. Two different concentrations of nitrogen were employed to determine the difference in capacity between high and low pressure. This difference in loading is related to the effective capacity in a PSA unit. Using these breakthrough curves, the amount of nitrogen adsorbed for the four samples was determined (Table 4.12).

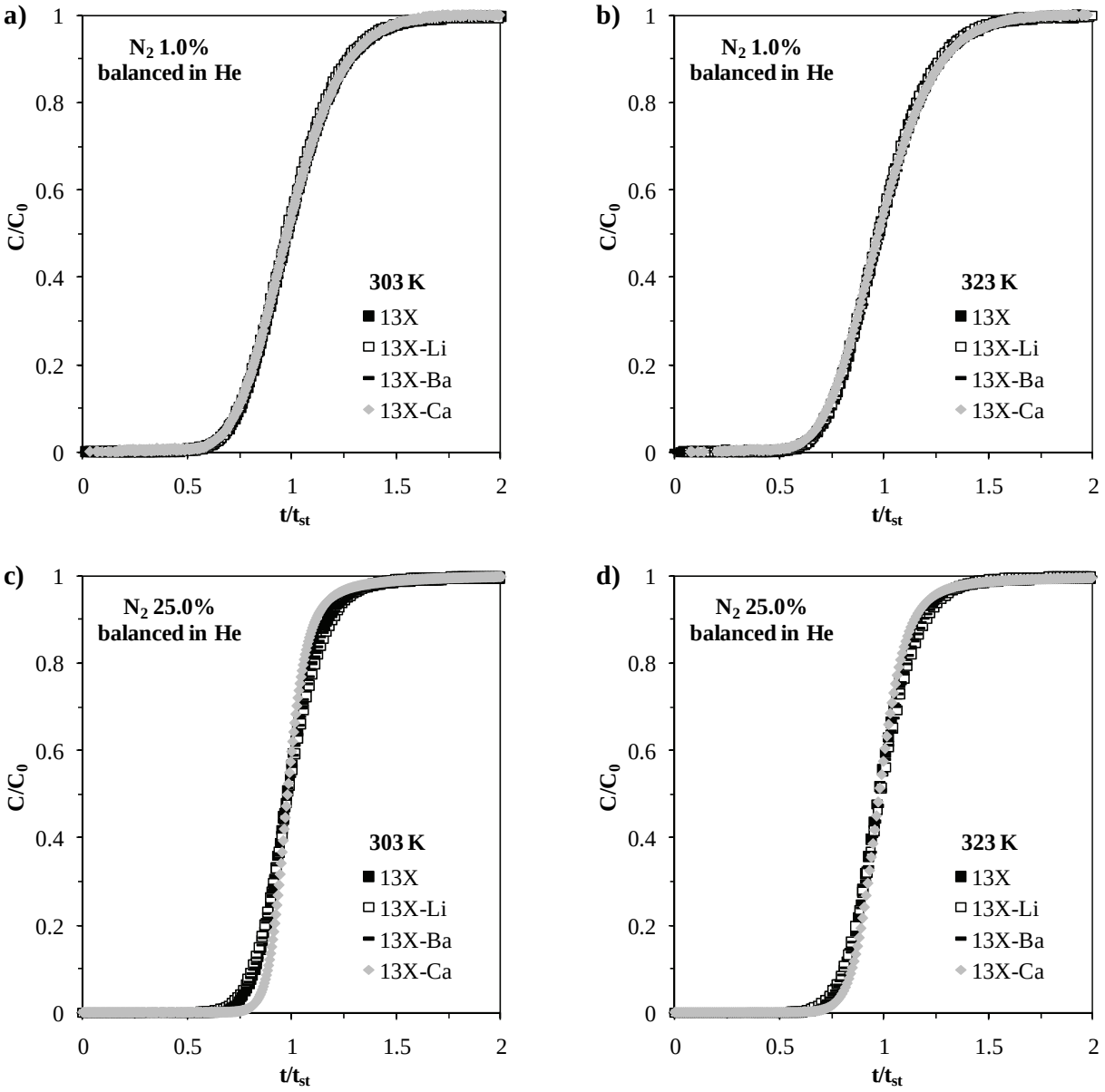


Figure 4.16. Breakthrough curves of 0.01 bar of N_2 balanced in He [a) 303 K and b) 323 K] and 0.25 bar of N_2 balanced in He [c) 303 K and d) 323 K] on the zeolite 13X (■), 13X-Li (□), 13X-Ba ( ) and 13X-Ca (◆); experimental conditions and results reported in Table 4.11 and Table 4.12.

The breakthrough curves were also employed to determine diffusion parameters in the different samples. In previous studies, it was reported that diffusion within zeolite extrudates of 13X was controlled by macropore diffusion [41]. However, the diameter of zeolite crystals in this sample is much larger as well as the pore network of the binder. For these reasons, we have observed that the diffusion mechanism is controlled within the crystals of the zeolite. The crystal diffusivities in the four zeolite samples were also determined for nitrogen at 303 and 323 K using

Table 4.12. Breakthrough experimental results obtained for nitrogen (mixtures of 1.0% or 25.0% of N_2 balanced in He) in zeolites 13X, 13X-Li, 13X-Ba and 13X-Ca at 303 and 323 K and 1 bar of total pressure.

p_{N_2} [bar]	Zeolite	13X		13X-Li		13X-Ba		13X-Ca	
	Temperature [K]	303	323	303	323	303	323	303	323
0.01	μ_1 [s]	110.9	75.7	80.0	57.5	131.1	85.4	287.3	141.1
	σ^2 [s^2]	587.7	327.0	421.6	250.6	771.7	387.2	3097	893.0
	$u_0 \times 10^2$ [m s^{-1}]	0.854	0.911	0.854	0.911	0.854	0.911	0.854	0.911
	$u_i \times 10^2$ [m s^{-1}]	2.16	2.30	2.15	2.30	2.16	2.31	2.16	2.30
	$q \times 10^3$ [mol kg^{-1}]	2.936	1.947	2.753	1.926	3.758	2.394	9.026	4.145
	K_H [mol kg^{-1} bar^{-1}]	0.290	0.193	0.272	0.188	0.371	0.237	0.914	0.440
	$D_c/r_c^2 \times 10^2$ [s^{-1}]*	4.07	4.43	3.74	4.05	4.73	5.24	3.48	4.57
	$\frac{D_c\|_{\text{exchanged 13X}}}{D_c\|_{\text{13X}}}$ [-]	1.00	1.00	0.920	0.916	1.16	1.18	0.85	1.03
0.25	μ_1 [s]	107.7	74.4	75.5	56.1	121.9	82.1	199.7	121.2
	$q \times 10^2$ [mol kg^{-1}]	7.890	5.357	6.710	4.914	10.81	7.173	17.95	10.78
$\Delta q \times 10^2$ [mol kg^{-1}]#		7.596	5.162	6.435	4.721	10.43	6.934	17.05	10.37
$\frac{\Delta q\|_{\text{exchanged 13X}}}{\Delta q\|_{\text{13X}}}$ [-]		1.00	1.00	0.847	0.915	1.37	1.34	2.24	2.00

At 303 K: $Q = 6.44 \times 10^{-7}$ m^3 s^{-1} (at 303 K and 1 bar); $C_0 = 0.402$ mol m^{-3};
$D_{ax} = 3.38 \times 10^{-5}$ m^2 s^{-1}; $D_m = 7.18 \times 10^{-5}$ m^2 s^{-1}; $D_p = 3.59 \times 10^{-5}$ m^2 s^{-1}; $k_f = 0.1001$ m s^{-1}
At 323 K: $Q = 6.87 \times 10^{-7}$ m^3 s^{-1} (at 323 K and 1 bar); $C_0 = 0.377$ mol m^{-3};
$D_{ax} = 3.73 \times 10^{-5}$ m^2 s^{-1}; $D_m = 7.99 \times 10^{-5}$ m^2 s^{-1}; $D_p = 3.99 \times 10^{-5}$ m^2 s^{-1}; $k_f = 0.1109$ m s^{-1}

* Estimated using a tortuosity factor, $\tau_p = 2$
\# $\Delta q = (q|_{0.25\ bar} - q|_{0.01\ bar})$

the breakthrough curves with 1.0% N_2 balanced in helium. The results are reported in Table 4.12. No significant variations were observed in the shape of the curves indicating that the prepared samples do not present any additional resistance for diffusion. For the more concentrated experiments (Figure 4.16 c and Figure 4.16 d) the stronger non-linearity of the 13X-Ca sample results in a steeper concentration front.

According to the analysis of the derivative of each breakthrough curve, the contributions of mass transfer resistances were determined. Table 4.13 shows the contributions of mass transfer resistances for the N_2 breakthrough experiments in zeolites 13X, 13X-Li, 13X-Ba and 13X-Ca.

Table 4.12 shows a largest crystal diffusivity value at both temperatures for zeolite 13X-Ba, followed by zeolites 13X, 13X-Li, and 13X-Ca. The nitrogen crystal diffusivities (D_c) for the

Table 4.13. Contributions of the axial dispersion term, film mass transfer term, pore resistance term and crystal resistance term for N_2 in zeolites 13X, 13X-Li, 13X-Ba and 13X-Ca at 303 and 323 K and 1 bar of total pressure.

Adsorbent	Temp. [K]	Term contribution [%]			
		Axial Disp.	Film Res.	Pore Res.	Crystal. Res.
13X	303	39.7	1.3	2.0	57.0
	323	34.7	1.0	1.5	62.8
13X-Li	303	35.6	1.1	1.6	61.7
	323	31.4	0.9	1.3	66.4
13X-Ba	303	50.1	1.7	3.2	45.0
	323	44.3	1.4	2.5	51.9
13X-Ca	303	60.1	2.2	3.4	34.3
	323	52.0	1.7	2.7	43.6

$$\frac{\sigma^2}{2\mu_1^2} = \left\{\begin{matrix}\text{Axial}\\ \text{Disp.}\end{matrix}\right\} + \left(\frac{u_i}{L}\right)\left(\frac{\varepsilon}{1-\varepsilon}\right)\left(\left\{\begin{matrix}\text{Film}\\ \text{Res.}\end{matrix}\right\} + \left\{\begin{matrix}\text{Pore}\\ \text{Res.}\end{matrix}\right\} + \left\{\begin{matrix}\text{Crystal}\\ \text{Resist.}\end{matrix}\right\}\right)\left(1 + \frac{\varepsilon_p}{(1-\varepsilon_p)K_H \rho_p R_g T}\right)^{-2}$$

zeolite 13X published in the literature [42-43] are 3.00×10^{-8} and 4.00×10^{-8} $m^2 s^{-1}$ at 301 and 323 K, respectively. This means that the nitrogen crystal diffusivities obtained in this study are four orders of magnitude lower. However, the reported values were determined by microscopic methods (N. M. R.) and it is well known that important differences may be obtained in comparing values obtained by micro and macroscopic methods [44]. Table 4.12 also shows an increase of the adsorption capacity of all the ion exchanged samples of zeolite 13X for nitrogen, with the exception of zeolite 13X-Li. The difference of useful capacities between high and low pressure of zeolites 13X-Ba and 13X-Ca for nitrogen relative to the zeolite 13X are ~ 1.37 and ~ 2.24, respectively. Therefore, since the resistance of diffusion in all zeolite samples is similar, the ion exchange of zeolite 13X with Ba^{2+} and Ca^{2+} will favour the nitrogen adsorption for separations of this gas in a PSA unit. This result is not contradictory with air separation processes (where 13X-Li is employed) [45]. The main difference is that in this particular application, the partial pressure of N_2 is much smaller and 13X-Li isotherms (less steep) presenting lower loading at low partial pressures.

From these experiments we have determined that the adsorbent with a higher operating capacity for a PSA unit is the 13X-Ca sample and further studies were performed on this sample.

4.3.4 Adsorption kinetics of CO_2, CH_4, CO and H_2

4.3.4.1 Experimental

Similar breakthrough curves of those reported in section 4.3.3.1 but using 0.5% of gas diluted in helium were performed to determine the transport kinetics of carbon dioxide, methane and carbon monoxide in the sample with the highest adsorption capacity for nitrogen (Table 4.14). Pure breakthrough curves of H_2 were performed since H_2 isotherms are linear in the pressure range 0-1 bar.

Table 4.14. Experimental conditions used on the measurement of the breakthrough curves of CO_2, CH_4, CO (0.5% of adsorbate balanced in He) and of pure H_2 in zeolite 13X-Ca at 303 and 323 K and 1 bar of total pressure.

Adsorbate	CO_2, CH_4 and CO	H_2
Partial pressure [bar]	0.005	1
Mass of Adsorbent × 10^3 [kg]	4.498	
Bed height [m]	0.080	
Bed volume × 10^5 [m^3]	0.6034	
Bed porosity, ε	0.399	
Pellet porosity, ε_p	0.380	
Adsorbent density, ρ_p [kg m^{-3}]	1241	
Solid density, ρ_s = 2000 kg m^{-3}; Crystal radius, r_c = ~ 1.5 μm; Average pellet radius, R_p = 8.5 × 10^{-4} m; Average pellet length, L_p = ~ 5 × 10^{-3} m		

4.3.4.2 Results

The breakthrough curves of CO_2, CH_4, CO and H_2 for the exchanged zeolite 13X sample with the highest performance for nitrogen at 303 and 323 K are reported in Figure 4.17. The dispersive effects are more evident in the breakthrough curves of methane and carbon monoxide than for hydrogen or carbon dioxide. In the case of the CO_2 breakthroughs, the outlet front of this gas takes more time to completely leave the column due to the higher CO_2 adsorption capacity than for the other gases. The dispersion of the breakthrough curve shows that carbon dioxide has a slower diffusion than the other gases.

The reciprocal time constant for crystal diffusion (D_c/r_c^2) was determined for CO_2, CH_4, CO and H_2 in zeolite 13X-Ca at both temperatures and the results are reported in Table 4.15. According to the analysis of the derivative of each breakthrough curve, the most relevant

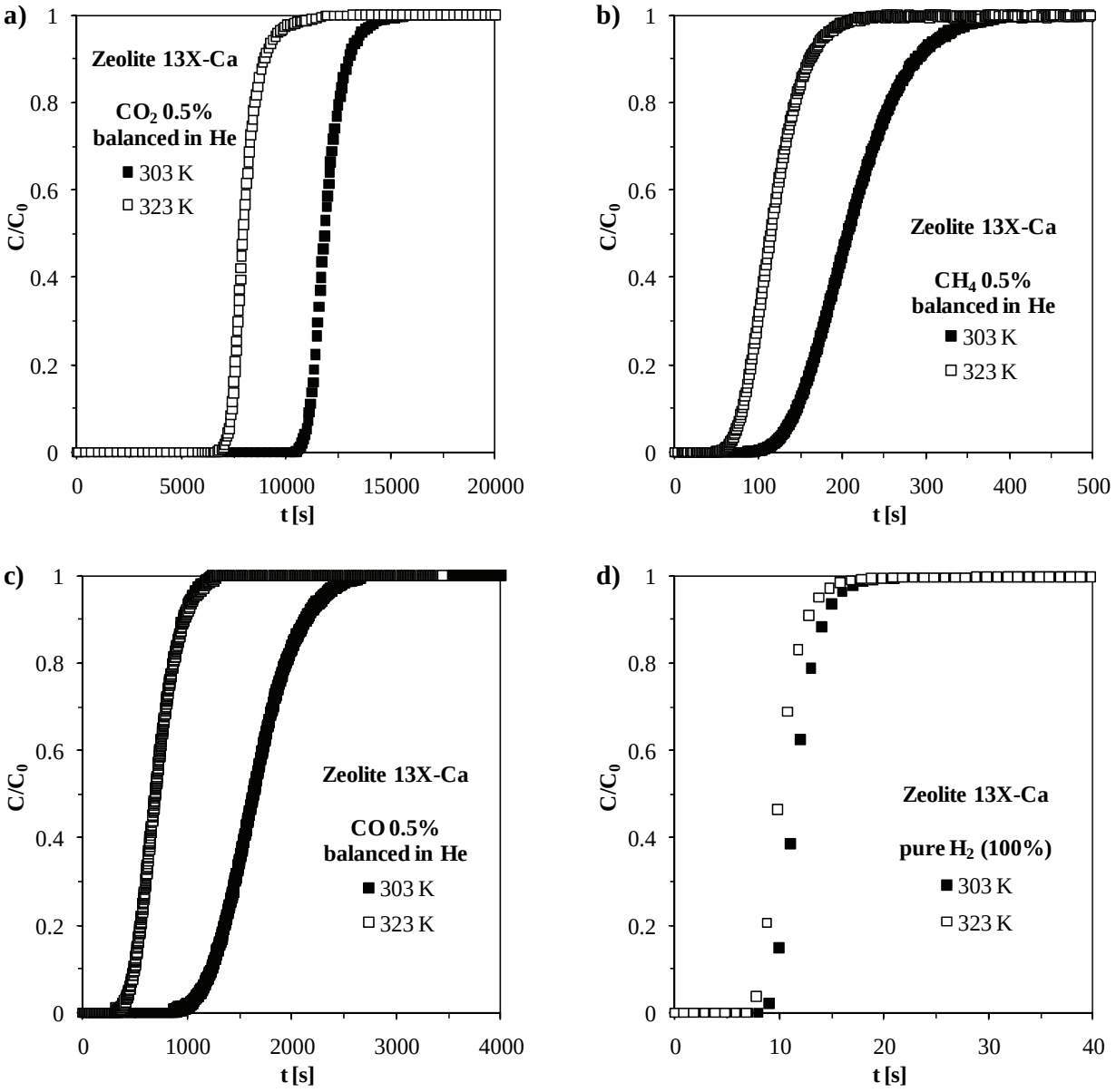


Figure 4.17. Diluted breakthrough curves (0.005 bar of adsorbate balanced in He) of CO_2 (a), CH_4 (b) and CO (c) and breakthrough of pure H_2 (d) on zeolite 13X-Ca at 303 (■) and 323 K (◇); experimental conditions and results reported in Table 4.14 and Table 4.15.

dispersive mechanism is the axial dispersion term and the micropore diffusivity is the controlling mechanism for all gases (comparing the contributions of the three mass transfer resistances). In Table 4.16, the contributions of mass transfer resistances for all gases (CO_2, H_2, CH_4, CO and N_2) in zeolite 13X-Ca are reported.

The crystal diffusivities were also studied varying the tortuosity and the axial dispersion coefficient correlation. Changing the tortuosity from 2 to 6, the estimation of the macropore

Table 4.15. Breakthrough experimental results obtained for carbon dioxide, methane, carbon monoxide and hydrogen in ion exchanged zeolite 13X-Ca at 303 and 323 K and 1 bar of total pressure.

Adsorbate	CO_2		CH_4		CO		H_2*	
Temperature [K]	303	323	303	323	303	323	303	323
μ_1 [s]	11864	8051	214.7	119.1	1657	713.7	11.94	10.38
σ^2 [s^2]	8374750	4011770	3490	1218	166236	34326	12.65	9.18
$D_m \times 10^5$ [$m^2\ s^{-1}$]	5.98	6.66	6.98	7.77	7.30	8.12	16.2	18.0
$D_{ax} \times 10^5$ [$m^2\ s^{-1}$]	2.92	3.22	3.30	3.64	3.42	3.78	6.83	7.56
$D_p \times 10^5$ [$m^2\ s^{-1}$]	2.99	3.33	3.49	3.88	3.65	4.06	8.11	9.02
k_f [$m\ s^{-1}$]	0.0841	0.0933	0.0972	0.1077	0.1015	0.1125	0.2179	0.2415
K_H (μ_1) [$mol\ kg^{-1}\ bar^{-1}$]	67.4	45.6	1.19	0.650	9.30	4.00	0.0179	0.0142
K_H (*fitting*)[$mol\ kg^{-1}\ bar^{-1}$]	53.5	19.9	1.77	0.72	4.86	3.16	0.0317	0.0237
$D_c/r_c^2 \times 10^2$ [s^{-1}]#	0.0544	0.0753	1.85	2.59	0.491	0.848	12.0	14.3
At 303 K: $Q = 6.38 \times 10^{-7}\ m^3\ s^{-1}$ (at 303 K, 1 bar); $C_0 = 0.201\ mol\ m^{-3}$ ($C_0 = 40.22\ mol\ m^{-3}$ for H_2); $u_0 = 0.845 \times 10^{-2}\ m\ s^{-1}$ ($u_0 = 0.863 \times 10^{-2}\ m\ s^{-1}$ for H_2); $u_i = 2.12 \times 10^{-2}\ m\ s^{-1}$ ($u_i = 2.16 \times 10^{-2}\ m\ s^{-1}$ for H_2).								
At 323 K: $Q = 6.80 \times 10^{-7}\ m^3\ s^{-1}$(at 323 K, 1 bar); $C_0 = 0.189\ mol\ m^{-3}$ ($C_0 = 37.73\ mol\ m^{-3}$ for H_2); $u_0 = 0.901 \times 10^{-2}\ m\ s^{-1}$ ($u_0 = 0.920 \times 10^{-2}\ m\ s^{-1}$ for H_2); $u_i = 2.26 \times 10^{-2}\ m\ s^{-1}$ ($u_i = 2.30 \times 10^{-2}\ m\ s^{-1}$ for H_2).								

* The adsorbate partial pressure is 1 bar for H_2; for the other gases is 0.005 bar.
# Estimated using a tortuosity factor, $\tau_p = 2$.

Table 4.16. Contributions of the axial dispersion term, film mass transfer term, pore resistance term and crystal resistance term for CO_2, H_2, CH_4, CO and N_2 in zeolite 13X-Ca at 303 and 323 K and 1 bar of total pressure.

Species	Temp. [K]	Term contribution [%]			
		Axial Disp.	Film Res.	Pore Res.	Crystal. Res.
CO_2	303	57.9	3.0	4.7	34.4
	323	57.6	2.8	4.3	35.3
H_2	303	51.25	0.10	0.15	48.50
	323	55.50	0.08	0.12	44.30
CH_4	303	51.5	2.0	3.0	43.5
	323	47.1	1.6	2.5	48.8
CO	303	66.8	2.4	3.8	27.0
	323	62.1	2.1	3.2	32.6
N_2	303	60.1	2.2	3.4	34.3
	323	52.0	1.7	2.7	43.6

$$\frac{\sigma^2}{2\mu_1^2} = \left\{\begin{matrix}\text{Axial}\\ \text{Disp.}\end{matrix}\right\} + \left(\frac{u_i}{L}\right)\left(\frac{\varepsilon}{1-\varepsilon}\right)\left(\left\{\begin{matrix}\text{Film}\\ \text{Res.}\end{matrix}\right\} + \left\{\begin{matrix}\text{Pore}\\ \text{Res.}\end{matrix}\right\} + \left\{\begin{matrix}\text{Crystal}\\ \text{Resist.}\end{matrix}\right\}\right)\left(1 + \frac{\varepsilon_p}{(1-\varepsilon_p)K_H \rho_p R_g T}\right)^{-2}$$

diffusivity will be slightly affected. The values are in the same order of magnitude and this leads to a maximum of ~ 40% variation in the crystal diffusivity coefficients (Table 4.12). On the other hand, changing the correlation of the axial dispersion coefficient to $D_{ax}^{*} = \varepsilon D_m + 0.35\, R_p u_i$, the variations in the estimation of the crystal diffusivity values are less significant (maximum variation of ~ 10%). Once again, the values D_{ax}^{*} and D_{ax} are in the same order of magnitude resulting in similar crystal diffusivity coefficients (Table 4.17).

Table 4.17. Breakthrough experimental results obtained for carbon dioxide, methane, carbon monoxide and hydrogen in ion exchanged zeolite 13X-Ca at 303 and 323 K and 1 bar of total pressure changing the tortuosity factor or axial dispersion correlation.

Adsorbate	CO_2		CH_4		CO		H_2*	
Temperature [K]	303	323	303	323	303	323	303	323
μ_1 [s]	11864	8051	214.7	119.1	1657	713.7	11.94	10.38
σ^2 [s^2]	8374750	4011770	3490	1218	166236	34326	12.65	9.18
$D_m \times 10^5$ [m^2 s^{-1}]	5.98	6.66	6.98	7.77	7.30	8.12	16.2	18.0
changing the tortuosity from 2 to 6								
$D_{ax} \times 10^5$ [m^2 s^{-1}]	2.92	3.22	3.30	3.64	3.42	3.78	6.83	7.56
$D_p\,(\tau_p = 2) \times 10^5$ [m^2 s^{-1}]	2.99	3.33	3.49	3.88	3.65	4.06	8.11	9.02
$D_p\,(\tau_p = 6) \times 10^5$ [m^2 s^{-1}]	1.00	1.11	1.16	1.29	1.22	1.35	2.70	3.01
k_f [m s^{-1}]	0.0841	0.0933	0.0972	0.1077	0.1015	0.1125	0.2179	0.2415
$K_H\,(\mu_1)$ [mol kg^{-1} bar^{-1}]	67.4	45.6	1.19	0.650	9.30	4.00	0.0179	0.0142
K_H (*fitting*)[mol kg^{-1} bar^{-1}]	53.5	19.9	1.77	0.72	4.86	3.16	0.0317	0.0237
$D_c/r_c^2\,(\tau_p = 2) \times 10^2$ [s^{-1}]	0.0544	0.0753	1.85	2.59	0.491	0.848	12.0	14.3
$D_c/r_c^2\,(\tau_p = 6) \times 10^2$ [s^{-1}]	0.0749	0.0998	2.15	2.89	0.681	1.06	12.1	14.4
changing the correlation of the axial dispersion coefficient to $D_{ax}^{*} = \varepsilon D_m + 0.35\, R_p u_i$								
$D_{ax} \times 10^5$ [m^2 s^{-1}]	2.92	3.22	3.30	3.64	3.42	3.78	6.83	7.56
$D_{ax}^{*} \times 10^5$ [m^2 s^{-1}]	3.02	3.33	3.42	3.77	3.55	3.92	7.05	7.81
$D_p \times 10^5$ [m^2 s^{-1}]	2.99	3.33	3.49	3.88	3.65	4.06	8.11	9.02
k_f [m s^{-1}]	0.0841	0.0933	0.0972	0.1077	0.1015	0.1125	0.2179	0.2415
$K_H\,(\mu_1)$ [mol kg^{-1} bar^{-1}]	67.4	45.6	1.19	0.650	9.30	4.00	0.0179	0.0142
K_H (*fitting*)[mol kg^{-1} bar^{-1}]	53.5	19.9	1.77	0.72	4.86	3.16	0.0317	0.0237
$D_c/r_c^2\,(D_{ax}) \times 10^2$ [s^{-1}]#	0.0544	0.0753	1.85	2.59	0.491	0.848	12.0	14.3
$D_c/r_c^2\,(D_{ax}^{*}) \times 10^2$ [s^{-1}]#	0.0577	0.0799	1.93	2.68	0.538	0.910	12.4	14.9
At 303 K: $Q = 6.38 \times 10^{-7}$ m^3 s^{-1} (at 303 K, 1 bar); $C_0 = 0.201$ mol m^{-3} ($C_0 = 40.22$ mol m^{-3} for H_2); $u_0 = 0.845 \times 10^{-2}$ m s^{-1} ($u_0 = 0.863 \times 10^{-2}$ m s^{-1} for H_2); $u_i = 2.12 \times 10^{-2}$ m s^{-1} ($u_i = 2.16 \times 10^{-2}$ m s^{-1} for H_2).								
At 323 K: $Q = 6.80 \times 10^{-7}$ m^3 s^{-1}(at 323 K, 1 bar); $C_0 = 0.189$ mol m^{-3} ($C_0 = 37.73$ mol m^{-3} for H_2); $u_0 = 0.901 \times 10^{-2}$ m s^{-1} ($u_0 = 0.920 \times 10^{-2}$ m s^{-1} for H_2); $u_i = 2.26 \times 10^{-2}$ m s^{-1} ($u_i = 2.30 \times 10^{-2}$ m s^{-1} for H_2).								

* The adsorbate partial pressure is 1 bar for H_2; for the other gases is 0.005 bar;
# Estimated using a tortuosity factor, $\tau_p = 2$.

It was observed that hydrogen has the fastest micropore diffusion in the zeolite 13X-Ca followed by nitrogen, methane, carbon monoxide and finally carbon dioxide. Diffusion of CO and CO_2 are much slower than the other gases due to stronger electrostatic interactions with the zeolite framework. In the case of methane and nitrogen, the interactions are less strong and thus diffusion is controlled by the kinetic diameter of the molecules (3.6 Å for N_2 and 3.8 Å for CH_4) [31]. The crystal diffusivities (D_c) published in the literature [42-43] are 3.92×10^{-15} m^2 s^{-1} (301 K) and 5.35×10^{-15} m^2 s^{-1} (323 K) for carbon dioxide and 3.00×10^{-8} m^2 s^{-1} (301 K) and 3.30×10^{-8} m^2 s^{-1} (323 K) for methane. The carbon dioxide crystal diffusivities obtained in this study are in the same order of magnitude as the published results. However for methane, the crystal diffusivities obtained are six orders of magnitude lower than the published results.

4.3.5 Adsorption equilibrium of N_2, CO_2, CH_4, CO and H_2

4.3.5.1 Experimental and theoretical

Adsorption equilibrium isotherms of N_2, CO_2, CH_4, CO and H_2 were measured for the exchanged zeolite 13X sample with the highest performance for nitrogen. The adsorption equilibrium measurements were performed in a magnetic suspension microbalance (Rubotherm, Germany) (± 10^{-5} g) at 303 and 323 K (± 0.1 K) within 0-7 bar (± 0.0014 bar). The experimental set-up detailed in chapter 2 were employed again for equilibrium measurements taking into consideration the corrections of the buoyancy effects. The experimental adsorption equilibrium data were fitted with the Virial adsorption isotherm model (described in the previous section 3.2.1 and summarized in Table 4.6 [24-25]).

Degassing of the sample was carried out with a heating rate of 1 K min^{-1} (± 0.1 K min^{-1}) under vacuum (< 10^{-7} bar) at 593 K (± 0.1 K) overnight. Once more, adsorption and desorption measurements were performed to confirm the reversibility of each isotherm.

The isosteric heats of adsorption ($-\Delta H_i$) were calculated through the Clausius-Clapeyron equation, where the derivative has to be evaluated at a constant amount adsorbed q:

$$\left(-\Delta H_i\right) = R_g T^2 \left(\frac{\partial \ln P_i}{\partial T}\right)_q \tag{4.1}$$

where P_i is the partial pressure of the component i, T is the temperature and R_g is the universal gas constant. Plotting $\ln P_i$ versus $1/T$, a straight line equation with slope equal to $(-\Delta H_i)/R_g$ is obtained.

4.3.5.2 Results

Adsorption equilibria of nitrogen on ion exchanged zeolite 13X-Ca was studied at 303 and 323 K over the pressure range 0-7 bar. Figure 4.18 shows the absolute amount of nitrogen adsorbed on zeolite 13X-Ca and compared to data reported in the literature [46-49]. Dantas *et al.* (2008) [47] reported the adsorption equilibrium of nitrogen at 301 K on the commercial zeolite 13X used for this study. At 303 K and 7 bar, the amount adsorbed of nitrogen on zeolites 13X and 13X-Ca are 1.47 [46], 1.16 [48], 1.18 [49] and 1.27 mol kg^{-1} [50], respectively. For the same temperature at 1 bar, the N_2 amount adsorbed on zeolites 13X are 0.288 [46], 0.258 (at 301 K) [47], 0.258 [48], 0.261 [49] and on 13X-Ca is 0.447 mol kg^{-1} [50]. Figure 4.18 shows the increase of the non-linearity of the N_2 isotherms on zeolite 13X-Ca. It is also possible to observe that the N_2 adsorption capacity on zeolite 13X-Ca is larger than on the original zeolite 13X below ~ 3 bar, which is usually within the nitrogen partial pressure range of the SMR off-gases. Besides, the differential N_2 loading between the high and low pressures of the PSA process is enlarged. Therefore the second layer (zeolite) can be smaller and the productivity of the PSA process for hydrogen purification is improved.

Also adsorption equilibria of H_2, CO_2, CH_4 and CO on the ion exchanged zeolite 13X-Ca were studied at the same temperature and pressure ranges (Figure 4.19). The amount of hydrogen

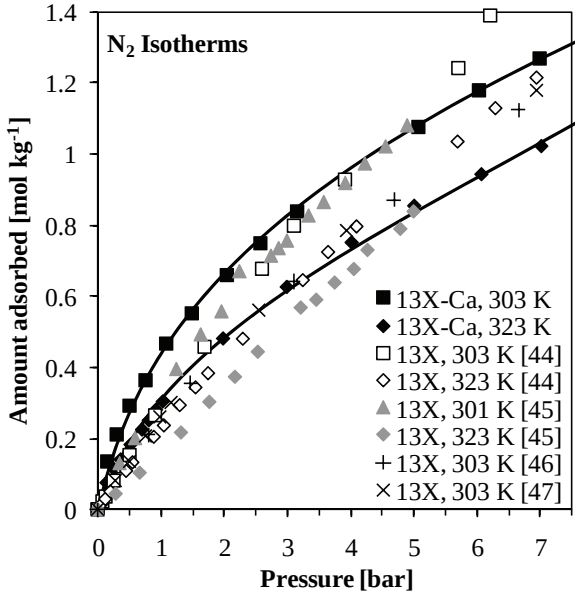


Figure 4.18. Amount adsorbed of N_2 on zeolite 13X-Ca: experimental points at 303 (■) and 323 K (◆) and —— Virial isotherm fitting; comparison to published results of N_2 amount adsorbed on the studied sample of zeolite 13X (▲,◆) and other samples of zeolite 13X (□,◇,+,×).

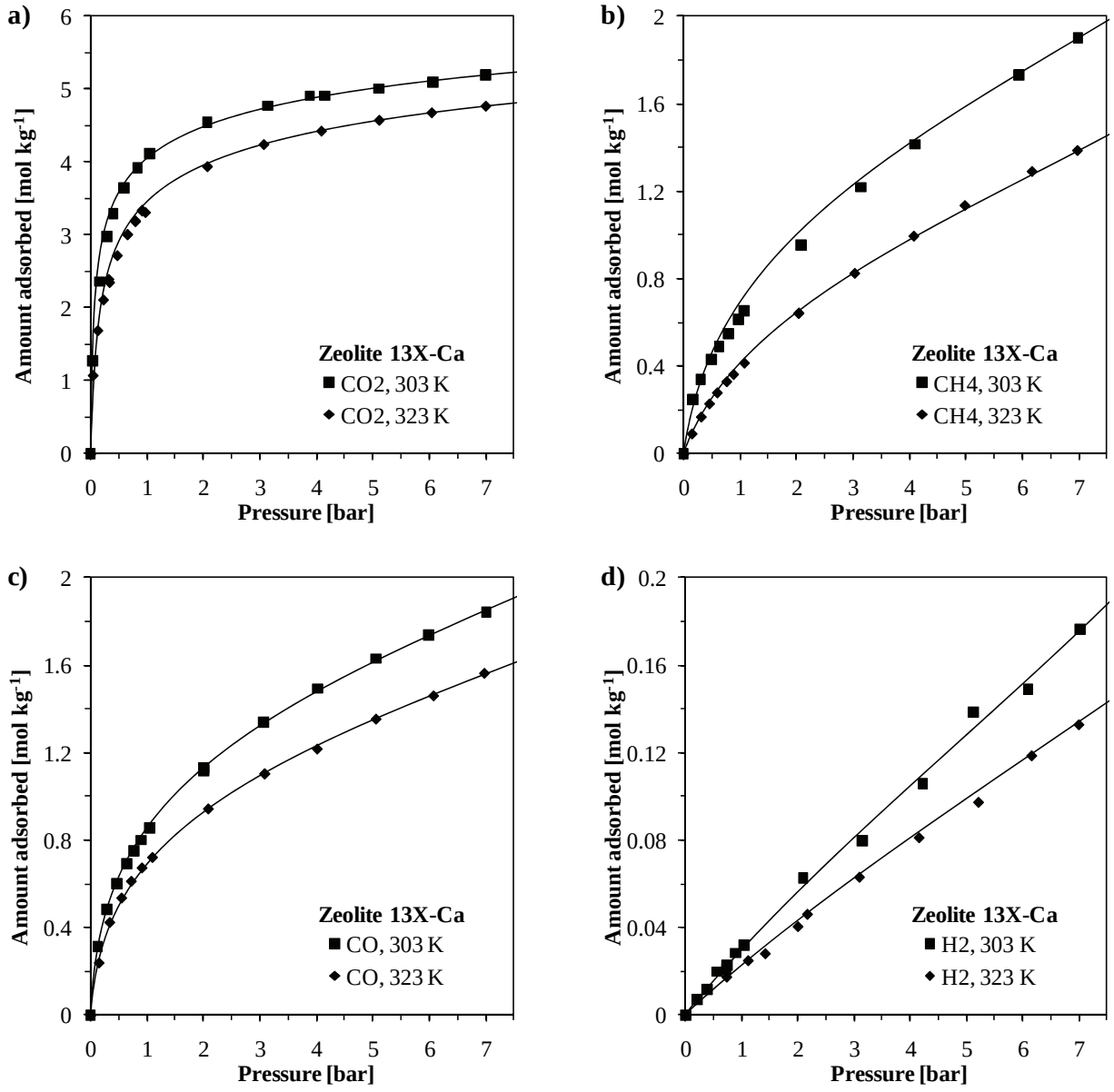


Figure 4.19. Amount adsorbed of CO_2 (a), CH_4 (b), CO (c) and H_2 (d) on zeolite 13X-Ca: experimental points at 303 (■) and 323 K (◆) and —— Virial isotherm fitting.

adsorbed on zeolite 13X-Ca is small and the linearity of the isotherm is observed. On the other hand, the CO_2 isotherm on the ion exchanged zeolite 13X-Ca shows a high steepness, eventually due to the high charge density of the calcium cation, with an amount adsorbed of ~ 5 mol kg^{-1} at 303 K and 7 bar. This high steepness results in an unfavourable desorption of carbon dioxide from the zeolite with a high heat of desorption. Therefore, it is important that no CO_2 passes through the first layer (activated carbon) to the second layer (zeolite) of the PSA column. The CH_4 and CO adsorption capacities of this material at 303 K and 7 bar are approximately the same (~ 2 mol kg^{-1}).

All adsorption data on the ion exchanged zeolite 13X-Ca at 303-323 K were fitted employing the Virial isotherm equation, which describes the adsorption isotherms in the whole temperature and pressure ranges studied. The Virial parameters are detailed in Table 4.18. For that, the temperature dependence of the Virial coefficients was truncated at the second term. Figure 4.18 and Figure 4.19 shows a good fitting for all the compounds (N_2, CO_2, CH_4, CO and H_2) over the whole pressure and temperature ranges studied. It was found that the isosteric heats of adsorption obtained through the Virial isotherm model are in agreement with the values calculated using the Clausius-Clapeyron equation (Figure 4.20).

Table 4.18. Virial adsorption isotherm fitting parameters of N_2, CO_2, CH_4, CO and H_2 for the ion exchanged zeolite 13X-Ca at 303-323 K.

Species	K_∞ [mol kg^{-1} bar^{-1}]	$(-\Delta H)$ [kJ mol^{-1}]	$A_0 \times 10^{-5}$ [m^2 mol^{-1}]	$A_1 \times 10^{-6}$ [m^2 K mol^{-1}]	$B_0 \times 10^{-11}$ [m^4 mol^{-2}]	$B_1 \times 10^{-11}$ [m^4 K mol^{-2}]
N_2	1.19×10^{-3}	16.52	48.0	-1222	-51.09	14926
CO_2	6.16×10^{-6}	40.25	0.028	-4.663	0.010	308.5
CH_4	8.89×10^{-7}	36.54	4.49	94.67	-14.46	3796
CO	4.81×10^{-3}	17.43	27.2	-468.2	-16.01	3979
H_2	2.93×10^{-4}	11.80	12.24	0.401	-56.71	4200

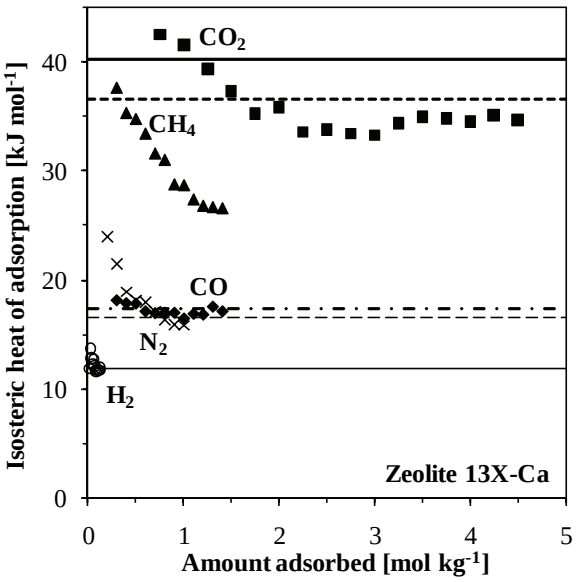


Figure 4.20. Isosteric heats of adsorption of CO_2 (■), CH_4 (▲), CO (◆), N_2 (×) and H_2 (○) on zeolite 13X-Ca as a function of equilibrium pressure in the temperature range of 303-323 K; lines are the values obtained through the Virial model.

When the Henry constant obtained from the first moment K_H (μ_1) are compared with the values obtained by fitting equilibrium data to the Virial isotherm expression K_H (*fitting*), it can be concluded that these results have the same order of magnitude (see Table 4.15 and Table 4.17).

4.4 Conclusions

The adsorption capacity of contaminants on commercial activated carbon was enhanced by further physical activation of the extrudates. Different physical activation experiments were applied to a commercially available activated carbon material using different flows of activating agent, temperatures, times and pressures. All samples prepared by activation in nitrogen and carbon dioxide at 1 bar increased the surface area and microporosity relatively to the original activated carbon. The maximum amount of micropores was obtained at 1173 K and 1 bar, using a carbon dioxide flow rate of 5.0×10^{-7} m^3 s^{-1} (measured at 298 K and 1 bar) during 2400 s. This experiment was tested for a scale-up of 10 g/sample and another of 400 g/sample and the reproducibility was verified. The experimental set-up developed for this work is able to produce batches with four hundred grams of the modified activated carbon. A total of four kilograms of adsorbent was prepared using this technique to be supplied to an industrial partner of HY2SEPS project [23].

Adsorption equilibrium of carbon dioxide is reported for the two scale-up samples of modified activated carbon (AC5-I and AC5-KS) and the results compared to the original activated carbon. The adsorption capacity of the modified adsorbent is higher than the adsorption capacity of the original activated carbon. The same conclusion was verified for H_2, CH_4, and N_2. All adsorption data on the modified AC5-KS at 303-323 K were fitted employing the Virial isotherm equation. It was found that this equation could describe the adsorption isotherms in the whole temperature and pressure ranges studied.

Adsorption kinetics of CO_2, H_2, CH_4, CO and N_2 were measured by breakthrough experiments at 303-323 K. The diffusivity parameters were estimated from the analysis of the derivatives of the breakthrough curves and it was observed that the axial dispersion term is the most relevant dispersive mechanism for all gases. Besides, it was observed that the contributions of film and macropore mass transfer resistances to the total dispersion were very small for all gases. The micropore diffusivities in the modified activated carbon differ in two orders of magnitude having the following order from the fastest to the slowest species: $H_2 > N_2 > CO > CH_4 > CO_2$.

With the modified activated carbon, the carbon dioxide adsorption loadings at high pressures of the PSA column used on a plant already under operation for the H_2-CO_2 separation

[23] are improved.

In this work, a complete study of the adsorption equilibrium of the SMR off-gases (CO_2, H_2, CH_4, CO and N_2) on different zeolites, such as, the zeolite 13X and the ion exchanged samples of zeolites 13X-Li, 13X-Ba and 13X-Ca was performed. For that, three ion exchanged zeolite samples (13X-Li, 13X-Ba and 13X-Ca) were prepared with Li^+, Ba^{2+} and Ca^{2+} starting from a commercial zeolite 13X. The zeolite 13X and the exchanged zeolite samples were characterized by SEM for the study of the morphology of the particles and by EDX for identification and quantification of the elemental composition. It was concluded that the crystals were not damaged or destroyed after performing the ion exchange and also a final total concentration of 0.076 $g_{calcium}/g_{material}$ on the structure of the modified zeolite 13X-Ca was achieved.

To study the adsorption equilibrium of nitrogen, breakthrough curves at 303 and 323 K were performed on all zeolite samples (13X, 13X-Li, 13X-Ba and 13X-Ca) with two pure nitrogen mixtures: (1) N_2 partial pressure of 0.01 bar and (2) N_2 partial pressure of 0.25 bar. The N_2 crystal diffusivity was estimated using the breakthrough experiments of 1.0% nitrogen balanced in helium. It was verified that the crystal diffusivities of all samples are of the same order of magnitude and they are approximately the same. At 303 K, the ratio of the difference in capacity between high and low pressure (0.25 and 0.01 bar) of the zeolites 13X-Ba and 13X is ~ 1.4, for zeolites 13X-Ca and 13X is ~ 2.2 and for zeolites 13X-Li and 13X is ~ 0.8. So, the use of zeolite 13X exchanged with barium and calcium will improve the nitrogen adsorption for separations of this gas. The transport kinetics of carbon dioxide, methane, carbon monoxide and hydrogen was also studied in the zeolite 13X-Ca by breakthrough curves at 303 and 323 K. The crystal diffusivities of N_2, CO_2, CH_4, CO and H_2 in the zeolite 13X-Ca differ by two orders of magnitude having the following order from the slowest to the fastest species: $CO_2 < CO < CH_4 < N_2 < H_2$.

Adsorption equilibria of nitrogen, carbon dioxide, methane, carbon monoxide and hydrogen are reported for zeolite 13X-Ca at 303 and 323 K. The nitrogen adsorption capacity of the ion exchanged zeolite 13X-Ca in the pressure range of 0-3 bar is higher than the adsorption capacity of the original zeolite 13X (at 1 bar it increases 36%).

It can be concluded that, the capacity towards nitrogen of the zeolite 13X can be enhanced by ion exchange of the zeolite material with Ca^{2+}. Therefore, the ion exchanged zeolite (13X-Ca) will provide a higher productivity to the layered PSA process applied for SMR off-gases separation.

4.5 Notation

Nomenclature

A	Virial coefficients (m^2 mol^{-1})
B	Virial coefficients (m^4 mol^{-2})
C	concentration (mol m^{-3})
C_0	initial gas phase concentration (mol m^{-3})
$C_{g,i}$	molar concentration of component *i* in the gas phase (mol m^{-3})
$C_{g,T}$	total gas phase concentration (mol m^{-3})
$C_{m,i}$	concentration of component *i* in the macropores (mol m^{-3})
$C_{m,T}$	total concentration in the macropores (mol m^{-3})
D_{ax}	axial dispersion coefficient (m^2 s^{-1})
D_c	micropore/crystal diffusivity (m^2 s^{-1})
D_c^0	limiting diffusivity at infinite temperatures (m^2 s^{-1})
D_{ij}	binary molecular diffusivity (m^2 s^{-1})
D_k	Knudsen diffusivity (m^2 s^{-1})
D_m	molecular diffusivity (m^2 s^{-1})
D_p	macropore diffusivity (m^2 s^{-1})
E_a	activation energy of micropore/crystal diffusion (kJ mol^{-1})
k_f	film mass transfer coefficient (m s^{-1})
k_s	geometrical factor of the particle or of the micropore or crystal: 0 - slab; 1 - cylinder; 2 - sphere
K_H	Henry constant (mol kg^{-1} bar^{-1})
K_∞	adsorption constant at infinite temperature (mol kg^{-1} bar^{-1})
L	column length (m)
m_{ads}	mass of adsorbed gas (kg)
m_s	mass of adsorbent (kg)
M_W	molecular weight of the gas (kg mol^{-1})
N	number of points of each isotherm
P	pressure (Pa)
p_{N2}	nitrogen partial pressure (Pa)
$P_{cal,T,q}$	calculated partial pressure for each temperature T and adsorbed phase concentration q (Pa)

$P_{exp,T,q}$ experimental partial pressure for each temperature T and adsorbed phase concentration q (Pa)

q_i absolute adsorbed phase concentration of adsorbate i (mol kg^{-1})

$\bar{q}_i$ micropore or crystal averaged adsorbed phase concentration of component i (mol kg^{-1})

$\langle \bar{q}_i \rangle$ particle averaged adsorbed phase concentration of component i (mol kg^{-1})

Q flow rate (m^3 s^{-1})

r radial coordinate of the micropore or crystal (m)

r_c micropore or crystal radius (m)

r_p mean pore radius (m)

R radial coordinate of the particle (m)

R_g universal gas constant (J mol^{-1} K^{-1})

R_p radius of the adsorbent extrudates (m)

Re Reynolds number

S adsorbent specific area (m^2 kg^{-1})

Sc Schmidt number

Sh Sherwood number

t time (s)

T temperature (K)

u_0 superficial velocity (m s^{-1})

u_i interstitial velocity (m s^{-1})

V_{ads} volume of adsorbed phase (m^3)

V_c volume of the cell where the adsorbent is located (m^3)

V_s volume of the solid adsorbent (m^3)

w weight *SOR-ARE* parameter, $0 \le w \le 1$

y_i molar fraction of component i

z partition of the column length L (m)

Greek letters

Δm difference of weight between two measurements (kg)

Δq difference of absolute adsorbed phase concentration for the partial pressure range 0.01-0.25 bar (mol kg^{-1})

$(-\Delta H)$ isosteric heat of adsorption (kJ mol^{-1})

ε bed porosity

ε_p	particle porosity
μ	gas viscosity (Pa s)
μ_1	first moment (s)
ρ_g	density of the gas phase (kg m^{-3})
ρ_ℓ	density of the adsorbed phase (kg m^{-3})
ρ_p	density of the adsorbent (kg m^{-3})
ρ_s	solid density (kg m^{-3})
σ^2	variance (s^2)
τ_p	pore tortuosity
Ω_c	linear driving force (LDF) factor of the micropore or crystal: $\Omega_c = (k_s + 1)(k_s + 3)$
Ω_p	linear driving force (LDF) factor of the particle: $\Omega_p = (k_s + 1)(k_s + 3)$

4.6 References

[1] I.A.A.C. Esteves, J.P.B. Mota, Simulation of a new hybrid membrane/pressure swing adsorption process for gas separation, Desalination. 148 (2002) 275-280.

[2] J.-H. Park, J.-N. Kim, S.-H. Cho, J.-D. Kim, R.T. Yang, Adsorber dynamics and optimal design of layered beds for multicomponent gas adsorption, Chemical Engineering Science. 53 (1998) 3951-3963.

[3] D.M. Ruthven, S. Farooq, K.S. Knabel, Pressure swing adsorption, VCH Publishers, New York, 1994.

[4] A. Ahmadpour, D.D. Do, Characterization of modified activated carbons: Equilibria and dynamics studies, Carbon. 33 (1995) 1393-1398.

[5] I.A.W. Tan, A.L. Ahmad, B.H. Hameed, Optimization of preparation conditions for activated carbons from coconut husk using response surface methodology, Chemical Engineering Journal. 137 (2008) 462-470.

[6] S. Ismadji, Y. Sudaryanto, S.B. Hartono, L.E.K. Setiawan, A. Ayucitra, Activated carbon from char obtained from vacuum pyrolysis of teak sawdust: Pore structure development and characterization, Bioresource Technology. 96 (2005) 1364-1369.

[7] T. Kopac, A. Toprak, Preparation of activated carbons from Zonguldak region coals by physical and chemical activations for hydrogen sorption, International Journal of Hydrogen Energy. 32 (2007) 5005-5014.

[8] M.J. Prauchner, F. Rodríguez-Reinoso, Preparation of granular activated carbons for adsorption of natural gas, Microporous and Mesoporous Materials. 109 (2008) 581-584.

[9] R. Murillo, M.V. Navarro, J.M. López, T. García, M.S. Callén, E. Aylón, A.M. Mastral, Activation of pyrolytic lignite char with CO_2. Kinetic study, Energy & Fuels. 20 (2006) 11-16.

[10] R.C. Bansal, J.-B. Donnet, F. Stoeckli, Active carbon, Marcel Dekker, Inc., New York and Basel, 1998.

[11] M.T. González, F. Rodríguez-Reinoso, A.N. García, A. Marcilla, Letters to the Editor: CO_2 activation of olive stones carbonized under different experimental conditions, Carbon. 35 (1997) 159-165.

[12] F. Rodríguez-Reinoso, M. Molina-Sabio, M.T. González, The use of steam and CO_2 as activating agents in the preparation of activated carbons, Carbon. 33 (1995) 15-23.

[13] J. Alcañiz-Monge, D. Cazorla-Amorós, A. Linares-Solano, Production of activated carbons:

Use of CO_2 versus H_2O as activating agent. A reply to a letter from P. L. Walker, Jr., Carbon. 35 (1997) 1665-1668.

[14] F. Rodríguez-Reinoso, A.C. Pastor, H. Marsh, M.A. Martínez, Preparation of activated carbon cloths from viscous rayon. Part II: Physical activation processes, Carbon. 38 (2000) 379-395.

[15] F. Stoeckli, E. Daguerre, A. Guillot, The development of micropore volumes and widths during physical activation of various precursors, Carbon. 37 (1999) 2075-2077.

[16] B. Feng, S.K. Bhatia, Variation of the pore structure of coal chars during gasification, Carbon. 41 (2003) 507-523.

[17] P.L. Walker Jr., Production of activated carbons: Use of CO_2 versus H_2O as activating agent, Carbon. 34 (1996) 1297-1299.

[18] M.V. Navarro, N.A. Seaton, A.M. Mastral, R. Murillo, Analysis of the evolution of the pore size distribution and the pore network connectivity of a porous carbon during activation, Carbon. 44 (2006) 2281-2288.

[19] X. Py, A. Guillot, B. Cagnon, Nanomorphology of activated carbon porosity: Geometrical models confronted to experimental facts, Carbon. 42 (2004) 1743-1754.

[20] M.B. Sweatman, N. Quirke, Characterization of porous materials by gas adsorption at ambient temperatures and high pressure, Journal of Physical Chemistry B. 105 (2001) 1403-1411.

[21] J.A. Maciá-Agulló, B.C. Moore, D. Cazorla-Amorós, A. Linares-Solano, Activation of coal tar pitch carbon fibres: Physical activation vs. chemical activation, Carbon. 42 (2004) 1367-1370.

[22] C.A. Grande, F.V.S. Lopes, A.M. Ribeiro, J.M. Loureiro, A.E. Rodrigues, Adsorption of off-gases from steam methane reforming (H_2, CO_2, CH_4, CO and N_2) on activated carbon, Separation Science and Technology. 43 (2008) 1338-1364.

[23] HY2SEPS, Hybrid Hydrogen Carbon Dioxide Separation Processes, E.U. Res. Project 2005, Available from: http://hy2seps.iceht.forth.gr/.

[24] R.M. Barrer, Sorption in porous crystals: equilibria and their interpretation, Journal of Chemical Technology and Biotechnology. 31 (1981) 71-85.

[25] A.V. Kiselev, Vapor adsorption on zeolites considered as crystalline species adsorbents, Molecular Sieve Zeolites-II, ACS series. 102 (1971) 37-68.

[26] S.M. Taqvi, M.D. LeVan, Virial description of two-component adsorption on homogeneous and heterogeneous surfaces, Industrial and Engineering Chemistry Research. 36 (1997)

2197-2206.

[27] D.M. Ruthven, Principles of adsorption and adsorption processes, John Wiley & Sons, New York, 1984.

[28] R.B. Bird, W.E. Stewart, E.N. Lightfoot, Transport phenomena, 2nd Edition, Wiley International, Singapore, 2002.

[29] C.R. Wilke, Diffusional properties of multicomponent gases, Chemical Engineering Progress. 46 (1950) 95-104.

[30] F.V.S. Lopes, C.A. Grande, A.M. Ribeiro, E.L.G. Oliveira, J.M. Loureiro, A.E. Rodrigues, Enhancing capacity of activated carbons for hydrogen production, Industrial and Engineering Chemistry Research. 48 (2009) 3978-3990.

[31] D.W. Breck, Zeolite molecular sieves, R. E. Krieger Publishing, Malabar, FL, 1998.

[32] P. Castaldi, L. Santona, C. Cozza, V. Giuliano, C. Abbruzzese, V. Nastro, P. Melis, Thermal and spectroscopic studies of zeolites exchanged with metal cations, Journal of Molecular Structure. 734 (2005) 99-105.

[33] N.D. Hutson, S.U. Rege, R.T. Yang, Mixed cation zeolites: LixAgy-X as a superior adsorbent for air separation, AIChE Journal. 45 (1999) 724-734.

[34] O. Ursini, E. Lilla, R. Montanari, The investigation on cationic exchange capacity of zeolites: The use as selective ion trappers in the electrokinetic soil technique, Journal of Hazardous Materials. B 137 (2006) 1079-1088.

[35] C. Jia, P. Beaunier, P. Massiani, Comparison of conventional and solid-state ion exchange procedures for the incorporation of lanthanum in H-beta zeolite, Microporous and Mesoporous Materials. 24 (1998) 69-82.

[36] T.C. Golden, R. Kumar, W.C. Kratz, Hydrogen purification (1990) U.S. Patent 4,957,514.

[37] C.G. Coe, J.F. Kirner, R. Pierantozzi, T.R. White, Nitrogen adsorption with Ca and or Sr exchanged lithium X-zeolites (1992) U.S. Patent 5,152,813.

[38] D. Plee, Purification of hydrogen flowstreams by selectively adsorbing impurities therefrom (2002) U.S. Patent 6,464,756 B1.

[39] G. Reiss, Molecular sieve zeolite for producing hydrogen by pressure variation adsorption technique (1984) U.S. Patent 4,477,267.

[40] K.W. Lemons, J.L. McAtee Jr., The parameters of induced thermoluminescence of some selected phyllosilicates: A crystal defect structure study, American Mineralogist. 68 (1983) 915-923.

[41] S. Cavenati, C.A. Grande, A.E. Rodrigues, Separation of $CH_4/CO_2/N_2$ mixtures by layered

pressure swing adsorption for upgrade of natural gas, Chemical Engineering Science. 61 (2006) 3893-3906.

[42] N.-K. Bar, P.L. McDaniel, C.G. Coe, G. Seiffert, J. Karger, Measurement of intracrystalline diffusion of nitrogen in zeolites NaX and NaCaA using pulsed field gradient n.m.r., Zeolites. 18 (1997) 71-74.

[43] J. Caro, M. Bülow, J. Kärger, A.G. Dixon, Y.H. M., C.A. S., Comment on hydrocarbon diffusivity in zeolites. Reply, Chemical Engineering Science. 40 (1985) 2169-2171.

[44] J. Kärger, D.M. Ruthven, Diffusion in zeolites and other microporous solids, 1st Edition, John Wiley & Sons, New York, 1992.

[45] S. Sircar, W.E. Waldron, Oxygen production by adsorption (2002) European Patent Application 1,214,964 A2.

[46] S. Cavenati, C.A. Grande, A.E. Rodrigues, Adsorption equilibrium of methane, carbon dioxide, and nitrogen on zeolite 13X at high pressures, Journal of Chemical and Engineering Data. 49 (2004) 1095-1101.

[47] T.L.P. Dantas, R.V.P. Rezende, A.E. Rodrigues, R.F.P.M. Moreira, Adsorção de CO_2 e N_2 sobre carvão ativado e zeólita 13X: Isotermas de equilíbrio através de medidas gravimétricas, in 7º Encontro Brasileiro sobre Adsorção - EBA, Campina Grande - PB, Brasil, 2008.

[48] D. Ko, R. Siriwardane, L.T. Biegler, Optimization of a pressure-swing adsorption process using zeolite 13X for CO_2 sequestration, Industrial and Engineering Chemistry Research. 42 (2003) 339-348.

[49] R.V. Siriwardane, M.-S. Shen, E.P. Fisher, Adsorption of CO_2 on zeolites at moderate temperature, Energy & Fuels. 19 (2005) 1153-1159.

[50] F.V.S. Lopes, C.A. Grande, A.M. Ribeiro, V.J.P. Vilar, J.M. Loureiro, A.E. Rodrigues, Effect of ion exchange on the adsorption of SMR off-gases on zeolite 13X, Journal of Chemical and Engineering Data. 55 (2010) 184-195.

5.

Multicomponent breakthrough curves and PSA performance[§]

5.1 Introduction

Low cost with high efficiency generation of electricity, able for megawatt-scale distribution in power applications and with almost no CO_2 emissions (nor other greenhouse gases) are some requirements of power systems in the future. Recently, the increased demand for the supply of pure hydrogen gained strength, especially by fuel cell industry. The main reason is that hydrogen fuel cells are extremely efficient energy conversion devices [1]. In its natural and elemental form hydrogen is scarce, becoming crucial its production. As mentioned in previous chapters, SMR remains one of the most economical routes to produce hydrogen [2-3]. However, the SMR reactor produces hydrogen with several impurities, such as, water vapour, carbon dioxide, methane, carbon

[§] The content of this chapter is part of the work published in the following articles:

C.A. Grande, F.V.S. Lopes, A.M. Ribeiro, J.M. Loureiro, A.E. Rodrigues, Adsorption of off-gases from steam methane reforming (H_2, CO_2, CH_4, CO and N_2) on activated carbon, Separation Science and Technology. 43 (2008) 1338-1364.

F.V.S. Lopes, C.A. Grande, A.M. Ribeiro, E.L.G. Oliveira, J.M. Loureiro, A.E. Rodrigues, Enhancing capacity of activated carbons for hydrogen production, Industrial and Engineering Chemistry Research. 48 (2009) 3978-3990.

F.V.S. Lopes, C.A. Grande, A.E. Rodrigues, Activated carbon for hydrogen purification by pressure swing adsorption: Multicomponent breakthrough curves and PSA performance, submitted for publication to Chemical Engineering Science (2010).

monoxide and, if present in natural gas, nitrogen [4]. For fuel cell applications, hydrogen with purity over 99.99% is required and so these impurities must be removed. In particular, carbon monoxide must be reduced to less than 10 ppm to be used in some types of fuel cells [5-6]. PSA units are commonly used in hydrogen purification from SMR off-gases [2, 4, 7-17]. This process involves a large number of design and operating parameters. As a consequence, to study the H_2 purification through PSA process is important to determine adsorption equilibrium and kinetics data of single and also multicomponent systems in order to do the complete design of the separation unit [18].

The purpose of this chapter is to provide adsorption data of multicomponent mixtures of SMR off-gases. Based on single component data already measured for several commercial and modified adsorbents (chapters 2, 3 and 4) [19-22] it is possible to estimate the behaviour of the mixture through the extension of results obtained for pure gases. However, it is convenient to validate these data, especially for the case of a mixture with five components. Therefore, breakthrough curves were performed considering different feed compositions and feed flow rates in order to determine some multicomponent adsorption data on these adsorbents (activated carbon R2030 and modified activated carbon AC5-KS). As mentioned before, the multicomponent mixtures of SMR off-gases comprise several gases and for that a detailed study is needed. Since there are available commercial adsorbents with enhanced adsorptive capacities for different gases (but not for all contaminants simultaneously), it is crucial to study different adsorbents and also evaluate their adsorption properties [19-22].

Modeling of the multicomponent adsorption data on AC5-KS was also performed testing the mathematical model to verify its predictions. Besides, a single column PSA experiment (bed packed with AC5-KS) was performed for the complete validation of the model. Finally, a cycle sequence of 6 steps and other of 10 steps were considered for the simulation of two single column PSA processes in order to achieve high H_2 purification process performances using the activated carbon AC5-KS.

5.2 Experimental

To measure the adsorption data of multicomponent mixtures, two experimental set-ups were used. Initially, a 1-column PSA-VSA unit developed by Da Silva (1999) [23] able to perform fixed-bed breakthrough curves of three components was applied for single He-CO_2, binary H_2-CO_2 and ternary H_2-CO_2-CH_4 and H_2-CO_2-CO experiments on activated carbons R2030 and AC5-KS.

Afterwards, an already existing experimental set-up composed of a 2-column PSA unit was used for further measurements. Within this work, a gas chromatograph analysis system for determination of bed outlet concentrations of multicomponent gas mixtures was built, calibrated and tested for the complete mixture of SMR off-gases (H_2, CO_2, CH_4, CO and N_2). Once the analysis system was operating in the PSA facility, both adsorption equilibrium and kinetic behaviour of binary H_2-CO_2, ternary H_2-CO_2-CO and five-component H_2-CO_2-CH_4-CO-N_2 mixtures were measured on activated carbon AC5-KS.

5.2.1 Multicomponent breakthrough experiments

5.2.1.1 Fixed-bed unit for ternary mixtures

In order to verify the adsorption equilibrium obtained by gravimetry and the adsorption kinetics of pure components reported in chapters 2 and 3, respectively, binary H_2-CO_2 and ternary H_2-CO_2-CH_4 breakthrough experiments were performed in a fixed-bed packed with activated carbon R2030 [19]. To perform the fixed-bed measurements, a 1-column PSA-VSA experimental set-up developed by Da Silva (1999) [23] was used and adapted for these experiments. The schematic view of the complete fixed-bed unit is shown in Figure 5.1. Carbon dioxide and methane

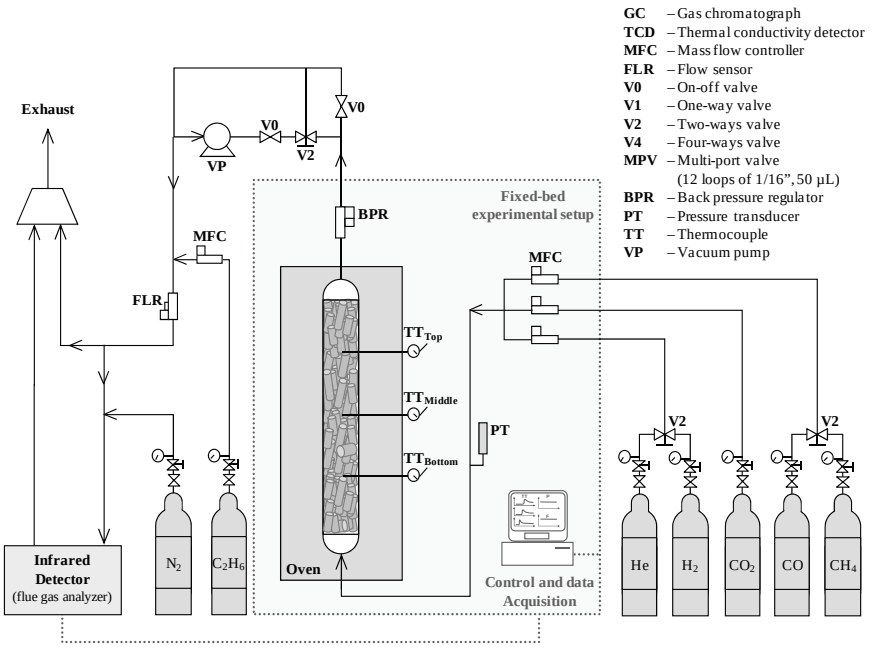


Figure 5.1: Schematic representation of the 1-column PSA-VSA experimental set-up used for multicomponent fixed-bed breakthroughs developed by Da Silva (1999) [23]: unit connected to a flue gas analyser to measure the bed outlet concentration.

concentrations exiting the column were measured by an infrared detector each ten seconds (Figure 5.2: flue gas analyzer, Madur, Austria). In the binary mixture, ethane was inserted as a tracer gas to measure the molar flow rate of the species [23]. The flow rate variations were determined with a flow sensor FLR1006 (Omega, USA) [19]. Due to a limitation of the flue gas analyzer (Madur, Austria), nitrogen was inserted as a tracer gas to achieve at least the minimum flow rate needed for the analysis of the feed composition. The temperature in the column was measured at three points along the column namely at 0.170 (TT_{Bottom}), 0.430 (TT_{Middle}) and 0.680 m (TT_{Top}) from the feed inlet. The properties of the column used and the experimental conditions of the fixed-bed breakthrough curves are described in Table 5.1.



Figure 5.2: Flue gas analyser (Madur, Austria) used for the measurements of the bed outlet concentration.

Afterwards, breakthrough experiments of He-CO_2 and ternary H_2-CO_2-CH_4 mixtures were performed in a column packed with the modified activated carbon AC5-KS in order to validate the transport and adsorption equilibrium data (previously studied in chapter 4 [21]). The breakthrough experiments were carried out at 303 K and the total pressure of 1.2 bar was kept constant with a back-pressure regulator. The column outlet stream was mixed with a stream of ethane of 1.87×10^{-6} m^3 s^{-1} (measured at 298 K and 1 bar) [23]. Once more, this gas was used as a tracer to determine flow rate variations due to adsorption. In this case, instead of using the infrared detector, samples of the outlet stream were stored in the loops of a multi-port valve system and afterwards analysed by the TCD and FID detectors (thermal conductivity detector and flame ionization detector) of a gas chromatograph (Chrompack CP9001, Holland) [21, 23]. Each loop is a 1/16" stainless steel tube with a volume of 50 µL and this system is able to store up to 11 samples. The

Table 5.1: Properties of the column used and experimental conditions of the fixed-bed breakthrough curves on the activated carbon R2030.

Breakthrough curves (BT)		Binary (H_2-CO_2)		Ternary (H_2-CO_2-CH_4)
Experiment no.		1	2	3
Adsorbate molar fraction	H_2	0.824	0.824	0.795
	CO_2	0.176	0.176	0.159
	CH_4	—	—	0.046
Feed flow rate × 10^5 [m^3 s^{-1}] #		1.596	1.596	1.584
C_2H_6 flow rate × 10^5 [m^3 s^{-1}] #			0.030	
N_2 flow rate × 10^5 [m^3 s^{-1}] #			7.530	
Temperature [K]		323	343	305
Pressure [bar]			2.5	
Thermocouple distance from feed inlet [m]	TT_{Bottom}		0.170	
	TT_{Middle}		0.430	
	TT_{Top}		0.680	
Mass of Adsorbent [kg]		0.1760	0.1760	0.1743
Bed height [m]			0.870	
Bed volume [m^3]			3.013×10^{-4}	
Bed porosity, ε		0.332	0.332	0.338

measured at 298 K and 1 bar

gas chromatograph was able to separate the components of the feed mixture using a capillary column (J&W Scientic GS-AL P/N 115-3532, 30 m × 0.53 mm, Folsom, USA). The bed outlet concentrations of multicomponent gas mixtures of hydrogen, carbon dioxide, carbon monoxide, methane and nitrogen were determined by TCD detector. Figure 5.3 shows the schematic view of the fixed-bed unit connected to a GC analysis system to measure the bed outlet concentration [23]. The temperature in the column was measured at three points along the column namely at 0.175 (TT_{Bottom}), 0.424 (TT_{Middle}) and 0.677 m (TT_{Top}) from the feed inlet. The properties of the column used for these experiments are described in Table 5.2. The experimental conditions of the fixed-bed breakthrough curves on AC5-KS are reported in the same table (Table 5.2).

Before each experiment, the activation of the two activated carbons (R2030 and AC5-KS) was done heating at 1 K min^{-1} until 423 K and left overnight, under a continuous flow of a inert gas (He) of 5.83×10^{-6} m^3 s^{-1} (measured at 298 K and 1 bar). All gases were provided by Air Liquide: hydrogen N60, carbon dioxide N48, methane N35, carbon monoxide N35, ethane N35 and helium N50 (purities greater than 99.9999, 99.998, 99.95, 99.95, 99.95 and 99.999%, respectively).

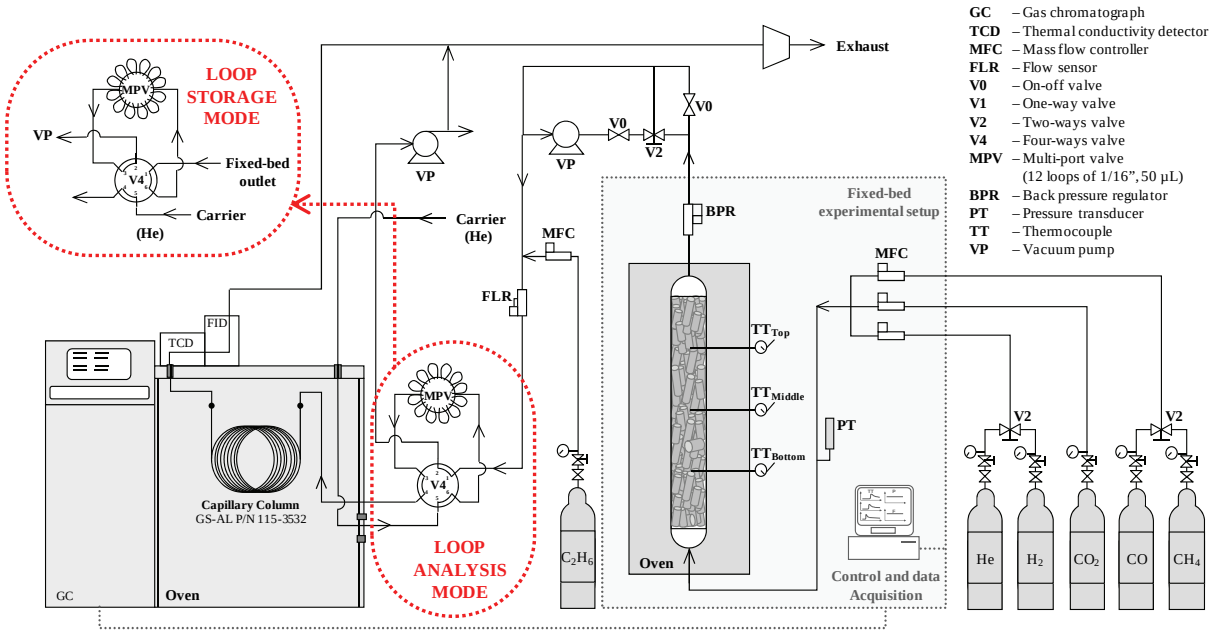


Figure 5.3: Schematic representation of the 1-column PSA-VSA experimental set-up used for multicomponent fixed-bed breakthroughs developed by Da Silva (1999) [23]: unit connected to a GC analysis system to measure the bed outlet concentration.

Table 5.2: Properties of the column used and experimental conditions of the fixed-bed breakthrough curves on the modified activated carbon AC5-KS.

Breakthrough curves (BT)		Single (He-CO_2)		Ternary (H_2-CO_2-CH_4)	
Experiment no.		1	2	3	4
Adsorbate molar fraction	He	0.852	0.369	—	—
	H_2	—	—	0.137	0.138
	CO_2	0.148	0.631	0.690	0.580
	CH_4	—	—	0.173	0.282
Feed flow rate × 10^5 [m^3 s^{-1}] #		1.543	1.575	1.848	1.871
C_2H_6 flow rate × 10^5 [m^3 s^{-1}] #		0.187			
Temperature [K]		303			
Pressure [bar]		1.2			
Thermocouple distance from feed inlet [m]	TT_{Bottom}	0.175			
	TT_{Middle}	0.424			
	TT_{Top}	0.677			
Mass of Adsorbent [kg]		0.139			
Bed height [m]		0.842			
Bed volume [m^3]		2.916×10^{-4}			
Bed porosity, ε		0.393			

measured at 298 K and 1 bar

5.2.1.2 Two-column "compact" PSA unit for multicomponent mixtures

Breakthrough curves were performed in a 2-column PSA experimental set-up (Figure 5.4) able to operate with gas mixtures of three (or more) components and with feed flow rates between 1.67×10^{-6} and 8.33×10^{-5} m^3 s^{-1} (measured at 298 K and 1 bar). This unit can work in the pressure range of 0.1-5 bar and at temperatures between 298 and 423 K. The schematic view of the complete unit is shown in Figure 5.5. The column used in the "compact" PSA unit and a schematic representation of the column with the flexible insulated heater are shown in Figure 5.6. The gas chromatograph analysis system installed in this set-up is composed by a gas chromatograph (Varian CP-3800, Holland) equipped with a multi-port valve (Vici, Valco) able to store up to 15 samples: each loop is a 1/16" stainless steel tube with a volume of 50 µL. A packed column (Supelco 60/80 Carboxen-1000 12390-U, USA) was placed in the oven of the gas chromatograph, operating at 453 K and using an inert carrier (He) flow rate of 8.33×10^{-7} m^3 s^{-1} (measured at 298 K and 1 bar) to allow the complete component separation of H_2-CO_2-CH_4-CO-N_2. The bed outlet concentrations of multicomponent gas mixtures of hydrogen, carbon dioxide, carbon monoxide, methane and nitrogen were determined by TCD detector. Note that, the gas exiting the 2-column PSA experimental set-up is at near atmospheric pressure before reaches this apparatus and the pressure decay produced by the 1/16" loops will be large enough to produce loss of the sample to the exhaust system [24]. Consequently, a vacuum pump (ILMVAC 400174, Germany) placed at the end of the line secured the loops of the multi-port valve to be filled with the bed outlet sample. Only a purge line of the gas exiting the 2-column PSA experimental set-up is used due to

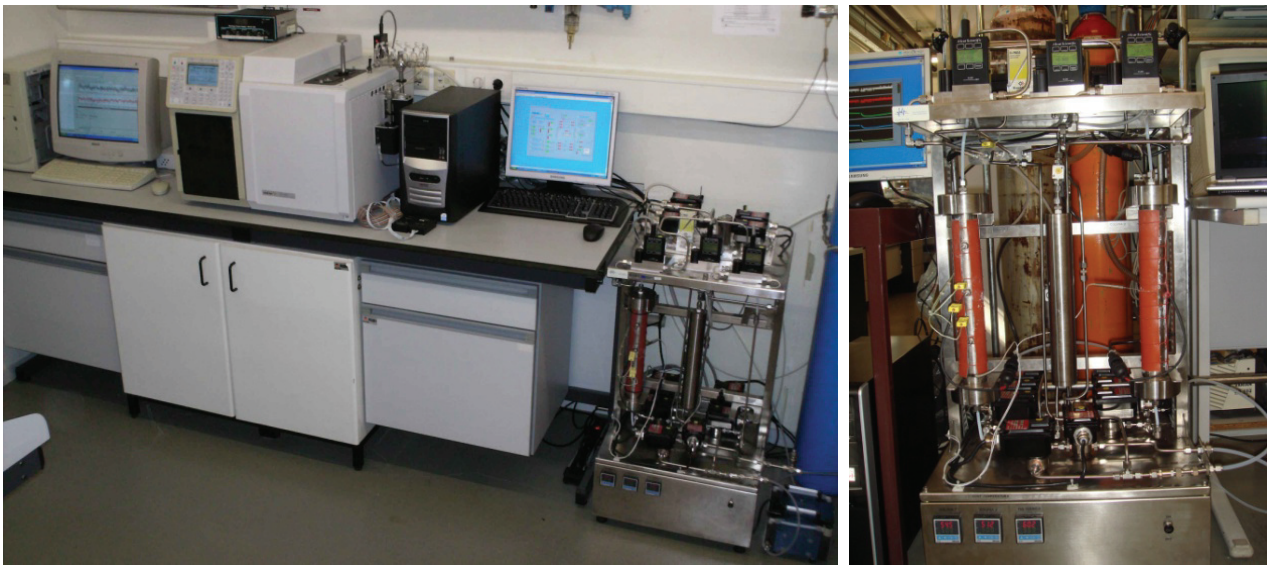


Figure 5.4: The 2-column PSA experimental set-up connected to a GC analysis system.

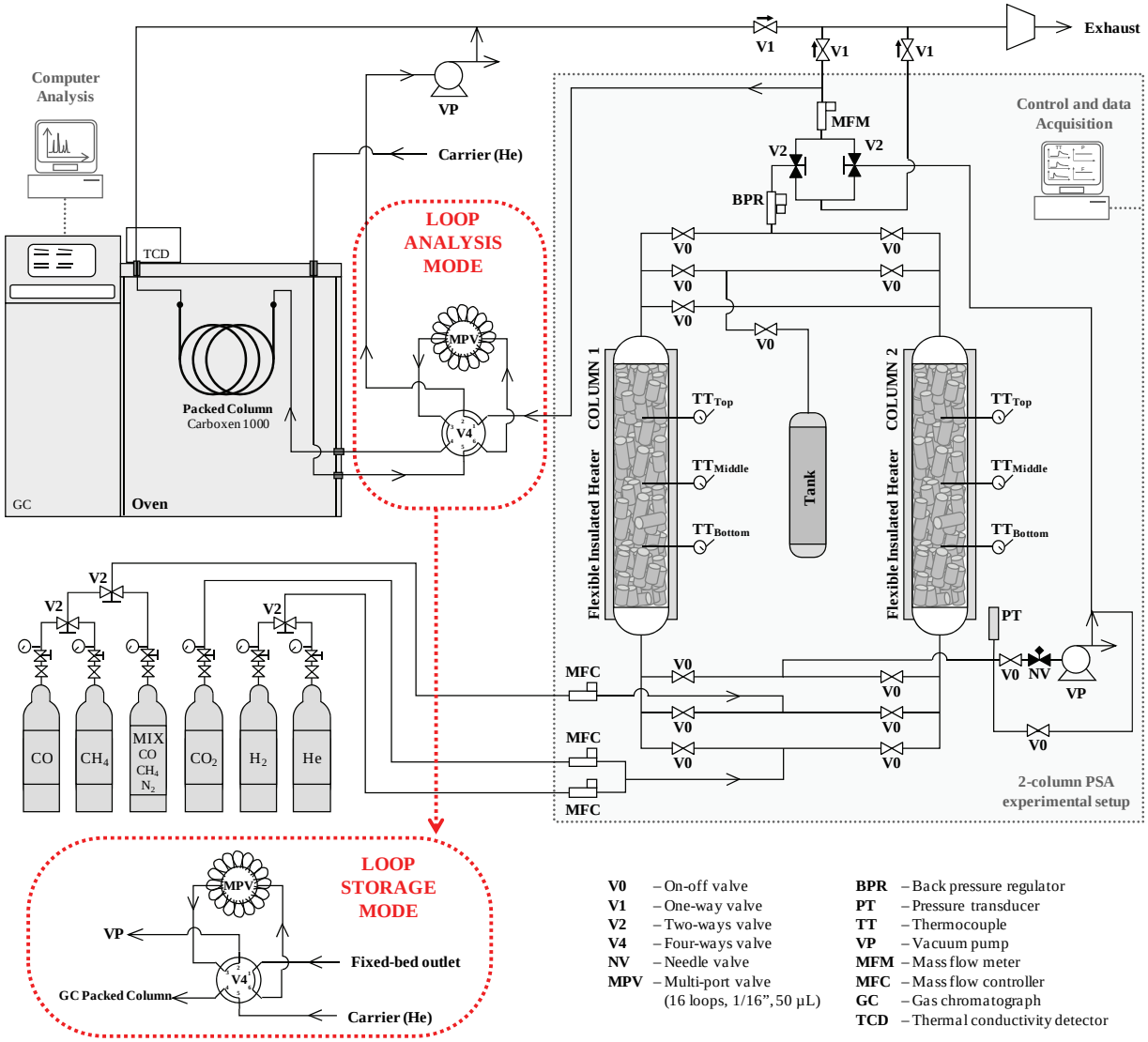


Figure 5.5: Schematic representation of the 2-column "compact" PSA experimental set-up used for multicomponent fixed-bed breakthroughs and PSA experiments connected to a GC analysis system to measure the bed outlet concentration.

the high pressures and flow rates used in the breakthrough experiments. This apparatus was used for the study of hydrogen purification from SMR off-gases (H_2, CO_2, CH_4, CO and N_2).

Breakthrough experiments of binary H_2-CO_2, ternary H_2-CO_2-CO and five-component H_2-CO_2-CH_4-CO-N_2 mixtures were performed in a fixed-bed packed with the modified activated carbon AC5-KS (previously studied in chapter 4 [21]). The breakthrough experiments were carried out at 323 K and the total pressure of 5 bar was kept constant with a back-pressure regulator. Temperature variations along the bed were recorded by three thermocouples (TT) located at 0.059 (TT_{Bottom}), 0.151 (TT_{Middle}) and 0.239 m (TT_{Top}) from the feed inlet. The dimensions of the column

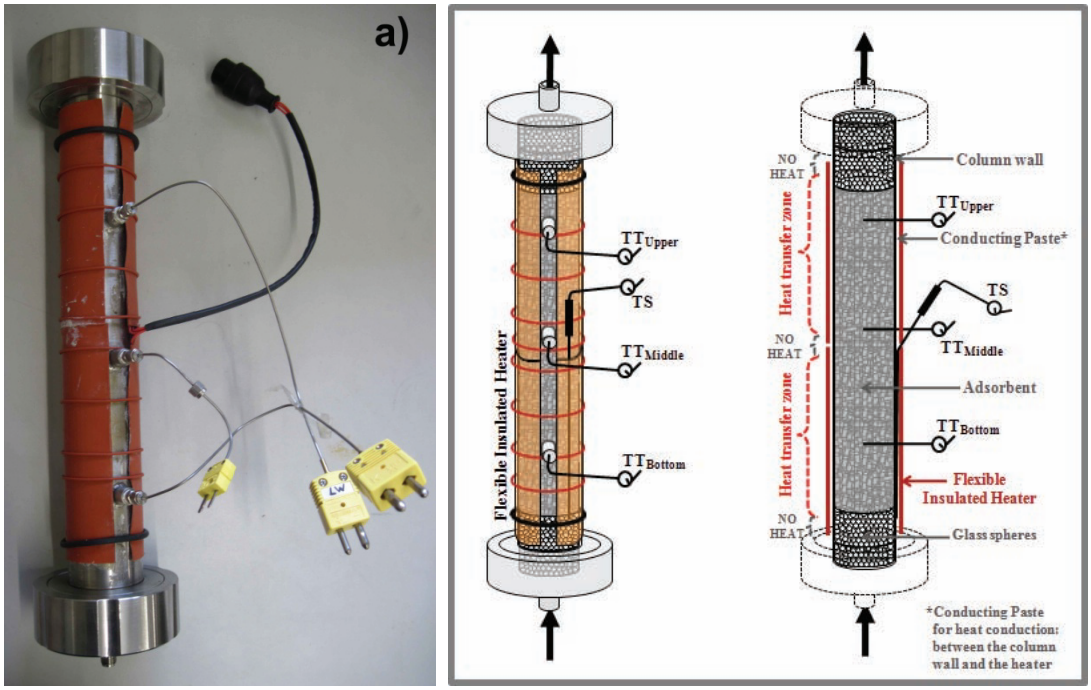


Figure 5.6: a) Column used in the "compact" PSA; b) Schematic representation with the heater.

Table 5.3: Properties of the column used and experimental conditions of the fixed-bed breakthrough curves on AC5-KS performed in the "compact" PSA.

Breakthrough curves (BT)		Binary (H_2-CO_2)			Ternary[a]	5-component[b]
Experiment no.		1	2	3	4	5
Adsorbate molar fraction	H_2	0.70	0.90	0.20	0.70	0.73
	CO_2	0.30	0.10	0.80	0.26	0.23
	CO	—	—	—	0.04	0.012
	CH_4	—	—	—	—	0.021
	N_2	—	—	—	—	0.007
Feed flow rate [$m^3\ s^{-1}$][#]		5.00×10^{-5}				
Temperature [K]		323				
Pressure [bar]		5				
Thermocouple distance from feed inlet [m]	TT_{Bottom}	0.059				
	TT_{Middle}	0.151				
	TT_{Top}	0.239				
Mass of Adsorbent [kg]		0.2456				
Bed height [m]		0.267				
Bed volume [m^3]		5.24×10^{-4}				
Bed porosity, ε		0.404				

[#] measured at 298 K and 1 bar
[a] Ternary (H_2-CO_2-CO) breakthrough curve
[b] Five-component (H_2-CO_2-CH_4-CO-N_2) breakthrough curve

used in these measurements and the adsorbent physical properties are given in Table 5.3. The experimental conditions of the fixed-bed breakthrough curves are reported in Table 5.3.

To degass the adsorbent sample before the experiments, a inert gas (He) flow of 5.00×10^{-6} m^3 s^{-1} (measured at 298 K and 1 bar) was used overnight at 423 K, after heating at heating rate of 1 K min^{-1}. The gases used in this study were provided by Air Liquide: hydrogen N60, carbon dioxide N48, carbon monoxide N47, methane N35, nitrogen N45 and helium N50 (purities greater than 99.9999, 99.998, 99.997, 99.95, 99.995 and 99.999%, respectively).

5.2.2 PSA experiment

The same column employed for the fixed-bed breakthrough curves described in the last section 5.2.1.2 was used for a PSA experiment (see properties in Table 5.3). A PSA cycle of 10 elementary steps was employed (see Figure 5.7): a co-current feed, three pressure equalizations-depressurizations, a counter-current blowdown, a counter-current purge with hydrogen, three pressure equalizations-pressurizations and a counter-current pressurization with hydrogen. The cycle is a Skarstrom cycle [25] with the integration of three pressure equalization steps used in PSA columns to increase H_2 recovery. The PSA cycle started with the co-current feed step considering that the column was filled with an inert gas (helium) at the feed temperature and feed pressure. The operating parameters of the PSA experiment are also detailed in Table 5.4.

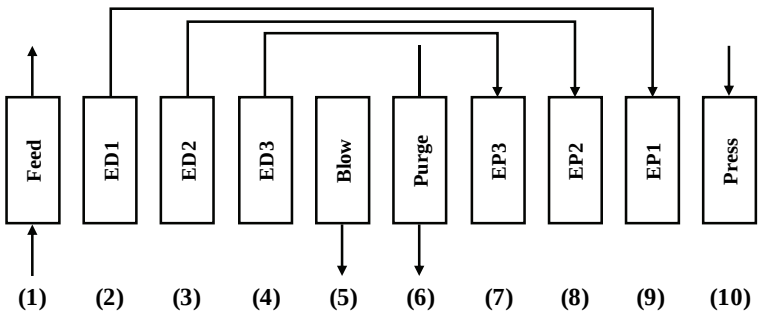


Figure 5.7: Schematic diagram of the cycle sequence used in the PSA experiment for H_2 purification: Cycle sequence: (1) co-current feed step; (2) first, (3) second and (4) third pressure equalization-depressurization steps; (5) counter-current blowdown step; (6) counter-current purge step with hydrogen; (7) third, (8) second and (9) first pressure equalization-pressurization steps; (10) counter-current pressurization step with hydrogen.

Table 5.4: Experimental conditions of the PSA experiment using the modified activated carbon AC5-KS.

PSA experiment	
Ads molar fraction	H_2: 0.79; CO_2: 0.17; CH_4: 0.021; CO: 0.012; N_2: 0.007
Feed temperature [K]	303
Feed flow rate [$m^3\ s^{-1}$] #	5.00×10^{-5}
Step pressures [bar]	P_{high} = 5 bar ; P_{inter1} = 3.875 bar ; P_{inter2} = 2.75 bar ; P_{inter3} = 1.625 bar ; P_{low} = 0.5 bar
Step times [s]	t_{Feed} = 101 s ; t_{Blow} = 201 s ; t_{Purge} = 40 s ; t_{Press} = 21 s ; $t_{ED1} = t_{ED2} = t_{ED3} = t_{EP3} = t_{EP2} = t_{EP1}$ = 16 s

measured at 298 K and 1 bar

5.3 Theoretical

Adsorption equilibrium and kinetics of pure hydrogen, carbon dioxide, carbon monoxide, methane and nitrogen on the activated carbons R2030 and AC5-KS were previously reported in chapters 2 and 3 and in chapter 4, respectively. The Virial adsorption model was used to describe adsorption equilibrium of these gases at 303, 323 and 343 K and in the pressure range 0-20 bar [19]. The same model was used to describe adsorption equilibrium of the pure gas on AC5-KS at 303 and 323 K and in the pressure range 0-7 bar [21]. The prediction of multicomponent fixed-bed experiments of He-CO_2, H_2-CO_2, H_2-CO_2-CH_4, H_2-CO_2-CO and H_2-CO_2-CH_4-CO-N_2 were performed applying the extended virial isotherm model [26-28] using the parameters previously obtained from pure component data (summarized in Table 5.5). The extension of the Virial isotherm to multicomponent systems proposed by Taqvi and LeVan (1997) [28] is defined by:

$$P_i = \frac{q_i}{K_{Hi}} \exp\left(\frac{2}{S} \sum_{j=1}^{N} A_{ij} q_i + \frac{3}{2S^2} \sum_{j=1}^{N} \sum_{k=1}^{N} B_{ijk} q_j q_k \right) \tag{5.1}$$

where A_{ij} and B_{ijk} are the mixing Virial coefficients. According to the ideal adsorbed solution theory, these coefficients are defined by equation (5.2) [29].

$$A_{ij} = \frac{\left(A_i + A_j\right)}{2} \quad , \quad B_{ijk} = \frac{\left(B_i + B_j + B_k\right)}{3} \tag{5.2}$$

A complete mathematical model that describes the dynamic behaviour of multicomponent adsorption in a fixed-bed is composed of material, momentum and energy balances. The energy balance should be taken into account because adsorption is an exothermic process that releases energy and may produce non isothermal behaviour of the system. The momentum balance should also be included as the velocity varies along the bed.

Table 5.5: Virial isotherm fitting parameters of pure H_2, CO_2, CO, CH_4 and N_2 at 303-323 K on activated carbons R2030 and AC5-KS.

Species	K_∞ [mol kg^{-1} bar^{-1}]	$(-\Delta H)$ [kJ mol^{-1}]	$A_0 \times 10^{-5}$ [m^2 mol^{-1}]	$A_1 \times 10^{-6}$ [m^2 K mol^{-1}]	$B_0 \times 10^{-11}$ [m^4 mol^{-2}]	$B_1 \times 10^{-6}$ [m^4 K mol^{-2}]
Activated carbon R2030						
H_2	8.20×10^{-3}	3.192	0.418	-0.001	0.454	0.000
CO_2	9.90×10^{-5}	27.870	-1.140	79.013	-0.021	-0.416
CO	4.62×10^{-4}	19.100	14.076	-422.77	0.264	299.25
CH_4	1.04×10^{-3}	17.652	4.616	-121.43	-0.831	308.53
N_2	2.54×10^{-3}	11.834	5.585	-163.77	3.385	-777.67
Modified activated carbon AC5-KS						
H_2	2.12×10^{-3}	7.26	-1.917	0.1994	-4.015	7315.4
CO_2	8.06×10^{-5}	28.02	0.081	45.31	-0.365	92.247
CO	7.63×10^{-5}	23.23	-0.149	-105.46	-2.407	528.18
CH_4	2.29×10^{-4}	23.18	12.808	-294.44	-6.101	1745.7
N_2	3.06×10^{-4}	18.27	11.989	-278.79	-13.758	3988.6

[*] obtained from the 303 K data

The dynamic behaviour of multicomponent adsorption was described taking into consideration the following assumptions in order to write the necessary conservation equations:

a) Ideal gas behaviour throughout the fixed-bed,
b) Constant porosity along the bed,
c) Bidisperse adsorbent where macro and micropore mass transfer is expressed by a bi-linear driving force (bi-LDF) model,
d) Axial dispersed plug flow mathematical model composed of mass, momentum and energy balances,
e) No temperature gradients inside each particle,
f) Radial gradients of temperature and concentration were also neglected,
g) No mass, heat or velocity gradients in the radial direction,
h) External mass and heat transfer resistances were expressed with the film model.

A schematic diagram of this adsorption system is shown in Figure 5.8 [30] where three phases can be distinguished: gas phase, solid phase where adsorption and diffusion take place and the column wall where energy may be transferred to (or from) the surroundings.

The gas phase exchanges mass and energy with the solid phase and only energy with the column wall. The material balance for each component in the gas phase is given by:

$$\frac{\partial}{\partial z}\left(\varepsilon D_{ax} C_{g,T} \frac{\partial y_i}{\partial z}\right) - \frac{\partial}{\partial z}\left(u_0 C_{g,i}\right) - \varepsilon \frac{\partial C_{g,i}}{\partial t} - (1-\varepsilon) a_p k_f \left(C_{g,i} - C_{s,i}\right) = 0 \tag{5.3}$$

where z is the axial position, t is the time, ε is the bed porosity, u_0 is the superficial velocity, $C_{g,T}$ and $C_{g,i}$ are respectively the total and component i gas phase concentration, y_i is the component i molar fraction, $C_{s,i}$ is the concentration of component i at the solid surface, D_{ax} is the mass axial dispersion coefficient, k_f is the film mass transfer coefficient and a_p is the particle specific area.

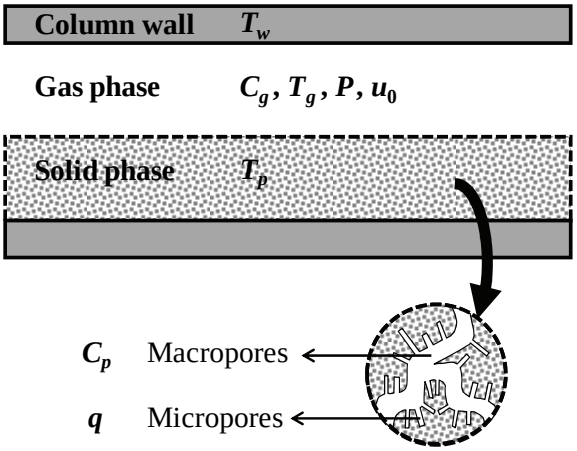


Figure 5.8: Schematic representation of the adsorption bed: column wall, gas phase and solid phase composed by bidisperse adsorbent (macro and micropores) [30].

In the momentum balance, only the terms of pressure drop and velocity change were considered, which are related through the Ergun equation defined as:

$$-\frac{\partial P}{\partial z} = \frac{150\mu(1-\varepsilon)^2}{\varepsilon^3 d_p^2} u_0 + \frac{1.75(1-\varepsilon)\rho_g}{\varepsilon^3 d_p} |u_0| u_0 \tag{5.4}$$

where P is the total pressure, μ is the gas viscosity, ρ_g is the gas density, and d_p is the particle diameter.

The energy balance in the gas phase is:

$$\begin{aligned}\frac{\partial}{\partial z}\left(\lambda \frac{\partial T_g}{\partial z}\right) - u_0 C_{g,T} C_p \frac{\partial T_g}{\partial z} + \varepsilon R_g T_g \frac{\partial C_{g,T}}{\partial t} \\ - (1-\varepsilon) a_p h_f \left(T_g - T_p\right) - \frac{4h_w}{d_{wi}}\left(T_g - T_w\right) - \varepsilon C_{g,T} C_v \frac{\partial T_g}{\partial t} = 0\end{aligned} \tag{5.5}$$

with T_g, T_p, and T_w respectively as the gas, particle and wall temperatures; C_v and C_p as the gas molar specific heat at constant volume and pressure respectively; R_g as the ideal gas constant; d_{wi} as the wall internal diameter, λ as the heat axial dispersion coefficient. The film heat transfer

coefficient between the gas phase and the particle is represented by h_f, while the film heat transfer coefficient between the gas phase and the wall is represented by h_w.

As mentioned above, the particle is considered bidisperse, composed by macropores that serve as main transport channels to the micropores (Figure 5.8). The macropores exchange mass both with the gas phase and the micropores. The linear driving force model (LDF) is employed to describe the mass transfer rates in the solid phase. This approximation has a large impact on the computational time. The LDF equations for the macropore and for the micropore/crystal are then given respectively by equations (5.6) and (5.7).

$$\frac{\partial \langle C_{m,i} \rangle}{\partial t} = \frac{\Omega_m D_{p,i}}{R_p^2}\left(C_{s,i} - \langle C_{m,i} \rangle\right) - \frac{\rho_p}{\varepsilon_p}\frac{\partial \langle \bar{q}_i \rangle}{\partial t} \tag{5.6}$$

$$\frac{\partial \bar{q}_i}{\partial t} = \frac{\Omega_c D_{c,i}}{r_c^2}\left(q_i^* - \bar{q}_i\right) \tag{5.7}$$

In these equations, ρ_p and ε_p are respectively the particle density and porosity, $D_{p,i}$ and $D_{c,i}$ are the macropore and micropore diffusivity coefficients, R_p is the particle radius, r_c is the "microparticle" or crystal radius, $\langle C_{m,i} \rangle$ is the particle average of the concentration in the macropores, $\langle \bar{q}_i \rangle$ is the particle averaged adsorbed concentration, $\bar{q}_i$ is the micropore/crystal averaged adsorbed concentration, and q_i^* is the adsorbed concentration in equilibrium with $C_{m,i}$ and Ω_m and Ω_c are the geometric LDF factors of the macropore and micropore/crystal, respectively.

As it is assumed that there are no temperature gradients inside a particle, the solid phase energy balance is given by:

$$\begin{aligned}\left(1-\varepsilon\right)\left[\varepsilon_p \sum_{i=1}^{n} C_{m,i} C_{v,i} + \rho_p \sum_{i=1}^{n} \langle \bar{q}_i \rangle C_{v,ads,i} + \rho_p \hat{C}_{p,s}\right]\frac{\partial T_p}{\partial t} \\ = \left(1-\varepsilon\right)\varepsilon_p R_g T_p \frac{\partial C_{m,T}}{\partial t} + \rho_b \sum_{i=1}^{n}\left(-\Delta H\right)_i \frac{\partial \langle \bar{q}_i \rangle}{\partial t} + \left(1-\varepsilon\right) a_p h_f \left(T_g - T_p\right)\end{aligned} \tag{5.8}$$

where ρ_b is the bulk density of the bed, $\hat{C}_{p,s}$ is the solid specific heat per mass unit and $(-\Delta H)_i$ is the isosteric heat of adsorption of component i.

The concentration of each component at the solid surface can be calculated with equation (5.9) obtained through the fluxes equality at the particle surface.

$$C_{s,i} = \frac{Bi_i C_{g,i} + C_{m,i}}{1 + Bi_i} \tag{5.9}$$

In this equation Bi_i is the Biot number of component i defined as:

$$Bi_i = \frac{a_p k_f R_p^2}{\varepsilon_p \Omega_m D_{p,i}} \tag{5.10}$$

Finally, the energy balance to the column wall considers that it interchanges energy with the gas phase inside the column and with the external environment being expressed as:

$$\rho_w \hat{C}_{p,w} \frac{\partial T_w}{\partial t} = \alpha_w h_w \left(T_g - T_w\right) - \alpha_{w\ell} U \left(T_w - T_\infty\right) \tag{5.11}$$

where T_w and T_∞ are the wall and external temperatures, respectively, ρ_w is the wall density, $\hat{C}_{p,w}$ is the wall specific heat per mass unit, U is the overall heat transfer coefficient and α_w and $\alpha_{w\ell}$ are defined by:

$$\alpha_w = d_{wi} / \left[e\left(d_{wi} + e\right)\right] \tag{5.12}$$

$$\alpha_{w\ell} = 1 / \left[\left(d_{wi} + e\right) \ln\left(\left(d_{wi} + e\right) / d_{wi}\right)\right] \tag{5.13}$$

where e is the wall thickness.

In order to solve this system of partial differential equations, boundary and initial conditions are needed. In the case of fixed-bed operation where pressure is controlled at the end of the column, starting with a column filled with an inert gas, such conditions are as follows. The boundary conditions for feed inlet ($z = 0$) are:

$$\begin{aligned} u_{0inlet} C_{inlet,i} &= u_0 C_{g,i} - \varepsilon D_{ax} C_{g,T} \frac{\partial y_i}{\partial z} \\ u_{0inlet} C_{inlet,T} &= u_0 C_{g,T} \\ u_{0inlet} C_{inlet,T} C_p T_{inlet} &= u_0 C_{g,T} C_p T_g - \lambda \frac{\partial T_g}{\partial z} \end{aligned} \tag{5.14}$$

and the boundary conditions for the product end ($z = L$) are:

$$\begin{aligned} &\frac{\partial C_{g,i}}{\partial z} = 0 \\ &P = P_{exit} \\ &\frac{\partial T_g}{\partial z} = 0 \end{aligned} \tag{5.15}$$

The initial conditions for the fixed-bed initially filled with inert gas are:

$$\begin{aligned} &y_i = C_{m,i} = q_i = 0 \quad \text{for } i \neq inert \\ &y_{inert} = 1 \\ &C_{m,inert} = C_{g,T} \\ &T_g = T_p = T_w = T_{inlet} \end{aligned} \tag{5.16}$$

As can be seen from the model equations, some transport parameters are needed. General properties of the gases, like density, viscosity, and thermal conductivity were calculated according to Bird *et al.* (2002) [31]. The pore diffusivity and the molecular diffusivity for the mixture and the

Knudsen diffusivity were calculated according to equations (5.17) to (5.19), respectively and previously reported in chapter 3, equations (3.6) to (3.13). The pore diffusivity was calculated with the Bosanquet equation:

$$\frac{1}{D_p} = \tau_p \left(\frac{1}{D_m} + \frac{1}{D_k} \right) \tag{5.17}$$

where D_m is the molecular diffusivity, D_k is Knudsen diffusivity and τ_p is the pore tortuosity. The molecular diffusivity for the mixture was approximated with:

$$D_m = \frac{1 - y_i}{\sum_{\substack{j=1 \\ j \neq i}}^{n} \frac{y_i}{D_{ij}}} \tag{5.18}$$

where the binary molecular diffusivity D_{ij} was calculated with the Chapman-Enskog equation [31]. The Knudsen diffusivity (D_k in $m^2\ s^{-1}$) is calculated by:

$$D_k = 97.0\ r_p \sqrt{\frac{T}{M_W}} \tag{5.19}$$

where r_p is the mean pore radius (in meters) and M_W is the molecular weight of the adsorbate.

The axial heat dispersion coefficient, as well as, the heat convective coefficient were calculated using the Wakao and Funazkri correlations [32-34]:

$$\frac{\varepsilon D_{ax}}{D_m} = 20 + 0.5 ScRe \tag{5.20}$$

$$\frac{\lambda}{k_g} = 7 + 0.5 PrRe \tag{5.21}$$

$$Nu = 2.0 + 1.1 Re^{0.6} Pr^{1/3} \tag{5.22}$$

$$Sh = 2.0 + 1.1 Re^{0.6} Sc^{1/3} \tag{5.23}$$

The axial mass transfer coefficient calculated by equation (5.20) is valid for a large range of Reynolds numbers ($3 < Re < 10000$) and was employed for modeling multicomponent breakthrough curves reported in this work. The dimensional Reynolds (*Re*), Schmidt (*Sc*), Prandtl (*Pr*), Sherwood (*Sh*) and Nusselt (*Nu*) numbers are defined as:

$$Re = \frac{\rho_g u_0 d_p}{\mu} \tag{5.24}$$

$$Sc = \frac{\mu}{\rho_g D_m} \tag{5.25}$$

$$Pr = \frac{\hat{C}_p \mu}{k_g} \tag{5.26}$$

$$Sh = \frac{k_f d_p}{D_m} \tag{5.27}$$

$$Nu = \frac{h_f d_p}{k_g} \tag{5.28}$$

The global heat transfer coefficient (U) was calculated according to [35]:

$$\frac{1}{U} = \frac{1}{h_w} + \frac{e d_{wi}}{\lambda_w d_{\ell n}} + \frac{d_{wi}}{d_{we} h_{ex}} \tag{5.29}$$

where λ_w is the wall conductivity, d_{we} is the external diameter of the column, h_{ex} is the external convective heat transfer coefficient and $d_{\ell n}$ defined by equation (5.30).

$$d_{\ell n} = \frac{d_{we} - d_{wi}}{\ln\left(\frac{d_{we}}{d_{wi}}\right)} \tag{5.30}$$

The internal convective heat transfer coefficient (h_w) between gas and the wall column can be estimated with the Wasch and Froment correlation [36]:

$$\frac{h_w d_{wi}}{k_g} = 140 + 0.013396 \frac{d_{wi}^2}{d_p k_g} Re \tag{5.31}$$

The external convective heat transfer coefficient was estimated with the Churchill and Chu correlation [35]:

$$\frac{h_{ex} L}{k_{g,ex}} = 0.68 + \frac{0.67 Ra^{1/4}}{\left[1 + \left(\frac{0.492}{Pr}\right)^{9/16}\right]^{4/9}} \tag{5.32}$$

where the sub-index ex represent the properties of the external gas surrounding the column. The Rayleigh number (Ra) and the Grashof number (Gr) are defined by equations (5.33) and (5.34), respectively:

$$Ra = Gr\,Pr \tag{5.33}$$

$$Gr = \frac{g\beta(T_w - T_\infty)L^3}{\nu\alpha} \tag{5.34}$$

where g is the acceleration due to gravity (g = 9.8 m s^{-2}), ν is the kinematic viscosity of the external gas, α is the external thermal diffusivity and β is the thermal expansion coefficient. The properties of the external gas are evaluated at the film temperature:

$$T_{film} = \frac{T_w + T_\infty}{2} \tag{5.35}$$

This mathematical model was previously employed for simulations of fixed-bed behaviour and/or PSA applications of different mixtures showing very good agreement between predictions and experimental data [19, 37-39]. The simulations were performed with gPROMS (PSE Enterprise, UK). For the fixed-bed simulations described in section 5.2.1.1, two methods were used: for activated carbon R2030 simulations, the orthogonal collocation on finite elements was the numerical method used. The number of elements used was 120 with forth order polynomials (three interior collocation points). For AC5-KS, the simulations were performed using centered finite differences as the numerical method, with 270 discretization intervals and approximation of second order for partial derivatives and integrals. The transport parameters applied in these simulations are reported in Table 5.6. For the fixed-bed experiments described in section 5.2.1.2, the runs were

Table 5.6: Transport parameters used in the breakthrough simulations of activated carbons R2030 and AC5-KS performed in the fixed-bed unit for ternary mixtures.

Run		Activated carbon R2030			Modified activated carbon AC5-KS			
		1	2	3	1	2	3	4
$D_{ax} \times 10^5$[m^2 s^{-1}]		4.04	4.34	3.61	7.53	6.85	7.08	7.15
λ [J s^{-1} m^{-1} K^{-1}]		0.99	1.03	0.92	1.15	0.43	0.32	0.33
$k_f \times 10^2$ [m s^{-1}]		3.98	4.36	3.19	7.00	8.00	6.00	6.00
h_f [J s^{-1} m^{-2} K^{-1}]		164	169	154	183	86	64	67
h_w [J s^{-1} m^{-2} K^{-1}]		66.7	69.6	62.0	60.0	80.0	75.0	75.0
U [J s^{-1} m^{-2} K^{-1}]		31.3	33.6	30.25	25.0	30.0	40.0	40.0
$D_p \times 10^6$ [m^2 s^{-1}][#]	He	—	—	—	25.3	25.3	—	—
	H_2	4.80	5.32	4.47	—	—	28.1	28.5
	CO_2	4.48	4.94	3.57	25.3	25.3	10.5	9.38
	CH_4	—	—	3.10	—	—	8.14	8.33

Species	T [K]	Activated carbon R2030		Modified activated carbon AC5-KS	
		D_c/r_c^2 [s^{-1}]	E_a [kJ mol^{-1}]	D_c/r_c^2 [s^{-1}]	E_a [kJ mol^{-1}]
H_2	303	1.35×10^{-1}	—	8.130	8.51
	323	—		10.04	
CO_2	303	4.27×10^{-2}	25.5	3.70×10^{-2}	17.6
	323	6.13×10^{-2}		4.73×10^{-2}	
	343	6.67×10^{-2}		—	
CH_4	303	1.55×10^{-2}	9.75	7.56×10^{-2}	26.4
	323	3.01×10^{-2}		1.44×10^{-1}	
	343	5.04×10^{-2}		—	

[#] values at inlet conditions

simulated using the orthogonal collocation on finite elements method (40 elements with two interior collocation points). The transport parameters applied in the simulations using the modified activated carbon AC5-KS are reported in Table 5.7. All the simulations were performed with an absolute and relative tolerances of 1×10^{-5}.

Table 5.7: Transport parameters used in the breakthrough simulations of modified activated carbon AC5-KS performed in the "compact" PSA unit for multicomponent mixtures.

Run		1	2	3	4	5
$D_{ax} \times 10^5$[m^2 s^{-1}]		1.46	1.46	1.46	1.37	1.33
λ [J s^{-1} m^{-1} K^{-1}]		0.766	1.109	0.296	0.778	0.823
$k_f \times 10^2$ [m s^{-1}]		1.83	1.69	2.04	1.53	1.40
h_f [J s^{-1} m^{-2} K^{-1}]		123	161	57	125	130
h_w [J s^{-1} m^{-2} K^{-1}]		55	55	55	55	55
U [J s^{-1} m^{-2} K^{-1}]		50	50	50	50	50
$D_p \times 10^6$ [m^2 s^{-1}]$^{\#}$	H_2	7.36	7.36	7.36	7.54	7.51
	CO_2	7.36	7.36	7.36	6.29	6.40
	CO	—	—	—	4.26	4.43
	CH_4	—	—	—	—	4.56
	N_2	—	—	—	—	4.38
D_c^0/r_c^2 [s^{-1}] ; E_a [kJ mol^{-1}]	H_2	46.35 ; 8.51				
	CO_2	35.64 ; 17.6				
	CO	4.955 ; 10.8				
	CH_4	35.52 ; 26.4				
	N_2	349.7 ; 19.8				

$^{\#}$ values at inlet conditions

The model described in equations (5.3) to (5.13) and the correlations of equations (5.17) to (5.35) were also applied for the simulation of single column PSA processes [19, 23, 31-36]. The mathematical model was employed to simulate two different PSA cycles reported in Figure 5.9. Cycles A and B are Skarstrom-type cycles for PSA processes using only one and three pressure equalization steps, respectively [25]. The runs were simulated using the operation conditions described in Table 5.8 and the transport parameters reported in Table 5.9.

Table 5.8: H_2 PSA simulations using a single bed packed with AC5-KS.

Cycle A			
Simulation	t_{Feed} [s]	t_{Blow} [s]	t_{Purge} [s]
1[a,*]	100	200	30
2[a,*]	100	200	45
5[b,*]	100	200	30
6[b,*]	120	200	30
$t_{ED} = t_{EP} = 45$ s ; $t_{Press} = 20$ s			
a) $P_{high} = 5$ bar ; $P_{inter} = 2.75$ bar ; $P_{low} = 0.5$ bar b) $P_{high} = 10$ bar ; $P_{inter} = 5.5$ bar ; $P_{low} = 1$ bar			
Feed:	$y_{H_2} = 0.79$; $y_{CO_2} = 0.17$; $y_{CH_4} = 0.021$; $y_{CO} = 0.012$; $y_{N_2} = 0.007$ $Q = 5 \times 10^{-5}$ m^3 s^{-1} (measured at 298 K and 1 bar)		
Cycle B			
Simulation	t_{Feed} [s]	t_{Blow} [s]	t_{Purge} [s]
3[c,*]	100	200	30
4[c,*]	100	200	45
7[d,*]	100	200	30
8[d,*]	120	200	30
9[d,*]	120	150	30
10[d,*]	120	150	20
11[d,*]	110	150	20
12[d,*]	110	100	20
13[d,*]	110	70	20
14[d,*]	120	70	20
15[d,#]	100	200	30
16[d,#]	120	70	20
17[d,#]	120	70	35
$t_{ED1} = t_{ED2} = t_{ED3} = t_{EP3} = t_{EP2} = t_{EP1} = 15$ s ; $t_{Press} = 20$ s			
c) $P_{high} = 5$ bar ; $P_{inter1} = 3.875$ bar ; $P_{inter2} = 2.75$ bar ; $P_{inter2} = 1.625$ bar ; $P_{low} = 0.5$ bar d) $P_{high} = 10$ bar ; $P_{inter1} = 7.75$ bar ; $P_{inter2} = 5.5$ bar ; $P_{inter3} = 3.25$ bar ; $P_{low} = 1$ bar			
Feed:	$y_{H_2} = 0.79$; $y_{CO_2} = 0.17$; $y_{CH_4} = 0.021$; $y_{CO} = 0.012$; $y_{N_2} = 0.007$ $Q = 5 \times 10^{-5}$ m^3 s^{-1} (measured at 298 K and 1 bar)		

[*] $T = 303$ K
[#] $T = 323$ K

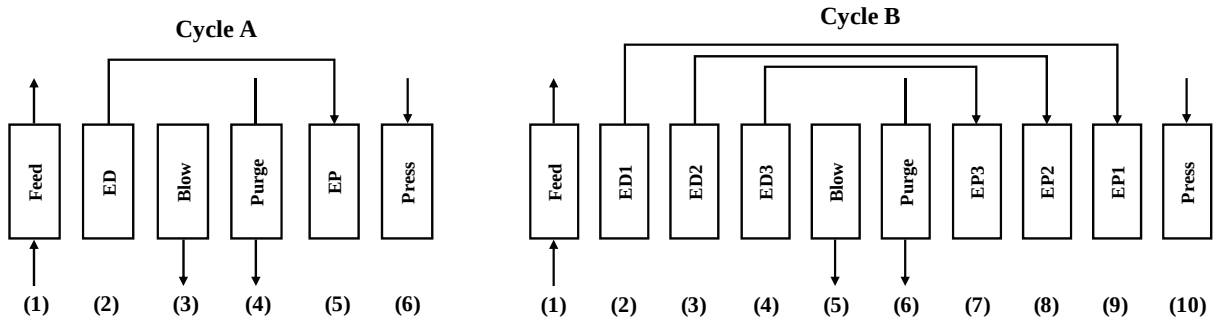


Figure 5.9: Schematic diagram of the cycle sequences used in the PSA simulations for H_2 purification: Cycle A: (1) co-current feed step; (2) pressure equalization-depressurization step; (3) counter-current blowdown step; (4) counter-current purge step with hydrogen; (5) pressure equalization-pressurization step; (6) counter-current pressurization step with hydrogen; Cycle B: (1) co-current feed step; (2) first, (3) second and (4) third pressure equalization-depressurization steps; (5) counter-current blowdown step; (6) counter-current purge step with hydrogen; (7) third, (8) second and (9) first pressure equalization-pressurization steps; (10) counter-current pressurization step with hydrogen.

Table 5.9: Transport parameters used in the PSA simulations of modified activated carbon AC5-KS performed in the "compact" PSA unit for multicomponent mixtures.

Simulation		1-4	5-14	15-17
$D_{ax} \times 10^5$[m^2 s^{-1}]		1.26	0.628	0.679
λ [J s^{-1} m^{-1} K^{-1}]		0.881	0.881	0.921
$k_f \times 10^2$ [m s^{-1}]		1.31	0.65	0.72
h_f [J s^{-1} m^{-2} K^{-1}]		136	136	141
h_w [J s^{-1} m^{-2} K^{-1}]		55	55	55
U [J s^{-1} m^{-2} K^{-1}]		50	50	50
$D_p \times 10^6$ [m^2 s^{-1}]$^{\#}$	H_2	6.77	3.38	3.78
	CO_2	5.78	2.89	3.23
	CO	4.51	2.26	2.53
	CH_4	4.58	2.29	2.57
	N_2	4.45	2.23	2.49
D_c^0/r_c^2 [s^{-1}] ; E_a [kJ mol^{-1}]	H_2		46.35 ; 8.51	
	CO_2		35.64 ; 17.6	
	CO		4.955 ; 10.8	
	CH_4		35.52 ; 26.4	
	N_2		349.7 ; 19.8	

$^{\#}$ values at inlet conditions

The initial conditions used in the PSA simulations were the same as for the fixed-bed experiments. The boundary conditions for each step are summarized below.

For the co-current feed step, the boundary conditions for $z = 0$ (inlet) are:

$$\begin{aligned} & u_{0inlet} C_{inlet,i} = u_0 C_{g,i} - \varepsilon D_{ax} C_{g,T} \frac{\partial y_i}{\partial z} \\ & P = P_{inlet} \\ & u_{0inlet} C_{inlet,T} C_p T_{inlet} = u_0 C_{g,T} C_p T_g - \lambda \frac{\partial T_g}{\partial z} \end{aligned} \tag{5.36}$$

and the boundary conditions for $z = L$ (outlet) are:

$$\begin{aligned} & \frac{\partial C_{g,i}}{\partial z} = 0 \\ & P = P_{exit} \\ & \frac{\partial T_g}{\partial z} = 0 \end{aligned} \tag{5.37}$$

For the pressure equalization-depressurization step, the boundary conditions for $z = 0$ are:

$$\begin{aligned} & \frac{\partial C_{g,i}}{\partial z} = 0 \\ & u_0 = 0 \\ & \frac{\partial T_g}{\partial z} = 0 \end{aligned} \tag{5.38}$$

and the boundary conditions for $z = L$ (outlet) are:

$$\begin{aligned} & \frac{\partial C_{g,i}}{\partial z} = 0 \\ & P = P_{inter} + \left(P_{inter} - P_{high}\right)\left[1 - \exp\left(-\beta_p t\right)\right] \\ & \frac{\partial T_g}{\partial z} = 0 \end{aligned} \tag{5.39}$$

The boundary conditions for the counter-current blowdown step for $z = 0$ (outlet) are:

$$\begin{aligned} & \frac{\partial C_{g,i}}{\partial z} = 0 \\ & P = P_{inter} + \left(P_{low} - P_{inter}\right)\left[1 - \exp\left(-\beta_p t\right)\right] \\ & \frac{\partial T_g}{\partial z} = 0 \end{aligned} \tag{5.40}$$

and the boundary conditions for $z = L$ are:

$$\frac{\partial C_{g,i}}{\partial z} = 0$$
$$u_0 = 0 \tag{5.41}$$
$$\frac{\partial T_g}{\partial z} = 0$$

For the counter-current purge with hydrogen step, boundary conditions for $z = 0$ (outlet) are:

$$\frac{\partial C_{g,i}}{\partial z} = 0$$
$$P = P_{exit} \tag{5.42}$$
$$\frac{\partial T_g}{\partial z} = 0$$

and the boundary conditions for $z = L$ (inlet) are:

$$u_{0inlet} C_{inlet,i} = u_0 C_{g,i} - \varepsilon D_{ax} C_{g,T} \frac{\partial y_i}{\partial z}$$
$$u_{0inlet} C_{inlet,T} = u_0 C_{g,T} \tag{5.43}$$
$$u_{0inlet} C_{inlet,T} C_p T_{inlet} = u_0 C_{g,T} C_p T_g - \lambda \frac{\partial T_g}{\partial z}$$

The boundary conditions for the pressure equalization-pressurization step for $z = 0$ are:

$$\frac{\partial C_{g,i}}{\partial z} = 0$$
$$u_0 = 0 \tag{5.44}$$
$$\frac{\partial T_g}{\partial z} = 0$$

and the boundary conditions for $z = L$ (inlet) are:

$$u_{0inlet} C_{inlet,i} = u_0 C_{g,i} - \varepsilon D_{ax} C_{g,T} \frac{\partial y_i}{\partial z}$$
$$u_{0inlet} C_{inlet,T} = u_0 C_{g,T} \tag{5.45}$$
$$u_{0inlet} C_{inlet,T} C_p T_{inlet} = u_0 C_{g,T} C_p T_g - \lambda \frac{\partial T_g}{\partial z}$$

Finally, for the counter-current pressurization with hydrogen step, the boundary conditions for $z = 0$ are:

$$\frac{\partial C_{g,i}}{\partial z} = 0$$
$$u_0 = 0 \tag{5.46}$$
$$\frac{\partial T_g}{\partial z} = 0$$

and the boundary conditions for $z = L$ (inlet) are:

$$u_{0inlet} C_{inlet,i} = u_0 C_{g,T} C_p T_g - \lambda \frac{\partial T_g}{\partial z}$$
$$P = P_{inter} + \left(P_{high} - P_{inter}\right)\left[t / t_{press}\right] \tag{5.47}$$
$$u_{0inlet} C_{inlet,T} C_p T_{inlet} = u_0 C_{g,i} - \varepsilon D_{ax} C_{g,T} \frac{\partial y_i}{\partial z}$$

The performances of the different simulations of the two PSA processes were evaluated according to three performance parameters: product purity, product recovery and productivity of the process [40]. These parameters are defined in the following equations:

$$\mathrm{H_2\ Purity}\,(\%) = \frac{\int_{t=0}^{t_{Feed}} C_{H_2} u_0 \big|_{z=L}\, dt}{\sum_{i=0}^{n} \int_{t=0}^{t_{Feed}} C_i u_0 \big|_{z=L}\, dt} \tag{5.48}$$

$$\mathrm{H_2\ Recovery}\,(\%) = \frac{\int_{t=0}^{t_{Feed}} C_{H_2} u_0 \big|_{z=L}\, dt - \int_{t=0}^{t_{Press}} C_{H_2} u_0 \big|_{z=L}\, dt - \int_{t=0}^{t_{Purge}} C_{H_2} u_0 \big|_{z=L}\, dt}{\int_{t=0}^{t_{Feed}} C_{H_2} u_0 \big|_{z=0}\, dt} \tag{5.49}$$

$$\mathrm{Productivity}\left(\frac{mol_{H_2}}{kg_{ads} day}\right) = \frac{A_{bed}}{t_{cycle} w_{ads}} \left(\int_{t=0}^{t_{Feed}} C_{H_2} u_0 \big|_{z=L}\, dt - \int_{t=0}^{t_{Press}} C_{H_2} u_0 \big|_{z=L}\, dt - \int_{t=0}^{t_{Purge}} C_{H_2} u_0 \big|_{z=L}\, dt \right) \tag{5.50}$$

For the PSA simulations, the mathematical model was solved in gPROMS using the orthogonal collocation on finite elements method (40 elements with two interior collocation points; 1×10^{-5} of absolute and relative tolerance). The simulations of the depressurization steps were performed using an exponential decay function until a pre-defined pressure (P_{inter}) is achieved (see equation (5.39)). When three successive pressure equalizations take place, three different pressure intervals are defined using exponential functions with the same exponential decay rate constant (β_P).

5.4 Results and discussion

In a PSA unit, the multicomponent mixture is fed to a set of columns operating according to a pre-defined scheduling. Thus, the modelling of fixed-bed behaviour of the multicomponent mixture in a fixed-bed is essential to define a PSA unit.

Prediction of multicomponent adsorption equilibrium data is normally carried out by extending the mathematical models (Virial, Langmuir, multisite Langmuir, etc) using the

coefficients determined for pure components. One of the objectives of this chapter was to validate the results predicted by the extension of the multicomponent Virial isotherm based on previously reported data of pure components for activated carbons R2030 and AC5-KS [19, 21]. Experimental validation was performed by different breakthrough experiments in two different fixed-bed set-ups.

5.4.1 Multicomponent breakthrough experiments

5.4.1.1 Breakthrough curves in fixed-bed unit for ternary mixtures

Initially, a breakthrough curve of a H_2-CO_2 mixture was performed and then a ternary H_2-CO_2-CH_4 mixture was employed using the fixed-bed packed with activated carbon R2030. The operating conditions at which those experiments were performed were shown in Table 5.1 (section 5.2.1.1). The experimental results of the H_2-CO_2 binary mixture for two different temperatures (323 and 343 K) are shown in Figure 5.10. The bed was initially filled with helium and a very fast breakthrough of hydrogen can be observed according to the simulations. The typical roll-up of a weak adsorbed compound displaced by a more strongly adsorbed species was observed for hydrogen. The adsorption of CO_2 is accompanied with a marked increase in temperature inside the column. Note that the experimental value measured at z = 0.680 m corresponds to the temperature of the column wall. The prediction of the mathematical model employing information obtained from pure component data of adsorption equilibrium and kinetics is also shown in Figure 5.10 (solid lines). The transport parameters values used in the simulations were given in Table 5.6 (section 5.3). A good agreement was observed between the experimental data and the predicted concentration history at the end of the column. The temperature evolution within the column was also well predicted. As mentioned before the thermocouple placed at z = 0.680 m from feed inlet is close to the column wall. For this reason, the prediction of the column wall temperature is also shown and it can be observed that the experimental data is close to the prediction of the column wall temperature but may be have some influence of the gas temperature, reason why the experimental value lays between these two values.

For the same adsorbent (R2030), the experimental results of the ternary H_2-CO_2-CH_4 mixture are reported in Figure 5.11. The experimental total flow rate history obtained for the ternary H_2-CO_2-CH_4 breakthrough curve is shown in Figure 5.12. In this case, hydrogen as the less adsorbed species pass through two plateaus until reaching the feed concentration, once the column is in equilibrium with all the adsorbates. The roll-up is also observed by methane being displaced by CO_2, which is strongly adsorbed compound. The temperature profiles within the column are

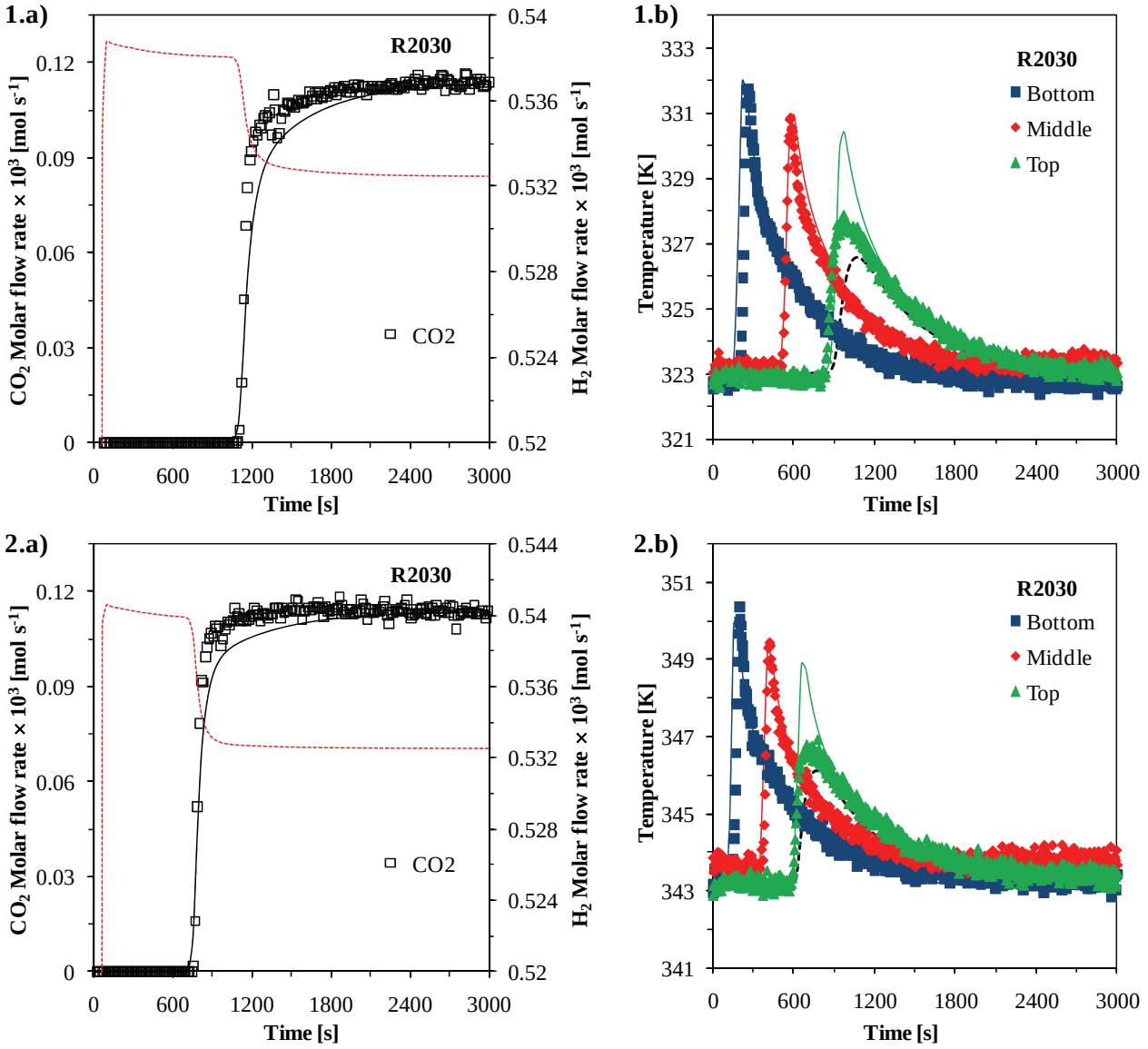


Figure 5.10: H_2 (----) and CO_2 (□,——) molar flow rate histories at the column outlet (a) and temperature histories (b) obtained for binary H_2-CO_2 breakthrough curves at 323 (1) and 343 K (2) and 2.5 bar on activated carbon R2030; Mixture: 17.6% of CO_2 balanced with H_2; Temperatures measured at 0.170 m (Bottom (■,——)), 0.430 m (Middle (◆,——)) and 0.680 m (Top (▲,——)) from feed inlet and the wall temperature T_w at 0.680 m (- - -); Flow rate of 1.596×10^{-5} m^3 s^{-1} (measured at 298 K and 1 bar); Experimental data (symbols); Simulation (lines).

well defined, particularly at the end of the column where an initial increase in temperature due to methane adsorption can be observed followed by a stronger peak of CO_2 adsorption. In this experiment, there was a deviation lower than 10% between the adsorbed amount obtained experimentally and the predicted by the mathematical model. This may be due to two possible (and different) reasons. The first one is related to a small experimental error in the determination of

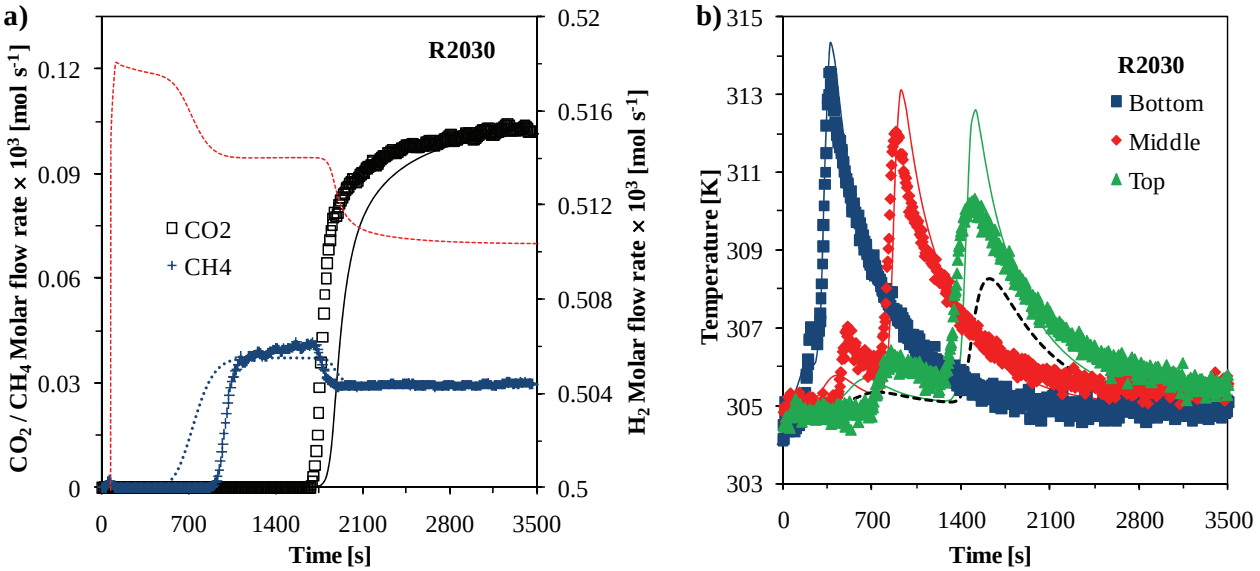


Figure 5.11: H_2 (----), CO_2 (□,——) and CH_4 (+,·····) molar flow rate histories at the column outlet (a) and temperature histories (b) obtained for the ternary H_2-CO_2-CH_4 breakthrough curve at 305 K and 2.5 bar on activated carbon R2030; Mixture: 15.5% of CO_2 and 4.5% of CH_4 balanced with H_2; Temperatures measured at 0.170 m (Bottom (■,——)), 0.430 m (Middle (◆,——)) and 0.680 m (Top (▲,——)) from feed inlet and the wall temperature T_w at 0.680 m (- - -); Flow rate of 1.584×10^{-5} m^3 s^{-1} (measured at 298 K and 1 bar); Experimental data (symbols); Simulation (lines).

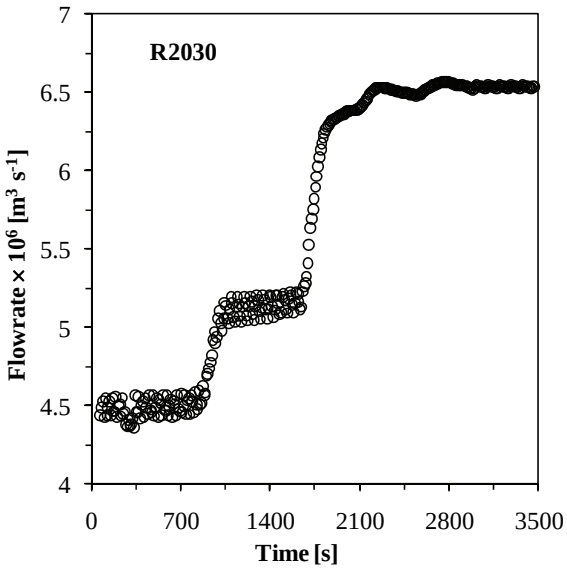


Figure 5.12: Total flow rate (○) at the column outlet obtained for the ternary H_2-CO_2-CH_4 breakthrough curve at 305 K and 2.5 bar on R2030; Mixture: 15.5% of CO_2 and 4.5% of CH_4 balanced with H_2.

methane: the molar fraction employed in the experiment is very small and minor errors will lead to large differences. The second possibility is that the capacity of methane predicted by the

multicomponent extension of the Virial model is smaller at low partial pressures. As the model predicts a lower adsorption capacity for methane, its simulated concentration front reaches the end of the column sooner than the experimental concentration. It should be mentioned that the model used to predict multicomponent data is based on parameters estimated from pure component isotherms. Also, the estimation of Virial coefficients A_{ij} and B_{ijk} was done by a simple arithmetic average obtained from Amagat's rule instead of a geometric average [28]. The disagreement in the adsorption capacity is also reflected as a time-deviation and intensity in the prediction of the temperature histories in the column. In agreement with the experimental results, two different temperature increases are observed: the first one due to methane and the second because of CO_2 adsorption.

According to the experimental results observed using the fixed-bed packed with R2030, it was shown that the activated carbon employed can be used for selective removal of CO_2 and CH_4 in off-gases of methane steam reforming [13].

For the modified activated carbon AC5-KS, different fixed-bed experiments were performed using mixtures of CO_2-He and multicomponent mixtures of CO_2-H_2-CH_4 at different experimental conditions (see Table 5.2 from section 5.2.1.1). These breakthrough curves were also simulated using the mathematical model and the correlations reported in section 5.3, equations (5.3) to (5.35). The transport parameters used in the simulations were given in Table 5.6. The multicomponent extension of the Virial isotherm model was used to predict the adsorption equilibrium of the mixtures for which the multicomponent behaviour is purely based on the information obtained from pure component adsorption equilibrium data. Single-component CO_2 breakthrough experiments at 303 K and 1.2 bar for two different CO_2 molar fractions (14.8% and 63.1%, both balanced with He) are reported in Figure 5.13. Ternary CO_2-H_2-CH_4 breakthrough experiments at 303 K and 1.2 bar are reported in Figure 5.14: one employing a mixture with 69.9% of CO_2 and 17.3% of CH_4 and the other with 58.0% of CO_2 and 28.2% of CH_4, both balanced with H_2. It can be seen that the mathematical model represents well the experimental results. A good estimation of the multicomponent adsorption capacity is obtained from the multicomponent Virial isotherm. The predicted temperature histories are also in agreement with the values obtained experimentally where temperature variations of approximately 7 and 20 K are observed respectively for the experiments with the lowest and highest CO_2 feed molar fractions. These temperature variations are important because they will negatively affect the performance of an industrial PSA system operating almost adiabatically.

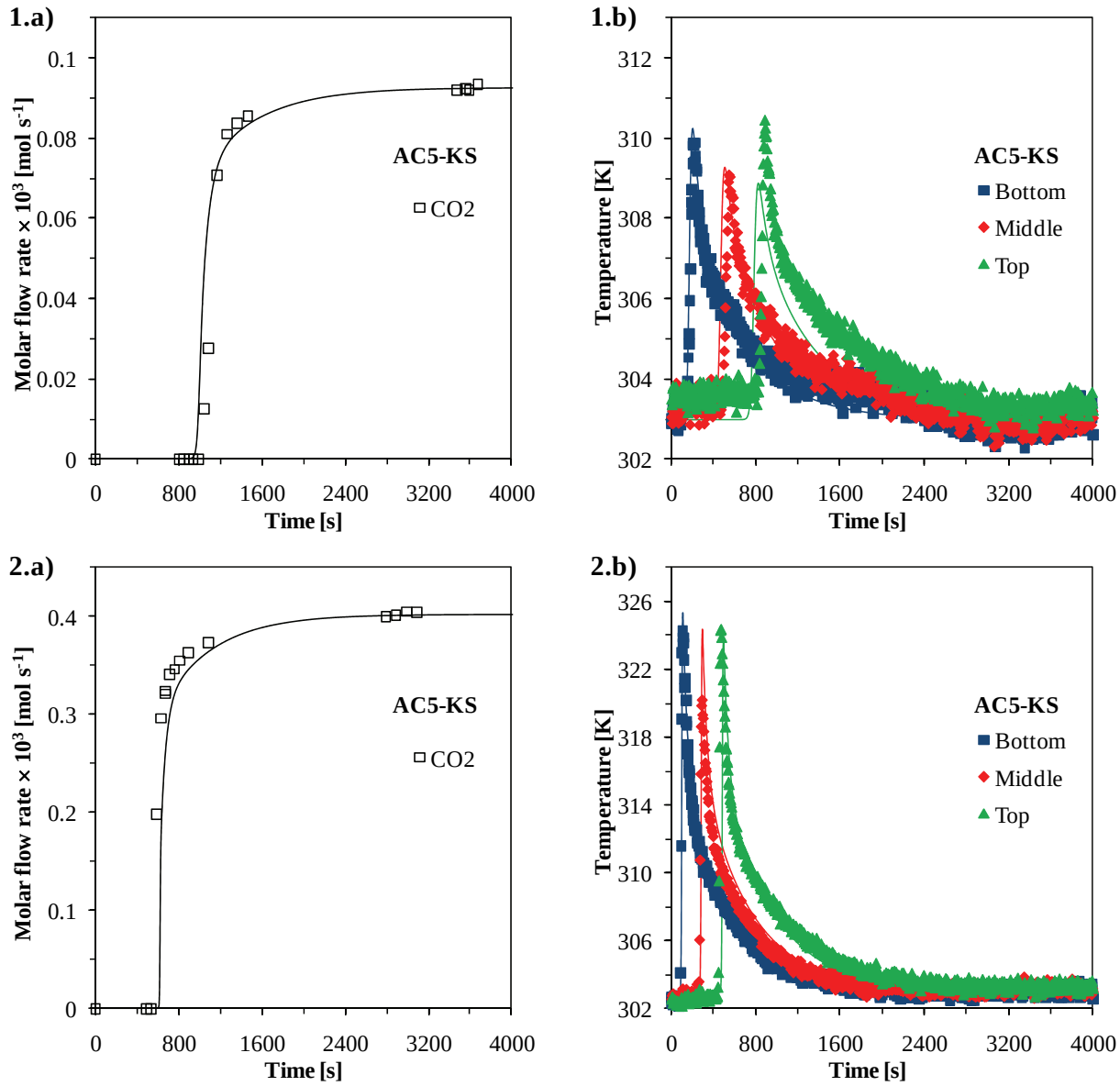


Figure 5.13: CO_2 (□,——) molar flow rate history at the column outlet (a) and temperature histories (b) obtained for the CO_2 breakthrough curve at 303 K and 1.2 bar on activated carbon AC5-KS; Mixtures: 14.8% of CO_2 balanced with He (1) and 63.1% of CO_2 balanced with He (2); Temperatures measured at 0.175 m (Bottom (■,——)), 0.424 m (Middle (◆,——)) and 0.677 m (Top (▲,——)) from feed inlet; Flow rates (measured at 298 K and 1 bar) of 1.543×10^{-5} (1) and 1.575×10^{-5} $m^3\ s^{-1}$ (2); Experimental data (symbols); Simulation (lines).

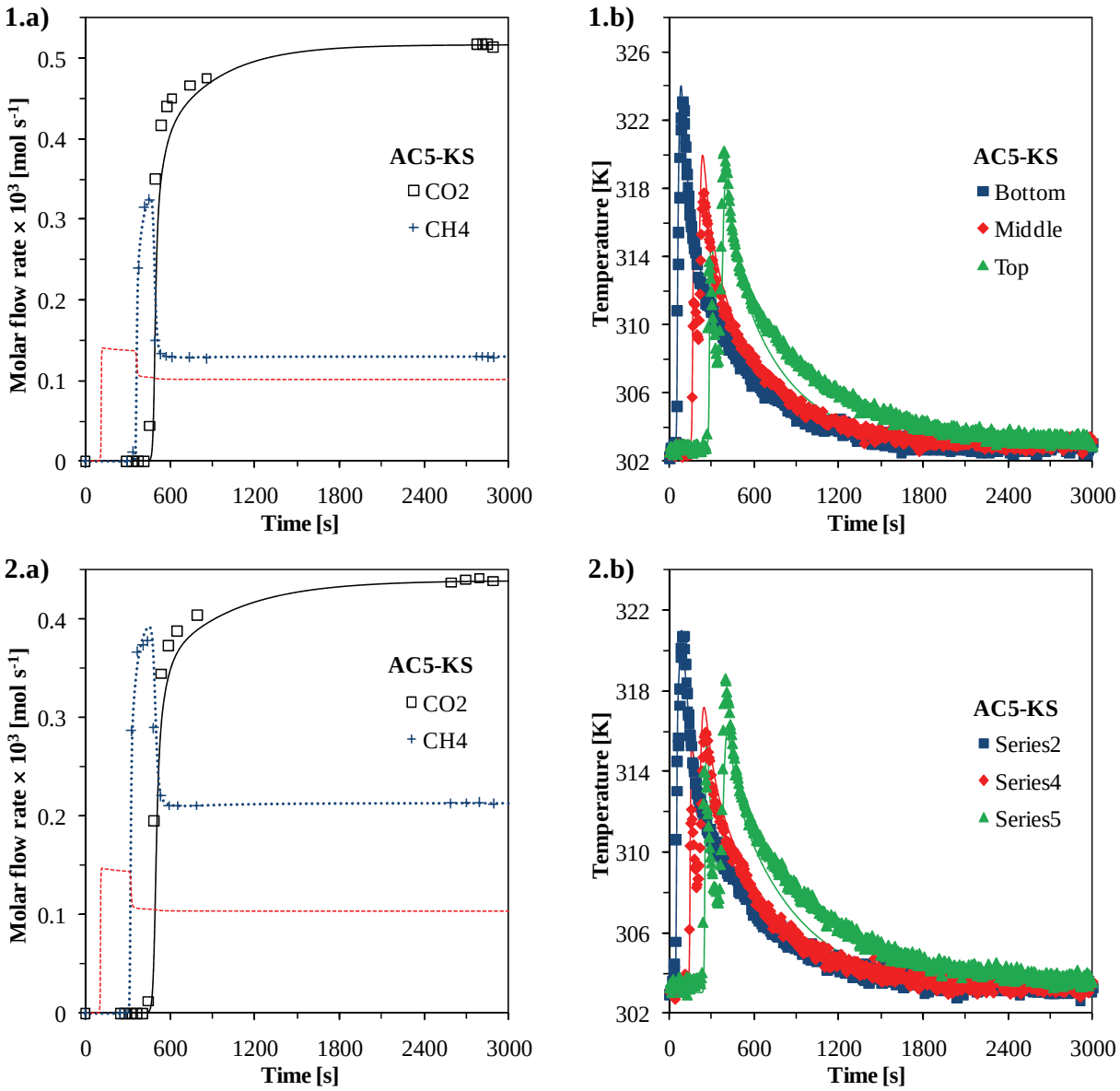


Figure 5.14: H_2 (----), CO_2 (□,——) and CH_4 (+,·····) molar flow rate histories at the column outlet (a) and temperature histories (b) obtained for the ternary H_2-CO_2-CH_4 breakthrough curve at 303 K and 1.2 bar on activated carbon AC5-KS; Mixtures: 69.0% of CO_2 and 17.3% of CH_4 (1) and 58.0% of CO_2 and 28.2% of CH_4 (2) both balanced with H_2; Temperatures measured at 0.175 m (Bottom (■,——)), 0.424 m (Middle (◆,——)) and 0.677 m (Top (▲,——)) from feed inlet; Flow rates (measured at 298 K and 1 bar) of 1.848×10^{-5} (1) and 1.871×10^{-5} $m^3\ s^{-1}$ (2); Experimental data (symbols); Simulation (lines).

5.4.1.2 Breakthrough curves in the "compact" PSA unit

Using one column of the unit packed with the modified activated carbon AC5-KS, fixed-bed experiments of H_2-CO_2 mixtures, followed by a H_2-CO_2-CO mixture and finally a H_2-CO_2-CO-CH_4-N_2 mixture were performed. The experimental conditions were reported in Table 5.3 (section 5.3).

Binary H_2-CO_2 breakthrough curves were performed for mixtures with different CO_2 content (balanced with H_2): 30% (run 1), 10% (run 2) and 80% (run 3) and using the modified activated carbon AC5-KS. All these experiments were carried out at 323 K of temperature, 5 bar of total feed pressure and using a feed flow rate of 5.00×10^{-5} m^3 s^{-1} (measured at 298 K and 1 bar). The results are reported in Figure 5.15. For each breakthrough experiment the temperature profile was measured in three different positions of the column (0.059, 0.151 and 0.239 m from the feed inlet). It can be observed that when the concentration of CO_2 increases, the heat generated by adsorption of CO_2 is higher resulting in higher temperatures inside the column. Since H_2 is only slightly adsorbed, it breaks through the column very fast. The CO_2 profiles at the column exit are very sharp, especially at higher CO_2 partial pressures due to the non-linearity of the isotherm. The mathematical model could satisfactorily describe the binary data. This binary system is particularly important because one gas is the desired product and the other gas is the main contaminant. It should be mentioned however, that part of these curves were used to adjust thermal parameters (h_w and U).

The results of the ternary H_2-CO_2-CO breakthrough curve (run 4, 26% of CO_2, 4% of CO balanced with H_2) on AC5-KS are shown in Figure 5.16. Ternary mixtures with carbon monoxide should be well described since the specifications for high-quality hydrogen are in the ppm level. It can be observed in Figure 5.16 that the breakthrough time of CO can be predicted by the model confirming the validity of the multicomponent extension of the Virial model for this ternary mixture (at least for this composition). Since CO is the intermediate compound adsorbed, it presents two different plateaus. Although it is not possible to see in detail in Figure 5.16, the adsorption of CO produces an independent temperature peak before the larger peak due to adsorption of CO_2.

Finally, a five-component H_2-CO_2-CO-CH_4-N_2 breakthrough curve (23% of CO_2, 2.1% of CH_4, 1.2% of CO and 0.7% of N_2 balanced with H_2) for the same feed flow rate was performed using the modified activated carbon AC5-KS (run 5). The experimental and simulated results obtained are reported in Figure 5.17. Again, for the five-component mixture, the mathematical

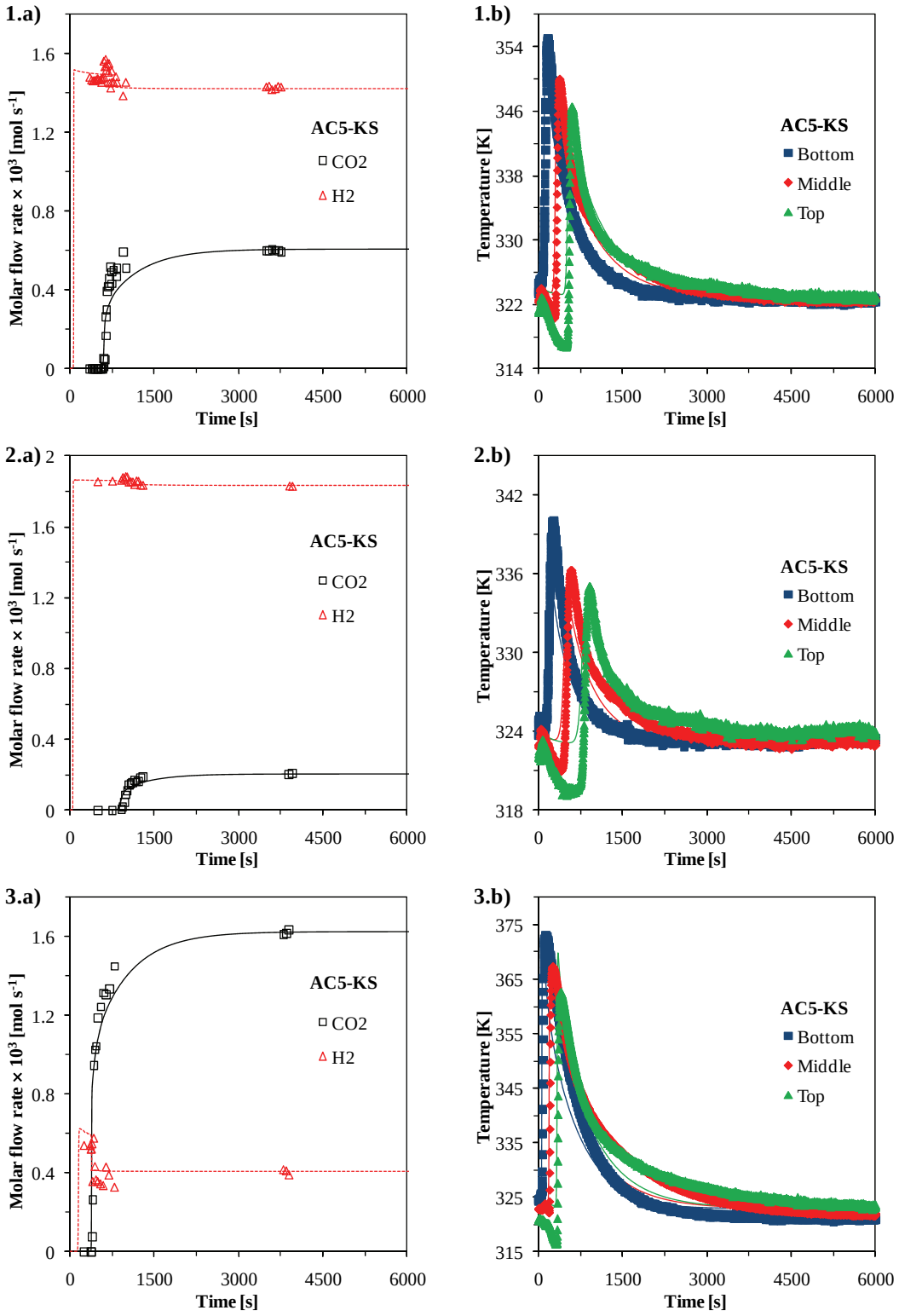


Figure 5.15: H_2 (△,----) and CO_2 (□,——) molar flow rate histories (a) at the column outlet and temperature histories (b) obtained for binary H_2-CO_2 breakthrough curves at 323 K and 5 bar on activated carbon AC5-KS; Mixtures: CO_2 content (balanced with H_2) of 30% (1), 10% (2) and 80% (3); Temperatures measured at 0.059 m (Bottom (■,——)), 0.151 m (Middle (◆,——)) and 0.239 m (Top (▲,——)) from feed inlet; Flow rate of 5.00×10^{-5} m^3 s^{-1} (measured at 298 K and 1 bar); Experimental data (symbols); Simulation (lines).

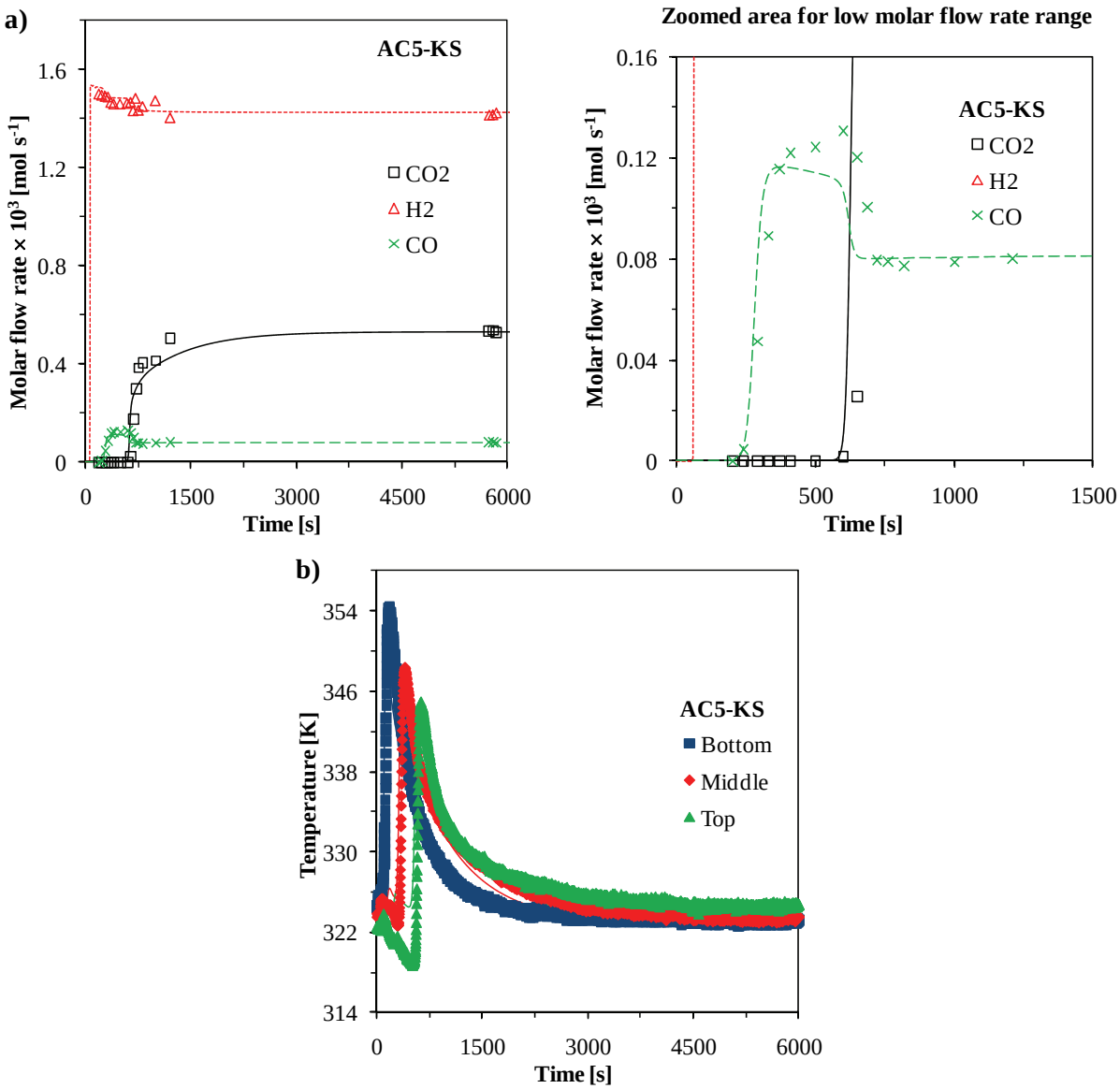


Figure 5.16: H_2 (△,----), CO_2 (□,——) and CO (×,— —) molar flow rate histories (a) at the column outlet and temperature histories (b) obtained for ternary H_2-CO_2-CO breakthrough curve at 323 K and 5 bar on activated carbon AC5-KS; Mixture: 26% of CO_2 and 4% of CO balanced with H_2; Temperatures measured at 0.059 m (Bottom (■,——)), 0.151 m (Middle (◆,——)) and 0.239 m (Top (▲,——)) from feed inlet; Flow rate of 5.00×10^{-5} m^3 s^{-1} (measured at 298 K and 1 bar); Experimental data (symbols); Simulation (lines).

model can successfully predict the data. In this experiment the concentration of N_2, CO and CH_4 is quite small so is difficult to observe the successive plateaus of the lighter components (N_2 and CO). However, it is clear that there is a good separation zone between hydrogen and the rest of the contaminants. The first contaminant to break-through the column is nitrogen, followed by carbon monoxide, methane and finally carbon dioxide.

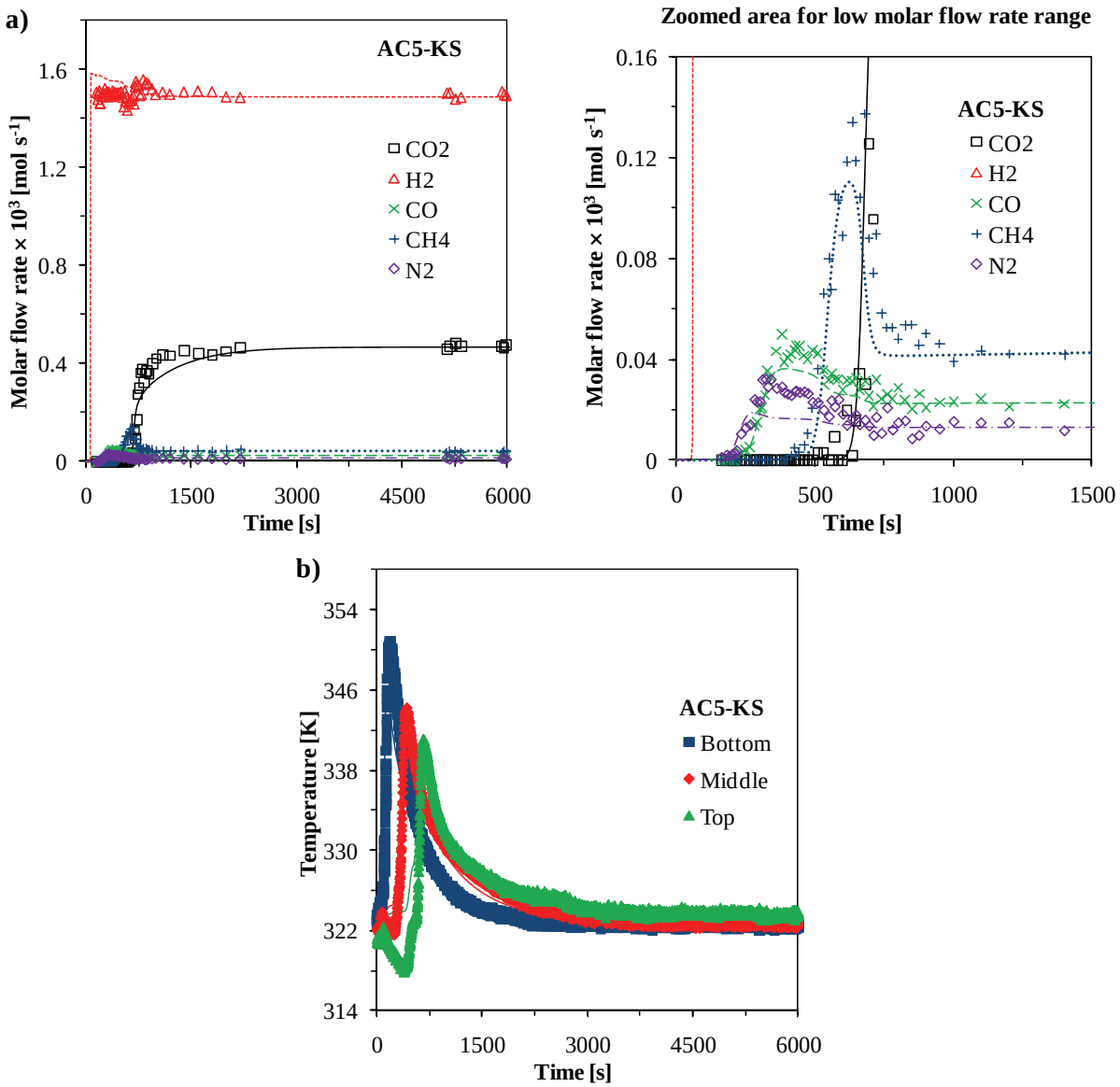


Figure 5.17: H_2 (△,----), CO_2 (□,——), CH_4 (+,·····), CO (×,— —) and N_2 (◇,—·—·) molar flow rate histories (a) at the column outlet and temperature histories (b) obtained for multicomponent H_2-CO_2-CH_4-CO-N_2 breakthrough curve at 323 K and 5 bar on activated carbon AC5-KS; Mixture: 23% of CO_2, 2.1% of CH_4, 1.2% of CO and 0.7% of N_2 balanced with H_2; Temperatures measured at 0.059 m (Bottom (■,——)), 0.151 m (Middle (◆,——)) and 0.239 m (Top (▲,——)) from feed inlet; Flow rate of 5.00×10^{-5} m^3 s^{-1} (measured at 298 K and 1 bar); Experimental data (symbols); Simulation (lines).

Note that, when the feed gas stream reaches the adsorbent at the beginning of each experiment, the heat of adsorption of the faster species present in the mixture starts to increase (locally) the temperature of the adsorbent. Consequently, the temperature of the column wall increases in the same area where the temperature sensor of the flexible insulated heater was placed

(in the beginning of the column, between the heater and the column wall). Therefore, the heater does not give more energy (it switches off) to heat the column and, so, the temperature in the remaining column decreases. For this reason, it can be observed in Figure 5.15 to Figure 5.17 a steep decrease of temperature at the initial period of time.

5.4.2 PSA experiment

After confirmation of the validity of multicomponent adsorption equilibrium and kinetic data on the modified activated carbon AC5-KS, a PSA experiment was also performed to validate the mathematical model in a cyclic experiment. A single column PSA experiment was performed using the cycle scheduling B illustrated in Figure 5.7 (see section 5.2.2). The experimental run was performed at 303 K with a feed flow rate of 5.00×10^{-5} m^3 s^{-1} (measured at 298 K and 1 bar) and the following composition: 79% of H_2, 17% of CO_2, 2.1% of CH_4, 1.2% of CO and 0.7% of N_2. The feed (P_{high}) pressure was fixed at 5 bar and the blowdown pressure (P_{low}) was 0.5 bar. The experimental conditions of the experiment were shown in Table 5.4 from section 5.2.2. In this single-column experiment, the pressure equalization was divided into three different steps to simulate the behaviour of an industrial PSA unit where several pressure equalization steps are required to increase H_2 recovery.

The pressure history for cycle 1 and the temperature histories for the first ten cycles are shown in Figure 5.18. The H_2, CO_2, CH_4, CO and N_2 molar flow rate histories obtained for cycles 1 and 37 at bed outlet are reported in Figure 5.19.

According to the simulation, the process takes 240 cycles to reach CSS. In these two cycles, a good agreement between the simulations and the experimental molar flow rates can be observed. During the pressure equalization steps a considerable amount of hydrogen is released from the column, which can be used for pressure equalization or for purge. The temperature predicted by the mathematical model is in reasonable agreement with the experimental results, with deviations lower than 1 K. It should be observed that temperature variations are larger in the initial portion of the column, where CO_2 is adsorbed. In the rest of the column (used to remove the other contaminants) the temperature oscillations are smaller than 4 K.

The performance of the single-column PSA process experiment was evaluated according to the parameters reported in equations (5.48) to (5.50): product purity, product recovery and productivity of the process. It was observed that, 81.6% of hydrogen was recovered with a purity of 99.9805% contaminated with 63.0 ppm of carbon monoxide. The productivity attained was 101.1

mol_{H2} kg_{ads}^{-1} day^{-1}. Simulated results of Ribeiro *et al*. (2008) [30] reported a hydrogen recovery of 51.84% for a single column layered bed (activated carbon and zeolite) PSA system that produces 99.9994% of pure hydrogen operating with a feed pressure of 7 bar and temperature of 303 K. For a similar system (H_2, CO_2, CH_4 and CO; feed flow rate of 1.17×10^{-4} m^3 s^{-1} (measured at 298 K and 1 bar); feed pressure of 9.12 bar), Lee *et al*. (2008) [10] reported single column PSA simulations able to purify 74-76% of hydrogen with much lower purities of 99.4-99.7%. It should be mentioned that the feed pressure of this experiment is quite low when compared to most reported values from literature (using normally 20 bar). The main conclusion from this experiment is that the mathematical model can successfully predict the experimental results and thus the model can be used to have a deeper understanding of the cycle and of the important operating variables of the process.

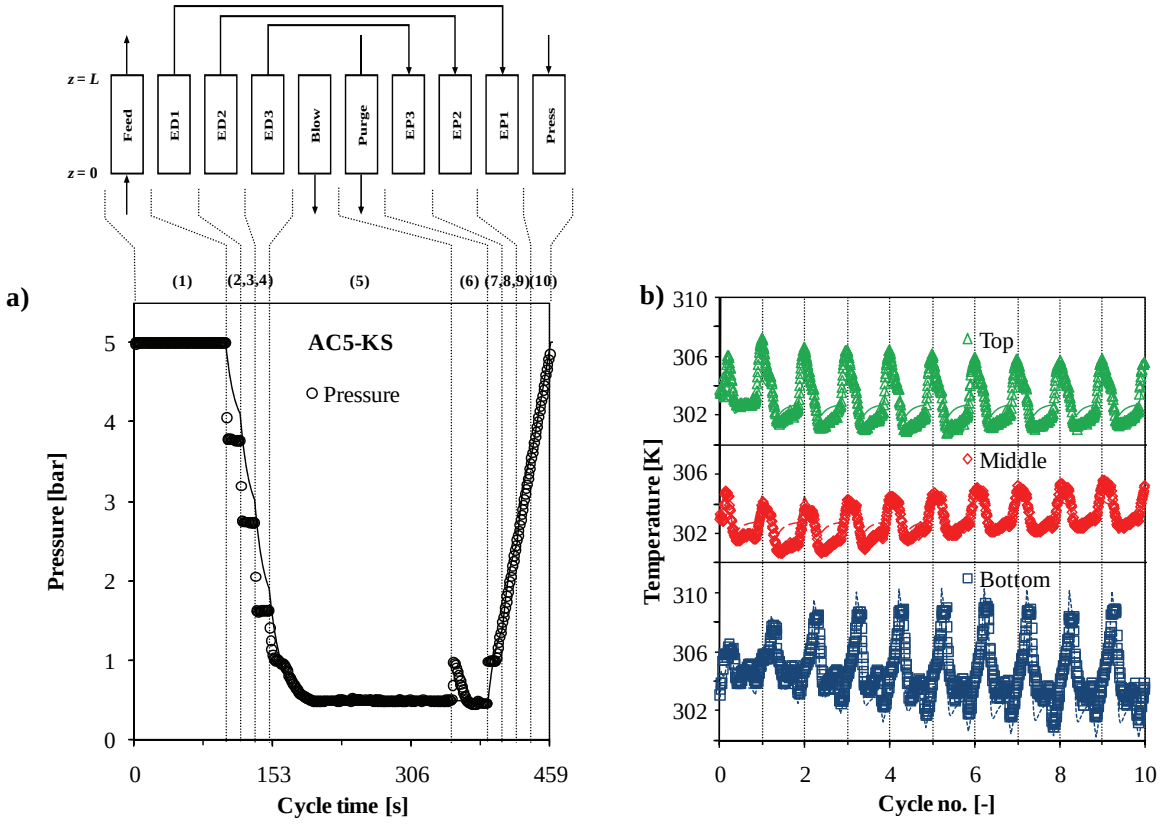


Figure 5.18: Pressure (a; ○,——) and temperature (b) histories; Cycle sequence: (1) co-current feed step; (2) first, (3) second and (4) third pressure equalization-depressurization steps; (5) counter-current blowdown step; (6) counter-current purge step with hydrogen; (7) third, (8) second and (9) first pressure equalization-pressurization steps; (10) counter-current pressurization step with hydrogen; Temperatures measured at 0.059 (Bottom (□,----)), 0.151 (Middle (◇,– –)) and 0.239 m (Top (△,——)) from feed inlet; Adsorbent: AC5-KS; Experimental data (symbols); Simulation (lines).

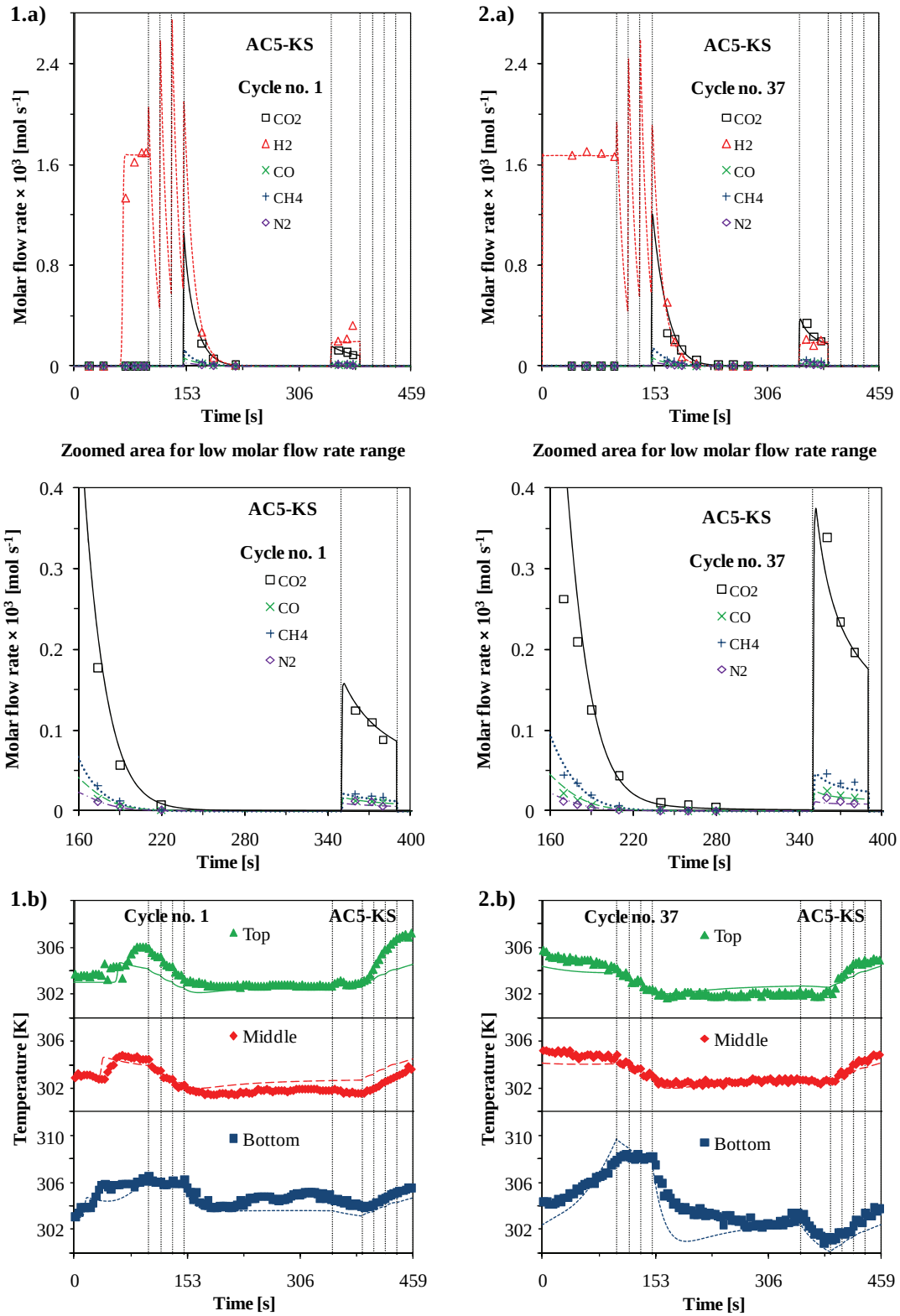


Figure 5.19: H_2 (△,----), CO_2 (□,——), CH_4 (+,·····), CO (×,— —) and N_2 (◇,—·—·) molar flow rate histories (a) obtained for cycle 1 (1) and 37 (2) at the outlet of a bed packed with AC5-KS; Temperature histories (b) measured for cycle 1 (1) and 37 (2) at 0.059 m (Bottom (■,----)), 0.151 m (Middle (◆,— —)) and 0.239 m (Top (▲,——)) from feed inlet; Flow rate of 5.00×10^{-5} m^3 s^{-1} (measured at 298 K and 1 bar); Experimental data (symbols); Simulation (lines).

5.4.3 PSA simulations

In the design of a PSA for H_2 purification, two different types of variables can be differentiated. The first ones are the operating variables related to feed conditions (composition, pressure and temperature). The second ones are related to the design of the unit (process variables) which are the step times and the blowdown and purge pressures as well as the cycle proposed.

In the operating variables, simulations at low pressures were performed and it is also interesting to explore the performance of the process at higher pressures. Among the design variables, the effect of pressure equalization steps should be accounted for. If a cycle with three pressure equalization steps is employed, a large number of columns should be used. However, using three pressure equalizations, the pressure reduction in the blowdown step is only of 1/4 of the ratio P_{high}/P_{low} (from 1.625 to 0.500 bar) in the previous example. If only one pressure equalization step is used, the ratio increases to 1/2, releasing much more H_2 in the blowdown step, losing it.

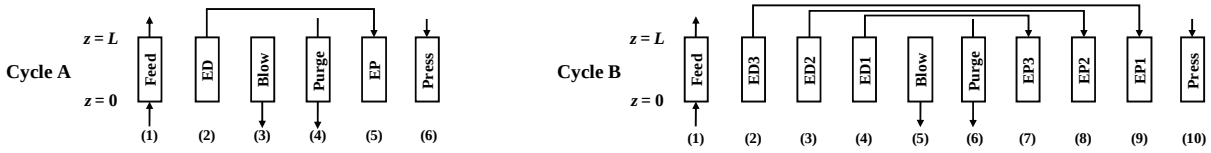
Considering a bed packed with activated carbon AC5-KS, different simulations were performed for a mixture with feed composition of 0.79 H_2 / 0.17 CO_2 / 0.021 CH_4 / 0.012 CO / 0.007 N_2 and for a feed flow rate of 5.00×10^{-5} m^3 s^{-1} (measured at 298 K and 1 bar) available at 303 or at 323 K. The same column properties as in the experimental set-up were used for the simulations (see details in Table 5.3 from section 5.2.1.2). The full set of operating conditions of the simulations is reported in Table 5.10, together with the performance parameters of the cycle in CSS (H_2 purity, H_2 recovery and productivity of the process).

Initially, a 6 steps (cycle A in Figure 5.9) single column PSA process was simulated (only one pressure equalization step). Two different purge times (simulations 1 and 2) were tested to analyse its influence in the hydrogen purity stream at the end of the feed step. It was observed that, increasing the purge time 50%, a significant reduction in the contamination with carbon monoxide of the product stream was attained. For a PSA cycle sequence that comprises a single pressure equalization (cycle A in Figure 5.9), the blowdown starts from a intermediate pressure very high and, thus, the amounts of hydrogen “lost” in the this step is significant. The step times used in simulation 1 were close to the ones used in the PSA experiment (see Table 5.10). It can be observed that with only one pressure equalization, the purity of H_2 obtained is much higher at the expense of losing 10% more of H_2 in the blowdown. In fact, when more pressure equalizations are employed, the concentration of contaminants increases at the product end, contaminating the stream of H_2.

To reduce the amount of hydrogen lost in the blowdown step, a PSA cycle with three

Table 5.10: Performance parameters for the H_2 PSA simulations using a bed packed with AC5-KS.

Cycle A							
Simulation	t_{Feed} [s]	t_{Blow} [s]	t_{Purge} [s]	H_2 Pur. [%]	CO Cont. [ppm]	H_2 Rec. [%]	Productivity [$mol_{H2}\ kg_{ads}^{-1}\ day^{-1}$]
1[a,*]	100	200	30	99.99207	15.2	70.96	91.56
2[a,*]	100	200	45	99.99941	0.705	68.68	85.56
5[b,*]	100	200	30	100.0000	0.000199	47.10	60.48
6[b,*]	120	200	30	99.99997	0.0477	57.17	84.66
$t_{ED} = t_{EP} = 45$ s ; $t_{Press} = 20$ s							
a) $P_{high} = 5$ bar ; $P_{inter} = 2.75$ bar ; $P_{low} = 0.5$ bar							
b) $P_{high} = 10$ bar ; $P_{inter} = 5.5$ bar ; $P_{low} = 1$ bar							
Cycle B							
Simulation	t_{Feed} [s]	t_{Blow} [s]	t_{Purge} [s]	H_2 Pur. [%]	CO Cont. [ppm]	H_2 Rec. [%]	Productivity [$mol_{H2}\ kg_{ads}^{-1}\ day^{-1}$]
3[c,*]	100	200	30	99.95555	160	82.40	106.3
4[c,*]	100	200	45	99.99265	18.0	79.98	99.36
7[d,*]	100	200	30	99.99998	0.0262	67.50	86.40
8[d,*]	120	200	30	99.99795	5.01	74.17	109.4
9[d,*]	120	150	30	99.99744	6.41	74.34	122.7
10[d,*]	120	150	20	99.99111	26.0	75.77	128.8
11[d,*]	110	150	20	99.99874	2.95	72.55	115.6
12[d,*]	110	100	20	99.99814	4.45	72.77	133.1
13[d,*]	110	70	20	99.99799	4.85	72.88	146.0
14[d,*]	120	70	20	99.98701	37.4	76.14	161.6
15[d,#]	100	200	30	99.99986	0.340	70.26	90.30
16[d,#]	120	70	20	99.97192	112	78.48	165.9
17[d,#]	120	70	35	99.99309	27.1	76.34	154.7
$t_{ED1} = t_{ED2} = t_{ED3} = t_{EP3} = t_{EP2} = t_{EP1} = 15$ s ; $t_{Press} = 20$ s							
c) $P_{high} = 5$ bar ; $P_{inter1} = 3.875$ bar ; $P_{inter2} = 2.75$ bar ; $P_{inter2} = 1.625$ bar ; $P_{low} = 0.5$ bar							
d) $P_{high} = 10$ bar ; $P_{inter1} = 7.75$ bar ; $P_{inter2} = 5.5$ bar ; $P_{inter3} = 3.25$ bar ; $P_{low} = 1$ bar							
Feed:	$y_{H2} = 0.79$; $y_{CO2} = 0.17$; $y_{CH4} = 0.021$; $y_{CO} = 0.012$; $y_{N2} = 0.007$ $Q = 5 \times 10^{-5}\ m^3\ s^{-1}$ (measured at 298 K and 1 bar)						



[*] $T = 303$ K
[#] $T = 323$ K

pressure equalizations was used: cycle B in Figure 5.9. Simulations 3 and 4 were performed applying: the same step times of simulations 1 and 2, respectively; considering that the total pressure equalization step times were kept constant, i.e., t_{ED} (cycle A) is equal to the sum of t_{ED1}, t_{ED2} and t_{ED3} (cycle B); the same step pressures and the same temperature. As expected, the hydrogen recovery attained in this process was higher (increased 16%). Nevertheless, the purity of the hydrogen produced decreased considerably, reaching levels of CO contamination two orders of magnitude higher. The effect of purge can also be evaluated in these simulations: increasing the purge time in 50% a drastic reduction of CO contamination can be achieved, losing less than 3% of H_2.

Alternatively, another pressure range was studied for both PSA processes in order to avoid use of vacuum in blowdown and purge steps. In the simulation 5, the high and low pressures applied in the 6 steps (cycle A in Figure 5.9) PSA process were 10 and 1 bar, respectively. Observing Table 5.10, almost 100% pure H_2 was produced. However, the amount of hydrogen recovered and the productivity of the process significantly decreased. Even when the feed step time was increased 20% (simulation 6), both process performance parameters (hydrogen recovery and process productivity) remained very low. Making similar simulations using the cycle sequence B of Figure 5.9 (simulations 7 and 8, respectively), much higher H_2 recoveries are obtained at the expense of reducing its purity. However, in most of the simulations, the H_2 purity is higher than 99.99% which is the target purity. In these simulations, since feed step time has increased, higher unit productivities are obtained.

Afterwards, the blowdown, purge and feed step times were analysed. First, reducing the blowdown step time in 25% (to 150 s), it was verified that the hydrogen purity was not significantly affected (but the productivity has increased 5% as shown in simulation 9). A decrease of 33% of the purge step time result in better process productivity and recovery, but at the expense of having 26 ppm of CO in the product.

Other important consideration is the temperature of the feed stream. Simulations considering that feed temperature is 323 K were also performed. In this case, using similar step times than in previous simulations (compare simulation 15 with simulation 7) a higher contamination of CO was found. In fact, at higher temperature the loading of all contaminants is smaller and they can breakthrough faster, contaminating the product. Reductions in the blowdown step result in similar effects than at 303 K, but with poorer performance mainly due to a lower capacity for contaminants. Higher purity can also be obtained increasing the purge time, with the expense of 2% less of hydrogen recovery.

In order to understand the simulated results in detail, in Figure 5.20 to Figure 5.23 several results are shown of the single-column PSA process simulation 13 reported in Table 5.10. The pressure evolution along one cycle at the outlet of the bed is shown for the simulation 13 in Figure 5.20. The same figure shows the molar flow rates obtained for the five gases of the feed mixture during one cycle in cyclic steady state (CSS) at the outlet of the bed. As previously stated, the high amounts of pure hydrogen released from the column during the pressure equalization-depressurization steps can be recycled, improving the recovery of the process. However, a significant amount of hydrogen is lost in the blowdown step. Moreover, for the pressurization of the column a fraction of the hydrogen produced is used decreasing the recovery of the process. Therefore, the reuse of the hydrogen released from the column during the pressure equalization-depressurization steps is crucial to attain high hydrogen process recoveries.

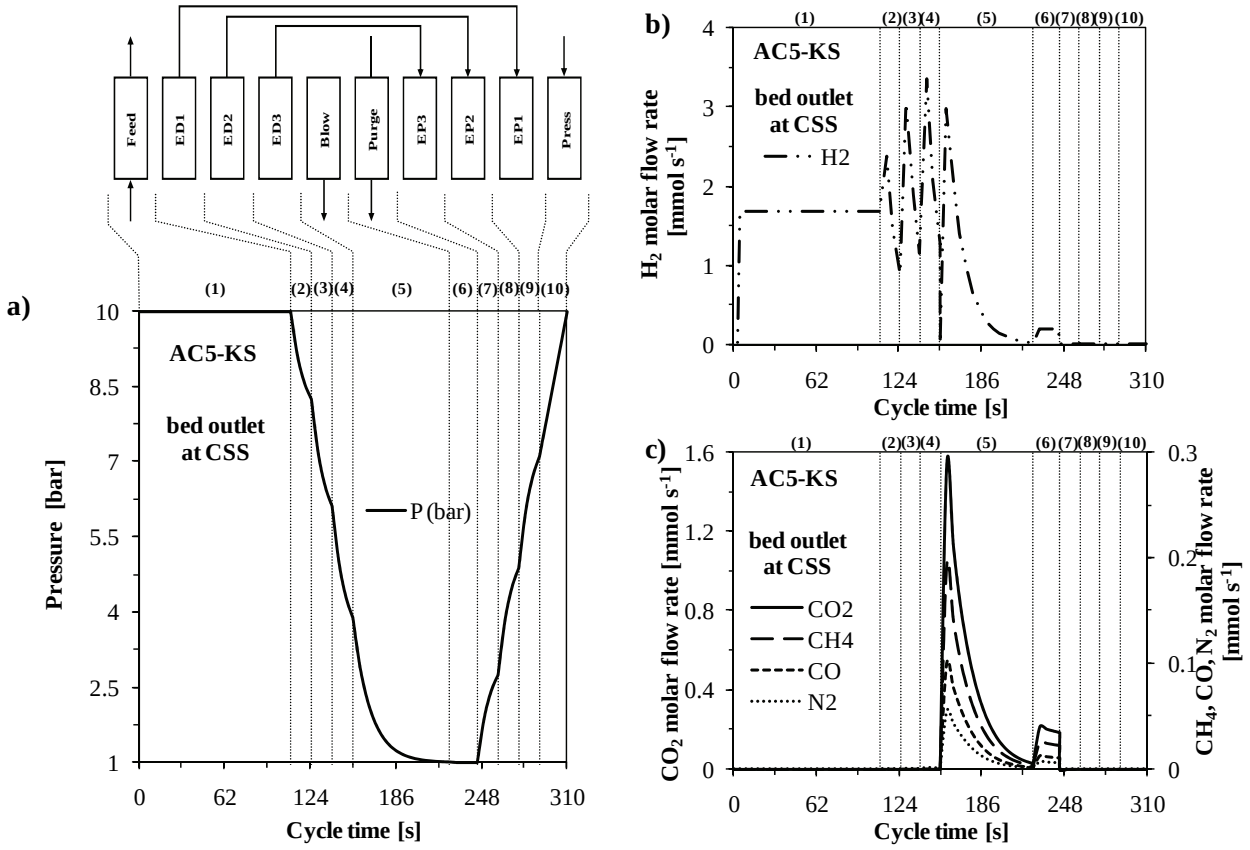


Figure 5.20: Pressure (a) and molar flow rate (b, c) histories obtained for simulation 13 at the outlet of a bed packed with AC5-KS and at cyclic steady state: (1) co-current feed step; (2) first, (3) second and (4) third pressure equalization-depressurization steps; (5) counter-current blowdown step; (6) counter-current purge step with hydrogen; (7) third, (8) second and (9) first pressure equalization-pressurization steps; (10) counter-current pressurization step with hydrogen.

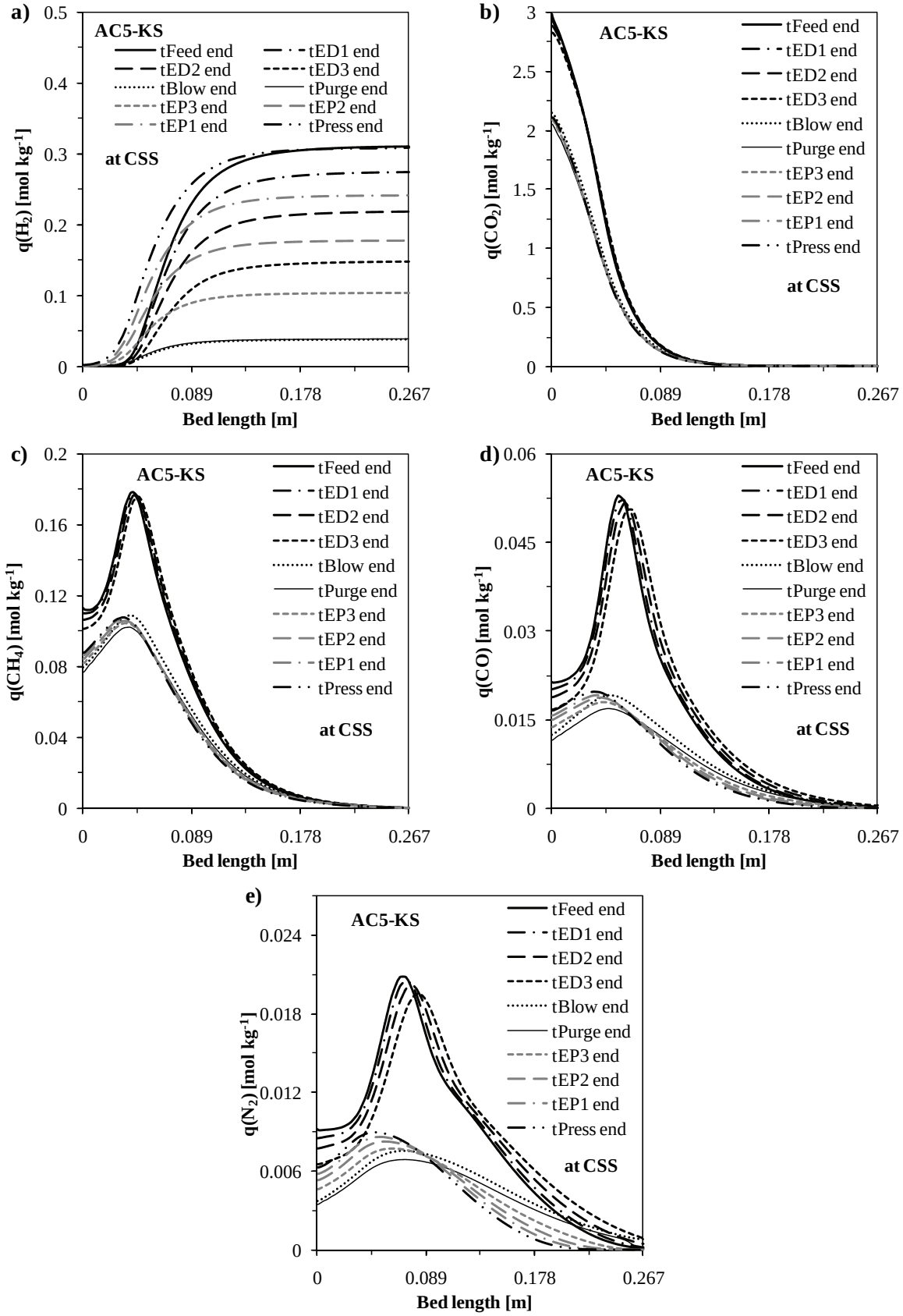


Figure 5.21: Solid phase concentration profiles of H_2 (a), CO_2 (b), CH_4 (c), CO (d) and N_2 (e) obtained for simulation 13 along the bed packed with AC5-KS at the end of each step at cyclic steady state.

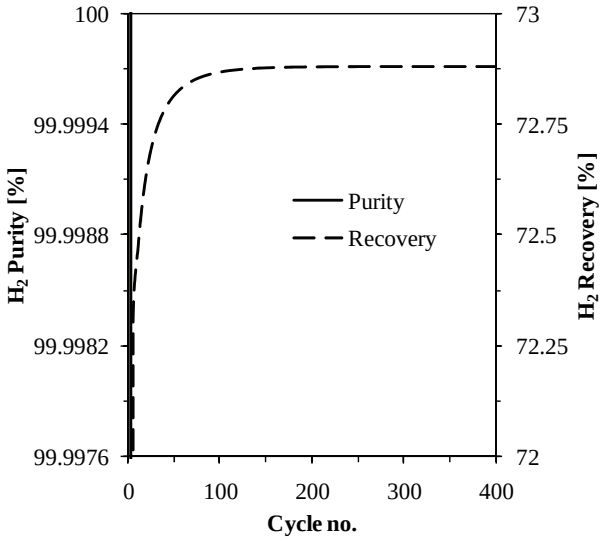


Figure 5.22: Hydrogen purity and recovery evolution along the cycles of simulation 13 for an PSA adsorption process using a single adsorbent bed packed with AC5-KS.

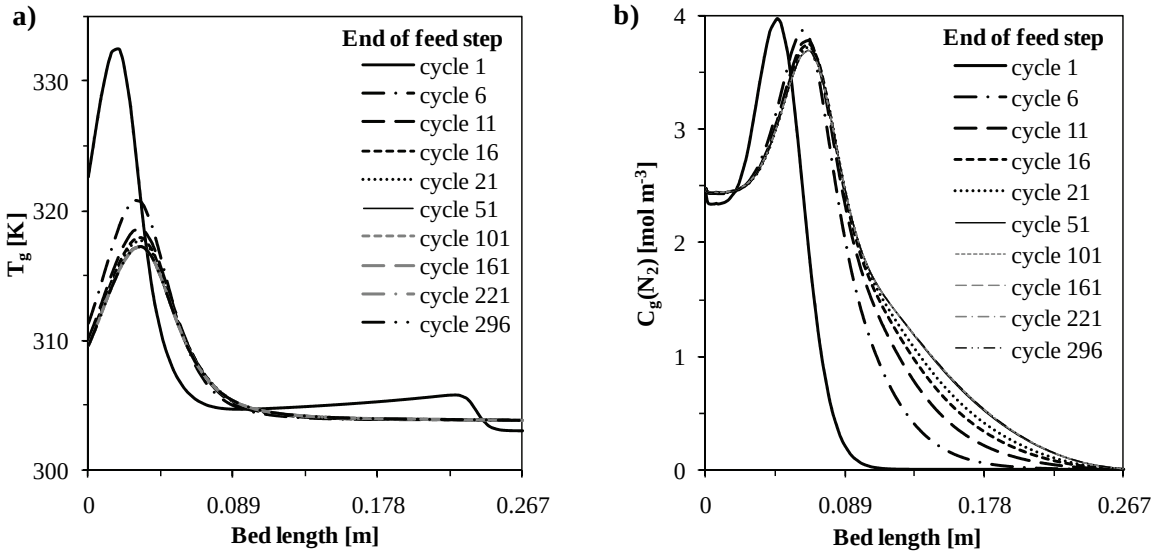


Figure 5.23: Evolution of the gas temperature (a) and nitrogen gas phase concentration (b) profiles with the cycle number at the end of the feed step obtained for simulation 13; Bed packed with AC5-KS.

The solid phase concentration profiles obtained along the bed at the end of each step at CSS are presented in Figure 5.21. Observing these figures, it can be concluded that the impurities detected at the feed outlet stream were CH_4, CO and, mainly N_2. This fact is in agreement with the adsorption capacities and diffusivity time constants of the pure gases within this activated carbon as stated in chapter 4: carbon dioxide has the higher adsorption capacity followed by CH_4, CO, N_2 and finally H_2; hydrogen has the highest micropore diffusivity follow by N_2, CO, CH_4 and finally

CO_2 [21].

Figure 5.22 shows the evolution of the hydrogen purity and recovery along the cycle number for the simulation 13. For the same simulation, the evolution of the gas temperature profile and gas phase concentration profile of the less adsorbed contaminant specie (N_2) at the end of the feed step with the cycle number are reported in Figure 5.23. Observing Figure 5.23, it can led us to think that CSS was reached after 50 cycles. However, the "very" small variations in the stabilization of the temperatures and gas phase concentrations profiles within the bed delayed the achievement of the CSS generating long simulation times. By this reason and as it is possible to observe in Figure 5.22, the CSS was reached only after approximately 200 cycles.

5.5 Conclusions

Within this chapter, hydrogen purification studies through PSA technologies were performed. A complex hydrogen mixture was considered to be purified: the off-gases from the SMR reactor, comprising H_2 contaminated with CO_2, CH_4, CO and N_2. Therefore, the experimental studies implied the integration of a new analysis system coupled with a "compact" PSA facility already existing at LSRE.

Multicomponent breakthrough experiments (single He-CO_2, binary H_2-CO_2, ternary H_2-CO_2-CH_4, ternary H_2-CO_2-CO and/or five-component H_2-CO_2-CO-CH_4-N_2) were performed at different operating conditions in activated carbon extrudates (R2030 and AC5-KS) to validate single component adsorption equilibrium. To measure the adsorption data of multicomponent mixtures, two fixed-bed experimental set-ups were used: a) 1-column PSA-VSA experimental set-up (developed by Da Silva (1999) [23]) connected to a flue gas analyser or a GC analysis system to measure the bed outlet concentration; b) 2-column PSA unit connected to a GC analysis system for complete determination of bed outlet concentrations of multicomponent gas mixtures of SMR off-gases (H_2, CO_2, CH_4, CO and N_2). The experiments show that the multicomponent extension of the Virial model could successfully predict the adsorption equilibrium capacity of all mixtures (using single-component parameters). Thus, computation time of the PSA process simulation can be reduced. Furthermore, the mathematical model used for the fixed-bed could also be used to predict the column behaviour of the multicomponent mixtures.

A single-column PSA experiment (bed packed with activated carbon AC5-KS) was performed for the complete validation of the mathematical model under cyclic conditions. A PSA cycle comprising feed, three different depressurizations, blowdown, purge, three pressure

equalizations and pressurization was used. In the experiment, a H_2 stream with 99.98054% hydrogen purity (63 ppm CO contaminated) was produced, with a recovery of 81.6% and process productivity of 101.1 mol_{H2} kg_{ads}^{-1} day^{-1}.

Several PSA simulations were also performed for different cycles and operating conditions considering a bed packed with activated carbon AC5-KS. It was observed that using three different pressure equalizations it is possible to achieve H_2 recoveries 15% higher than using only one pressure equalization. However, when multiple equalizations are used, the concentration of the contaminants reaches the product end faster, contaminating the product. According to simulations it was also noticed that increasing the feed pressure it is possible to increase the productivity keeping H_2 purity over 99.99% with carbon monoxide contamination lower than 10 ppm.

5.6 Notation

Nomenclature

a_p	particle specific area (m^{-1})
A	virial coefficients (m^2 mol^{-1})
B	virial coefficients (m^4 mol^{-2})
Bi_i	mass Biot number of component *i*
C	concentration (mol m^{-3})
$C_{g,i}$	component *i* gas phase concentration (mol m^{-3})
$C_{g,T}$	total gas phase concentration (mol m^{-3})
$C_{m,i}$	concentration of component *i* in the macropores (mol m^{-3})
$\langle C_{m,i} \rangle$	particle average of the concentration of component *i* in the macropores (mol m^{-3})
$C_{m,T}$	total concentration in the macropores (mol m^{-3})
C_p	gas mixture molar specific heat at constant pressure (J mol^{-1} K^{-1})
$\hat{C}_{p,s}$	particle specific heat at constant pressure [per mass unit] (J kg^{-1} K^{-1})
$\hat{C}_{p,w}$	wall specific heat at constant pressure [per mass unit] (J kg^{-1} K^{-1})
$C_{s,i}$	component *i* concentration at the solid surface (mol m^{-3})
C_v	gas mixture molar specific heat at constant volume (J mol^{-1} K^{-1})
$C_{v,i}$	molar specific heat of component *i* at constant volume (J mol^{-1} K^{-1})
$C_{v,ads,i}$	molar specific heat of component *i* in the adsorbed phase at constant volume (J mol^{-1} K^{-1})
d_p	particle diameter (m)
d_{we}	wall external diameter (m)
d_{wi}	wall internal diameter (m)
D_{ax}	axial dispersion coefficient (m^2 s^{-1})
D_c	micropore or crystal diffusivity (m^2 s^{-1})
D_c^0	limiting diffusivity at infinite temperature (m^2 s^{-1})
D_{ij}	binary molecular diffusivity (m^2 s^{-1})
D_k	Knudsen diffusivity (m^2 s^{-1})
D_m	molecular diffusivity (m^2 s^{-1})
D_p	macropore diffusivity (m^2 s^{-1})
e	wall thickness (m)
E_a	activation energy of micropore/crystal diffusion (kJ mol^{-1})

g	acceleration due to gravity (m s^{-2})
Gr	Grashof number
h_{ex}	external convective heat transfer coefficient (J s^{-1} m^{-2} K^{-1})
h_f	film heat transfer coefficient between the gas phase and particle (J s^{-1} m^{-2} K^{-1})
h_w	film heat transfer coefficient between the gas phase and wall (J s^{-1} m^{-2} K^{-1})
k_f	film mass transfer coefficient (m s^{-1})
k_g	gas conductivity (J s^{-1} m^{-1} K^{-1})
K_H	Henry constant (mol kg^{-1} bar^{-1})
K_∞	adsorption constant at infinite temperature (mol kg^{-1} bar^{-1})
L	column length (m)
Nu	Nusselt number
P	pressure (Pa)
Pr	Prandt number
q_i	absolute adsorbed phase concentration of component i (mol kg^{-1})
$\overline{q}_i$	micropore or crystal averaged adsorbed phase concentration of component i (mol kg^{-1})
$\langle \overline{q}_i \rangle$	particle averaged adsorbed phase concentration of component i (mol kg^{-1})
q_i^*	adsorbed concentration in equilibrium with $C_{m,i}$ (mol kg^{-1})
Q	flow rate (m^3 s^{-1})
r_c	micropore or crystal radius (m)
r_p	mean pore radius (m)
R_g	universal gas constant (J mol^{-1} K^{-1})
R_p	radius of the adsorbent extrudates (m)
Ra	Rayleigh number
Re	Reynolds number
S	adsorbent specific area (m^2 kg^{-1})
Sc	Schmidt number
Sh	Sherwood number
t	time (s)
T	temperature (K)
T_{film}	film temperature (K)
T_g	gas temperature (K)
T_p	particle temperature (K)
T_w	wall temperature (K)

T_∞	external temperature (K)
u_0	superficial velocity (m s^{-1})
u_i	interstitial velocity (m s^{-1})
U	overall heat transfer coefficient (J s^{-1} m^{-2} K^{-1})
y_i	molar fraction of component i
z	partition of the column length L (m)

Greek letters

α	external thermal diffusivity (W m^{-1} K^{-1})
α_w	ratio of the internal surface area to the volume of the column wall (m^{-1})
$\alpha_{w\ell}$	ratio of the logarithmic mean surface area of the column shell to the volume of the column wall (m^{-1})
β	thermal expansion coefficient (m m^{-1} K^{-1})
β_p	exponential decay rate constant
$(-\Delta H)$	isosteric heat of adsorption (kJ mol^{-1})
ε	bed porosity
ε_p	particle porosity
λ	heat axial dispersion coefficient (J s^{-1} m^{-1} K^{-1})
λ_w	wall conductivity (J s^{-1} m^{-1} K^{-1})
μ	gas viscosity (Pa s)
ν	kinematic viscosity of the external gas (m^2 s^{-1})
ρ_b	bulk density of the bed (kg m^{-3})
ρ_g	density of the gas phase (kg m^{-3})
ρ_p	density of the adsorbent (kg m^{-3})
ρ_w	wall density (kg m^{-3})
τ_p	pore tortuosity

5.7 References

[1] J. Kärger, D.M. Ruthven, Diffusion in zeolites and other microporous solids, 1st Edition, John Wiley & Sons, New York, 1992.

[2] D.M. Ruthven, S. Farooq, K.S. Knabel, Pressure swing adsorption, VCH Publishers, New York, 1994.

[3] A.E. Rodrigues, G.-H. Xiu, P. Li, C.A. Grande, E.L.G. Oliveira, Strategies for H_2 production by pressure swing adsorption reactor, in Sorption Enhanced Reaction Concepts for Hydrogen Production: Materials & Processes, S. Sircar and K.B. Lee, Editors, Research Signpost, Kerala, India, 2010.

[4] S. Sircar, W.E. Waldron, M.B. Rao, M. Anand, Hydrogen production by hybrid SMR-PSA-SSF membrane system, Separation and Purification Technology. 17 (1999) 11-20.

[5] DOE, Fuel cell handbook, 5th Edition, DOE, EG&G Services, Parsons, Inc. Science Applications International Corporation. Contract No. DE-AM26-99FT40575, 2000.

[6] OECD/IEA, Hydrogen & Fuel cells: Review of National R&D Programs, Organisation for Economic Co-operation and Development & International Energy Agency. ISBN 92-64-108-831, 2004.

[7] H. Ahn, C.-H. Lee, B. Seo, J. Yang, K. Baek, Backfill cycle of a layered bed H_2 PSA process, Adsorption. 5 (1999) 419-433.

[8] R.L. Bec, Method for purifying hydrogen-based gas mixtures using calcium X-zeolite (2005) U.S. Patent 6,849,106 B2.

[9] I.A.A.C. Esteves, J.P.B. Mota, Simulation of a new hybrid membrane/pressure swing adsorption process for gas separation, Desalination. 148 (2002) 275-280.

[10] J.-J. Lee, M.-K. Kim, D.-G. Lee, H. Ahn, M.-J. Kim, C.-H. Lee, Heat-exchange pressure swing adsorption process for hydrogen separation, AIChE Journal. 54 (2008) 2054-2064.

[11] A. Malek, S. Farooq, Hydrogen purification from refinery fuel gas by pressure swing adsorption, AIChE Journal. 44 (1998) 1985-1992.

[12] J.-H. Park, J.-N. Kim, S.-H. Cho, Performance analysis of a four-bed H_2 PSA process using layered beds, AIChE Journal. 46 (2000) 790-802.

[13] S. Sircar, T.C. Golden, Purification of hydrogen by pressure swing adsorption, Separation Science and Technology. 35 (2000) 667-687.

[14] J.L. Wagner, Selective adsorption process (1969) U.S. Patent 3,430,418.

[15] J. Yang, S. Han, C. Cho, C.-H. Lee, H. Lee, Bulk separation of hydrogen mixtures by a

one-column PSA process, Separations Technology. 5 (1995) 239-349.

[16] J. Yang, C.-H. Lee, Adsorption dynamics of a layered bed PSA for H_2 recovery from coke oven gas, AIChE Journal. 44 (1998) 1325-1334.

[17] L. Zhou, C.-Z. Lü, S.-J. Bian, Y.-P. Zhou, Pure hydrogen from the dry gas of refineries via a novel pressure swing adsorption process, Industrial and Engineering Chemistry Research. 41 (2002) 5290-5297.

[18] J.A. Ritter, R.T. Yang, Equilibrium adsorption of multicomponent gas mixtures at elevated pressures, Industrial and Engineering Chemistry Research. 26 (1987) 1679-1686.

[19] C.A. Grande, F.V.S. Lopes, A.M. Ribeiro, J.M. Loureiro, A.E. Rodrigues, Adsorption of off-gases from steam methane reforming (H_2, CO_2, CH_4, CO and N_2) on activated carbon, Separation Science and Technology. 43 (2008) 1338-1364.

[20] F.V.S. Lopes, C.A. Grande, A.M. Ribeiro, J.M. Loureiro, O. Evaggelos, V. Nikolakis, A.E. Rodrigues, Adsorption of H_2, CO_2, CH_4, CO, N_2 and H_2O in activated carbon and zeolite for hydrogen production, Separation Science and Technology. 44 (2009) 1045-1073.

[21] F.V.S. Lopes, C.A. Grande, A.M. Ribeiro, E.L.G. Oliveira, J.M. Loureiro, A.E. Rodrigues, Enhancing capacity of activated carbons for hydrogen production, Industrial and Engineering Chemistry Research. 48 (2009) 3978-3990.

[22] F.V.S. Lopes, C.A. Grande, A.M. Ribeiro, V.J.P. Vilar, J.M. Loureiro, A.E. Rodrigues, Effect of ion exchange on the adsorption of SMR off-gases on zeolite 13X, Journal of Chemical and Engineering Data. 55 (2010) 184-195.

[23] F.A. Da Silva, Cyclic adsorption processes: Application to propane/propylene separation, Ph.D. Dissertation, University of Porto, Porto, Portugal, 1999.

[24] C.A. Grande, Propane/propylene separation by pressure swing adsorption, Ph.D. Dissertation, University of Porto, Porto, Portugal, 2005.

[25] C.W. Skarstrom, Fractionating gas mixtures by adsorption (1960) U.S. Patent 2,944,627.

[26] R.M. Barrer, Sorption in porous crystals: equilibria and their interpretation, Journal of Chemical Technology and Biotechnology. 31 (1981) 71-85.

[27] A.V. Kiselev, Vapor adsorption on zeolites considered as crystalline species adsorbents, Molecular Sieve Zeolites-II, ACS series. 102 (1971) 37-68.

[28] S.M. Taqvi, M.D. LeVan, Virial description of two-component adsorption on homogeneous and heterogeneous surfaces, Industrial and Engineering Chemistry Research. 36 (1997) 2197-2206.

[29] J.M. Prausnitz, R.N. Lichtenthaler, E.G. De Azevedo, Molecular thermodynamics of fluid-

phase equilibria, Prentice Hall, Englewood Cliffs, NJ, 1996.

[30] A.M. Ribeiro, C.A. Grande, F.V.S. Lopes, J.M. Loureiro, A.E. Rodrigues, A parametric study of layered bed PSA for hydrogen purification, Chemical Engineering Science. 63 (2008) 5258-5273.

[31] R.B. Bird, W.E. Stewart, E.N. Lightfoot, Transport phenomena, 2nd Edition, Wiley International, Singapore, 2002.

[32] D.M. Ruthven, Principles of adsorption and adsorption processes, John Wiley & Sons, New York, 1984.

[33] N. Wakao, T. Funazkri, Effect of fluid dispersion coefficients on particle-to-fluid mass transfer coefficients in packed beds - Correlation of Sherwood numbers, Chemical Engineering Science. 33 (1978) 1375-1384.

[34] R.T. Yang, Gas separation by adsorption processes, Butterworths, Boston, 1987.

[35] F.P. Incropera, D.P.D. Witt, Fundamentals of heat and mass transfer, 4th Edition, John Wiley & Sons, New York, 1996.

[36] A.P.D. Wasch, G.F. Froment, Heat transfer in packed beds, Chemical Engineering Science. 27 (1972) 567-576.

[37] S. Cavenati, C.A. Grande, A.E. Rodrigues, Separation of $CH_4/CO_2/N_2$ mixtures by layered pressure swing adsorption for upgrade of natural gas, Chemical Engineering Science. 61 (2006) 3893-3906.

[38] F.A. Da Silva, J.A. Silva, A.E. Rodrigues, A general package for the simulation of cyclic adsorption processes, Adsorption. 5 (1999) 229-244.

[39] C.A. Grande, A.E. Rodrigues, Propane/propylene separation by pressure swing adsorption using zeolite 4A, Industrial and Engineering Chemistry Research. 44 (2005) 8815-8829.

[40] R. Rota, P.C. Wankat, Intensification of pressure swing adsorption processes, AIChE Journal. 36 (1990) 1299-1312.

6.

Fast cycling PSA

6.1 Introduction

Growth in research and development of innovative operation of pressure swing adsorption (PSA) has been extraordinary in the last 30 years, particularly in relation to three key process applications: air conditioning, hydrogen purification and oxygen/nitrogen separation from air [1-3]. Progresses in PSA modelling and design and operation as well as the adsorbent technology emerged in the last two decades. One of the results of combined efforts in materials science, innovative engineering work and process design is the development of PSA units able to complete adsorption and regeneration in only a few seconds [2-8]. These fast cycling PSA units are normally termed as Rapid Pressure Swing Adsorption (RPSA).

RPSA mainly differs from conventional PSA by the shorter cycle times it employs. Thus, with total cycle times of seconds instead of minutes, the productivity of the process can be enhanced by one order of magnitude or more [2, 9-10]. For this reason, to produce a desired volume of product gas in a given time, the required volume of the bed of the RPSA is reduced and therefore the physical size of system decreases [11]. The reduction of total cycle time is normally associated to changes in the PSA unit to withstand this particular operation mode. Examples of these changes are novel hardware such as rotary valves, different beds and/or different process designs that can be applied to reach the desired high productivities [2, 9-10, 12-15]. Moreover, the fast cycling can be limited by the mass transfer or adsorption dynamics and/or restricted by some

hydrodynamic constraints (uneven gas distribution, adsorbent fluidization, column pressure drop) limiting the gas flow rates through the beds. Consequently, all the limitations mentioned before may affect the product purity and recovery of the process [2, 16]. Furthermore, for a conventional PSA process it is frequently assumed that the thermal equilibrium between the gas and the adsorbent inside the bed is instantaneous. Nevertheless, after studying the influence of gas-solid heat transfer on RPSA, Sircar concluded that this assumption may not be valid for RPSA systems using low feed flow rates, fast adsorption kinetics and small cycle times (less than 20 s) [17]. Despite the fact that RPSA processes are capable of attaining greater productivity than conventional PSA processes, the main disadvantage of RPSA is the much larger energy demand by the higher operating power costs [8, 18].

This chapter deals with basic research of fast cycling PSA (or RPSA) for purification of hydrogen. Since this is an introductory research to understand the basics of how the system can be improved by fast cycling, the results were focused to obtain high-purity hydrogen from a binary mixture of H_2-CO_2. This chapter contains a state of the art of RPSA followed by some breakthrough curves performed at high superficial velocity. Furthermore, experimental and modelling work of RPSA for H_2-CO_2 mixture is presented.

6.2 Literature & Patent review

Although the application of RPSA in diverse gas separation units is recent, the concept has almost 40 years. The RPSA systems were initially proposed by Turnock and Kadlec (1971) [19] and Klower and Kadlec (1972) [20-21]. The RPSA systems became commercial processes for use in oxygen production operations, namely portable medical oxygen concentrators that recover oxygen from air, by Union Carbide Corporation. In the beginning of the 80s, Earls and Long (1980) [22-23] and also Jones *et al.* (1980) [15, 24] filled in U.S. Patents 4,194,891 and 4,194,892, respectively, two adiabatic RPSA processes for gas separation, particularly, for oxygen concentration. Earls and Long [22-23, 25] disclosed an adiabatic RPSA system for air separation to produce oxygen-enriched gas using multiple (two or three) beds of crystalline zeolite molecular sieve (zeolites 5A and 13X). The authors claimed that, operating at very rapid processing cycles (total cycle time of less than 18 s and for a desorption period at least ½ the adsorption period), this system is capable to recover at least 35% of oxygen with a purity of 90% [22-23, 25]. Alternatively, Jones *et al.* (1980) [15, 24, 26] disclosed a single adsorbent bed adiabatic RPSA process for separating gas mixtures having selectively adsorbable components, such as nitrogen

from air, ethylene from nitrogen, and methane and/or carbon monoxide from hydrogen. The system described in their invention is able to selectively adsorb one component (nitrogen from air and also ethylene from nitrogen, and methane and/or carbon monoxide from hydrogen) during a cycle time lower than 30 s and for a desorption period at least twice the adsorption period. Moreover, Jones *et al.* (1980) [15, 24, 26] disclosed an adsorbent bed that was reduced (cross section) in three different sections of different diameters. This reduction of adsorbent used in the bed resulted in a increase of the productivity and a decrease of moles of feed gas needed to reach the desired pressure inside the bed at a constant O_2 production rate. The authors claimed a production of oxygen with purity in the range of 85-95% and a recovery of 21-72% [15, 24, 26]. Jones *et al.* (1980) [15, 24, 26] disclosed that their RPSA process could also be used to purify steam reformer hydrogen containing as impurities CO_2, CH_4 and CO. According to a series of experiments using feed mixtures of 74.5% of H_2, 21.0% of CO_2, 2.5% of CO and 2.0% of CH_4, hydrogen recoveries of 41.4-53.0% were achieved with a production of a 99.999% pure hydrogen stream. Finally the authors stated that the H_2 recovery could be 10% improved when a layered bed of activated carbon and zeolite 5A is used.

Two years later, Keller II and Kua (1982) [8] proposed an enhanced gas separation method by selective adsorption of a “rapid” cycling PSA for enabling productivity to be increased at reduced operating costs. The method disclosed by the Union Carbide Corporation group in the U.S. Patent 4,354,859 was different of a traditional RPSA process. In this case, driving pistons were employed in total communication with each end of the adsorption bed to impose cyclic gas flow and pressure variations. The authors reported examples with highly desirable pure products in both stream ends of a O_2-N_2 separation system: 99.9% of pure nitrogen and 95% of oxygen (N_2 and O_2 recoveries of 98.5% and 99.8%, respectively). According to the authors, this RPSA process could also be extremely efficient for a H_2-CH_4 separation. Using a activated carbon bed, both hydrogen and methane can be highly recovered (more than 90%) from a feed mixture of 50-50% of H_2-CH_4 with significantly high purity on the two product streams (99.9%) [8]. Research in this area (piston-driven PSA) was also performed by the group of Prof. Farooq in the National University of Singapore [27-28].

In 1983, the Union Carbide Corporation signed a patent for a multi-bed (at least two adsorbent beds) RPSA process that operates with a 3 step cyclic sequence: (1) high pressure feed step; (2) counter-current depressurization step; (3) repressurization step [29]. In the U.S. Patent 4,406,675, the authors Dangieri and Cassidy claimed that this process was capable of enhancing productivity for a given product gas without an increase in the physical size of the system [29]. They also stated that the RPSA process cycle might have a delay period (of less than 10 times the

feed) to allow the further penetration of the pressure front into the bed and, so, to further enhance the overall process performance. The process was only exemplified for the production of an enriched O_2 stream with a purity of 94.5%. Thus, to attain a recovery of oxygen of 11.9-20.8% in a 94.5% O_2 stream, the cycle sequence (with a preferable total cycle time of 2-10 s) might be changed to: feed step followed by a delay, then the counter-current depressurization step and finally the repressurization step [29].

Later, the Union Carbide Corporation signed a European Patent Application 0,139,247 A1 [30] and a W.O. Patent 85/001451 [31] to use improved materials in RPSA processes, particularly adsorbents in milimetric scale with smooth and round form and having enhanced structural integrity and superior crush strength. Just as Dangieri and Cassidy (1983) [29], also Betlem *et al.* (1998) [18] reported the importance of a delay period after the high pressure feed step. They also stated that, occasionally, a second delay period might be added after the counter-current depressurization step. Betlem *et al.* (1998) suggested the addition of a "heavy product" recycle step (for difficult separations) or a "light product" recycle step at the end of the depressurization step in order to increase the recovery and in some cases, the process productivity [18].

Afterwards, Dangieri and Cassidy filled in 1986 a European Patent Application 0,175,804 A1 [32] and a W.O. Patent 86/002015 [33]. The RPSA processes were carried out for single adsorbent bed or multi-bed systems, using the cycle sequence described in the previous patents (feed step; delay; counter-current depressurization step; repressurization step) and with a desorption period / adsorption period ratio of 0.4 to 1.8. Moreover, as Jones *et al.* (1980) [15, 24] reported in the U.S. Patent 4,194,892 and European Patent Application 0,008,619 A1, also Dangieri and Cassidy studied the cross section reduction of the adsorbent bed for different diameters. The authors claimed a ratio of the cross sectional area at the feed end and the discharge end of the bed of 2 to 20, preferable about 5. Thus the enhanced process productivity and the product recovery can be achieved together with the reduction in power consumption and adsorbent inventory requirements [32-33].

In 1991, Sircar (Air Products and Chemicals, Inc.) filled a patent for a adiabatic layered-bed RPSA process to separate multicomponent gas mixtures, preferably, any binary gas mixture comprising a more adsorbable compound and a less strongly adsorbed compound [34-36]. The author claimed an improved RPSA process composed by one or more adsorption layered beds (packed with relatively small size adsorbent particles) operating alternatively by a pressurized continuous feed stream. Sircar suggested that each bed should have: small length; a first layer of a desiccant (activated alumina) at the feed air inlet end to remove the water; a final layer of a zeolite

for selective adsorption of nitrogen from the dry air; spaced apart from the other(s) layer(s) by perforated metal plates. The author claimed that is preferable to have a layer diameter / layer length ratio higher than 1.5 (ideal: higher than 3), contrarily to the practiced in a conventional PSA process that is higher than 0.3. The cyclic sequence of the RPSA process for oxygen production proposed by Sircar (1991) was: (1) simultaneous pressurization with air and adsorption of nitrogen for oxygen production; (2) simultaneous depressurization and counter-current purge with a portion of the oxygen produced for the adsorbent regeneration. For this cycle, the preferable total cycle time was 8-12 s. In order to increase the productivity, Sircar concluded that the cycle time should not be reduced indefinitely because of finite adsorbate mass transfer resistances. The author also reported that this process could be very efficient using NaX zolite for production of 25-50% oxygen enriched air with a reasonable recovery of >30% (at 50% O_2) [34-36]. Results of this research were also published in open literature by Sircar and Hanley (1995) [16]. In 1996, Sircar also integrated a O_2 production RPSA process with an enhanced combustion application system that allowed thermal swing adsorption for water removal followed by the RPSA process. Thus, for the same cyclic sequence and step times described before, the capital and energy costs of the oxygen produced were significantly reduced due to a significant decrease of the RPSA operating pressure range from 2-20 bar to 1-2 bar. Still regarding to the examples disclosed by Sircar (1991) [34] in the U.S. Patent 5,071,449, the adiabatic layered-bed RPSA process was also efficient for hydrogen purification from binary mixtures (H_2-CH_4, H_2-CO and H_2-CO_2) or multicomponent mixtures (40-90% of H_2 contaminated with CO_2, CO, hydrocarbons, N_2 and H_2O). In this case, the author suggested an zeolite molecular sieve or an activated carbon as the main adsorbent in the bed for the production of 95-99.99% pure hydrogen [34].

LaBuda *et al.* (also from Air Products and Chemicals, Inc.) “continued” the studies on oxygen production through RPSA processes. In 2008, LaBuda *et al.* (2008) [6-7] disclosed in the U.S. Patent Application 2008/0083331 A1 and European Patent Application 1,917,994 A1 an improved RPSA process for the removal of contaminants (particularly water) from air to produce oxygen. Sircar already patented RPSA processes with multilayered beds for oxygen concentration using activated alumina for the removal of water and different layers of zeolites (13X, NaX, etc.) [34-36]. The cyclic sequence of the RPSA process proposed by LaBuda *et al.* (2008) was: (1) high pressure feed step; (2) counter-current depressurization step; (3) repressurization step with the oxygen produced or air. The authors claimed that, for a feed step duration of 0.75-30 s and a total cycle time between 6 to 60 s, this RPSA process was capable of recovering more than 35% of oxygen in a 93% O_2 enriched product stream with a flow rate of 0.4-3.5 LPM [6-7].

Simulations of a three-step one-column pressure swing adsorption process were performed by Lu *et al.* (1993) [37] based on the data reported by Cheng and Hill (1985) [38]. The simulations were performed for a fixed cycle time of 7.5 s. The authors studied several operating conditions such as the effects of isotherm capacity and nonlinearity, incomplete pressurization and blowdown, dead volumes at the ends of the column, feed composition and also isothermal and adiabatic operation. [37].

The Impact MST, Inc. signed the U.S. Patents 5,827,358 and 6,068,680 for a rapid cycle multi-bed PSA method and apparatus for oxygen concentration [4-5]. Kulish and Swank (1998, 2000) [4-5] disclosed a 6-layered-beds RPSA system that utilized less energy and operated more efficiently than the apparatus of the prior art producing 2-5 LPM of oxygen with a purity of 90-96%. Each bed comprised three layers of molecular sieves. The asymmetry of the cycle proposed (adsorption period of 1-2 s and desorption period of 5-10 s) allowed higher regeneration of the adsorbent, increasing the performance of the process [4-5]. Even having only been studied for separation of air, this RPSA system is of great interest due to the high efficiency.

It was already reported that numerous hydrodynamic constraints may limit gas flow rates through the adsorbent bed. In order to reduce such limitation, many such designs have been proposed and developed which allow faster cycles, higher gas throughputs at lower pressure drops, and complete absence of fluidization [2, 39-40]. Chiang and Hong (1995) studied a RPSA process with radial flow geometry that operates under a cycle time of less than 30 s and compared it to a conventional RPSA with axial flow [41]. The authors concluded that much smaller particles (in micrometer scale) could be employed in the process because of the larger cross sectional area and thus the smaller pressure drop of the radial flow RPSA system. Besides, Chiang and Hong (1995) concluded that the smaller particle size facilitated a faster adsorption kinetics and therefore the equilibrium could be reached almost instantaneously even under faster cycles. According to the authors, the radial geometry RPSA system is more effective and productive than an axial flow RPSA since it allows more adsorbent utilization due to the deeper feed distribution [41]. Later, Huang and Chou (2003) [42] compared a radial and an axial flow RPSA processes through simulations. The authors concluded that the separation performance of the radial flow RPSA process overcomes the axial flow RPSA process when smaller particle size adsorbents and longer radial lengths are used [42]. However, the beds with radial flow geometry are more expensive [2].

In the beginning of this century, new schemes with rapid cycling processing for hydrogen purification systems were published and patented. In 2000, Keefer and Doman (from SoFinoy Societte Financiere d'Innovation Inc.) filled a patent entitled flow regulated PSA system (U.S

Patent 6,063,161) [13]. Keefer (2001) [43] and then Keefer and Doman (2004) [14] continued the studies on flow regulated PSA systems filling the U.S Patent 6,176,897 B1 (signed by Questor Industries Inc.) and U.S. Reissued Patent RE38,493 E (signed by QuestAir Technologies Inc.), respectively. The invention disclosed in the mentioned patents relates to a layered multi-bed PSA separation system for a gas mixture (hydrogen purification, air, etc) using rotary multiport distributer valves. The rotary multiport distributer valves control the timing sequence of the cycle steps between beds and, with flow controls cooperation, the volume rates of gas flows to and from the beds at different cycle steps (blowdown, purge, equalization and repressurization). The authors stated that the productivity of the process is enhanced by minimizing the duration of the low flow valve switching times. However, the rotary devices may be impracticable for large PSA units due to the weight of the rotary assembly and possible leakage from large rotary seals. Systems with hazardous gases such as hydrogen need a rotary valve completely enclosed in a containment shroud. Besides, adsorbent bed attrition, mass transfer influences and rotary valve frictional heating are limitations that need to be considered [14].

In 2002, the QuestAir Technologies, Inc. disclosed in the U.S. Patent 6,406,523 B1 [44] a rotary PSA apparatus comprising multi-laminated sheet adsorbers within only one adsorption bed and a rotor for high frequency timing control. This proposal resulted in a compact and rapid H_2 purification PSA unit.

One year later, Golden *et al.* (2003) [45] from Air Products and Chemicals, Inc. disclosed a multilayered bed packed using a high density adsorbent (at least $0.3\ g\ cc^{-1}$) followed by a low density adsorbent (less than $0.3\ g\ cc^{-1}$), both having a surface area of at least $500\ m^2\ g^{-1}$. These materials were used, not only in PSA studies, but also in rapid PSA (RPSA) studies for the preparation of high purity hydrogen (and other products). Few months before, Golden *et al.* (2003) [46] already filled the U.S. Patent 6,565,627 B1 disclosing the use of an adsorbent with an average pore diameter of > 5 Å and/or a CO_2 mass transfer coefficient of $\geq 0.5\ s^{-1}$ for purification of hydrogen through RPSA processes. These adsorbents are essentially activated carbons (also zeolites, alumina and silica gel) impregnated with metal salts, oxidized, reduced and/or ion exchanged. The authors stated that the materials mentioned before (with low pressure drop, fast mass transfer, large film and solid mass transfer coefficients, high working capacities and small void volume to minimize the size of the bed) can be used in RPSA processes for which the molecules residence time in the bed must be short. Golden *et al.* (2003) [46] claimed a product purity of 99.9% and a product recovery of at least 70% can be achieved in a RPSA unit. Golden *et al.* (2003) [47] continued the RPSA studies filling a U.S. Patent entitled activated carbon as sole

absorbent in rapid cycle hydrogen PSA. In this patent the authors disclosed the use of an activated carbon bed substantially free of zeolite adsorbents and an RPSA system operating with a feed time lower than 20 s. Golden *et al.* claimed that this process is particularly suitable for use with fuel cells and other applications requiring compact and rapid cycling systems capable of a production of high purity hydrogen with a rate of hydrogen recovery greater than 82%. Later the same authors and Novosat (Air Products and Chemicals, Inc.) disclosed the U.S. Patent Application 2006/0236862 A1 and the U.S. Patent 7,404,846 B2 for adsorbents for rapid cycle pressure swing adsorption processes [48-49]. The authors reported two PSA processes for hydrogen purification from mixtures containing carbon monoxide and nitrogen: one comprises 4 beds with 7 steps and other of 5 beds with 11 steps. The authors claim that, using only one adsorbent in all beds (zeolite 5A exchanged 70-95% with calcium) or using layered beds (activated carbon followed by a zeolite 5A, 13X, BaX or 5A exchanged 70-95% with calcium), highly purified hydrogen with less than 10 ppm of carbon monoxide can be produced for a feed step duration of < 30 s.

As Golden *et al.* (2003) [45-47] patented in 2003, also Keefer *et al.* (2004) [50] in the U.S. Patent 6,692,626 B2 proposed methods for the formation of adsorbent laminate structures for use in PSA or RPSA processes. In this case, the authors from QuestAir Technologies, Inc. disclosed an electrophoretic method to deposit the adsorbent material (zeolites X, A or Y, chabazite and/or silicalite) onto the metal (aluminium, steel, stainless steel) or alloy support, forming a coated support having a layer thickness of 5-100 μm. Then, the coated supports are fired to activate the adsorbent and assembled into a laminate bed with ventilation gaps between supports.

Two years later, the ExxonMobil Research and Engineering Company signed the U.S. Patent Application 2006/0174764 A1 [10] and, three years later, the U.S. Patent 7,591,879 B2 [9] disclosing a RPSA process capable to produce hydrogen at purities higher than 99% and recoveries higher than 81% over a range of flow rates. The authors reported several experiments for different feed compositions using a RPSA process that operates with a 5 step cyclic sequence: (1) high pressure feed step; (2) co-current depressurization step; (3) counter-current depressurization step; (4) counter-current purge step; (5) repressurization step with product [9-10]. The time duration of the feed step of each experiment was equal to the entire duration of the steps 2 to 5 and, typically, the total cycle was between 0.5 and 2 s. In some cases, the authors discarded the counter-current depressurization step achieving even so high process performances: > 99% of H_2 purity and > 85% of H_2 recovery for the separation of a mixture of 74% of hydrogen contaminated with hydrocarbons [9-10].

Later, Alizadeh-Khiavi *et al.* (2007) [11] from QuestAir Technologies, Inc. disclosed in the U.S. Patent Application 2007/0125228 A1 a RPSA system for the production of a hydrogen enriched product from syngas mixtures. The multilayered adsorbent beds used in the RPSA process (at least 3 beds) comprised 7% of activated alumina, 13% of activated carbon, 40% of zeolite 13XA and 40% of calcium exchanged zeolite molecular sieve. Thus, authors claimed that more than 80% of hydrogen can be recovered with a H_2 purity of at least 99% (with less than 1% of CO_2 and less than 50 ppm of CO) from a catalytic steam reformer reformate mixture containing 72% of H_2, 19% of CO_2 and 9% of CO (at 353 K and 15 bar). The RPSA cycle comprised three pressure equalizations between the adsorbent beds and the total cycle time was 12 s [11].

It can be observed from the state of the art of RPSA that most of the research in this area was carried out in industry. Initial work and most important advances were developed in oxygen concentration from air. In the last years, the search for alternative energy sources has triggered out research in hydrogen purification processes and thus RPSA has been adapted for this application. As the market of hydrogen systems grows, it is a very opportune moment to develop improved cycles for PSA or RPSA processes in order to increase the productivity and product recovery, having always in consideration the decrease in the operating costs of the overall system.

6.3 RPSA experimental unit

The experimental set-up described in chapter 5, composed by a 2-column PSA unit connected to a gas chromatograph analysis system for determination of bed outlet concentrations of multicomponent gas mixtures, was adapted for RPSA experiments. This “adapted” facility is able to operate with gas mixtures of three components, feed flow rates of 1.67×10^{-6} to 8.33×10^{-5} m^3 s^{-1} (measured at 298 K and 1 bar), pressures of 0.1 to 5 bar and temperatures of 298 to 423 K. To increase the number of components in the feed, a gas bottle with the desired content of contaminants should be prepared. In this modified set-up, two new stainless steel columns with a cross section diameter of 1 inch (2.54 cm) were installed (see Figure 6.1). The main purposes of this modification are to reduce the amount of adsorbent in the column (enabling a faster pressurization step) and achieve higher superficial velocities (up to 0.24 m s^{-1}). The schematic view of the complete RPSA unit is shown in Figure 6.2. This apparatus was used for the study of hydrogen purification from a binary mixture of two main compounds of the SMR off-gases (H_2 and CO_2).

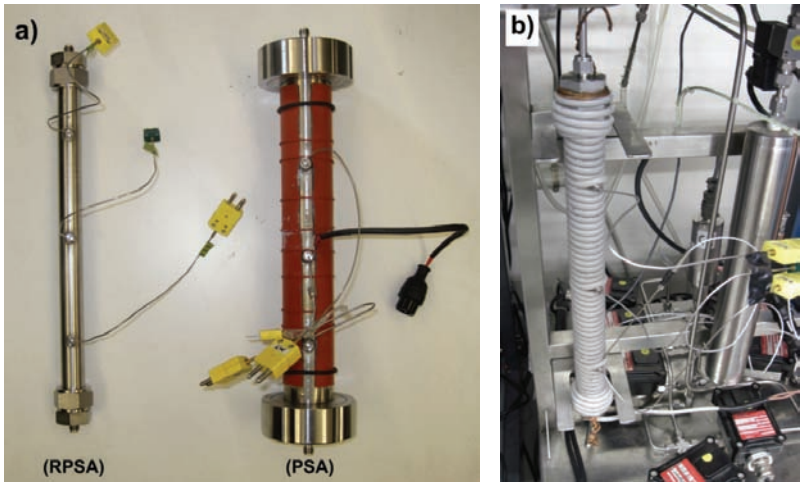


Figure 6.1: a) Column used in the previous experiments of PSA processes (right) and column used in the RPSA experiments (left); b) Column installed in the "adapted" RPSA facility with the flexible heating rope for the degassing of the adsorbent.

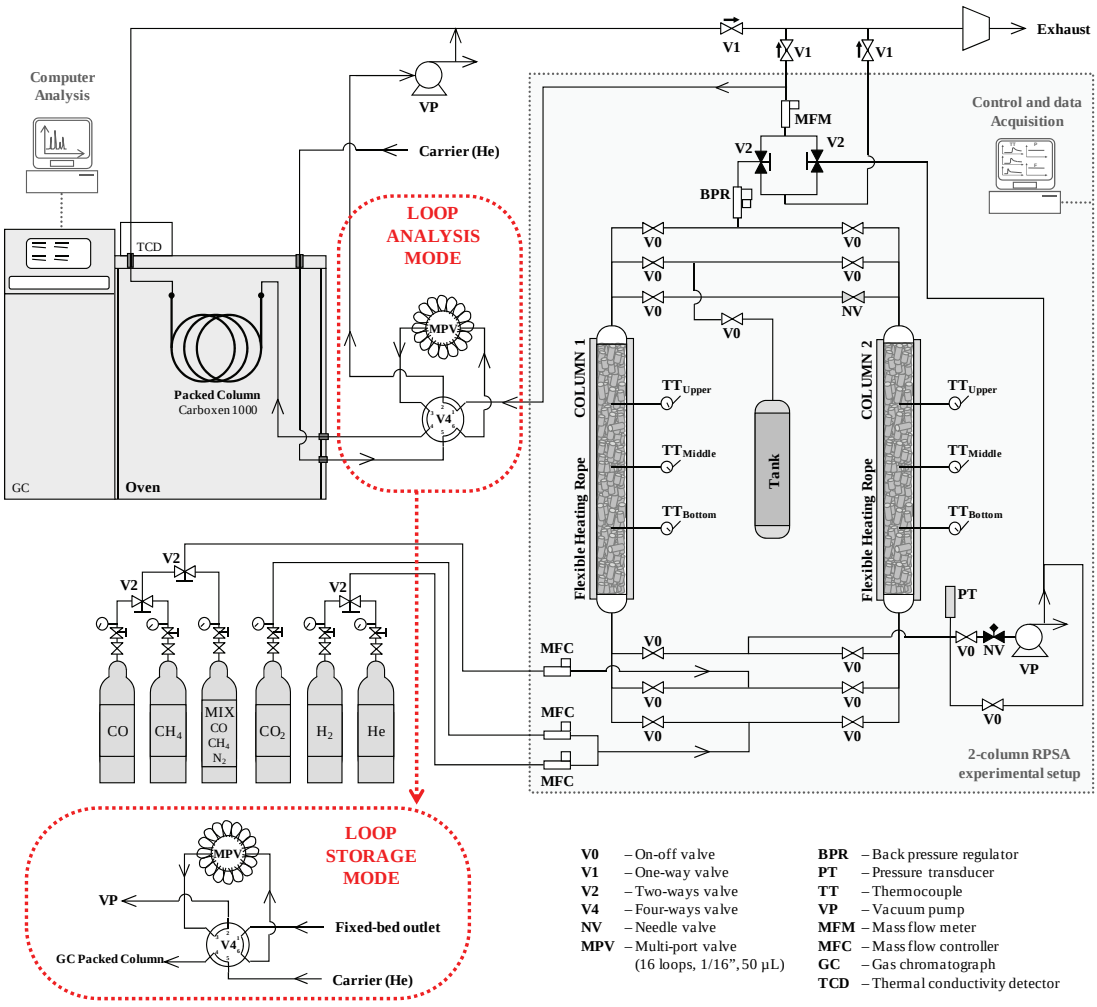


Figure 6.2: Schematic representation of the 2-column RPSA experimental set-up connected to a GC analysis system to measure the bed outlet concentration.

It should be mentioned that the unit used was not specifically designed to operate in RPSA mode and thus several calibrations / verifications were carried out before its utilization. The electronic equipment stabilization, particularly for mass flow controllers (MFC), flow meter (FM), back pressure regulator (BPR), pressure transducer (PT), etc, need to be taken into consideration, particularly when small step times of RPSA processes are applied. To stabilize the input or output signals of the electronic devices, a short period of time is needed. However, it was important to analyze for each case (flow rates, pressure, etc), how these stabilization times might affect the overall process.

The flow rate signal obtained by the mass flow controllers MFC 1 and MFC 2 placed at the column inlet of the RPSA unit is reported in Figure 6.3 as a function of time at different feed flow

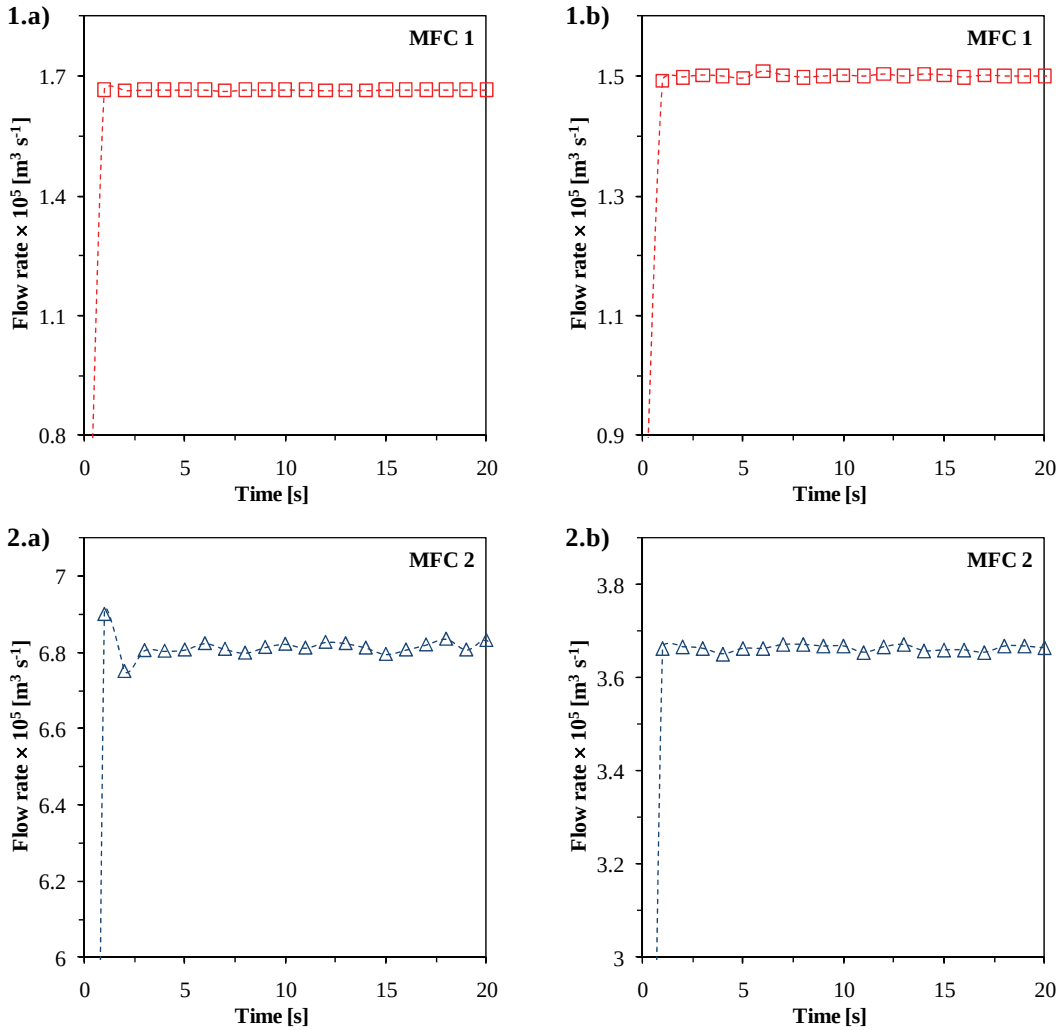


Figure 6.3: Flow rate signal obtained by the mass flow controllers (MFC) installed in the RPSA unit at column inlet: 1) MFC 1 (--□--); 2) MFC 2 (--△--); flow rates of 1.67×10^{-5} m^3 s^{-1} (a) and 1.50×10^{-6} m^3 s^{-1} (b), both measured at 298 K and 1 bar.

rates. MFC 1 was programmed to control the flow rate at 1.67×10^{-5} m^3 s^{-1} (a) and 1.50×10^{-6} m^3 s^{-1} (b), both measured at 298 K and 1 bar. The MFC 2 was set to flow rates of 6.80×10^{-5} m^3 s^{-1} (a) and 3.67×10^{-6} m^3 s^{-1} (b), again measured at 298 K and 1 bar. It was observed that both mass flow controllers need 1 s to attain a stable signal. Only for higher flow rates (e.g., 6.80×10^{-5} m^3 s^{-1} (measured at 298 K and 1 bar), in Figure 6.3, 2.a), the mass flow controller MFC 2 needed higher time for complete stabilization: around 2 s. Since MFC 2 is able to control flow rates of 0 to 8.33×10^{-5} m^3 s^{-1} (measured at 298 K and 1 bar), it was observed that the signal oscillations increased for flow rates near the maximum limit.

The flow rate signal measured by the flow meter (FM) placed at the column outlet of the RPSA unit are reported in Figure 6.4. In the two cases reported in the figure, the oscillations were much higher than the oscillations obtained in the mass flow controllers (at least 2 s). Besides, it was possible to conclude that, for small flow rates, the oscillation in the FM signal increased significantly. The main reason for that is the range of the FM which can measure the flow rate (from 0 to 1.67×10^{-4} m^3 s^{-1}, measured at 298 K and 1 bar), being difficult for the equipment to measure flow rates with high accuracy at the higher and lower limits.

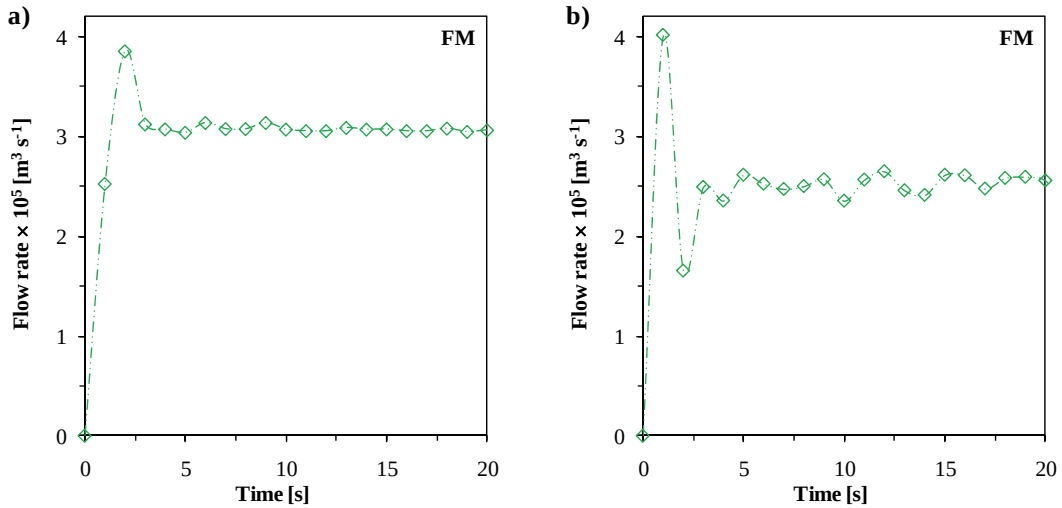


Figure 6.4: Flow rate signal measured by the flow meter (FM, ·-◇-·) installed in the RPSA unit at column outlet; flow rates of 2.50×10^{-5} m^3 s^{-1} (a) and 3.00×10^{-5} m^3 s^{-1} (b), both measured at 298 K and 1 bar.

The oscillations of the signal of the back-pressure regulator placed at the column outlet of the RPSA unit were also analyzed. The pressure signals obtained by the BPR for two different sets

of pressures (1.5 and 5 bar) are reported in Figure 6.5. It was observed that the signal oscillations of the BPR did not affect the overall process, for both high and low pressures.

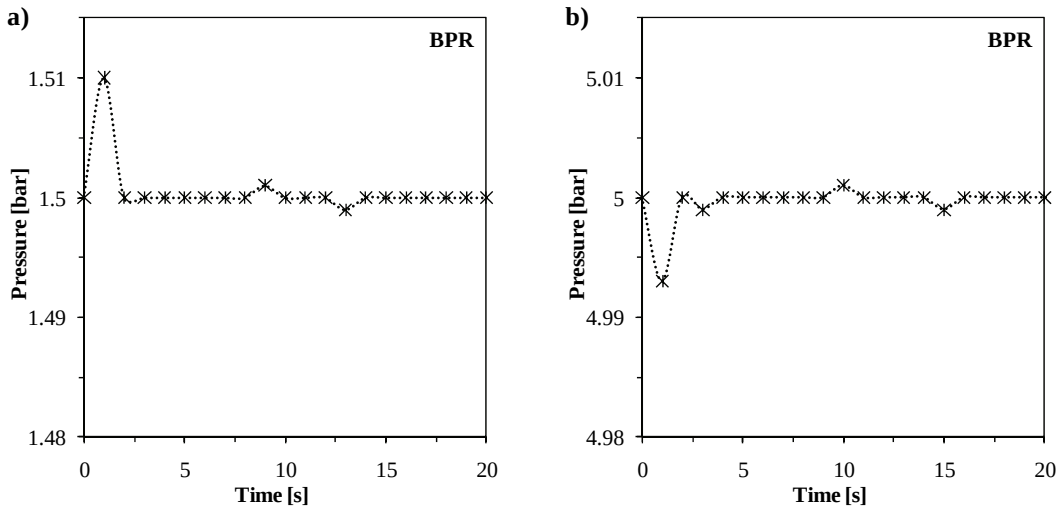


Figure 6.5: Pressure signal obtained by the back-pressure regulator (BPR) at column outlet: pressure of 1.5 bar (a) and 5 bar (b).

The volume of each stainless steel column used in the RPSA unit was substantially reduced (approximately 80%, from 5.24×10^{-4} to 1.08×10^{-4} m^3). Thus, it was important to account for the dead volumes of the system and determine their effect. In Figure 6.6, the dead volumes of all sections of the 2-column RPSA experimental set-up connected to the GC analysis system are highlighted.

The importance of the dead volumes increases with the reduction of the size of the adsorbent beds. Considering a pressure equalization step using a 2-column RPSA unit, when the pressure inside the columns is measured using the pressure transducer, the dead volumes between both columns and also from column 2 until the pressure transducer affect the equalization. As an example, during a pressure equalization step where column 1 was initially pressurized with an inert gas at 5 bar and column 2 at 1 bar, the pressure history during the equalization step was measured by the pressure transducer. It was expected that final pressure is 3.0 bar, but the measured value was smaller than this value. These results obtained and also pressure equalization steps of 4 bar / 1 bar and 3 bar / 1 bar are reported in Figure 6.7. Note that the dead volumes between the columns and the on-off valves are approximately the same and thus do not affect the equalization. However, to measure the pressure inside the columns during the equalization step, more

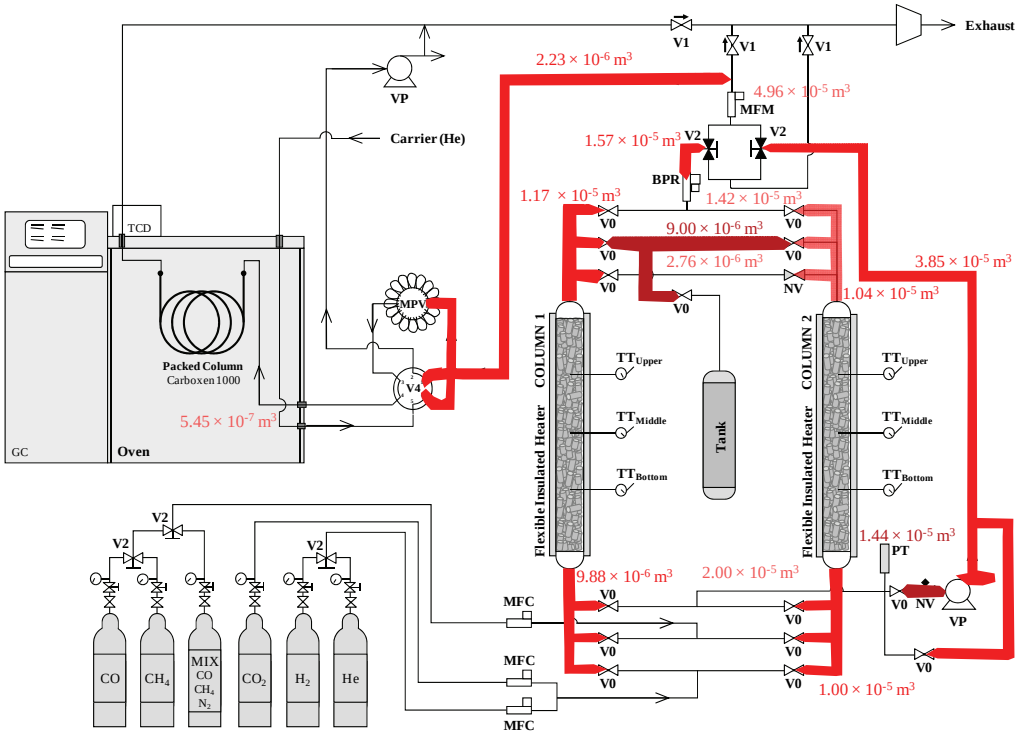


Figure 6.6: Schematic representation of the dead volumes (highlighted in red) of the different sections of the RPSA unit and GC analysis system.

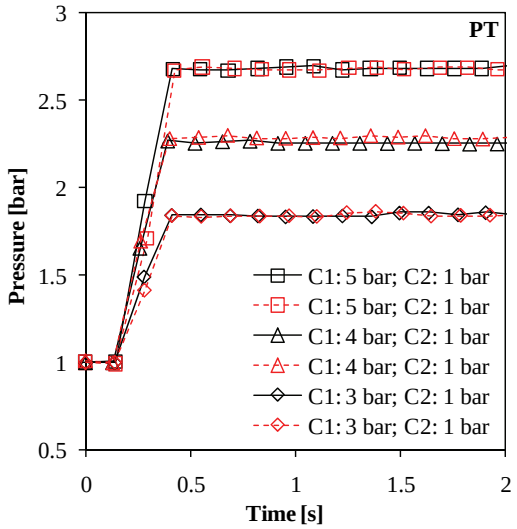


Figure 6.7: Pressure signal obtained by the pressure transducer (PT) placed at the outlet of column 2 (initially pressurized at 1 bar) during different equalization steps: column 1 was pressurized at 5 bar (—□—,--□--), 4 bar (—△—,--△--) and 3 bar (—◇—,--◇--).

2.90×10^{-5} m^3 of dead volume were used: connection between column 1 and 2 and connection between column 2 and the pressure transducer. This led to lower pressures in the final times of

equalizations steps: 2.68, 2.28 and 1.85 bar instead of 3, 2.5 and 2 bar, respectively. Since the dead volumes may result in significant changes to the experimental results, in this chapter, only experiments involving the fast cycling of a single-column PSA are reported.

Due to the experimental oscillations observed in flow controllers and flow rate measurements and also to accurately analyze exit gas composition, it is not possible to design cycles in the order of 20 seconds. In fact, due to experimental limitations, the cycle could never take less than 40 seconds and the initial target of this chapter is to study cycles of around one minute (60 seconds).

The experimental set-up described in Figure 6.2 was not previously used for fast cycling experiments. To understand better the limits of the unit for this particular binary gas mixture (when used in fast cycling experiments), binary breakthrough experiments were initially performed.

6.4 Cycle modelling and RPSA simulations

The cycle sequence applied in the RPSA experimental study and simulations was composed by 5 elementary steps: co-current feed, co-current depressurization, counter-current blowdown, counter-current purge with hydrogen and co-current pressurization with feed. The scheme of a column within one cycle is shown in Figure 6.8. This cycle is a Skarstrom-type cycle [51] commonly used in the PSA processes with the integration of a co-current depressurization step to increase the hydrogen recovery of the RPSA process. The RPSA cycle started with the co-current feed step. The column was packed with activated carbon AC5-KS and before the experiment starts, the bed was pressurized with the less adsorbed gas (hydrogen) at the feed temperature and pressure.

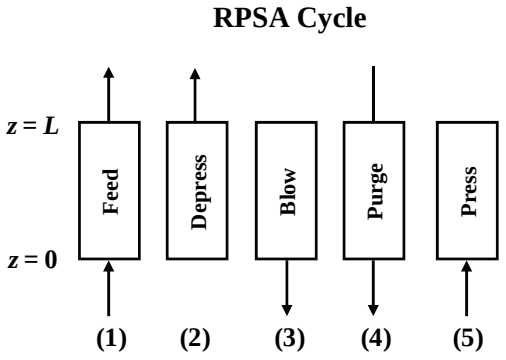


Figure 6.8: Schematic diagram of the cycle sequence used in the RPSA experiments and simulations for H_2 purification: (1) co-current feed step; (2) co-current depressurization step; (3) counter-current blowdown step; (4) counter-current purge step with hydrogen; (5) co-current pressurization step with feed.

The mathematical model applied for the simulation of single column PSA processes that was described in chapter 5 was also employed in the RPSA process simulations. This model was applied in the simulation of a RPSA process for different operating conditions using the cycle sequence reported in Figure 6.8.

The same parameters as the ones used to study the PSA process performance in chapter 5 (such as the hydrogen purity, hydrogen recovery and process productivity) were employed in the RPSA performance evaluation [52]. For this cycle, the process was evaluated according to the following equations:

$$\mathrm{H_2\ Purity}\,(\%) = \frac{\int_{t=0}^{t_{Feed}} C_{H_2} u_0 \big|_{z=L}\, dt}{\sum_{i=0}^{n} \int_{t=0}^{t_{Feed}} C_i u_0 \big|_{z=L}\, dt} \tag{6.1}$$

$$\mathrm{H_2\ Recovery}\,(\%) = \frac{\int_{t=0}^{t_{Feed}} C_{H_2} u_0 \big|_{z=L}\, dt + \int_{t=0}^{t_{Depress}} C_{H_2} u_0 \big|_{z=L}\, dt - \int_{t=0}^{t_{Purge}} C_{H_2} u_0 \big|_{z=L}\, dt}{\int_{t=0}^{t_{Feed}} C_{H_2} u_0 \big|_{z=0}\, dt + \int_{t=0}^{t_{Press}} C_{H_2} u_0 \big|_{z=0}\, dt} \tag{6.2}$$

$$\mathrm{Productivity}\left(\frac{mol_{H_2}}{kg_{ads}\, day}\right) = \frac{A_{bed}}{t_{cycle}\, w_{ads}} \left(\int_{t=0}^{t_{Feed}} C_{H_2} u_0 \big|_{z=L}\, dt + \int_{t=0}^{t_{Depress}} C_{H_2} u_0 \big|_{z=L}\, dt - \int_{t=0}^{t_{Purge}} C_{H_2} u_0 \big|_{z=L}\, dt \right) \tag{6.3}$$

6.5 Experimental

Initial experiments consist of binary H_2-CO_2 breakthrough experiments in the column packed with activated carbon AC5-KS [53]. Since the superficial velocity employed is significantly higher than in previous measurements, it should be verified that no undesired kinetic effects take place: gas mal-distribution within the column, significant film mass transfer resistance, etc. Also, these experiments allow the identification of the dominating mass transfer mechanism for high velocities inside the column.

Before breakthrough experiments, degassing of the adsorbent sample was carried out using a helium gas (inert) flow rate of 5.00×10^{-6} m^3 s^{-1} (measured at 298 K and 1 bar) overnight at 423 K (heating rate of 1 K min^{-1}). Afterwards, to determine the overall heat transfer coefficient (U), a cooling experiment from 334 K until 298 K was performed using an inert (helium) gas flow rate of 5.00×10^{-5} m^3 s^{-1} (measured at 298 K and 1 bar). All gases used were provided by Air Liquide: hydrogen N60, carbon dioxide N48 and helium N50 (purities greater than 99.9999, 99.998 and 99.999 %, respectively).

6.5.1 Multicomponent breakthrough experiments

Binary breakthrough experiments of the two main species of the SMR off-gases (H_2 and CO_2) were performed using the maximum attainable velocities inside the column (feed flow rates from 1.167×10^{-5} to 8.33×10^{-5} m^3 s^{-1}, measured at 298 K and 1 bar). Table 6.1 shows the dimensions of the column used in these measurements and the adsorbent physical properties. Three thermocouples (TT) located at 0.050 (TT_{Bottom}), 0.159 (TT_{Middle}) and 0.271 m (TT_{Top}) from the feed inlet were used to record the temperature variations along the bed. The breakthrough experiments were carried out at 298 K and the total pressure at the exit of the column was kept constant with a back-pressure regulator. During each experiment, samples of the outlet stream were stored in the loops of a multi-port valve system and afterwards analysed by the TCD detector (thermal conductivity detector) of a gas chromatograph (Varian CP-3800, Holland). In Table 6.1, the experimental conditions of the binary breakthrough curves are reported.

Table 6.1: Properties of the column used and experimental conditions of the fixed-bed breakthrough curves on the modified activated carbon AC5-KS performed in the "adapted" RPSA facility.

Run		Binary (H_2-CO_2) breakthrough experiments		
		1	2	3
Feed molar fraction	H_2	0.70	0.70	0.80
	CO_2	0.30	0.30	0.20
Inlet sup. velocity [m s^{-1}]		0.007	0.029	0.161
Feed flow rate × 10^5 [m^3 s^{-1}][#]		1.167	5.00	8.33
Pressure [bar]		5	5	1.5
Temperature [K]		298		
Thermocouple distance from feed inlet [m]	TT_{Bottom}	0.050		
	TT_{Middle}	0.159		
	TT_{Top}	0.271		
Mass of Adsorbent [kg]		0.05147		
Bed height [m]		0.313		
Bed volume [m^3]		1.08×10^{-4}		
Bed porosity, ε		0.396		

[#] measured at 298 K and 1 bar

6.5.2 RPSA experiment

The column employed for the fixed-bed breakthrough curves (described in the last section 6.5.1) was used for a RPSA experiment. The cycle sequence of 5 steps reported in Figure 6.8 was employed. The first step of the RPSA cycle was the co-current feed step. The column was packed with the activated carbon AC5-KS and pressurized with helium (inert gas) at the feed temperature and pressure. The operating parameters of the RPSA experiment are detailed in Table 6.2.

Table 6.2: Experimental conditions of the RPSA experiment using the activated carbon AC5-KS; Virial isotherm fitting parameters of pure H_2 and CO_2 at 303-323 K on the same adsorbent.

	RPSA experiment
Ads molar fraction	H_2: 0.83; CO_2: 0.17
Feed temperature [K]	298
Feed flow rate [$m^3\ s^{-1}$][#]	5.00×10^{-5}
Inlet sup. velocity [$m\ s^{-1}$]	$u_{0,Feed}$ = 0.048 $m\ s^{-1}$; $u_{0,Purge}$ = 0.096 $m\ s^{-1}$
Step pressures [bar]	P_{high} = 3 bar ; P_{inter} = 1 bar ; P_{low} = 0.3 bar
Step times [s]	t_{Feed} = 10 s ; $t_{Depress}$ = 5 s ; t_{Blow} = 5 s ; t_{Purge} = 20 s ; t_{Press} = 12 s

[#] measured at 298 K and 1 bar

6.6 Results and discussion

Prior to the binary breakthroughs and RPSA experiments, the overall heat transfer coefficient (U) was determined for the fixed-bed packed with the activated carbon AC5-KS. For that, a cooling experimental run from 334 K until room temperature (298 K) was performed using helium as inert gas with a flow rate of $5.00 \times 10^{-5}\ m^3\ s^{-1}$ (measured at 298 K and 1 bar). The temperature was measured at 0.271 m from feed inlet during the cooling experiment. The results are reported in Figure 6.9. This experiment was used to fit the overall heat transfer coefficient and the value obtained from the fitting is 22 $J\ s^{-1}\ m^{-2}\ K^{-1}$. Although is known that the value of the overall heat transfer coefficient decreases with temperature, in this example the temperature change is not so large and using a single (invariant) value of 22 $J\ s^{-1}\ m^{-2}\ K^{-1}$ the experiment can be entirely well described.

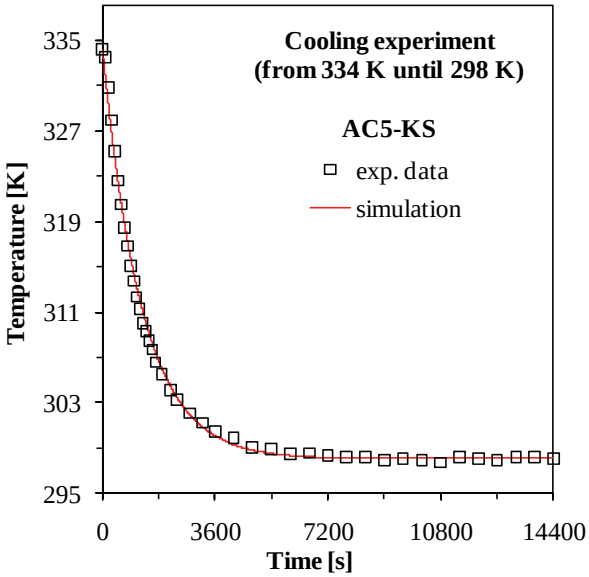


Figure 6.9: Temperature measured at 0.271 m (□,——) from feed inlet during a cooling experiment from 334 K until 298 K; Helium flow rate of 5.00×10^{-5} m^3 s^{-1} (measured at 298 K and 1 bar); Experimental data (symbols); Simulation (lines).

6.6.1 Multicomponent breakthrough experiments

The adsorption equilibrium data of pure components on activated carbon AC5-KS is reported in chapter 4. In a RPSA unit, the multicomponent mixture fed to the column raises higher superficial velocities inside the bed: it could reach 0.24 m s^{-1}. Therefore it is important to verify experimentally that no undesired kinetic effects occur, such as gas mal-distribution within the column, significant increase in the film heat transfer resistance, etc. It is also very important to understand the changes in the mass transfer zone due to the inter and intra-particle resistances when increasing gas velocity. To accomplish this objective, different binary breakthrough experiments of H_2 and CO_2 were performed in the fixed-bed set-up of the RPSA unit at different velocities. The operating conditions at which those experiments were performed are shown in Table 6.1 (section 6.5.1).

Initially, a binary breakthrough curve of a H_2-CO_2 mixture was performed for a low feed flow rate of 1.167×10^{-5} m^3 s^{-1} (measured at 298 K and 1 bar). This experiment was done with a similar superficial velocity inside the column as the one used in the PSA experiment reported in the previous chapter. The experimental results of the binary H_2-CO_2 breakthrough curve were reported in Figure 6.10. Then, a binary H_2-CO_2 breakthrough curve was performed for a feed flow rate of 5.00×10^{-5} m^3 s^{-1}, measured at 298 K and 1 bar. The experimental results of this breakthrough curve were reported in Figure 6.11. Finally, a binary H_2-CO_2 breakthrough curve was performed

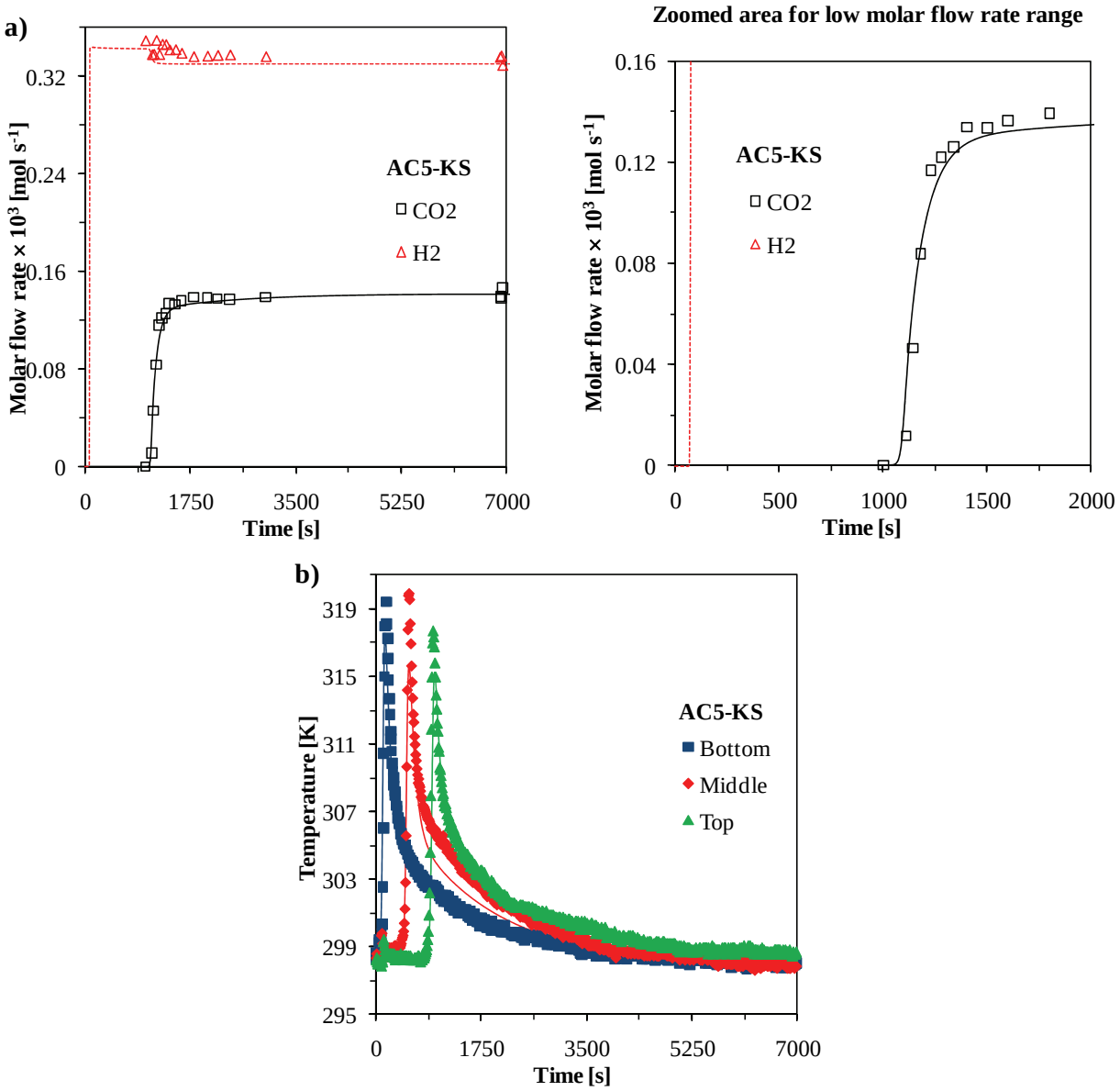


Figure 6.10: H_2 (△,----) and CO_2 (□,——) molar flow rate histories (a) at the column outlet and temperature histories (b) obtained for binary H_2-CO_2 breakthrough curve (run 1) at 298 K and 5 bar on activated carbon AC5-KS; Mixture: 30% of CO_2 balanced with H_2; Temperatures measured at 0.050 m (Bottom (■,——)), 0.159 m (Middle (◆,——)) and 0.271 m (Top (▲,——)) from feed inlet; Flow rate of 1.167×10^{-5} m^3 s^{-1} (measured at 298 K and 1 bar); Experimental data (symbols); Simulation (lines).

near the operational condition limit of the mass flow controllers installed in the RPSA unit. The total feed flow rate used in this experiment was 8.33×10^{-5} m^3 s^{-1} (measured at 298 K and 1 bar). Also, a smaller total pressure was used in order to further increase the velocity within the column. The results obtained are reported in Figure 6.12. With these breakthrough experiments, the study of the dispersion effects could be carried out for the binary H_2-CO_2 system. The mathematical model

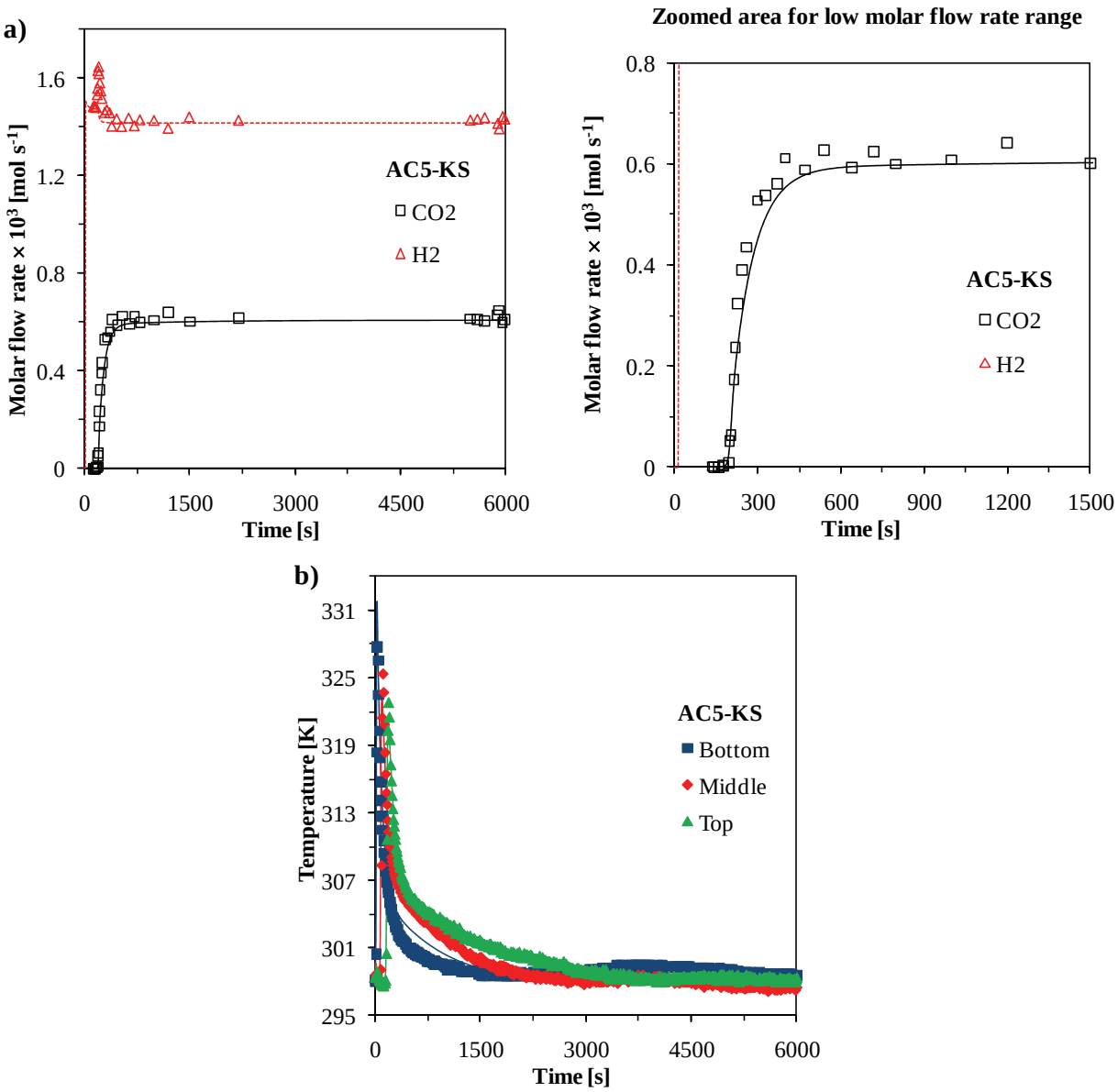


Figure 6.11: H_2 (△,----) and CO_2 (□,——) molar flow rate histories (a) at the column outlet and temperature histories (b) obtained for binary H_2-CO_2 breakthrough curve (run 2) at 298 K and 5 bar on activated carbon AC5-KS; Mixture: 30% of CO_2 balanced with H_2; Temperatures measured at 0.050 m (Bottom (■,——)), 0.159 m (Middle (◆,——)) and 0.271 m (Top (▲,——)) from feed inlet; Flow rate of 5.00×10^{-5} m^3 s^{-1} (measured at 298 K and 1 bar); Experimental data (symbols); Simulation (lines).

described in section 6.4 (originally reported in chapter 5) was used for the prediction of the experimental results. The transport parameters reported in Table 6.3 were applied in the simulations (reported in the end of this section). The adsorption equilibrium and kinetic data obtained from pure hydrogen and carbon dioxide (reported in chapter 4) were employed in the model. These model predictions were also shown in Figure 6.10 to Figure 6.12, represented by the

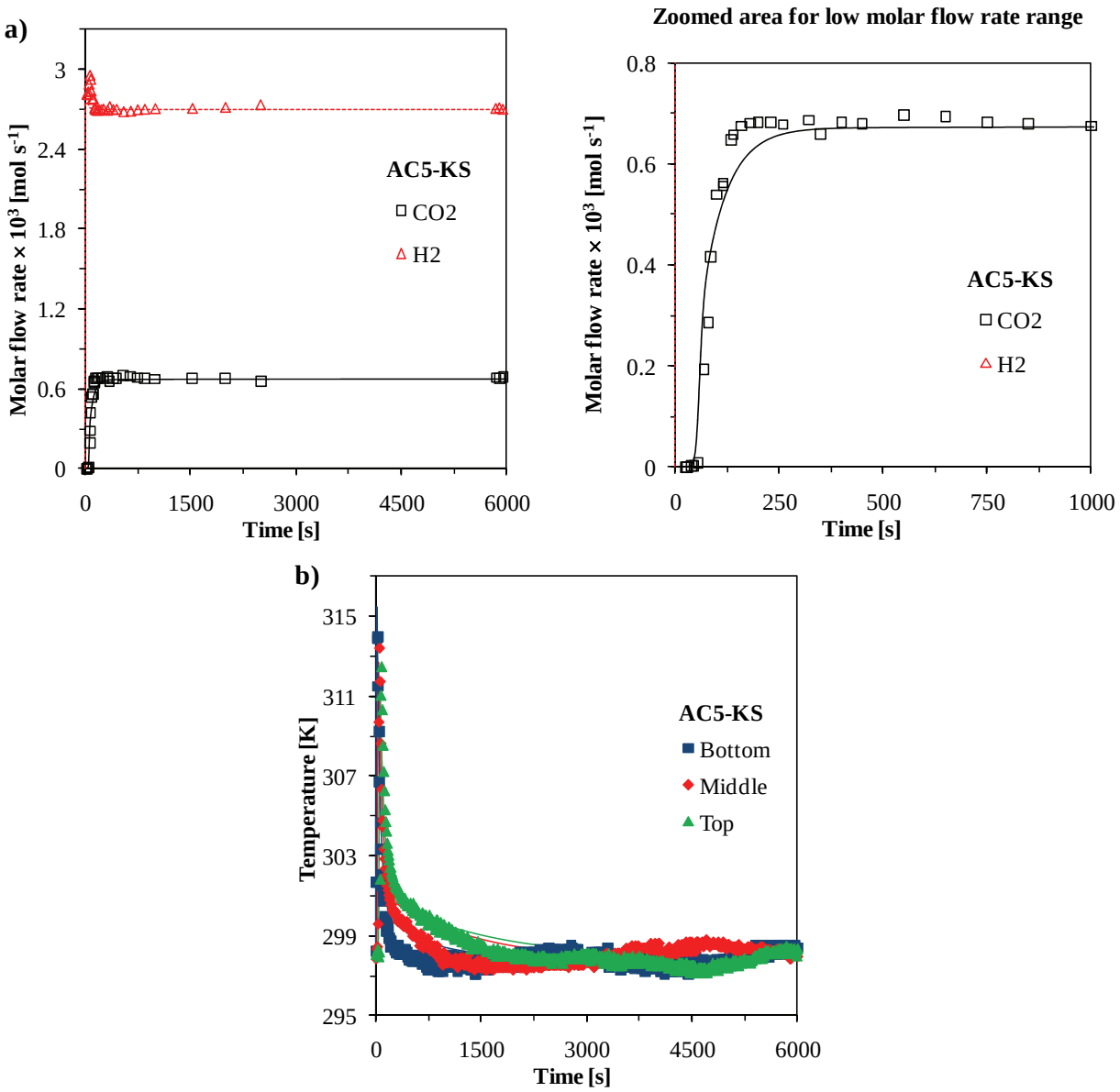


Figure 6.12: H_2 (△,----) and CO_2 (□,——) molar flow rate histories (a) at the column outlet and temperature histories (b) obtained for binary H_2-CO_2 breakthrough curve (run 3) at 298 K and 1.5 bar on activated carbon AC5-KS; Mixture: 20% of CO_2 balanced with H_2; Temperatures measured at 0.050 m (Bottom (■,——)), 0.159 m (Middle (◆,——)) and 0.271 m (Top (▲,——)) from feed inlet; Flow rate of 8.33×10^{-5} m^3 s^{-1} (measured at 298 K and 1 bar); Experimental data (symbols); Simulation (lines).

solid lines.

In all the breakthrough experiments, the bed was initially filled with helium. Figure 6.10 shows a very fast breakthrough of hydrogen due to the small adsorption capacity of H_2 in the activated carbon. Besides, a slight decrease of the hydrogen flow rate can be observed when carbon dioxide breaks through the column. This effect is normally termed as “roll-up” of the less-adsorbed

Table 6.3: Transport parameters applied in the simulations of the fixed-bed experiments using a column packed with the activated carbon AC5-KS.

Run		Binary (H_2-CO_2) breakthrough experiments		
		1	2	3
$D_{ax} \times 10^5$[m^2 s^{-1}]		1.37	4.22	22.3
λ [J s^{-1} m^{-1} K^{-1}]		0.733	0.936	1.249
$k_f \times 10^2$ [m s^{-1}]		1.69	2.81	11.03
h_f [J s^{-1} m^{-2} K^{-1}]		123	203	275
h_w [J s^{-1} m^{-2} K^{-1}]		80	80	80
U [J s^{-1} m^{-2} K^{-1}]		22	22	22
$D_p \times 10^6$ [m^2 s^{-1}]$^{\#}$	H_2	6.40	6.40	21.3
	CO_2	6.40	6.40	21.3
D_c^0/r_c^2 [s^{-1}] ;	H_2	46.35 ;	8.51	
E_a [kJ mol^{-1}]	CO_2	35.64 ;	17.6	

$^{\#}$ values at inlet conditions

compound. In the case of CO_2, the non-linearity of the isotherm contributes for an initial sharpness of the breakthroughs (more pronounced at lower velocities). The curve gets dispersed due to the intra-particle resistance (micropore resistance controls the diffusion mechanism within the extrudates) and also heat transfer. Moreover, calculating the time constants of all the mass transfer resistances, it was noted that the axial dispersion contribution is around 30%, which also contributes to the dispersed concentration profile at the exit of the column.

Figure 6.11 and Figure 6.12 show breakthrough curves performed at higher velocities. It can be observed how curves get dispersed when feed velocity increases. The reason for that is less time is allowed for gas-solid contact, increasing the importance of transport resistances. Changing the gas velocity within the column, the controlling mechanism for diffusion can also modify. As previously mentioned, operating at low velocity (run 1, Table 6.1) the controlling mechanism for diffusion is within the micropores, with 30% contribution of axial dispersion. When the feed velocity increases, the axial dispersion coefficient increases, however its overall importance becomes less relevant when compared to intra-particle diffusion (micropores). The ratio of time constants of convection ($\varepsilon L/u_0$) and axial dispersion (L^2/D_{ax}) is proportional to $c_1 + c_2 u_0^{-1}$; the ratio of time constants for convection and film mass transfer (R_p/k_f) is proportional to $c_3 u_0^{-0.4} + c_4 u_0^{-1}$; the ratio of time constants for convection and micropore diffusion (r_c^2/D_c) [or macropore diffusion (R_p^2/D_p)] is proportional to u_0^{-1} (c_1 to c_4 are constants). This indicates that, when gas velocity

increases, intra-particle resistances become more important to mass transfer within the column. Consequently, the influence of 30% of axial dispersion in the first breakthrough curve drops to 2% in the last one at higher velocity. Furthermore, increasing the flow rate, the CO_2 heat of adsorption is released at a faster rate and less time is allowed to exchange heat with the surroundings; thus, the thermal effects become stronger. The stronger thermal increase due to higher velocity can be observed comparing Figure 6.10 b and Figure 6.11.

A good agreement was observed between the experimental data and the predicted molar flow rate history at the end of the column and temperature evolution for all the binary breakthrough curves.

Since the mathematical model could predict the experimental data, it is possible to understand the behaviour of the system by the simulated results. Figure 6.13 to Figure 6.15 show the CO_2 gas phase concentration histories at the outlet (bed packed with AC5-KS) for the binary H_2-CO_2 breakthrough experimental runs 1, 2 and 3, respectively. According to the results obtained for the different binary breakthrough curves, it can be concluded that the film heat transfer coefficient between the gas phase and particle in the three experiments do not kinetically affect the process.

In addition, Figure 6.13 b to Figure 6.15 b report the temperature histories at three different points of the column (0.050, 0.159 and 0.271 m from feed inlet) for the binary breakthrough experimental runs 1 to 3, respectively. In the experiments carried out at high velocities, the breakthrough is fast and does not provide enough time to exchange heat with the surroundings and thus for these experiments, the thermal effects are more important. It should be noted that for extremely fast cycles, the process should operate close to adiabatic conditions.

Moreover, Figure 6.13 to Figure 6.15 show the adsorbed phase concentration profiles of carbon dioxide at breakthrough time (when $C_g(CO_2) > 1 \times 10^{-4}$ mol m^{-3}) and at equilibrium for the same binary breakthrough experiments. Figure 6.13 c, Figure 6.14 c and Figure 6.15 c show that, when CO_2 starts to break through the column, only in the experiment with the lower superficial velocity (0.007 m s^{-1}) the adsorption equilibrium of CO_2 in the initial partition of the bed was reached. In the other binary breakthrough runs (2 and 3, where the superficial velocities were 0.029 and 0.161 m s^{-1}, respectively) the initial partition of the bed did not reached the equilibrium when the CO_2 brakes through the column (see Figure 6.14 and Figure 6.15). Even after a certain time, the CO_2 amount that breaks trhough the bed reaches significant amounts and still the initial partition of the column is not in equilibrium. It can be said that in those experiments, the mass transfer zone is larger than the column length. The utilization of the adsorbent for these different velocities can also

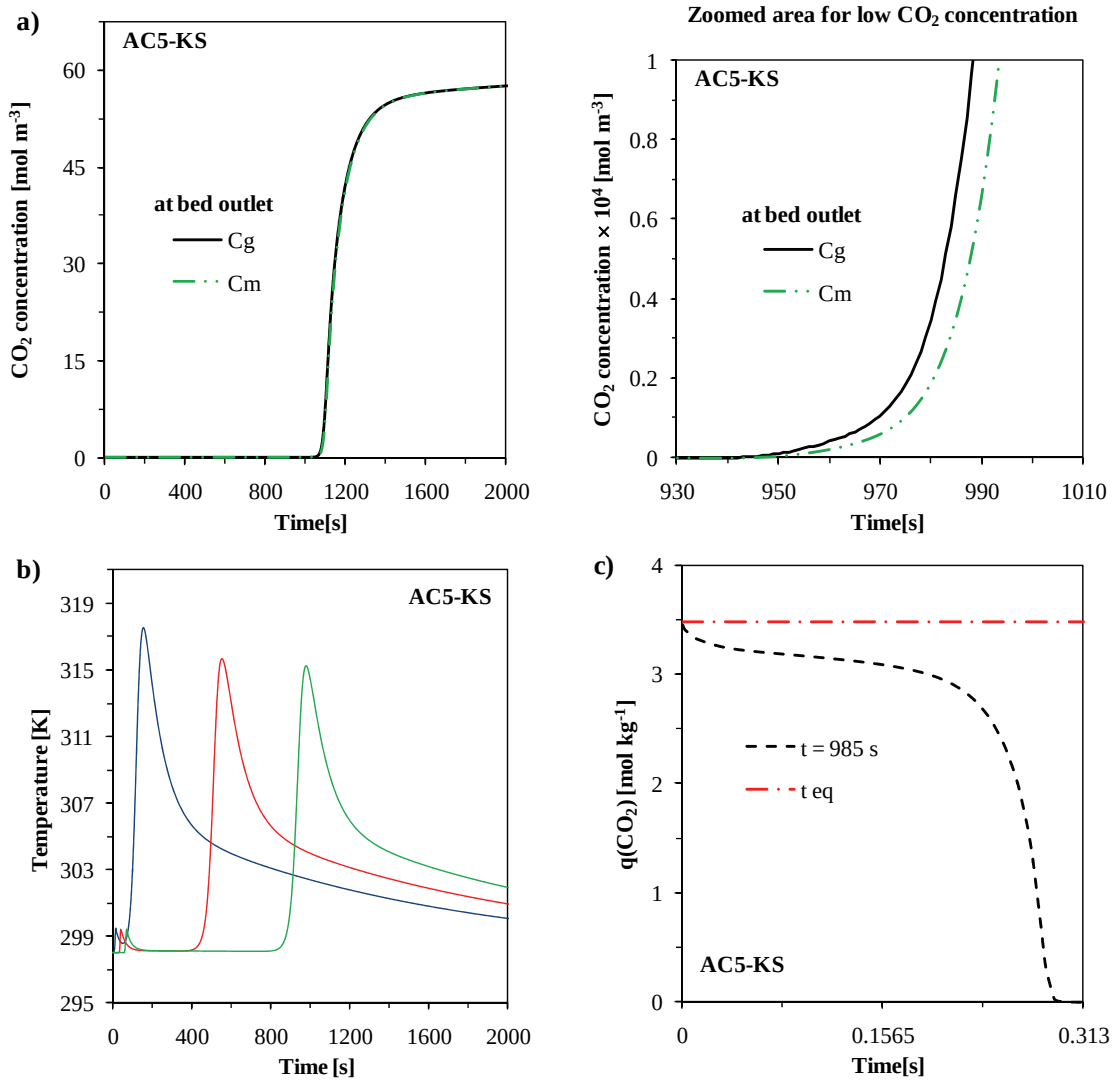


Figure 6.13: a) CO_2 gas phase concentration histories (——) and CO_2 concentration in the macropores (—·—) at the bed outlet; b) Temperature histories at 0.050 m (Bottom (——)), 0.159 m (Middle (——)) and 0.271 m (Top (——)) from feed inlet; c) Adsorbed phase concentration profiles of CO_2 at breakthrough time (----) [$C_g(CO_2) > 1 \times 10^{-4}$ mol m^{-3}] and at equilibrium (—·—); Results for the binary breakthrough experimental run 1; Column packed with AC5-KS; Mixture: 30% of CO_2 balanced with H_2; Pressure of 5 bar, temperature of 298 K and flow rate of 1.167×10^{-5} m^3 s^{-1} (measured at 298 K and 1 bar).

be observed in Figure 6.16 where CO_2 concentration profiles are displayed at the time of CO_2 breakthrough. When higher feed flow rates are employed, the decrease of contact time between gas and solid phases result in more dispersed curves enhancing the mass transfer zone and reducing the

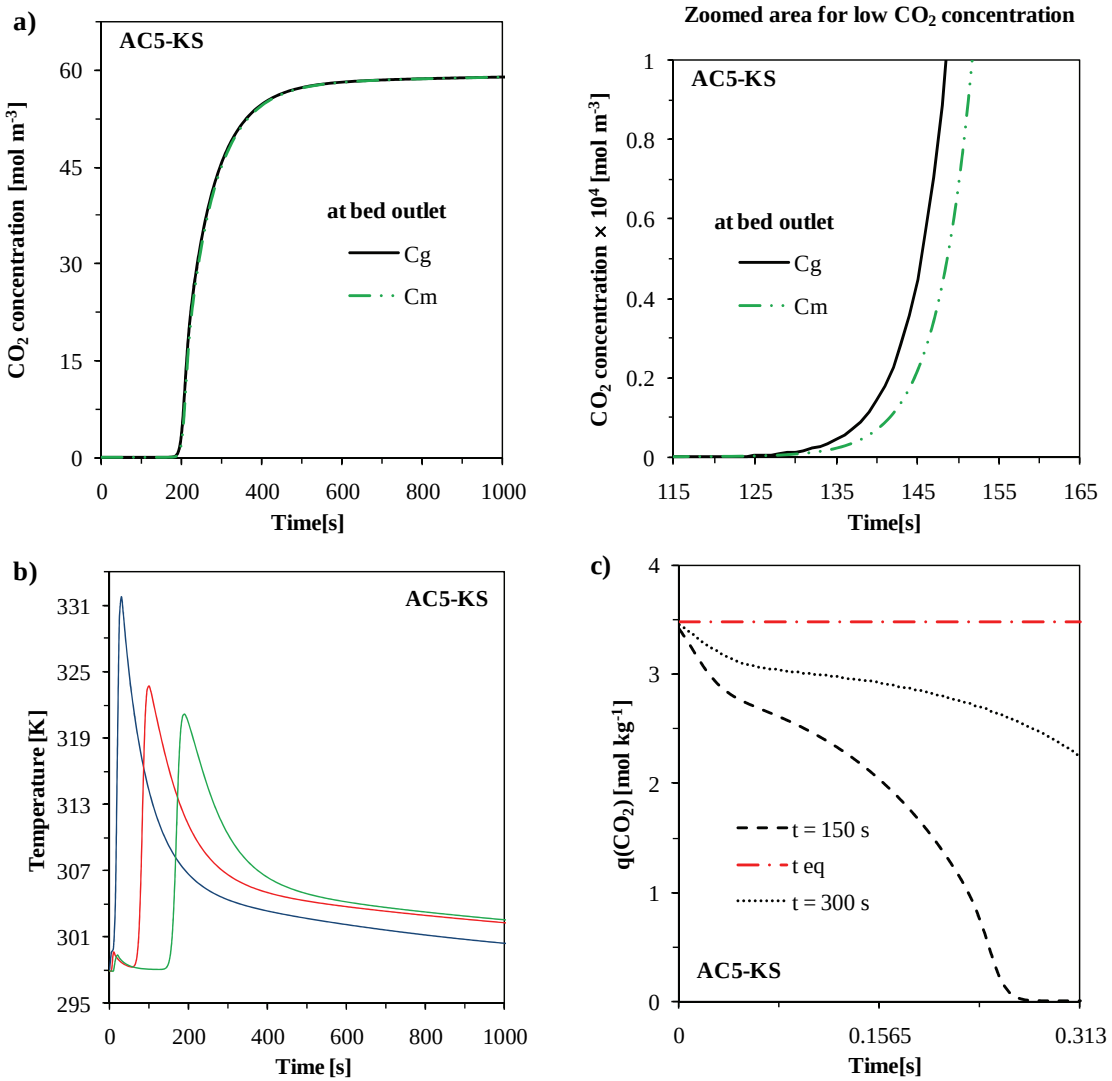


Figure 6.14: a) CO_2 gas phase concentration histories (——) and CO_2 concentration in the macropores (—·· ·—) at the bed outlet; b) Temperature histories at 0.050 m (Bottom (——)), 0.159 m (Middle (——)) and 0.271 m (Top (——)) from feed inlet; c) Adsorbed phase concentration profiles of CO_2 at breakthrough time (----) [$C_g(CO_2) > 1 \times 10^{-4}$ mol m^{-3}] and at equilibrium (—·—); Results for the binary breakthrough experimental run 2; Column packed with AC5-KS; Mixture: 30% of CO_2 balanced with H_2; Pressure of 5 bar, temperature of 298 K and flow rate of 5.00×10^{-5} m^3 s^{-1} (measured at 298 K and 1 bar).

utilization of the adsorbent. The lower values of adsorption loading before breakthrough are also influenced by stronger thermal effects: temperature of the bed is higher before CO_2 breakthrough reducing its loading even more. These results indicate that the important enhancement of

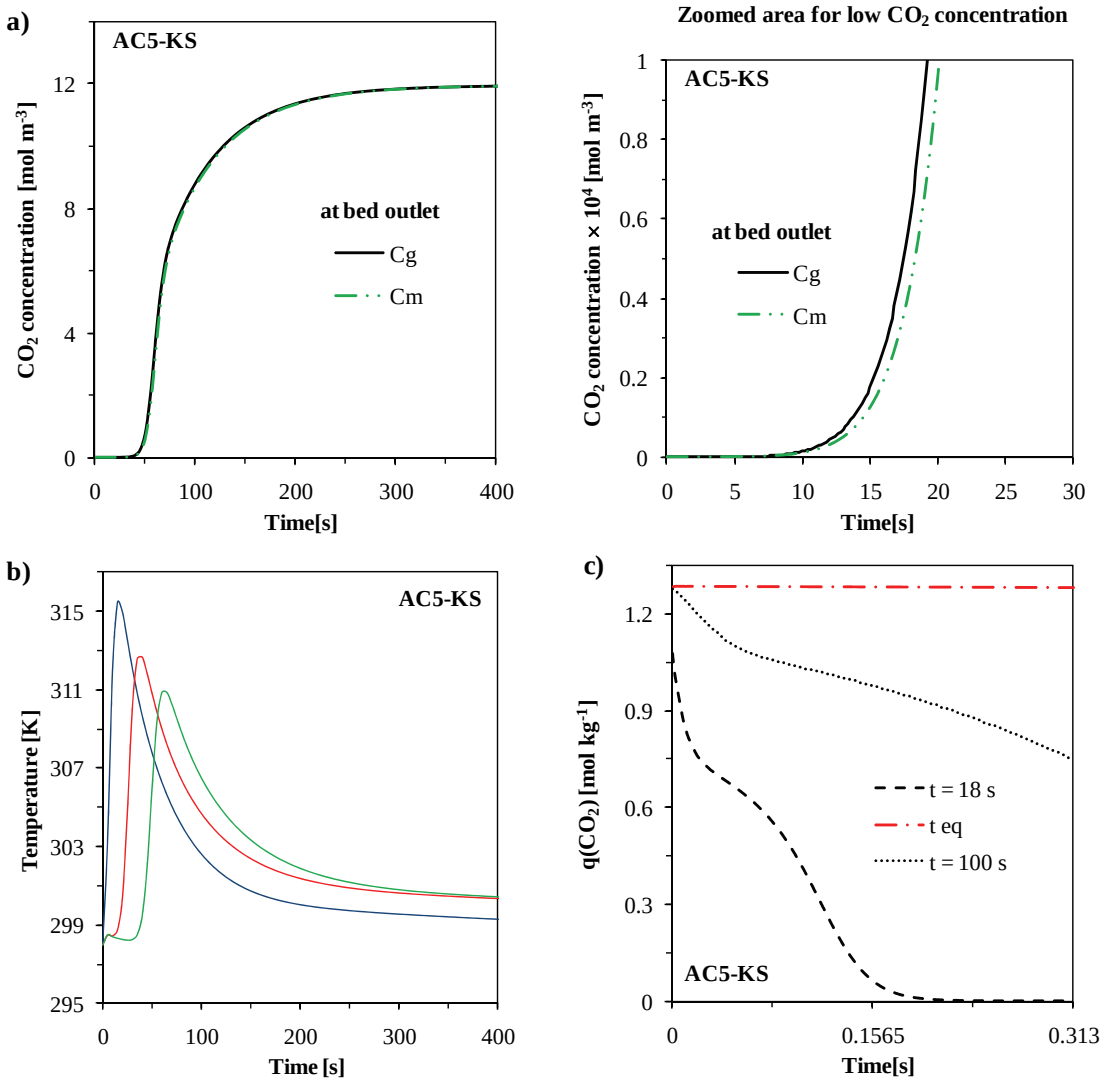


Figure 6.15: a) CO_2 gas phase concentration histories (——) and CO_2 concentration in the macropores (—·—) at the bed outlet; b) Temperature histories at 0.050 m (Bottom (——)), 0.159 m (Middle (——)) and 0.271 m (Top (——)) from feed inlet; c) Adsorbed phase concentration profiles of CO_2 at breakthrough time (----) [$C_g(CO_2) > 1 \times 10^{-4}$ mol m^{-3}] and at equilibrium (—·—); Results for the binary breakthrough experimental run 3; Column packed with AC5-KS; Mixture: 20% of CO_2 balanced with H_2; Pressure of 1.5 bar, temperature of 298 K and flow rate of 8.33×10^{-5} m^3 s^{-1} (measured at 298 K and 1 bar).

productivity due to time reductions is counter-balanced by a significant increase in the mass transfer zone, reducing the effective utilization of the column.

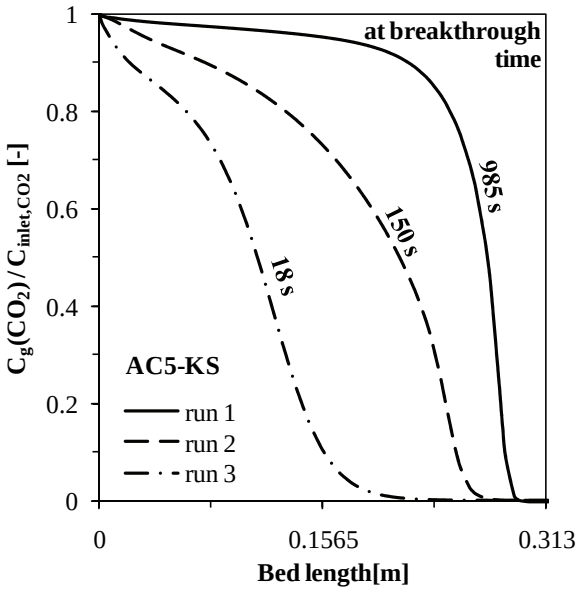


Figure 6.16: Normalized gas phase concentration profiles of CO_2 at breakthrough time [$C_g(CO_2) > 1 \times 10^{-4}$ mol m^{-3}] for each breakthrough run: 1 (──), 2 (─ ─) and 3 (─ · ─).

6.6.2 RPSA experiment

The binary breakthrough experiments reported in the previous section were carried out increasing the superficial velocity at the inlet of the column until the experimental limits of the RPSA unit. Once that the mathematical model could predict the behaviour of the column, a RPSA experiment was carried out in order to verify if the cyclic state can also be well described, validating the model for further simulations. The RPSA experiment was performed using a single column packed with AC5-KS (the same employed in the breakthrough experiments) and applying the cycle scheduling illustrated in Figure 6.8 (see section 6.4). For this experiment, a feed composition of 83% of H_2 and 17% of CO_2 was used with a total feed flow rate of 5.00×10^{-5} m^3 s^{-1} (measured at 298 K and 1 bar). The experimental run was performed at 298 K. A feed step pressure (P_{high}) and a purge step pressure (P_{low}) fixed at 3 and 0.3 bar, respectively, were employed to work with the same P_{high}/P_{low} ratio (P_{high}/P_{low} = 10) as employed in the PSA experiment studied in chapter 5. Since the operational condition limits of pressure of the RPSA unit are 0.1-5 bar, the experiments could also have been performed at 0.5-5 bar (P_{low}-P_{high}). However, after performing simulation tests, it was observed that the hydrogen recoveries obtained for the process were lower than 50%. Operating with this pressure range, higher purge step times were needed to successfully regenerate the column, reason why pressure swing was changed to 0.3-3 bar.

In this single-column experiment, before the blowdown step, a co-current depressurization step was performed. During this depressurisation step, the column released an H_2 enriched gas stream until an intermediate pressure of 1 bar (P_{inter}). Applying this step in the RPSA cyclic sequence, the hydrogen recovery of the overall process is improved. Then a blowdown step was performed with vacuum until reaching 0.3 bar of pressure (P_{low}). The operating conditions of the RPSA experiment were reported in Table 6.2 from section 6.5.2. The mathematical model described in section 6.4 and originally reported in chapter 5 was used for the simulation of this experimental RPSA process. The transport parameters required in the mathematical model for the simulation of the RPSA process were summarized in Table 6.4.

Table 6.4: Transport parameters applied in the simulation of the RPSA process using a single column packed with the activated carbon AC5-KS.

RPSA experiment					
$D_{ax} \times 10^5$[m^2 s^{-1}]	7.03	h_f [J s^{-1} m^{-2} K^{-1}]			230
λ [J s^{-1} m^{-1} K^{-1}]	1.125	h_w [J s^{-1} m^{-2} K^{-1}]			80
$k_f \times 10^2$ [m s^{-1}]	4.37	U [J s^{-1} m^{-2} K^{-1}]			22
$D_p \times 10^5$ [m^2 s^{-1}]$^{\#}$		H_2	1.07		
		CO_2	1.07		
D_c^0/r_c^2 [s^{-1}] ; E_a [kJ mol^{-1}]		H_2	46.35	;	8.51
		CO_2	35.64	;	17.6

$^{\#}$ values at inlet conditions

The pressure history for the first cycle and also the temperature histories from cycle 1 until cycle 30 (measured at 0.050 (TT_{Bottom}), 0.159 (TT_{Middle}) and 0.271 m (TT_{Top}) from the feed inlet) are reported in Figure 6.17. The hydrogen and carbon dioxide molar flow rate histories obtained for cycles 1 and 2 and also cycles 60 and 250 at bed outlet were reported in Figure 6.18 and Figure 6.19, respectively. According to the experimental data obtained for the temperature histories in Figure 6.19, no variations in the recorded variables were observed after 60 cycles, suggesting that the cyclic steady state (CSS) was reached. However, the simulations confirmed that the CSS was only attained after approximately 250 cycles when the adsorbed phase concentration of carbon dioxide in the column was the same for two consecutive cycles. In fact, after the stabilization of temperatures within the column (after 25 cycles), the changes in the other variables are very small. However, since the purity of hydrogen is extremely high, even very small changes should be

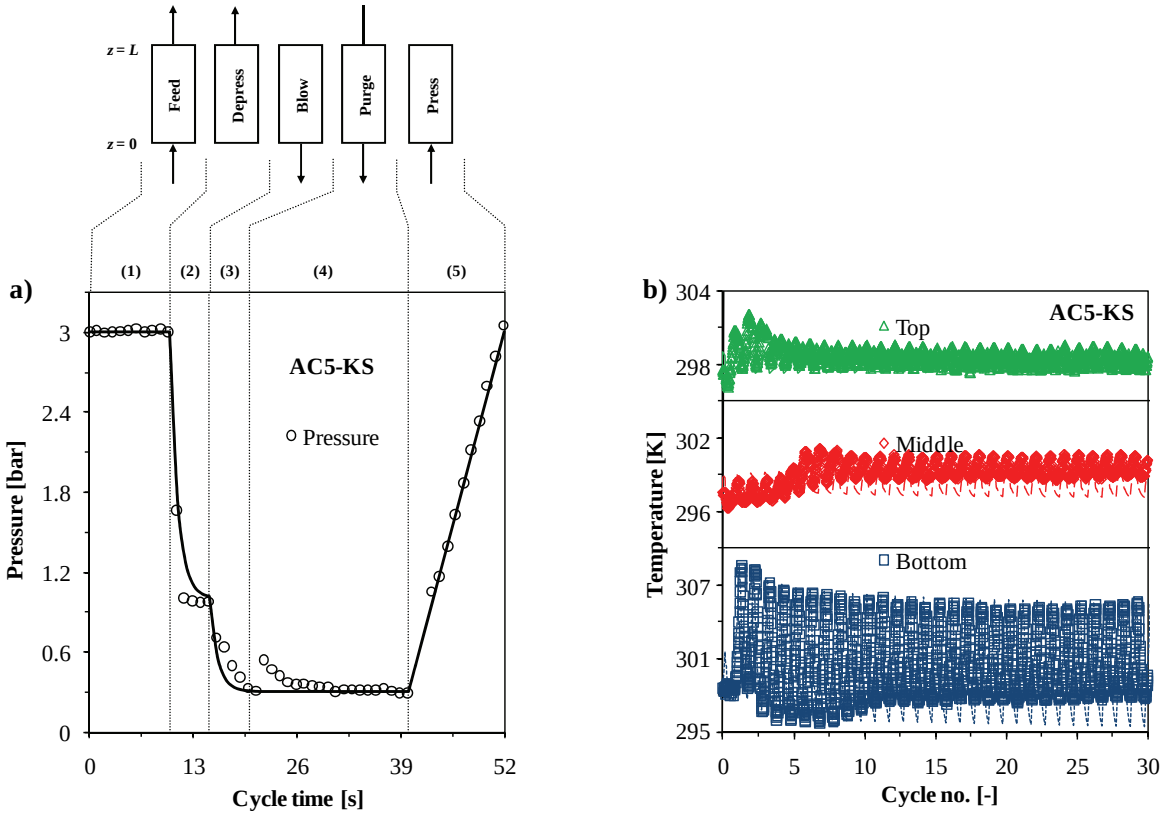


Figure 6.17: Pressure (a; ○,——) and temperature (b) histories; Cycle sequence: (1) co-current feed step, (2) co-current depressurization step, (3) counter-current blowdown step, (4) counter-current purge step with hydrogen, (5) co-current pressurization step with feed; Temperatures measured at 0.050 (Bottom (□,----)), 0.159 (Middle (◇,— —)) and 0.271 m (Top (△,——)) from feed inlet; Adsorbent: AC5-KS; Experimental data (symbols); Simulation (lines).

considered important to define CSS of this process.

In the four cycles reported in Figure 6.18 and Figure 6.19, a good agreement between the simulated results and the experimental molar flow rates was observed. A significant amount of hydrogen was released from the column in the depressurization step. Since this amount of hydrogen can be re-used (e.g., in the purge step), it was accounted in the hydrogen recovery of the process. The mathematical model predicted the experimental temperature inside the column at three different points along the bed with a reasonable agreement. The maximum deviations were observed for the thermocouple placed at 0.050 m from feed inlet (TT_{Bottom}) and these values were around 2 K. This thermocouple was placed in the initial portion of the column. As it was possible to observe in the figures, it was in this part of the column where the larger amounts of CO_2 are adsorbed, originating the largest temperature variations. For the other thermocouples (TT_{Middle} and TT_{Top}), the average of the temperature variations was around 2-3 K and deviations of the predicted

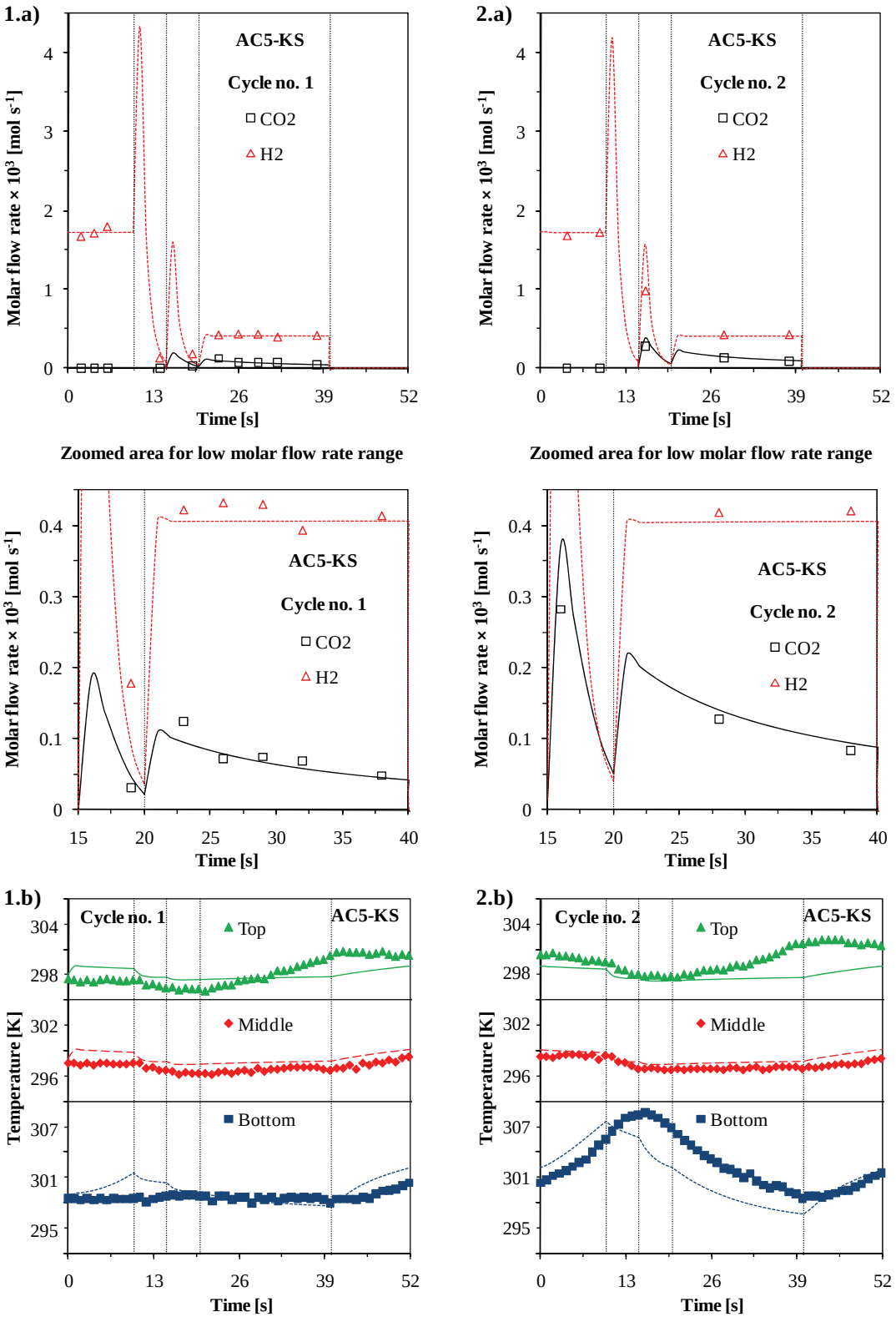


Figure 6.18: H_2 (△,----) and CO_2 (□,——) molar flow rate histories (a) obtained for cycle 1 (1) and 2 (2) at the outlet of a bed packed with AC5-KS; Temperature histories (b) measured for cycle 1 (1) and 2 (2) at 0.050 m (Bottom (■,----)), 0.159 m (Middle (◆,– –)) and 0.271 m (Top (▲,——)) from feed inlet; Flow rate of 5.00×10^{-5} m^3 s^{-1} (measured at 298 K and 1 bar); Experimental data (symbols); Simulation (lines).

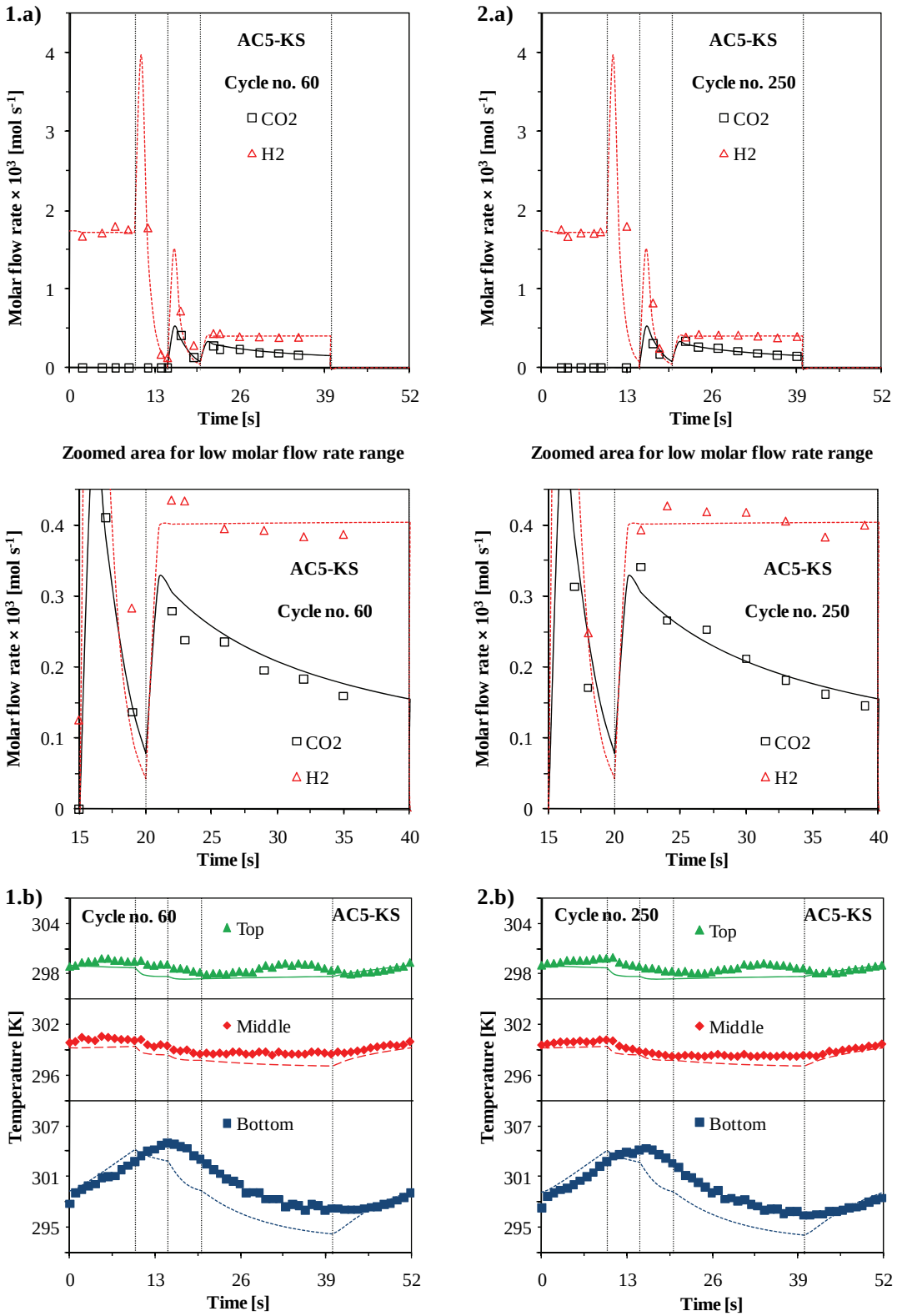


Figure 6.19: H_2 (△,----) and CO_2 (□,——) molar flow rate histories (a) obtained for cycle 60 (1) and 250 (2) at the outlet of a bed packed with AC5-KS; Temperature histories (b) measured for cycle 60 (1) and 250 (2) at 0.050 m (Bottom (■,----)), 0.159 m (Middle (◆,– –)) and 0.271 m (Top (▲,——)) from feed inlet; Flow rate of 5.00×10^{-5} m^3 s^{-1} (measured at 298 K and 1 bar); Experimental data (symbols); Simulation (lines).

temperatures were smaller than 1 K. A correct description of the observed variations in the thermocouples is crucial for this operation. These variables are continuously recorded (at least 1 point per second) in all cycles while measurement of gas concentration is not continuous due to the time delay of each GC analysis.

The hydrogen purity and recovery and also the process productivity (equations (6.1) to (6.3) reported in section 6.4) are the parameters used for the evaluation of the performance of the RPSA process experiment. Due to the small number of experimental points, report experimental values of these performance parameters may not be very accurate. Since the simulation predicts with good accuracy the experimental results obtained, the performance parameters based on simulated results were reported. In this RPSA experiment, 61.80% of hydrogen was recovered with a purity of >99.99%.

In comparison to the PSA processes reported in chapter 5, the hydrogen recovery decreased but the productivity attained by the RPSA process was substantially improved. According to the simulation of the RPSA process experiment, a productivity of 598.8 $mol_{H2}\ kg_{ads}^{-1}\ day^{-1}$ was attained. This means that a productivity improvement of 600% was reached when compared to the best productivity result obtained through the simulations of the PSA process reported in chapter 5.

There was a successful prediction of the mathematical model under RPSA conditions tested in this work with total cycle time slightly smaller than one minute. However it should be mentioned that, for very fast cycling processes (cycle times smaller than 20 s), several limitations may occur. Besides mass transfer limitations due to large intra particle resistances, instantaneous thermal equilibrium between the gas and the adsorbent inside an adsorber may not be valid: the thermal film mass transfer resistance cannot be neglected [17].

6.6.3 RPSA simulations

Considering that the mathematical model could successfully describe the RPSA experiment, several simulations were carried out to understand the effect of different operating variables of this process. The cycle sequence described in Figure 6.8 was employed in all the simulations. A single column packed with the activated carbon AC5-KS was considered in the simulations. The column was initially pressurized at 3 bar with hydrogen. In all the simulations, a binary mixture of 83% of hydrogen and 17% of carbon dioxide fed the column at 298 K and 3 bar of pressure, with a flow rate of $5.00 \times 10^{-5}\ m^3\ s^{-1}$, measured at 298 K and 1 bar. For these simulations, a column with the same properties as in the experimental set-up was used (the details

of the properties of the column are summarized in section 6.5, Table 6.1). The operation conditions used in the simulations are described in Table 6.5. In this table, the performance parameters of each simulation (in the CSS), are also reported.

Table 6.5: Performance parameters for the H_2 RPSA simulations using a bed packed with AC5-KS.

Simulation	t_{Feed} [s]	t_{Purge} [s]	H_2 Pur. [%]	H_2 Rec. [%]	Productivity [$mol_{H2}\ kg_{ads}^{-1}\ day^{-1}$]
1[a]	5	15	99.81309	69.70	584.1
2[a]	5	20	99.96877	65.13	469.9
3[a]	5	30	99.99825	55.88	358.6
4[a]	6	30	99.99719	59.10	400.8
5[a]	7	30	99.99555	61.89	441.3
6[a]	8	30	99.99304	64.35	480.4
7[b]	8	30	99.99983	41.99	317.4
8[b]	8	20	99.99671	56.88	511.0
9[b]	10	20	99.99280	61.80	598.8

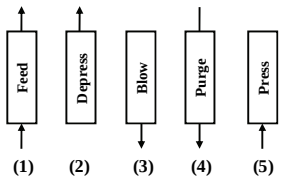
$t_{Depress}$ = 5 s ; t_{Blow} = 5 s ; t_{Press} = 12 s

P_{high} = 3 bar ; P_{inter} = 1 bar; P_{low} = 0.3 bar

a) Purge/Feed ratio = 0.1 ; b) Purge/Feed ratio = 0.2

Feed: y_{H2} = 0.83 ; y_{CO2} = 0.17; T = 298 K ; P = 3 bar; $Q = 5.00 \times 10^{-5}\ m^3 \cdot s^{-1}$ *

Cycle



* measured at 298 K and 1 bar

The transport parameters previously reported in Table 6.4 (section 6.6.2) were employed in the mathematical model for the simulation of the RPSA process.

First, the effect of the purge step time in the process performance was tested for a cycle sequence with 12 s of co-current pressurization with feed and 5 s for each of the other steps (feed, co-current depressurization and counter-current blowdown). Three different purge times were considered: 15, 20 and 30 s (simulations 1, 2 and 3, respectively). According to the results reported in Table 6.5 it can be observed that a significant increase in the hydrogen purity of the product stream can be attained when the purge time is increased. However, since the amount of hydrogen

used in the purge increased, there is a significant reduction of the hydrogen recovery and process productivity. To increase the H_2 recovery, small increases of 1 s in the feed step time were tested (simulations 4 to 6), keeping constant the other step times and operating parameters. It was observed that, even when the feed step time was increased 60%, up to 8 s (simulation 6), the hydrogen purity of the product stream remained higher than 99.99%, decreasing only 0.004%. Nevertheless, both the hydrogen recovery and process productivity appreciably increased: more 5% of H_2 recovery and an increase of 20% for the productivity of the process.

The influence of the purge/feed ratio in the RPSA process performance was also studied. For the simulations 1 to 6 reported in Table 6.5, a purge/feed ratio of 0.1 was applied. Considering the same step pressures times of simulation 6, the purge/feed ratio was doubled (simulation 7, Table 6.5); the volumetric purge flow rate was doubled. As expected, the regeneration of the column was more efficient and thus the hydrogen purity increased from 99.99304 to 99.99983%. On the other hand, the hydrogen recovery and process productivity attained in this process were lower due to the higher amount of hydrogen used during the purge step. In order to increase these performance parameters and without significantly affecting the hydrogen purity, the cycle time was reduced by the decrease of the purge step time (simulation 8). It was observed an improvement of 61% in the productivity of the process and the hydrogen recovery increased from 41.99 to 56.88%. Since the hydrogen purity was still above 99.99%, another simulation (simulation 9) was performed to improve hydrogen recovery and process productivity. For that, a feed step time of 10 s was used without changing any other operating parameter and step times of simulation 8. It was verified that the hydrogen purity was not significantly affected but the hydrogen recovery and the productivity of the process increased 5 and 17%, respectively.

After these initial simulations, more operating variables were modified in order to get more insights of the RPSA process operation to separate this binary mixture. The results obtained are shown in Figure 6.20 to Figure 6.22.

The effect of different feed flow rates considering constant the other parameters (the parameters used were the same of simulation 9) is shown in Figure 6.20. Increasing the feed flow rate, the hydrogen purity decreased to values lower than 99.9%; unsustainable high amounts of CO_2 are fed to the column and cannot be purged at the same rate, contaminating the product. On the oher side, an increase of 45.5% on the H_2 recovery can be observed when the feed flow rate was increased from 1.67×10^{-5} to 1.67×10^{-4} $m^3\ s^{-1}$ (measured at 298 K and 1 bar). Furthermore, due to the increase of recovery (and also because the amount of hydrogen in the purge remained constant) the process productivity raised 7.7 times, up to 1845 $mol_{H2}\ kg_{ads}^{-1}\ day^{-1}$. High purity

hydrogen (purity >99.99%) could be obtained only with the smaller feed flow rate. Increasing the feed flow rate, the CO_2 concentration front advanced too deep in the column and could not be efficiently regenerated with the purge employed. It should be remembered that the hydrogen purity used as target is extremely high reason why the bulk of CO_2 adsorption is carried out only in the initial portion of the column.

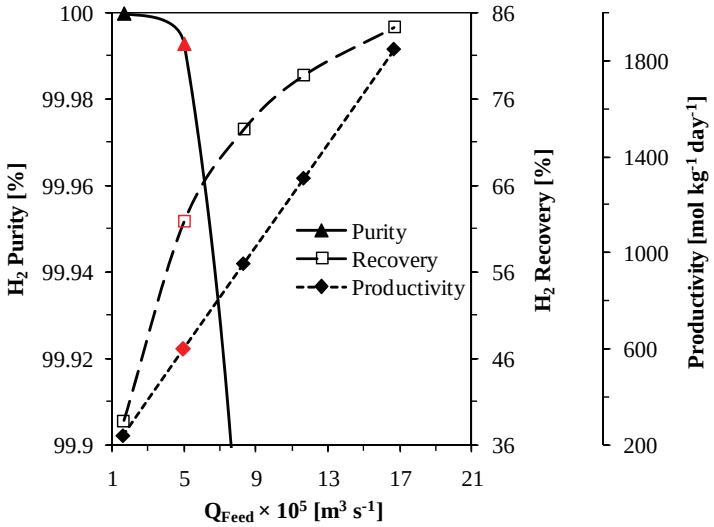


Figure 6.20: Hydrogen purity, hydrogen recovery and process productivity for different feed flow rates using the same parameters described in simulation 9; Simulation of the RPSA adsorption process using a single adsorbent bed packed with AC5-KS; Red symbols (RPSA simulation 9).

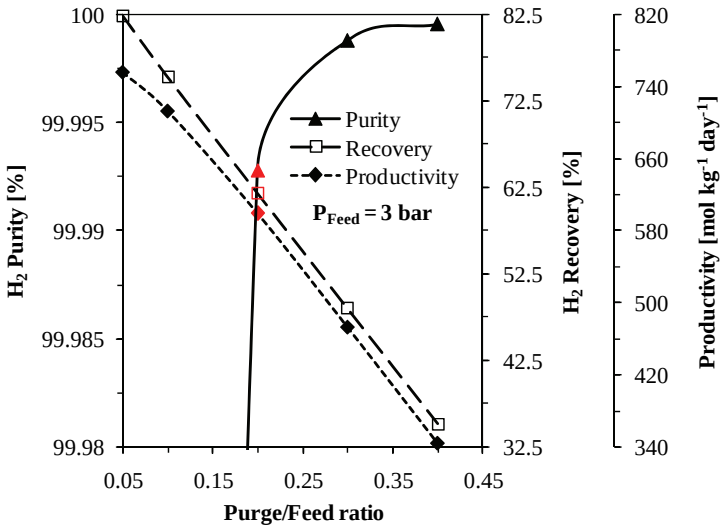


Figure 6.21: Hydrogen purity, hydrogen recovery and process productivity for different purge/feed ratios using the same parameters described in simulation 9; Simulation of the RPSA adsorption process using a single adsorbent bed packed with AC5-KS; Red symbols (RPSA simulation 9).

Figure 6.21 shows the influence of the purge/feed ratio in the RPSA performance. Increasing the superficial velocity inside the column during the purge step, the amount of hydrogen used in the regeneration of the column increases. Thus, the purity of the hydrogen stream produced is significantly enhanced (>99.999%) while the H_2 recovery and process productivity decreases (see Figure 6.21). On the other hand, when the purge/feed ratio was reduced, the hydrogen purity considerably dropped to values lower than 99.8% followed by an increase of both recovery and productivity. It can be seen that, after a certain point (Purge/Feed ratio higher than 0.3), increasing the amount of hydrogen to purge the column results in very small changes in hydrogen purity.

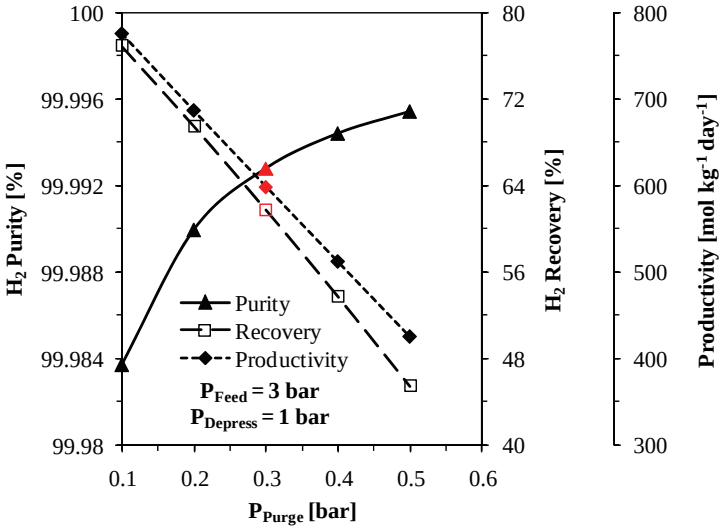


Figure 6.22: Hydrogen purity, hydrogen recovery and process productivity for different purge pressures using the same parameters described in simulation 9; Simulation of the RPSA adsorption process using a single adsorbent bed packed with AC5-KS; Red symbols (RPSA simulation 9).

The effect of the purge pressure in the RPSA performance is shown in Figure 6.22. In this case, the effect of the purge pressure was studied considering also that the superficial velocity inside the column (keeping constants all other conditions as in simulation 9). Since the purge pressure was changed, to keep constant the inlet purge flow rate, the superficial velocity was also changed and this image shows a combination between the effect of pressure but also the effect of purge flow rate. In fact, reducing the pressure of the purge step, it was expectable to achieve higher productivities because of a "deeper" regeneration. However it was observed that for smaller purge pressures, the H_2 purity decreases. Even when more CO_2 can be removed in the blowdown step, the amount of hydrogen employed in the purge was not sufficient to displace the adsorbed CO_2,

contaminating the product. This trend is overcame at higher purge pressures, when more hydrogen is used in the purge, effectively displacing CO_2 from the adsorbent. However, the larger amounts of hydrogen employed at higher purge pressures result in a net decrease of hydrogen recovery (and thus process productivity).

According to the results obtained, it was observed that the amount of gas employed in the purge step is very important to regulate the purity of the hydrogen obtained as product. In the simulations carried out in this work, to attain a H_2 purity of 99.99%, the optimum purge/feed ratio is 0.187, obtaining a H_2 recovery of 63.54% and a productivity of the process of 615.2 mol_{H2} kg_{ads}^{-1} day^{-1}.

After determining the effect of several operating variables in RPSA process for H_2-CO_2 separation, it can be mentioned that there is a great potential to use this technology in hydrogen purification, also perhaps combining this operation mode with other process (either PSA, membranes or absorption) to effectively reduce the size of a purification plant and increase the hydrogen recovery.

6.7 Conclusions

In this chapter, an introductory research work of fast cycling pressure swing adsorption process was performed. Initial insights of this technology were assessed by focusing on a binary mixture of H_2-CO_2. The experimental unit used was a “compact” PSA equipment and it was necessary to “adapt” the facility for RPSA processes. Initially it was necessary to analyse the adequacy of the electronic equipment (e.g., mass flow controllers, flow meter, back-pressure regulator and pressure transducer) to be used in fast cycling, observing the time needed for the stabilization of the signal as well as the signal oscillations. After that it was concluded that it was possible to reduce the cycling time to values around one minute.

Binary breakthrough experiments of hydrogen and carbon dioxide were performed at different operating conditions in the activated carbon AC5-KS (the modified activated carbon developed within this thesis and reported in chapter 4). The breakthroughs were used to verify the possibility of occurring dispersive effects that may affect the RPSA process. For that, the breakthrough experimental runs were performed in the operational condition limits of feed flow rate (from 1.167×10^{-5} to 8.33×10^{-5} m^3 s^{-1}, measured at 298 K and 1 bar). It was concluded that, for higher feed flow rates, the axial dispersion contribution to the mass-transfer mechanism drops, becoming more relevant the contribution of the micropore resistance due to a smaller contact time

between gas and solid phases. It was also observed that operating at higher flow rates, the thermal effects are more important since less time is provided to exchange heat with the surroundings.

In addition, a single-column RPSA process experiment was performed, using the bed packed with AC5-KS (the same bed as for the breakthrough experiments). The cyclic sequence applied in this experiment comprised a co-current feed, co-current depressurization, counter-current blowdown, counter-current purge and finally a co-current pressurization with feed. The mathematical model previously used within this work could satisfactorily predict the cyclic performance of the unit. In this experiment, hydrogen recovery of 61.8% was obtained with a purity of 99.99280% (simulated value). The RPSA unit productivity was 598.8 $mol_{H2}\ kg_{ads}^{-1}\ day^{-1}$.

Finally, RPSA simulations were carried out for different step times and streams flow rates in order to understand the influence of each step in the overall process performance. It was concluded that the unit productivity of the RPSA process could increase around 600% (when compared to classical PSA) without affecting the product purity and reducing no more than 11% in the amount of hydrogen recovered. This study showed that RPSA may provide a valuable advance as a H_2 purification technique, both for small and large H_2 plants. In larger plants, the combination of RPSA with other separation technique can also improve further the H_2 recovery keeping small the overall size of the plant.

6.8 Notation

Nomenclature

c_1, c_2, c_3, c_4	constants
C	concentration (mol m^{-3})
$C_{g,i}$	component *i* gas phase concentration (mol m^{-3})
$C_{m,i}$	concentration of component *i* in the macropores (mol m^{-3})
D_{ax}	axial dispersion coefficient (m^2 s^{-1})
D_c^0	limiting diffusivity at infinite temperature (m^2 s^{-1})
D_p	macropore diffusivity (m^2 s^{-1})
E_a	activation energy of micropore/crystal diffusion (kJ mol^{-1})
h_f	film heat transfer coefficient between the gas phase and particle (J s^{-1} m^{-2} K^{-1})
h_w	film heat transfer coefficient between the gas phase and wall (J s^{-1} m^{-2} K^{-1})
k_f	film mass transfer coefficient (m s^{-1})
L	column length (m)
P	pressure (bar)
Q	flow rate (m^3 s^{-1})
r_c	micropore or crystal radius (m)
t	time (s)
T	temperature (K)
u_0	superficial velocity (m s^{-1})
U	overall heat transfer coefficient (J s^{-1} m^{-2} K^{-1})
y_i	molar fraction of component *i*
z	partition of the column length L (m)

Greek letters

ε	bed porosity
λ	heat axial dispersion coefficient (J s^{-1} m^{-1} K^{-1})

6.9 References

[1] D.M. Ruthven, Past progress and future challenges in adsorption research, Industrial and Engineering Chemistry Research. 39 (2000) 2127-2131.

[2] S. Sircar, Pressure swing adsorption, Industrial and Engineering Chemistry Research. 41 (2002) 1389-1392.

[3] R.S. Todd, P.A. Webley, Mass-transfer models for rapid pressure swing adsorption simulation, AIChE Journal. 52 (2006) 3126-3145.

[4] S. Kulish, R.P. Swank, Rapid cycle pressure swing adsorption oxygen concentration method and apparatus (1998) U.S. Patent 5,827,358.

[5] S. Kulish, R.P. Swank, Rapid cycle pressure swing adsorption oxygen concentration method and apparatus (2000) U.S. Patent 6,068,680.

[6] M.J. LaBuda, T.C. Golden, R.D. Whitley, C.E. Steigerwalt, Performance stability in rapid cycle pressure swing adsorption systems (2008) European Patent Application 1,917,994 A1.

[7] M.J. LaBuda, T.C. Golden, R.D. Whitley, C.E. Steigerwalt, Performance stability in rapid cycle pressure swing adsorption systems (2008) U.S. Patent Application Publication 2008/0083331 A1.

[8] G.E. Keller II, C.-H.A. Kua, Enhanced gas separation by selective adsorption (1982) U.S. Patent 4,354,859.

[9] N. Sundaram, B.K. Kaul, E.W. Corcoran, C.Y. Sabottke, R.L. Eckes, Integration of rapid cycle pressure swing adsorption with refinery process units (hydroprocessing, hydrocracking, etc.) (2009) U.S. Patent 7,591,879 B2.

[10] N. Sundaram, B.K. Kaul, E.W. Corcoran, C.Y. Sabottke, R.L. Eckes, Integration of rapid cycle pressure swing adsorption with refinery process units (hydroprocessing, hydrocracking, etc.) (2006) U.S. Patent Application Publication 2006/0174764 A1.

[11] S. Alizadeh-Khiavi, J.A. Sawada, A.C. Gibbs, J. Alvaji, Rapid cycle syngas pressure swing adsorption system (2007) U.S. Patent Application Publication 2007/0125228 A1.

[12] B.G. Keefer, D.G. Doman, Flow regulated pressure swing adsorption system (1997) W.O. Patent 97/39821.

[13] B.G. Keefer, D.G. Doman, Flow regulated pressure swing adsorption system (2000) U.S. Patent 6,063,161.

[14] B.G. Keefer, D.G. Doman, Flow regulated pressure swing adsorption system (2004) U.S.

Reissued Patent RE38,493 E.

[15] R.L. Jones, G.E. Keller II, R.C. Wells, Rapid pressure swing adsorption process with high enrichment factor (1980) U.S. Patent 4,194,892.

[16] S. Sircar, B.F. Hanley, Production of oxygen enriched air by rapid pressure swing adsorption, Adsorption. 1 (1995) 313-320.

[17] S. Sircar, Influence of gas-solid heat transfer on rapid PSA, Adsorption. 11 (2005) 509-513.

[18] B.H.L. Betlem, R.W.M. Gotink, H. Bosch, Optimal operation of rapid pressure swing adsorption with slop recycling, Computers & Chemical Engineering: European Symposium on Computer Aided Process Engineering. 22 (1998) S633-S636.

[19] P.H. Turnock, R.H. Kadlec, Separation of nitrogen and methane via periodic adsorption, AIChE Journal. 17 (1971) 335-342.

[20] D.E. Kowler, R.H. Kadlec, The optimal control of a periodic adsorber: Part I. Experiment, AIChE Journal. 18 (1972) 1207-1212.

[21] D.E. Kowler, R.H. Kadlec, The optimal control of a periodic adsorber: Part II. Theory, AIChE Journal. 18 (1972) 1212-1219.

[22] D.E. Earls, G.N. Long, Multiple bed rapid pressure swing adsorption for oxygen (1980) U.S. Patent 4,194,891.

[23] D.E. Earls, G.N. Long, Rapid adiabatic pressure swing adsorption process and apparatus for oxygen production using multiple beds of a zeolite molecular sieve (1980) European Patent Application 0,013,680 A1.

[24] R.L. Jones, G.E. Keller II, R.C. Wells, Rapid adiabatic pressure swing adsorption process (1980) European Patent Application 0,008,619 A1.

[25] D.E. Earls, G.N. Long, Rapid adiabatic pressure swing adsorption process and apparatus for oxygen production using multiple beds of a zeolite molecular sieve (1983) European Patent 0,013,680 B1.

[26] R.L. Jones, G.E. Keller II, R.C. Wells, Rapid adiabatic pressure swing adsorption process (1984) European Patent 0,008,619 B1.

[27] R. Arvind, S. Farooq, D.M. Ruthven, Analysis of a piston PSA process for air separation, Chemical Engineering Science. 57 (2002) 419-433.

[28] S. Farooq, C. Thaeron, D.M. Ruthven, Numerical simulation of a parallel-passage piston-driven PSA unit, Separation and Purification Technology. 13 (1998) 181-193.

[29] T.J. Dangieri, R.T. Cassidy, RPSA process (1983) U.S. Patent 4,406,675.

[30] T.J. Dangieri, A.L. Beck, R.T. Cassidy, Improved adsorbent for rapid pressure swing

adsorption process (1985) European Patent Application 0,139,247 A1.

[31] T.J. Dangieri, A.L. Beck, R.T. Cassidy, Improved adsorbent for rapid pressure swing adsorption process (1985) W.O. Patent 85/001451.

[32] T.J. Dangieri, R.T. Cassidy, Enhanced performance in rapid pressure swing adsorption processing (1986) European Patent Application 0,175,804 A1.

[33] T.J. Dangieri, R.T. Cassidy, Enhanced performance in rapid pressure swing adsorption processing (1986) W.O. Patent 86/002015.

[34] S. Sircar, Gas separation by rapid pressure swing adsorption (1991) U.S. Patent 5,071,449.

[35] S. Sircar, Gas separation by rapid pressure swing adsorption (1992) European Patent Application 0,486,926 A1.

[36] S. Sircar, Gas separation by rapid pressure swing adsorption (1995) European Patent 0,486,926 B1.

[37] Z.P. Lu, J.M. Loureiro, A.E. Rodrigues, M.D. Levan, Simulation of a three-step one-column pressure swing adsorption process, AIChE Journal. 39 (1993) 1483-1496.

[38] H.C. Cheng, F.B. Hill, Separation of helium-methane mixtures by pressure swing adsorption, AIChE Journal. 31 (1985) 95-102.

[39] J. Smolarek, F.W. Leavitt, J.J. Nowobilski, V.E. Bergsten, J.H. Fassbaugh, Radial bed vaccum/pressure swing adsorber vessel (1998) U.S. Patent 5,759,242.

[40] M. Poteau, S. Eteve, Adsorber comprising annular superposed beds of adsorbent materials (1993) U.S. Patent 5,232,479.

[41] A.S.T. Chiang, M.C. Hong, Radial flow rapid pressure swing adsorption, Adsorption. 1 (1995) 153-164.

[42] W.-C. Huang, C.-T. Chou, Comparison of radial- and axial-flow rapid pressure swing adsorption processes, Industrial and Engineering Chemistry Research. 42 (2003) 1998-2006.

[43] B.G. Keefer, High frequency pressure swing adsorption (2001) U.S. Patent 6,176,897 B1.

[44] D.J. Connor, D.G. Doman, L. Jeziorowski, B.G. Keefer, B. Larisch, C. Mclean, I. Shaw, Rotary pressure swing adsorption apparatus (2002) U.S. Patent 6,406,523 B1.

[45] C.M.A. Golden, T.C. Golden, P.J. Battavio, Multilayered adsorbent system for gas separations by pressure swing adsorption (2003) U.S. Patent Application Publication 2003/0205131 A1.

[46] T.C. Golden, C.M.A. Golden, D.P. Zwilling, Self-supported structured adsorbent for gas separation (2003) U.S. Patent 6,565,627 B1.

[47] T.C. Golden, E.L. Weist, Activated carbon as sole absorbent in rapid cycle hydrogen PSA (2003) U.S. Patent 6,660,064 B2.

[48] T.C. Golden, E.L. Weist Jr, P.A. Novosat, Adsorbents for rapid cycle pressure swing adsorption processes (2008) U.S. Patent 7,404,846 B2.

[49] T.C. Golden, E.L. Weist Jr, P.A. Novosat, Adsorbents for rapid cycle pressure swing adsorption processes (2006) U.S. Patent Application Publication 2006/0236862 A1.

[50] B.G. Keefer, A. Carel, B. Sellars, I. Shaw, B. Larisch, Adsorbent laminate structures (2004) U.S. Patent 6,692,626 B2.

[51] C.W. Skarstrom, Fractionating gas mixtures by adsorption (1960) U.S. Patent 2,944,627.

[52] R. Rota, P.C. Wankat, Intensification of pressure swing adsorption processes, AIChE Journal. 36 (1990) 1299-1312.

[53] F.V.S. Lopes, C.A. Grande, A.M. Ribeiro, E.L.G. Oliveira, J.M. Loureiro, A.E. Rodrigues, Enhancing capacity of activated carbons for hydrogen production, Industrial and Engineering Chemistry Research. 48 (2009) 3978-3990.

7.

Conclusions and suggestions for future work

7.1 Conclusions

The main goal of this thesis was the improvement of the hydrogen purification process through pressure swing technology from multicomponent mixtures such as the steam reformer off-gases. The work was developed within the European Project HY2SEPS (Hybrid Hydrogen – Carbon Dioxide Separation Systems) to produce high purity hydrogen (>99.99%) integrating a carbon capture technology.

The existing commercial hydrogen purification PSA processes use layered beds with an activated carbon layer (to completely remove strongly adsorbed compounds: H_2O and CO_2 and some CH_4) followed by a zeolite layer (to remove the light components: remaining CH_4, CO and N_2) [1-13]. Since PSA is a dynamic separation process, it is important to know the rate of diffusion of the gases in the porous structure of each adsorbent used and thus to verify if the process is equilibrium or kinetically controlled [14-15]. By these reasons both adsorption equilibrium and kinetics of pure gases are fundamental information for the theoretical design of an adsorption process. Thus, adsorption equilibrium and kinetic data of the gases exiting the SMR reactor were studied on different commercial activated carbons and zeolites.

This study started with the measurements of adsorption equilibrium and kinetics of pure H_2, CO_2, CH_4, CO, N_2 and H_2O in activated carbon R2030 (Norit, Netherlands). It was observed that H_2O was the most adsorbed gas on activated carbon R2030 followed by CO_2, CH_4, CO, N_2 and

finally H_2, the less adsorbed gas. To fit the experimental data of the pure gases on this adsorbent, the Virial isotherm equation was employed [16-17]. This model showed great flexibility to predict the complete set of adsorption equilibrium data of the different gases in the whole temperature and pressure range studied. Then, adsorption kinetics of CO_2, CH_4, CO were determined by ZLC experiments. For the pure gases studied, the results obtained through ZLC indicated that diffusion within micropores was the controlling mechanism of mass transfer, showing higher diffusivity coefficients for CO_2 followed by CO and then CH_4. In addition, pulse experiments of CH_4, H_2 and CO and diluted breakthroughs of CO_2 were also performed to determine the diffusivities of these gases. According to the data obtained through pulse and breakthrough experiments, it was concluded that perturbation chromatography techniques were more accurate to determine the diffusivity coefficients since the results were more representative of the overall resistance of the activated carbon extrudates.

Afterwards, measurements of adsorption equilibrium and kinetics of pure H_2 and pure CO_2 on the activated carbon ACM-3mm (CECA, France) were performed for comparison purposes with the adsorption data on activated carbon R2030. The adsorption equilibrium data were accurately described by the multisite Langmuir model [18] in the temperature and pressure ranges studied. Since the CO_2/H_2 equilibrium selectivity on this adsorbent was lower than the selectivity shown by activated carbon R2030, adsorption equilibrium of CH_4, CO and N_2 on ACM-3mm were not performed.

Then, two more commercial adsorbents were studied: the activated carbon HY2SEPS-AC and the zeolite HY2SEPS-ZEO, both provided by an industrial partner within the framework of the European Project HY2SEPS [19]. Experiments of adsorption equilibrium of pure gases (CO_2, H_2, CH_4, CO and N_2) were performed for both activated carbon HY2SEPS-AC and zeolite HY2SEPS-ZEO. Besides these measurements, water adsorption equilibrium on activated carbon HY2SEPS-AC was studied. For the activated carbon sample, H_2O was the most adsorbed gas followed by CO_2, CH_4, CO, N_2 and finally H_2. On the other hand, the following order of adsorption (from the most adsorbed compound to the less adsorbed gas) was observed in zeolite sample: $CO_2 > CO > CH_4 > N_2 > H_2$. The multisite Langmuir model was employed to fit the experimental data of H_2, CO_2, CH_4, CO and N_2 on activated carbon HY2SEPS-AC and zeolite HY2SEPS-ZEO. It was found that this model could describe the adsorption isotherms for both adsorbents in the temperature and pressure ranges studied. Adsorption kinetic experiments of H_2, CO_2, CH_4, CO and N_2 in the activated carbon HY2SEPS-AC and zeolite HY2SEPS-ZEO were performed in the same temperature range. The results indicate that, the mechanism controlling mass transfer in all gases is

micropore diffusion in the case of the activated carbon material and crystal diffusion for the zeolite sample. It was also observed that the contributions of film and macropore mass transfer resistances to the total dispersion were very small for both adsorbents. Breakthrough experiments of water vapour were also reported for the activated carbon HY2SEPS-AC. Due to the CO_2 capacity and regenerability (as well as water tolerance) on both activated carbons R2030 and HY2SEPS-AC exhibited within this study, it was concluded that each of these materials could be employed as the first adsorbent in a layered bed configuration of a PSA process. If the zeolite HY2SEPS-ZEO is employed as a second layer, the remaining CH_4, CO and N_2 will be removed. However, it is important that all CO_2 is removed within the activated carbon layer due to the higher steepness of the CO_2 isotherms in the zeolite sample that will difficult the regeneration of the adsorbent. The conditions used in both measurements (adsorption equilibrium and kinetics) were in accordance to a H_2/CO_2 separation plant under operation [19]. However, these experiments also covered a wide range of operating conditions for a high-purity (>99.99%) H_2 PSA unit.

The following accomplishments dealt with the production and characterization of large amounts (kilogram scale) of two adsorbents with enhanced capacity toward contaminants. A modified activated carbon with enhanced capacity of carbon dioxide (most abundant impurity) and an ion exchanged zeolite with enhanced capacity toward nitrogen (the less adsorbed contaminant that firstly breaks through the column) were the two adsorbents produced [20-21]. The production of large amounts of a material with enhanced capacity toward carbon dioxide was performed by additional physical activation with CO_2 of the commercial activated carbon R2030. The operating conditions to enhance CO_2 capacity without affecting its diffusion rate were determined. The operating conditions of the protocol were adapted to produce four hundred grams per batch of the modified activated carbon (denominated AC5-KS). Adsorption equilibrium isotherms of CO_2 and also H_2, CH_4, CO and N_2 on the scale-up samples AC5-I (10 g/sample) and AC5-KS (400 g/sample) were determined for the final characterization of the modified adsorbent. Employing the Virial isotherm equation, the adsorption data of pure gases on the modified AC5-KS were fitted with good agreement in the whole temperature and pressure ranges studied. After the comparison between these results and those obtained in the original activated carbon R2030, it was observed that the CO_2 adsorption capacity was enhanced 17.5% at 7 bar and 303 K (10% when it is considered in volumetric terms due to the decrease of density after the physical activation of the adsorbent). In fact, the H_2, CH_4, and N_2 adsorption capacities of the modified adsorbent AC5-KS were also higher when compared to the respective pure gas adsorption capacity on the original activated carbon. Breakthrough experiments of CO_2, H_2, CH_4, CO and N_2 on the modified

adsorbent were performed to estimate the diffusivity parameters. The results show that, contributions of the film and macropore mass transfer resistances to the total dispersion were very small and the axial dispersion term is the most relevant dispersive mechanism for all gases. According to the micropore diffusivities obtained, the compound that more rapidly diffuses on AC5-KS is hydrogen, followed by N_2, CO, CH_4 and finally CO_2. It should be mentioned that a total of four kilograms of adsorbent was prepared using this technique to be supplied to an industrial partner within the HY2SEPS project.

Three ion exchanged zeolite samples (13X-Li, 13X-Ba, and 13X-Ca) were prepared with Li^+, Ba^{2+}, and Ca^{2+} starting from a commercial zeolite 13X in the Na-form (Trade/Shanli, China) in order to determine a protocol to enhance the N_2 capacity of the zeolite. After the characterization performed by SEM and EDX analyses, it was concluded that the crystals were not damaged or destroyed after performing the ion exchange and also a final total concentration of 0.076 $g_{calcium}/g_{material}$ on the structure of the modified zeolite 13X-Ca was achieved. It was observed that the use of zeolites 13X-Ba and 13-Ca will improve the N_2 adsorption for separations of this gas and, due to the higher adsorption capacity of N_2, the adsorbent chosen was the 13X-Ca. Therefore, N_2, CO_2, CH_4, CO and H_2 adsorption equilibrium and kinetics on zeolite 13X-Ca were studied. It was observed that the crystal diffusivities of H_2 in the zeolite 13X-Ca were higher than the values obtained for N_2, followed by CH_4, CO and finally CO_2. According to the results obtained for the ion exchanged zeolite 13X-Ca, it was also observed that the nitrogen adsorption capacity increased 36% (at 303 K and 1 bar) when compared to the original zeolite 13X.

Besides the study of adsorption equilibrium and kinetics of pure gases, to do the complete design of the H_2 purification unit, it is also important to determine adsorption data of multicomponent systems [22]. Therefore, adsorption data of multicomponent mixtures (binary, ternary and five-component) of SMR off-gases were studied for the activated carbons R2030 and AC5-KS. These experiments were then predicted using the multicomponent extension of the Virial model; it was concluded that suitable predictions of the adsorption equilibrium capacities and temperatures can be achieved using single-component parameters. To complete the validation of the model under cyclic conditions, a 10 steps single column PSA experiment was also performed considering the bed filled with activated carbon AC5-KS. Since the model previously used could satisfactorily predict the cyclic performance of the unit, it was concluded that a hydrogen recovery of 81.6% was obtained in the PSA experiment with a H_2 purity of 99.98054% contaminated with 63 ppm of CO (simulated values) and a process productivity of 101.1 $mol_{H2}\, kg_{ads}^{-1}\, day^{-1}$. Additionally, simulations of single column PSA processes were performed for two different cycles

(with 6 or 10 steps, including one or three pressure equalization steps, respectively) and different operating conditions, considering a bed packed with activated carbon AC5-KS. According to the simulations performed, it was observed that using three different pressure equalizations it is possible to achieve H_2 recoveries 15% higher than using only one pressure equalization but the concentration of the contaminants reaches the product end faster, contaminating the product. The simulations performed also showed that higher unit productivities (keeping H_2 purity over 99.99% with <10 ppm CO contamination) can be attained when the feed pressure is increased.

The final accomplishment of this thesis dealt with the study of fast cycling pressure swing adsorption processes through experiments and simulations. Since the RPSA facility was "adapted" from a PSA unit, the adequacy of the electronic equipment was analysed and it was concluded that it was possible to reduce the cycling time of the process to values around one minute. Different operating conditions in the limits of feed flow rate (from 1.167×10^{-5} to 8.33×10^{-5} $m^3\ s^{-1}$) were applied in binary H_2-CO_2 breakthrough experiments on AC5-KS to verify the possibility of occurring dispersive effects that may affect the fast cycling process. The results obtained showed that the micropore resistance controls the diffusion process. Furthermore, when velocity increases the smaller contact time between gas and solid phases resulted in more dispersed breakthrough curves. Afterwards, a single-column packed with AC5-KS was used in a RPSA process experiment, applying a 5 step cyclic sequence. The mathematical model previously used was able to predict the cyclic performance of the unit; thus, it could be concluded that 61.8% of hydrogen recovery was attained in the RPSA experiment, with a purity of 99.99280% (simulated value) and a process productivity of 598.8 $mol_{H2}\ kg_{ads}^{-1}\ day^{-1}$. According to RPSA simulations performed for different step times and streams flow rates, it was concluded that, without affecting the H_2 purity and reducing the hydrogen recovery no more than 11%, the productivity of the RPSA unit could increase around 600% when compared to classical PSA.

7.2 Suggestions for future work

Within this thesis, a gas chromatograph analysis system for determination of bed outlet concentrations of multicomponent gas mixtures of SMR off-gases (H_2, CO_2, CH_4, CO and N_2) was integrated in a "compact" PSA facility already existing at LSRE. The new analysis system was able to determine the bed outlet concentrations of all gases. However, it was found that it is extremely difficult to determine such high purities using the analysis system installed. The bed outlet concentrations were limited to the signal detected by the gas chromatograph, with a

minimum limit of accuracy of 100 ppm. Since the H_2 purification PSA process studied required the production of a high purity hydrogen stream (> 99.99%, with a CO contamination lower than 10 ppm), it would be interesting to analyse the bed outlet concentrations of the multicomponent gas mixtures with higher precision. For that, a different detector should be installed, such as the portable gas detectors that are able to analyse gas mixtures with 1-10 ppm accuracy.

According to the revised literature, different adsorbents with enhanced capacity, fast diffusion and high density were disclosed. Novel metal-organic framework (MOF) materials are reported [23-30]: Cu-MOFs, MOF Zn(BDC)(4,4'-Bipy)$_{0.5}$ (MOF-508b), isoreticular MOFs (IRMOFs), molecular squares (MOF-2), pores decorated with open metal sites (MOF-505 and $Cu_3(BTC)_2$), hexagonally packed cylindrical channels (MOF-74), interpenetration (IRMOF-11), amino- and alkyl-functionalized pores (IRMOF-3 and IRMOF-6) and extra-high porosity frameworks (IRMOF-1 and MOF-177). It was disclosed by Eddaoudi *et al.* (2002) that, one of these compounds, IRMOF-6, has pore sizes in the mesoporous range (20 Å), a tremendously low crystal density and it exhibits extremely high methane storage capacity [26]. On the other hand, substantially greater capacities for CO_2 than the other MOFs are reported for the $Zn_4O(O_2C)_6$-type frameworks of IRMOFs-11, -3, -6, and -1 [23]. According to Millward and Yaghi (2005), the voluminous space enclosed by MOF-177 results in a CO_2 capacity of 33.5 mol kg^{-1} (at room temperature and 45 bar) [23]. Later, Rejifu *et al.* (2009) [31] disclosed re-activated carbon fibres (re-ACFs) with high surface areas (the original surface area of 1730 m^2 g^{-1} was enhanced to 2930 m^2 g^{-1} after re-activation). Performing the re-activation of the ACFs, the amounts of CH_4 and H_2 adsorbed were enhanced by 52% and 30%, respectively [31]. Furukawa *et al.* (2010) [32] reported the ultrahigh surface areas (near the ultimate limit for solid materials) exhibited by MOF-200 and MOF-210, which have a volume specific surface area in the range of 1000 to 2000 m^2 cm^{-3} [32]. Li *et al.* (2009) [33] reported different MOFs, zeolitic imidazolate frameworks (ZIFs) and covalent organic frameworks (COFs) having exceptional surface areas and high capacities: hydrogen (7.5 wt% at 77 K and 30-40 bar), methane (50 wt% at 298 K and 25 bar) and carbon dioxide (140 wt% at 298 K and 30 bar). Moreover, CO_2-CH_4 separation studies on a flexible porous chromium terephthalate Cr(OH)(O_2C–C_6H_4–CO_2) material from Institute Lavoisier, MIL-53(Cr), were reported at ambient temperature [34]. Hamon *et al.* (2009) disclosed the potentiality of use of MIL-53(Cr) in a PSA process for the CO_2-CH_4 separation [34]. Thus, with so many and different high density materials having enhanced capacity and fast diffusion of several gases, it would be interesting to study one of the previously reported adsorbents for hydrogen purification systems. According to the data presented before, the PSA process performance can be enhanced if one (or

more) of these materials is applied.

However, the adsorbents reported before (MOFs, MILs, ACFs, etc) are extremely expensive. To avoid the costs of using high amounts of one (or more) of these adsorbents in the large columns of a conventional PSA unit, it would be more convenient to use smaller units. Thus, the amount of adsorbent used is smaller and the operating conditions can work in fast cycling. Consequently and according to the study performed within this thesis, since it was observed that small and large H_2 purification processes can be advantageously improved if fast cycling schemes are applied, the use of these materials in a RPSA unit could be extremely interesting and useful.

7.3 References

[1] M.S.A. Baksh, M.W. Ackley, Pressure swing adsorption process for the production of hydrogen (2002) U.S. Patent 6,340,382.

[2] M.S.A. Baksh, C.E. Terbot, Pressure swing adsorption process for the production of hydrogen (2003) U.S. Patent 6,503,299.

[3] R. Kumar, Adsorption process for recovering two high purity gas products from multicomponent gas mixtures (1990) U.S. Patent 4,913,709.

[4] R.L. Le Bec, Method for purifying hydrogen-based gas mixtures using calcium X-zeolite (2005) U.S. Patent 6,849,106.

[5] A.E. Rodrigues, M.D. LeVan, D. Tondeur, Adsorption: Science and Technology, Kluwer, Boston, MA, 1989.

[6] S. Sircar, Separation of multicomponent gas mixtures (1979) U.S. Patent 4,171,206.

[7] S. Sircar, W.E. Waldron, M.B. Rao, M. Anand, Hydrogen production by hybrid SMR-PSA-SSF membrane system, Sep. Purif. Technol. 17 (1999) 11-20.

[8] R.T. Yang, Gas Separation by Adsorption Processes, Butterworths, Boston, 1987.

[9] M. Chlendi, D. Tondeur, Dynamic Behaviour of Layered Columns in Pressure Swing Adsorption, Gas Sep. Purif. 9 (1995) 231.

[10] J.-H. Park, J.-N. Kim, S.-H. Cho, J.-D. Kim, R.T. Yang, Adsorber dynamics and optimal design of layered beds for multicomponent gas adsorption, Chem. Eng. Sci. 53 (1998) 3951-3963.

[11] I.A.A.C. Esteves, J.P.B. Mota, Simulation of a new hybrid membrane/pressure swing adsorption process for gas separation, Desalination. 148 (2002) 275-280.

[12] J.-H. Park, J.-N. Kim, S.-H. Cho, J.-D. Kim, R.T. Yang, Adsorber dynamics and optimal design of layered beds for multicomponent gas adsorption, Chemical Engineering Science. 53 (1998) 3951-3963.

[13] D.M. Ruthven, S. Farooq, K.S. Knabel, Pressure swing adsorption, VCH Publishers, New York, 1994.

[14] A. Jayaraman, A.S. Chiao, J. Padin, R.T. Yang, C.L. Munson, Kinetic separation of methane/carbon dioxide by molecular sieve carbons, Separation Science and Technology. 37 (2002) 2505 -2528.

[15] R.P. Marathe, K. Mantri, M.P. Srinivasan, S. Farooq, Effect of ion exchange and dehydration temperature on the adsorption and diffusion of gases in ETS-4, Industrial and

Engineering Chemistry Research. 43 (2004) 5281-5290.

[16] R.M. Barrer, Sorption in porous crystals: equilibria and their interpretation, Journal of Chemical Technology and Biotechnology. 31 (1981) 71-85.

[17] A.V. Kiselev, Vapor adsorption on zeolites considered as crystalline species adsorbents, Molecular Sieve Zeolites-II, ACS series. 102 (1971) 37.

[18] T. Nitta, T. Shigetomi, M. Kuro-Oka, T. Katayama, An adsorption isotherm of multi-site occupancy model for homogeneous surface, Journal of Chemical Engineering of Japan. 17 (1984) 39-45.

[19] HY2SEPS, Hybrid Hydrogen Carbon Dioxide Separation Processes, E.U. Res. Project 2005, Available from: http://hy2seps.iceht.forth.gr/.

[20] F.V.S. Lopes, C.A. Grande, A.M. Ribeiro, E.L.G. Oliveira, J.M. Loureiro, A.E. Rodrigues, Enhancing capacity of activated carbons for hydrogen production, Industrial and Engineering Chemistry Research. 48 (2009) 3978-3990.

[21] F.V.S. Lopes, C.A. Grande, A.M. Ribeiro, V.J.P. Vilar, J.M. Loureiro, A.E. Rodrigues, Effect of ion exchange on the adsorption of SMR off-gases on zeolite 13X, Journal of Chemical and Engineering Data. 55 (2010) 184-195.

[22] J.A. Ritter, R.T. Yang, Equilibrium adsorption of multicomponent gas mixtures at elevated pressures, Industrial and Engineering Chemistry Research. 26 (1987) 1679-1686.

[23] A.R. Millward, O.M. Yaghi, Metal-organic frameworks with exceptionally high capacity for storage of carbon dioxide at room temperature, Journal of the American Chemical Society. 127 (2005) 17998-17999.

[24] K.S. Walton, A.R. Millward, D. Dubbeldam, H. Frost, J.J. Low, O.M. Yaghi, R.Q. Snurr, A.R. Millward, Understanding inflections and steps in carbon dioxide adsorption isotherms in metal-organic frameworks, Journal of the American Chemical Society. 130 (2008) 406-407.

[25] T. Düren, L. Sarkisov, O.M. Yaghi, R.Q. Snurr, Design of new materials for methane storage, Langmuir. 20 (2004) 2683-2689.

[26] M. Eddaoudi, J. Kim, N. Rosi, D. Vodak, J. Wachter, M. O'Keeffe, O.M. Yaghi, Systematic design of pore size and functionality in isoreticular MOFs and their application in methane storage, Science. 295 (2002) 469-472.

[27] S. Cavenati, C.A. Grande, A.E. Rodrigues, C. Kiener, U. Müller, Metal organic framework adsorbent for biogas upgrading, Industrial and Engineering Chemistry Research. 47 (2008) 6333-6335.

[28] P.S. Bárcia, L. Bastin, E.J. Hurtado, J.A.C. Silva, A.E. Rodrigues, B. Chen, Single and multicomponent sorption of CO_2, CH_4 and N_2 in a microporous metal-organic framework, Separation Science and Technology. 43 (2008) 3494 - 3521.

[29] L. Bastin, P.S. Barcia, E.J. Hurtado, J.A.C. Silva, A.E. Rodrigues, B. Chen, A microporous metal−organic framework for separation of CO_2/N_2 and CO_2/CH_4 by fixed-bed adsorption, The Journal of Physical Chemistry C. 112 (2008) 1575-1581.

[30] L. Hamon, E. Jolimaître, G.D. Pirngruber, CO_2 and CH_4 separation by adsorption using Cu-BTC metal−organic framework, Industrial and Engineering Chemistry Research. 49 (2010) 7497-7503.

[31] A. Rejifu, H. Noguchi, T. Ohba, H. Kanoh, F. Rodriguez-Reinoso, K. Kaneko, Adsorptivities of extremely high surface area activated carbon fibres for CH_4 and H_2, Adsorption Science and Technology. 27 (2009) 877-882.

[32] H. Furukawa, N. Ko, Y.B. Go, N. Aratani, S.B. Choi, E. Choi, A.O. Yazaydin, R.Q. Snurr, M. O'Keeffe, J. Kim, O.M. Yaghi, Ultrahigh porosity in metal-organic frameworks, Science. 329 (2010) 424-428.

[33] Q. Li, O.M. Yaghi, Reticular chemistry and metal-organic frameworks for clean energy, Materials Research Society: MRS Bulletin. 34 (2009) 682-690.

[34] L. Hamon, P.L. Llewellyn, T. Devic, A. Ghoufi, G. Clet, V. Guillerm, G.D. Pirngruber, G. Maurin, C. Serre, G. Driver, W. van Beek, E. Jolimaître, A. Vimont, M. Daturi, G. Férey, Co-adsorption and separation of CO_2-CH_4 mixtures in the highly flexible MIL-53(Cr) MOF, Journal of the American Chemical Society. 131 (2009) 17490–17499.